

マス・フォア・インダストリ研究 No.12

A decorative graphic consisting of two circles, one yellow and one green, positioned above a thick, wavy line that transitions from green on the left to yellow on the right. The main title is centered over this graphic.

Non-destructive inspection for concrete structures and related topics

Institute of Mathematics for Industry
Kyushu University

編集 滝口 孝志

九州大学マス・フォア・インダストリ研究所

About the Mathematics for Industry Research

The Mathematics for Industry Research was founded on the occasion of the certification of the Institute of Mathematics for Industry (IMI), established in April 2011, as a MEXT Joint Usage/Research Center – the Joint Research Center for Advanced and Fundamental Mathematics for Industry – by the Ministry of Education, Culture, Sports, Science and Technology (MEXT) in April 2013. This series publishes mainly proceedings of workshops and conferences on Mathematics for Industry (MfI). Each volume includes surveys and reviews of MfI from new viewpoints as well as up-to-date research studies to support the development of MfI.

October 2018

Osamu Saeki

Director

Institute of Mathematics for Industry

Non-destructive inspection for concrete structures and related topics

Mathematics for Industry Research No.12, Institute of Mathematics for Industry, Kyushu University

ISSN 2188-286X

Editors: Takashi Takiguchi

Date of issue: ○ February 2019

Publisher:

Institute of Mathematics for Industry, Kyushu University

Motooka 744, Nishi-ku, Fukuoka, 819-0395, JAPAN

Tel +81-(0)92-802-4402, Fax +81-(0)92-802-4405

URL <http://www.imi.kyushu-u.ac.jp/>

Printed by

Social Welfare Service Corporation Fukuoka Colony

1-11-1, Midorigahama, Shingu-machi Kasuya-gun, Fukuoka, 811-0119, Japan

TEL +81-(0)92-962-0764 FAX +81-(0)92-962-0768

Non-destructive inspection for
concrete structures and related
topics

編集 : 滝口 孝志

Table of contents

1. Development and operation of the non-destructive inspection devices for road structures	1
<i>Kenji Hashizume (West Nippon Expressway Engineering Shikoku Company Limited)</i>	
2. Introduction and Application of CED-based Fracture Mechanics	47
<i>Cheng Hua (Department of Aeronautics and Astronautics, Fudan University, Shanghai, China)</i>	
3. Structure of the least square solutions and its application to non-destructive inspections	103
<i>(Takashi Takiguchi (Department of Mathematics, National Defense Academy of Japan)</i>	
4. A non-destructive inspection to probe the reinforcing steel in RC structures by electromagnetic induction method	149
<i>(Takayuki Ochi (Shikoku Polytechnic College)</i>	
5. Nondestructive inspection of biological tissue by optical tomography	191
<i>Manabu Machida (Institute for Medical Photonics Research, Hamamatsu University School of Medicine)</i>	
6. Exact probe of the reinforcing steel in RC structures by application of ultrasonic CT	221
<i>Toshiaki Takabatake (West Nippon Expressway Engineering Shikoku Company Limited)</i>	

Preface

These are the proceedings of the workshop “Non-destructive inspection for concrete structures and related topics”, held at IMI, Kyushu University, from October twenty third to October twenty sixth, 2018. During the workshop, the following researches were reported and lively discussions were had on them.

- Dr. Kenji Hashizume : Development and operation of the non-destructive inspection devices for road structures.
- Prof. Cheng Hua : Introduction and Application of CED-based Fracture Mechanics
- Takashi Takiguchi : Structure of the least square solutions and its application to non-destructive inspections
- Prof. Takayuki Ochi : A non-destructive inspection for the reinforcing steel in RC structures by electromagnetic induction method
- Prof. Manabu Machida : Nondestructive inspection of biological tissue by optical tomography
- Mr. Toshiaki Takabatake : Exact probe of the reinforcing steel in RC structures by application of ultrasonic CT

On the first day of the workshop, Doctor Kenji Hashizume gave a talk to introduce the inspection techniques for the expressways developed by West Nippon Expressway Engineering Shikoku Company Limited. It is surprising that his talk necessarily contains new technology developed by West Nippon Expressway Engineering Shikoku Company Limited every year. In his talk, we created a new research task that non-integer dimensional analysis for the cracks on the road is very important to predict the outbreaks of the potholes.

In the morning on the second day, Professor Cheng Hua gave a talk on the problem “How to give a mathematical representation of the crack propagation in viscoelastic composite materials”, which may be a key research to predict when and where a pothole breaks out on the expressway happens. He proposed a mathematical treatment how to develop the CED method in order for it to be applied for viscoelastic crack propagation. During his talk, many questions are asked on the future development of the modification of CED method and lively discussions were had on this problem.

In the afternoon, the organiser introduced his research on the structure of the least square solutions to overdetermined systems, which would be applied in the theories by Prof. Ochi and by Mr. Takabatake in this workshop. The structure introduced in this talk will also play an important role in 3D reconstruction of asteroids by 2D pictures, which shall be studied in our forthcoming workshops.

In the morning on October 25th, Professor Takayuki Ochi presented how to detect the exact position of the rebar in RC (reinforced concrete) structures, which is recognized as a difficult open problem in the study of concrete structures for the time being. In this study, a device with electromagnetic induction was applied for the measurement of the position of the rebar and inaccuracy of the measurements were modified by application of the least square solution based on the theory of the organizer's talk. This work was based on the collaboration among architecture (Ochi), mathematics (Takiguchi) and a private company (Hashizume and Takabatake).

In the afternoon, Professor Manabu Machida introduced his research on the development of optical tomography. X-ray CT and MRI being superior non-invasive inspection technique, their costs are very expensive and negative effects of the X-ray to human body and the environment cannot be ignored, in view of which, new non-invasive technologies are under investigation. In this talk, Prof. Machida presented inverse problems of the transport equation for the development of optical tomography, where approximation of the transport equation by a diffusion equation was studiously discussed.

On the final day, Mister Toshiaki Takabatake talked about exact probe of the rebar in RC structures by ultrasonic measurements, where the improvement of Prof. Ochi's talk was attempted. In this talk, the structure of the least square solutions presented by the organizer on the second day played an important part. This work was based on the industry-academia collaboration among a private company (Hashizume and Takabatake), mathematics (Takiguchi) and architecture (Ochi).

In this workshop, we have created new research tasks to be solved by industry-academia and interdisciplinary collaboration. We wish that we would have more opportunities to hold such workshops to study these important problems. We also hope that such collaboration be much more popular.

At the end of Preface, I would express my gratefulness to Ms. Kazuko Ito and Ms. Chiemi Furutani, the secretaries of this workshop, for their help.

January 26, 2019

Takashi Takiguchi

Non-destructive inspection for concrete structures and related topics

October 23-26, 2018

IMI, Ito Campus, Kyushu Univeristy
Room M W1-C-513, West Zone 1,
744 Motooka, Nishi-ku Fukuoka 819-0395, Japan

October 23, Tuesday

13:50 Opening

(Chair: C. Hua)

14:00-15:30 Kenji Hashizume
(West Nippon Expressway Shikoku Engineering Company Limited, Japan)
Development and operation of the non-destructive inspection devices
for road structures

15:30-16:30 Discussion

October 24, Wednesday

(Chair: T. Ohe)

11:00-12:30 Cheng Hua (Fudan University, China)
Introduction and Application of CED-based Fracture Mechanics

12:30-14:00 Discussion over lunch

14:00-15:30 Takashi Takiguchi (National Defense Academy of Japan, Japan)
Structure of the least square solutions
and its application to non-destructive inspections

15:30-16:30 Discussion

October 25, Thursday

(Chair: T. Takiguchi)

11:00-12:30 Takayuki Ochi (Shikoku Polytechnic College, Japan)
A non-destructive inspection for the reinforcing steel
in RC structures by electromagnetic induction method

12:30-14:00 Discussion over lunch

14:00-15:30 Manabu Machida (Hamamatsu University School of Medicine, Japan)
Nondestructive inspection of biological tissue by optical tomography

15:30-16:30 Discussion

October 26, Friday

(Chair: N. Mita)

11:00-12:30 Toshiaki Takabatake
(West Nippon Expressway Shikoku Engineering Company Limited, Japan)
Exact probe of the reinforcing steel in RC structures
by application of ultrasonic CT

12:30-14:00 Discussion over lunch

14:00 Closing

Organizer:

Takashi Takiguchi (National Defense Academy of Japan)

Supported by:

IMI, Kyushu University

Development and operation of the non-destructive inspection devices for road structures

Kenji Hashizume

West Nippon Expressway Engineering Shikoku Company Limited
3-1-1 Hanazono-cho, Takamatsu-shi, Kagawa 760-0072, Japan
Email: kenji.hashizume@w-e-shikoku.co.jp

In this talk, we introduce the latest trend about our inspection devices and the techniques, which are introduced into the inspection of expressway. We suggest the development of the devices, which enable objective evaluation and record for inspection of bridge, tunnel and pavement. We also introduce how we manage roads by the devices we have developed.

Key Words: inspection, non-destructive, infrared, light cutting method

1. Introduction

In order to secure the social durability of infrastructure, the following matters are indispensable. (1) To maintain and manage the organized infrastructure efficiently and effectively. (2) To prevent the outbreak of risk events of damage due to aging of infrastructure. Therefore, it is important to inspect and repair the infrastructure efficiently and effectively.

Accordingly the efficient and effective inspection and repairing would be very important. For the given purpose, the efficient and effective inspections and maintenance practice shall be necessary. The inspection method using the non-destructive inspection devices for the bridges, tunnels, and pavements inspections with objective evaluations and keeping their records is now proposed. In this talk, we suggest the development of the devices, which enable objective evaluation and record for inspection of bridge, tunnel and pavement. We also introduce how we manage roads by the devices we have developed.

2. New devices for inspection

2.1 Bridge Inspections

We now explain the “J-System” (Figure-1) for the inspection method using the infrared cameras. The reinforced concrete fulfill its role with the joint functioning of rebar and concrete for the concrete structure. When the rebar gathers rust in the concrete, cracks appear on the concrete surface along the rebar, the surface concrete spalls, and so its durability is to be reduced. We have been inspecting the cracks triggered by the concrete delaminations along the rebar through the hammering. The infrared cameras inspection is the new one detecting the damaged areas such as concrete delaminations and cracks through photographing the concrete surface by using infrared cameras from remote palaces, and keeping the records of the concrete surface conditions using digital cameras. The inspections of bridges surface by infrared cameras are done by the passive method, and the followings are the important elements;



figure -1 J-system

i. Cameras Quality (Is the cameras suitable for the inspection environment?)

Inspections are done basically during night, so it is important to extend the surveillance hours of the day and increase the annual surveillance days by using the camera with a short-wave type which has no the environmental reflections during night and with a enforcing-cooling-system type with a small thermal resolution.

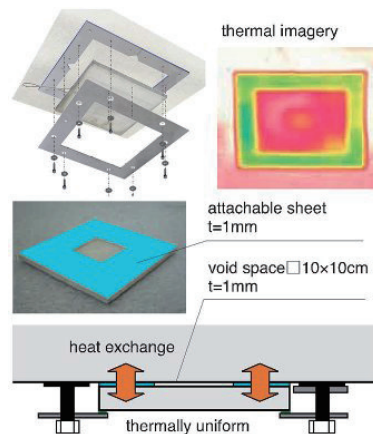


figure -2 J-system EM(S)

ii. Judgment on time zone of the day when inspections can be done (Do we inspect at a suitable time ?)

We implement the night- time inspection basically, because there are various bridge types and bridge members which are not suitable to inspect during daytime. The time zone of the day when inspection is possible is based on data

of the EMS (Environment Measuring System)(Figure-2) mounted on the inspection bridges.

iii. Simple and Objective Evaluation Method (Is it possible and easy to evaluate objectively?)

There could be, for individuals, differences among the inspection judgments because it is sometime impossible to judge the damage evaluation such as delamination and spalling for the bridge members and damaged parts only by looking at the infrared images. It is also impossible to judge the crack's depth along the rebar. However, the red, yellow, and blue cracks' judgment- images at the 1, 2, 3 cm depth from the surface are shown at the camera monitor (Figure

-3).



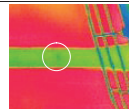
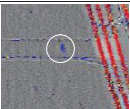


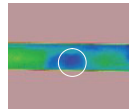
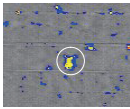


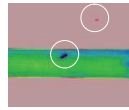
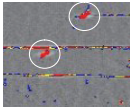
Damage grade	Visible image	Infrared image	3 level indication
Observation Abnormal sound 			
Caution Possibility of falling down near future 			
Warning Require emergency measure 			

figure -3 J-System Monitor Image

2.2 Tunnel and Pavement Inspection

2.2.1 Tunnel and Pavement Inspection

We now explain the “L & L System” (Figure-4) inspection method which uses the Line Censor Camera and Laser Marker. Line Censor cameras mount the visual image sensors, and can photograph seamless and continuous imageries. They can also be applied for the tunnel and pavement inspections. Light Cutting method is photographing the laser marker images from a upper and oblique position by using the laser which is irradiated vertically down on measuring surfaces and obtain the object shape. This method is used for road surface profile measuring.



figure -4 L&L System

i. Tunnel Inspection

It is possible to obtain the fine and colorful continuous images (Figure-5) of tunnel lining by using Line Censer cameras mounted on the inspection cars with high speed (less than 100km/h). The cracks of tunnel lining can be detected up to 0.2mm, and water leakage and lime isolation can be also found. The damage spreading drawings and their diagonal charts can easily be produced based on the captive pictures, and so we inspect only the areas where further close and detail investigations are necessary. And we can clearly watch the conditions of rusted accessories in tunnels, and so it is now possible to apply them for the accessories inspections.

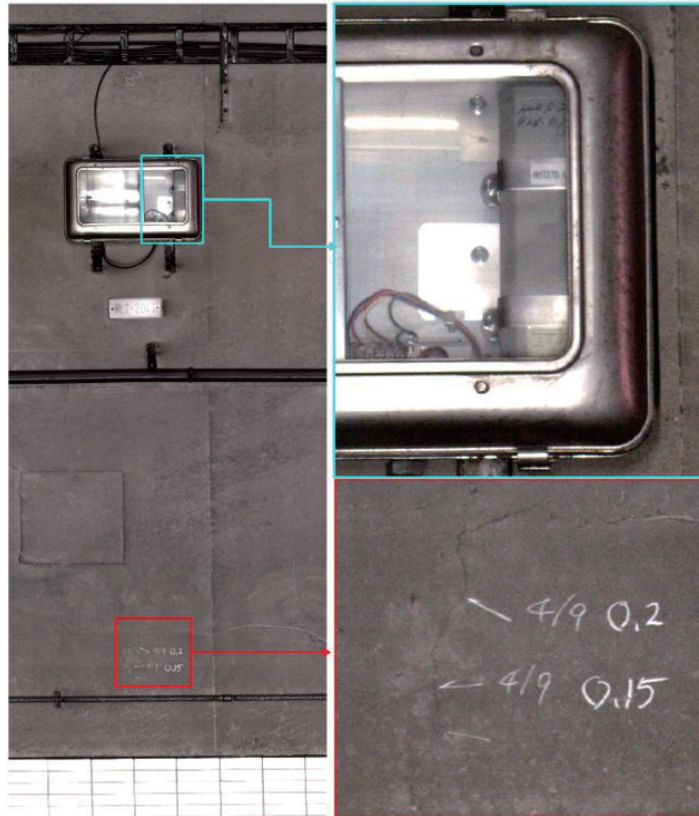


figure -5 Visual image with cracks and the accessories

ii. Pavement Inspection

We can inspect the pavement conditions such as cracks and potholes, and conditions of bridge expansion joints by using Line Censer cameras mounted on the vehicle with high speed (less than 100km/h). At the same time, we can also measure rutting, bumps, and upheaval through using laser cameras, and measure road surface profile such as height, and also evaluate the evenness, bump and IRI values.

We can also display the grade evaluation for the cracks, rutting, bumps,

evenness, and IRI values obtained by the road surface measurements, and we can also easily sort and extract some of the data with abnormal ranges which show more than a certain threshold (Figure-6). Thus, the repairing and renewal plans of road pavement and the bumps will be made easier.

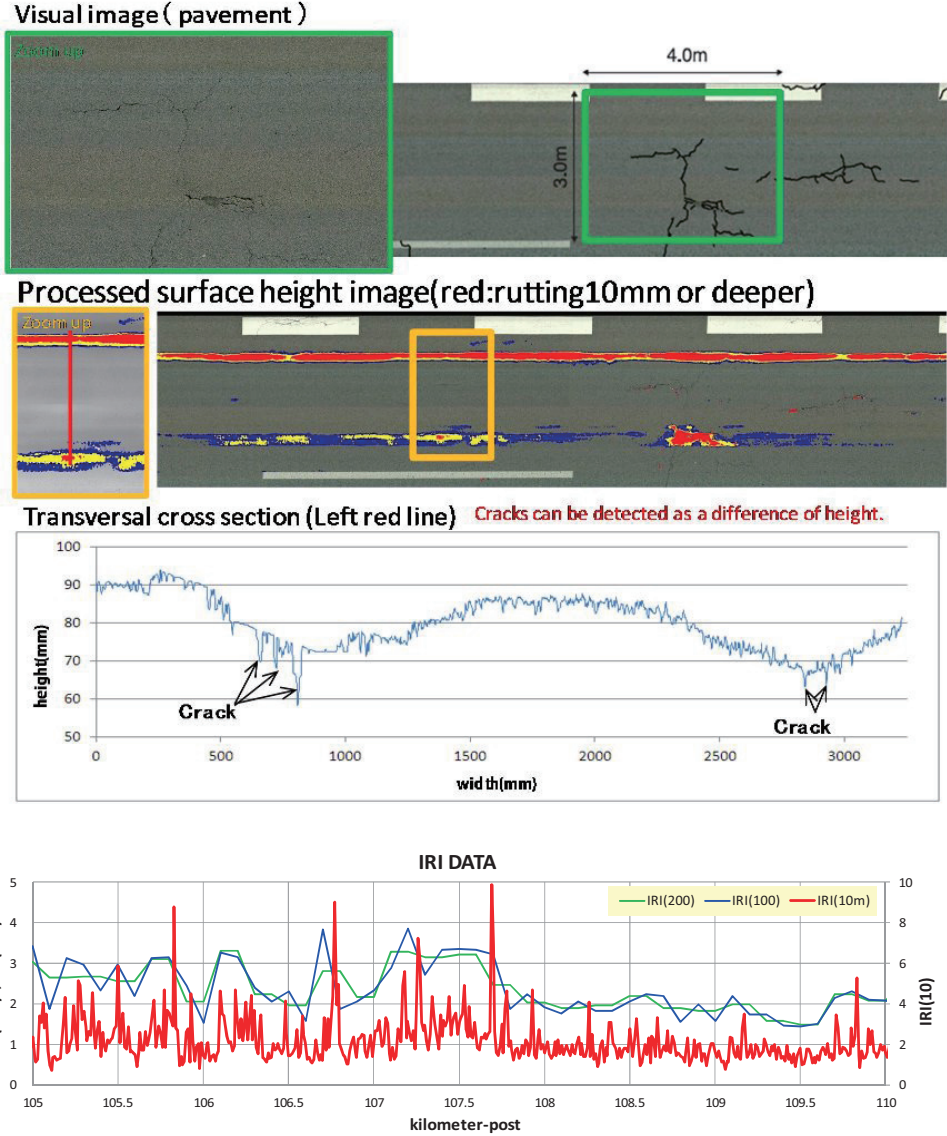


figure -6 Pavement evaluation

3. Topic technology

3.1 Tunnel Inspection new system “Smart-Eagle type-T”

We are considering a method to evaluate the risk of crashing of tunnel concrete (Figure-7). In this technique, we measure the unevenness of the surface with shape measurement precisely and judge the danger from its shape. In the future, I would like to propose unique evaluation methods based on visible and shape data.



figure -7 Smart Eagle type-T

3.2 Pavement Inspection new system “Smart-Eagle type-P”

Currently, a technology that can easily grasp each index of the road surface properties required for pavement management attracts attention (Figure-8). This technology reduces the investigation cost which was the problem of the conventional road surface property investigation, and shortens the analysis time.



figure -8 Smart Eagle type-P

This system has the following features

- Free equipment installation
- Automatic analysis
- Proposing a new evaluation indicator to extract damage(MPD by vehicle)

By measuring with high frequency, it is possible to grasp the current situation quickly. Also, by analyzing accumulated data, it can contribute to formulation of inspection and repair plan according to the actual situation.

4. Conclusion

The bridges, tunnels, and pavement inspections by cameras can be used for the assistances for the on-site inspections or their alternatives, and we can maintain the objective evaluations and predict the future damages through their annual transitions. Also the repairing plan can be made easily and efficiently. The proposed inspection method using the cameras makes it possible to use, select and combine those inspection tools economically and effectively in

accordance with budgets and utilization patterns of each organization based on their different road structure maintenance and repairing standards.

This work is partially based on the discussions at 2018 IMI Joint Use Research Program Workshop (II) "Non-destructive inspection for concrete structures and related topics"

Reference

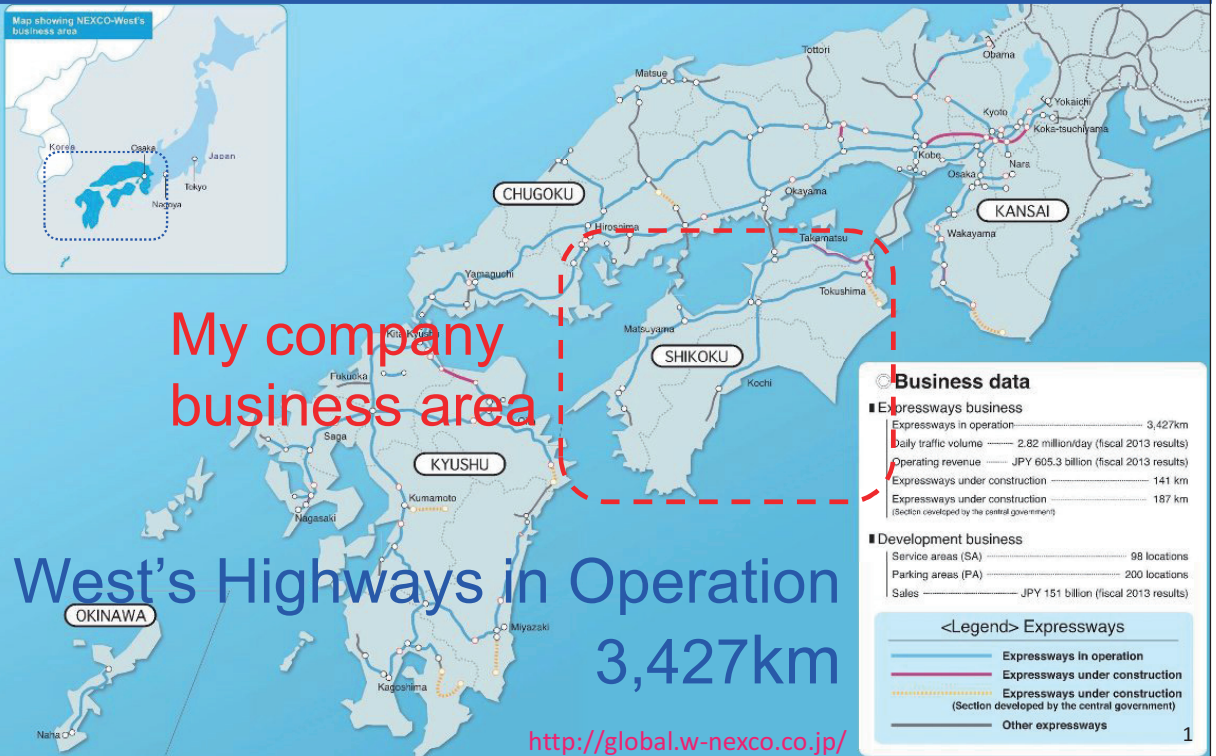
- 1) A study for detection accuracy improvement in the infrared thermography method, J.JCI, vol.34, No.1, 1696-1701, 2012
- 2) Predictive probability of the concrete delamination and damage by an infrared thermography method, J.JCI, vol.35, No.1, 1813-1818, 2013
- 3) One approach of the forecasting method for the pot-hole occurred by the deterioration of deeper than binder course on porous asphalt pavement, J.JSCE, Ser.E1, vol.70, No.3, I_17-I_24, 2014

Development and operation of the non-destructive inspection devices for road structures



West Nippon Expressway Shikoku Company Limited.

West's Japan highway business area Map



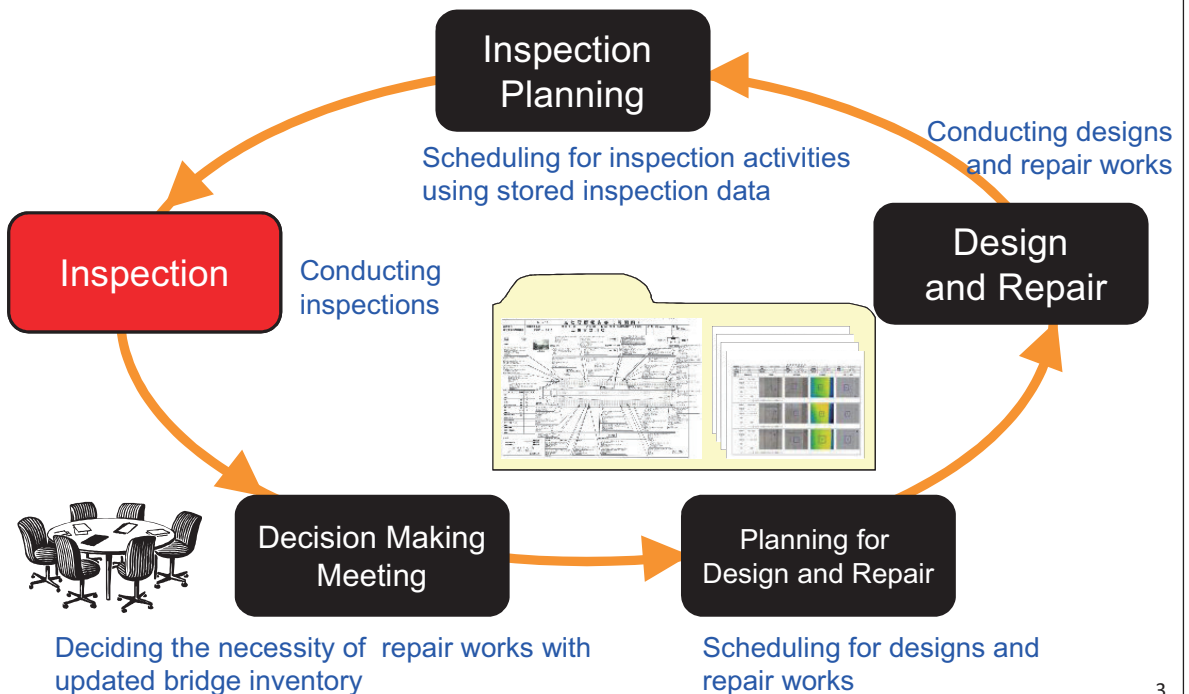
The NEXCO-West Group Policy

100% Safety and Reliability






2

Operation and Maintenance Management



3

Inspection Types

Type	Procedure	Frequency
Daily Inspection 	Visible unusual conditions and deformations of structures are daily inspected behind the wheels.	Once every two days to Once every four days (Dependent on traffic volume)
Routine Inspection 	The safety of the structure is regularly confirmed by distant visual inspection, cross visual inspection and hammering test.	More than once a year
Detailed Inspection 	The safety of the structure is understood by cross visual inspection and hammering test more in detail.	Once every five years

4

Proposal of our technology



J-System

- We developed this technology to gain effective inspection in order to comply Road Management rule
- After analyzing accumulated data we propose an Evaluation Indicator that related in order to understand deterior mechanism of Architectural structure and to do a preventive action



Eagle

【Our approachment】

Not just hand over a complete system, but we submit a proposal by finding out the needs from user and design the machine based on measurement accuracy as needed and customize soft ware that easy to use

5

Contents

I . Approach and issues for preventing concrete accident flaking

I -1. Bridge

(reinforced concrete structure)

I -2. Tunnel

(unreinforced concrete structure)

II . Approach and issues for identity of pavement damages

6

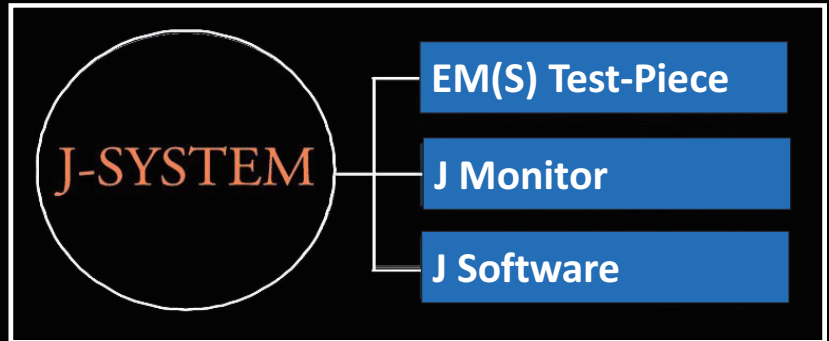


7

J -SYSTEM



A new concrete inspection and assessment method with safer manipulating, higher performance, and lower cost based on infrared thermography technology.



8

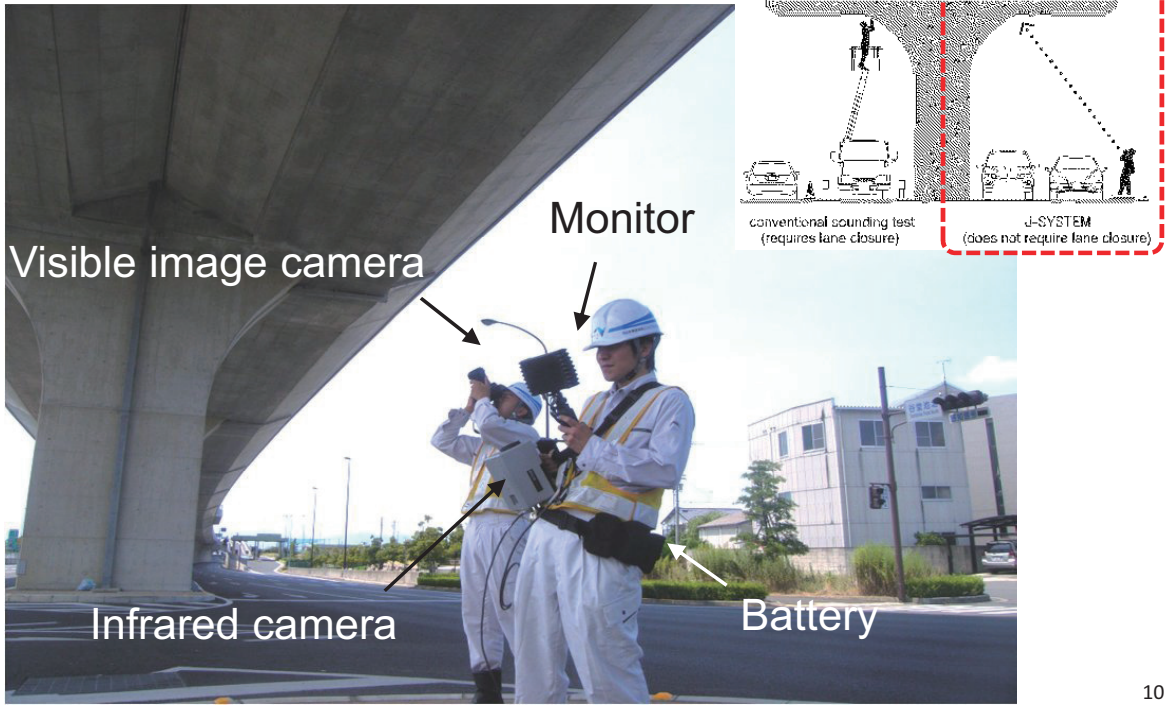
Sounding inspection for prevention measure against flaking



Present method needs a lot of costs and time

9

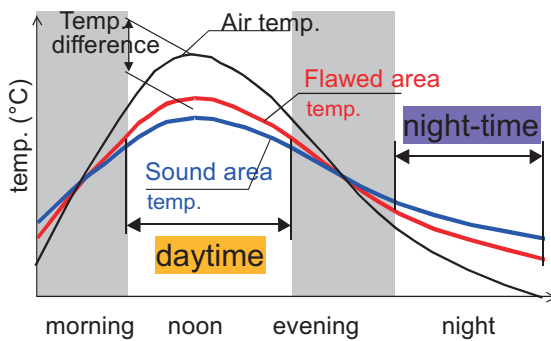
Infrared inspection situation



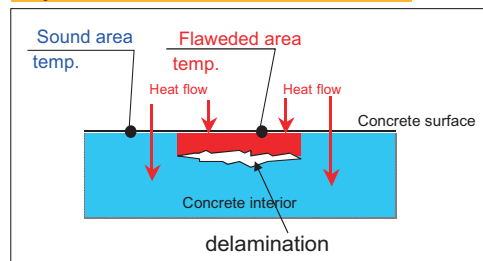
10

Basic Theory of Infrared Thermography

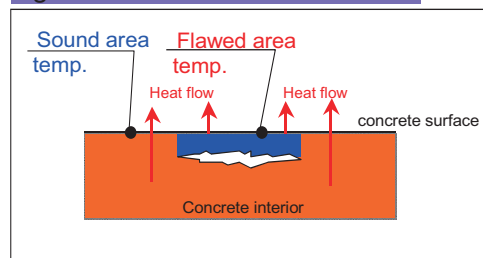
Inspection must be done when the temperature difference between air and concrete is large enough.



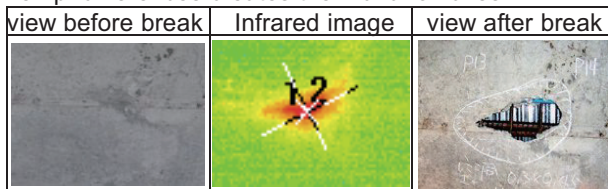
daytime : sound < flawed < air



night-time : sound > flawed > air



Temp. differences creates thermal anomalies



11

Relationship between Inspection time, and bridge type or part

Direction of heat flow and temperature in damage part

Section	Surface to be inspected	Direct effect	Indirect effect
All bridges			
Metal bridge		Surface to be inspected is not directly exposed to sunlight	
Box beam bridge		Surface to be inspected is not directly exposed to sunlight	

Inspection time should be selected by bridge type or part

12

Inspection time period of each bridge type

Seto Inland Sea climate during summer/autumn

Inspection time period

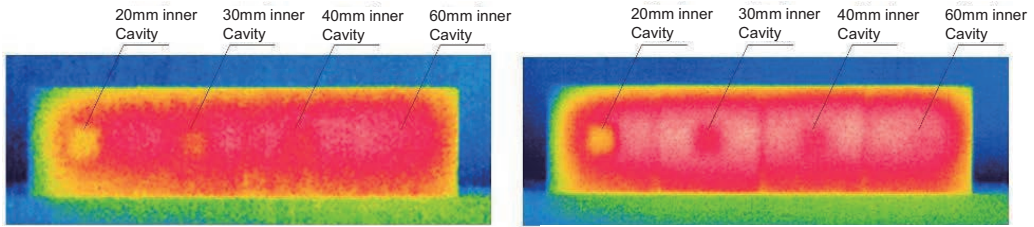
Bridge type	Section	Time												
		6	8	10	12	14	16	18	20	22	24	2	4	
All bridges	Wall balustrade		█	█	█	█		█	█	█	█	█	█	█
RC bridge	Overhang									█	█	█	█	█
	Floor slab			█	█	█	█					█	█	█
Me bridge	Overhang	█								█	█	█	█	█
	Floor slab	█								█	█	█	█	█
Box beam bridge	Overhang	█								█	█	█	█	█
	Floor slab									█	█	█	█	█
PC bridge	Overhang	█								█	█	█	█	█
	Girder			█	█	█	█					█	█	█
	Floor slab	█								█	█	█	█	█

Almost all bridge types and bridge sections can be investigated during night time.

13

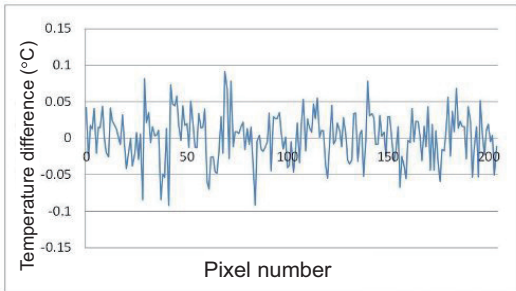
Images of damage from different minimum detected temperatures

Thermal images of different minimum detected temperatures (NETD)
 (Daily range = 10°C: photographed at 0 a.m.)



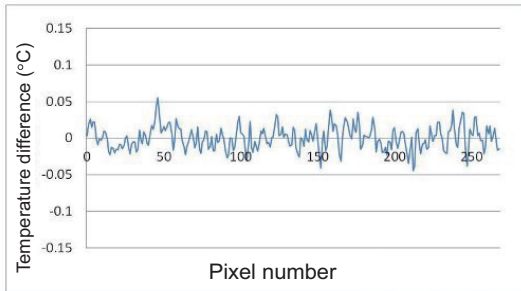
a) Thermal image photographed by Camera A

b) Thermal image photographed by Camera B



Standard deviation = 0.034 °C

a) Temperature variation of Camera A



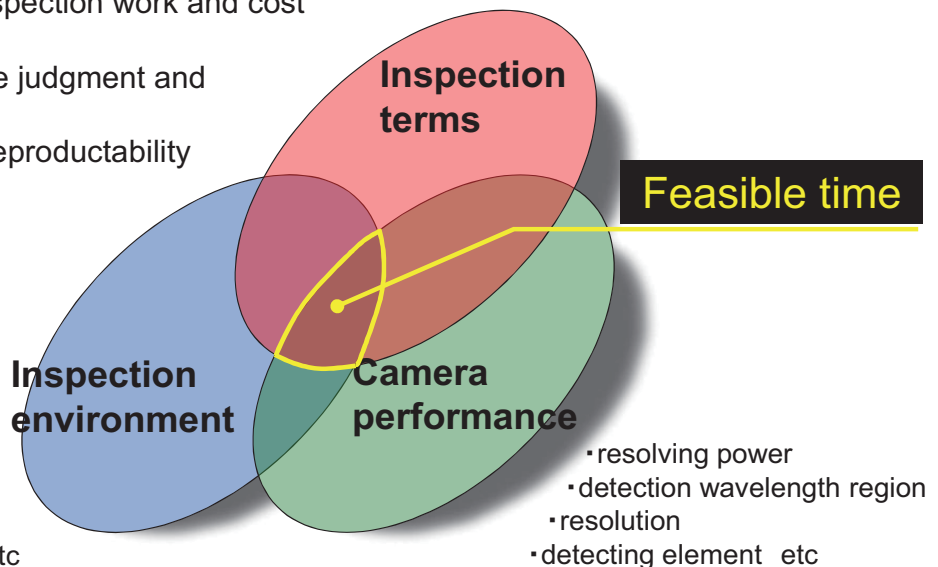
Standard deviation = 0.016 °C

b) Temperature variation of Camera B

Issues for accurate infrared inspection

- clarification of inspection depth
- quality guarantee and prevention of missing damage
- high efficient inspection work and cost performance
- efficient damage judgment and objectivity
- recording and reproductability

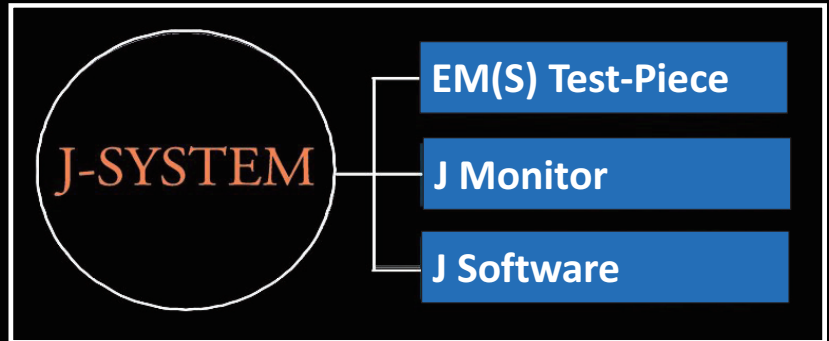
- kind of bridge, part
- detection depth
- photographing distance etc



J -SYSTEM

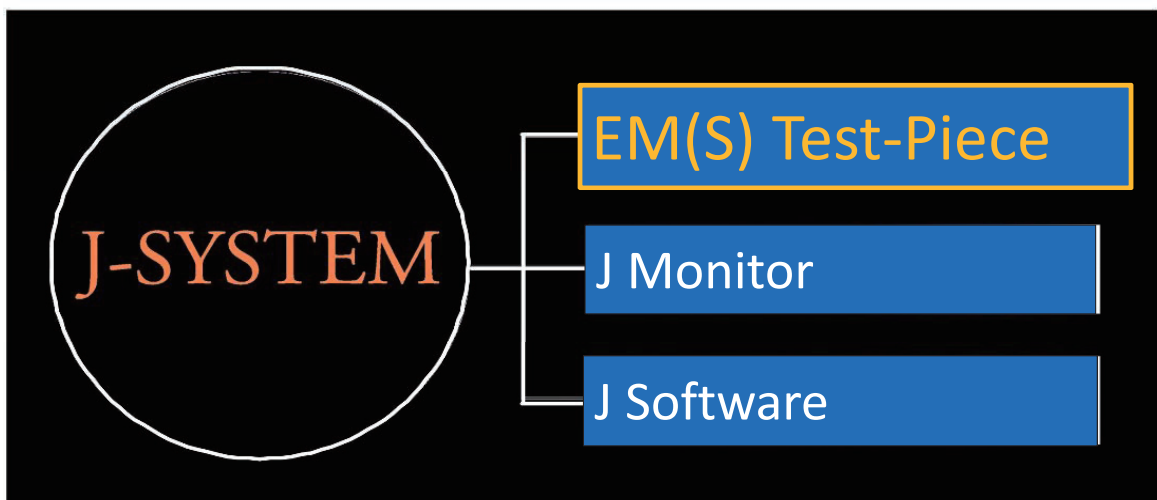


A new concrete inspection and assessment method with safer manipulating, higher performance, and lower cost based on infrared thermography technology.



16

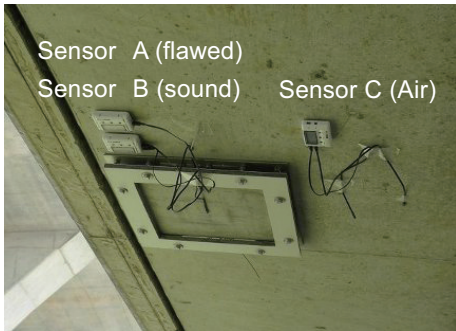
EM(S): On-the-spot Test Piece



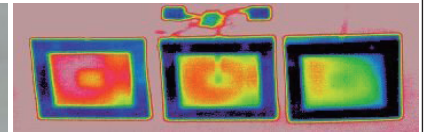
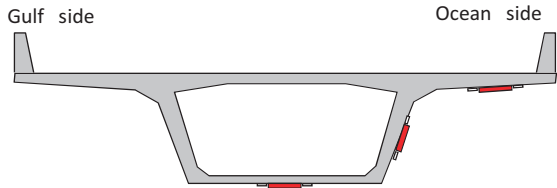
To ensure thermal condition of real structure for infrared testing before and during infrared inspection

17

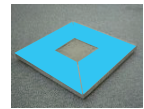
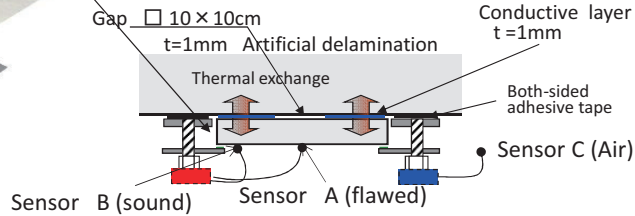
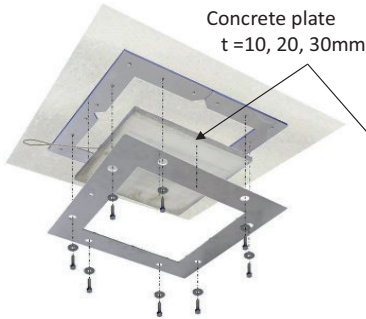
EM(S) : On-the-spot Test-Piece



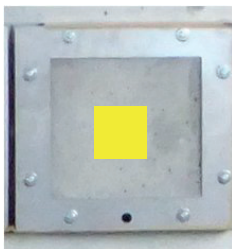
To obtain real temperature data under actual conditions element by element



t = 10mm 20mm 30mm

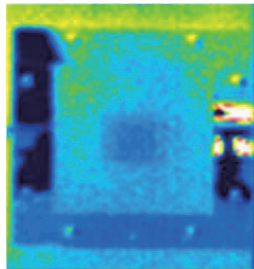


Do we inspect at a suitable time ?

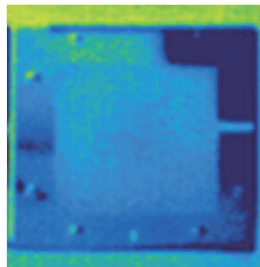


EM(S)

Checking central Void



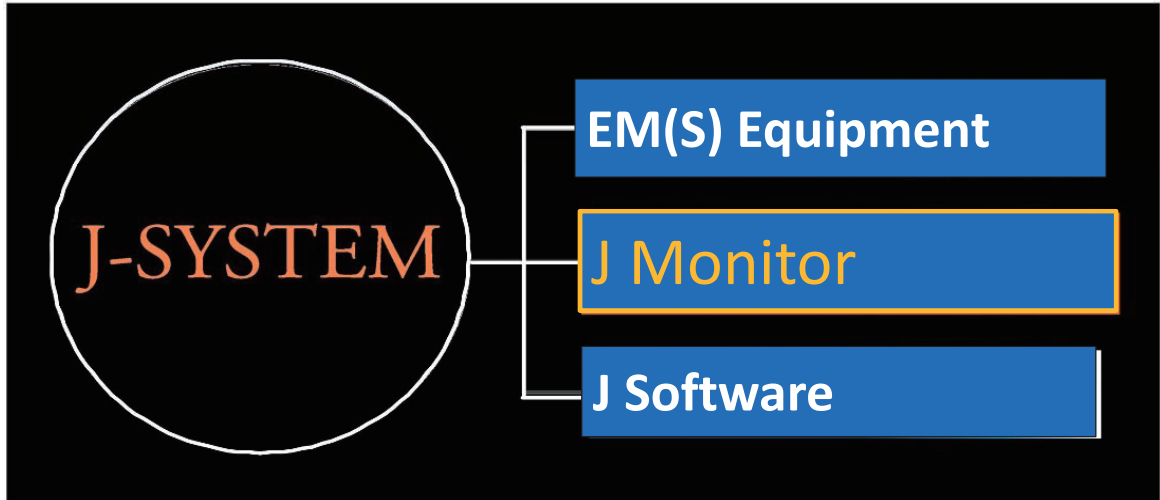
IR Image
Central cavity is observed.
→ OK



IR Image
Cavity is not observed.
→ NG

The thermal environment should be precisely obtained by an EM(S) device before any investigation

J Monitor: A Display for IR images in Real Time



20

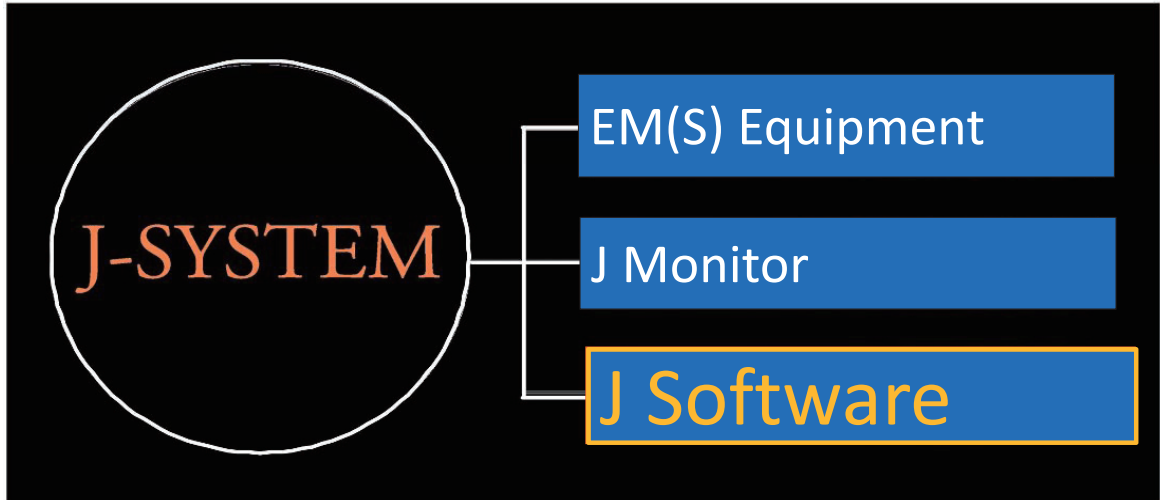
J Monitor

J Monitor

The screenshot displays the J Monitor software interface. It features two main image windows: "IR Raw Image" on the left, showing a thermal image with a color scale from blue (cold) to red (hot), and "IR Process Image" on the right, showing a processed version of the same image with a grayscale background and red and blue highlights. The interface includes a control panel at the bottom with various settings and buttons. On the right side, there is a vertical toolbar with icons for REC, PLAY, LIVE, PREU, NEXT, END SHOT, EJECT SAVE, and COPY/DELETE. The bottom control panel includes a color scale, camera settings (like focal length and zoom), and a status bar showing "診断: 正常" (Diagnosis: Normal).

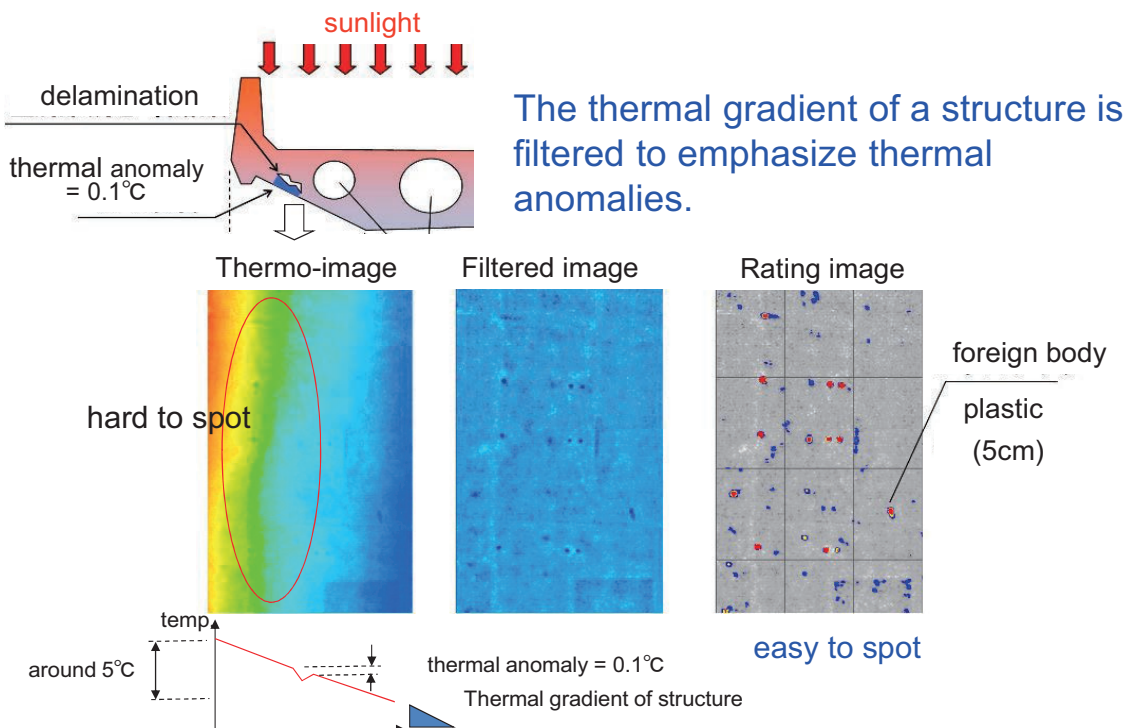
21

J Software: Infrared Image Processing Software



22

Image Emphasizing Thermal Anomalies



23

J Software: Damage Ratings

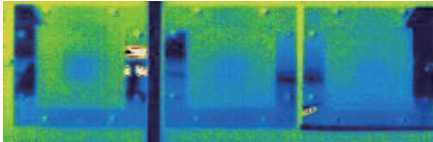
Temperature distribution is interpreted into damage ratings by using a comprehensive database of temperature patterns.

Visible image: EM(S) test-piece

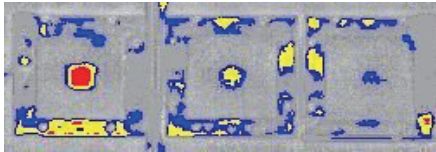


1cm 2cm 3cm

IR raw image



IR Process image



Damage level		
Damage pattern		indication
<p>Concrete surface</p>	<p>crack</p> <p>reinforcement</p> <p>Depth $\geq 4\text{cm}$</p>	<p>Observation (Insignificant)</p>
<p>Concrete surface</p>	<p>crack</p> <p>reinforcement</p> <p>Depth $\geq 2\text{cm}$</p>	<p>Caution</p>
<p>Concrete surface</p>	<p>reinforcement</p> <p>Reaching surface crack</p>	<p>Critical</p> <p>Emergency measures required</p>

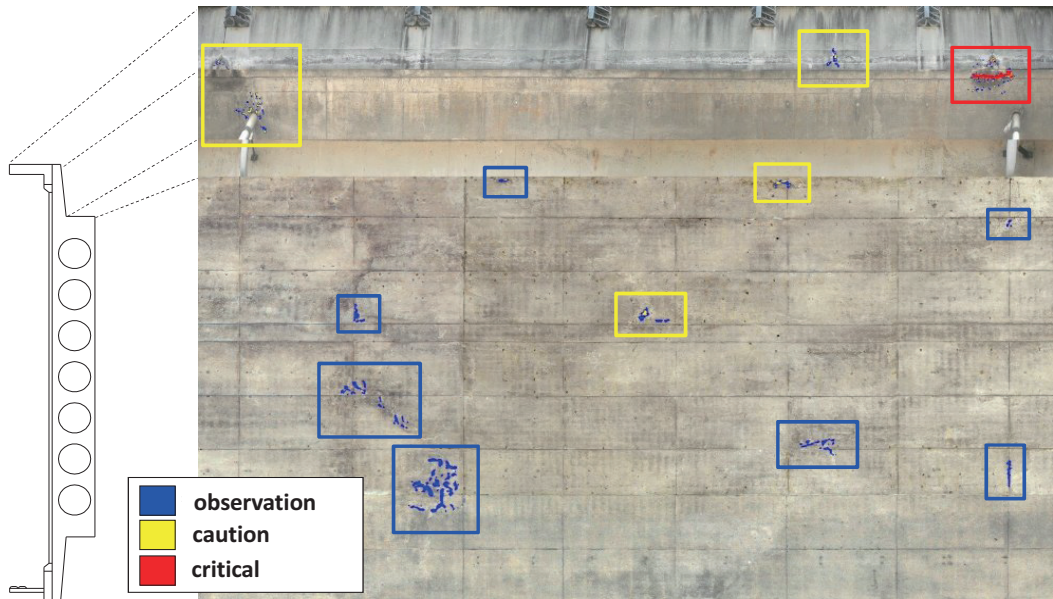
24

Comparison Between New and Conventional



25

Is it possible and easy to evaluate objectively?



Your resources can be focused on the areas that need the most work.

26

J-System Features

Proper investigable time can be assessed.

Damage depth can be obtained in real time

Absolute quality assurance

& Oversight prevention

“J-System” supports investigations conducted by customers

27

Tunnel Inspection



28

Background

Conventional visible inspection adds damage conditions of tunnel linings concrete , such as flaking concrete to be caused critical accident, adopted camera technical and developed vehicle to inspect higher accurate



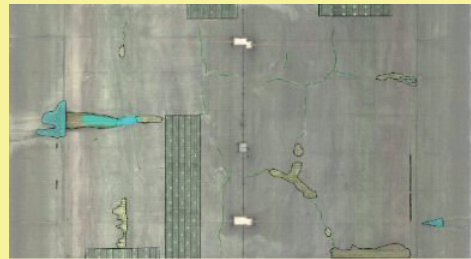
29

Flow chart for tunnel inspection

I . The captured image of the tunnel



III . Analyzing



II . Creating an image of the tunnel

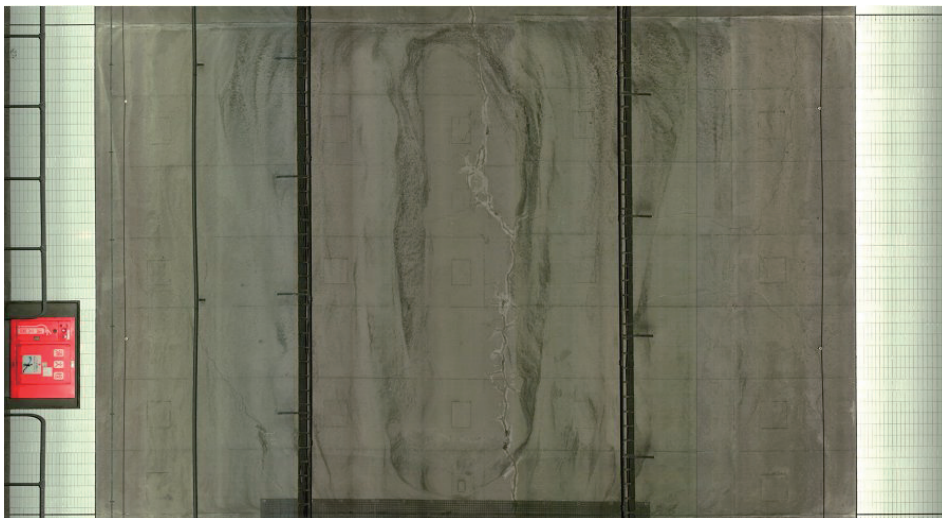


IV . Inspection



30

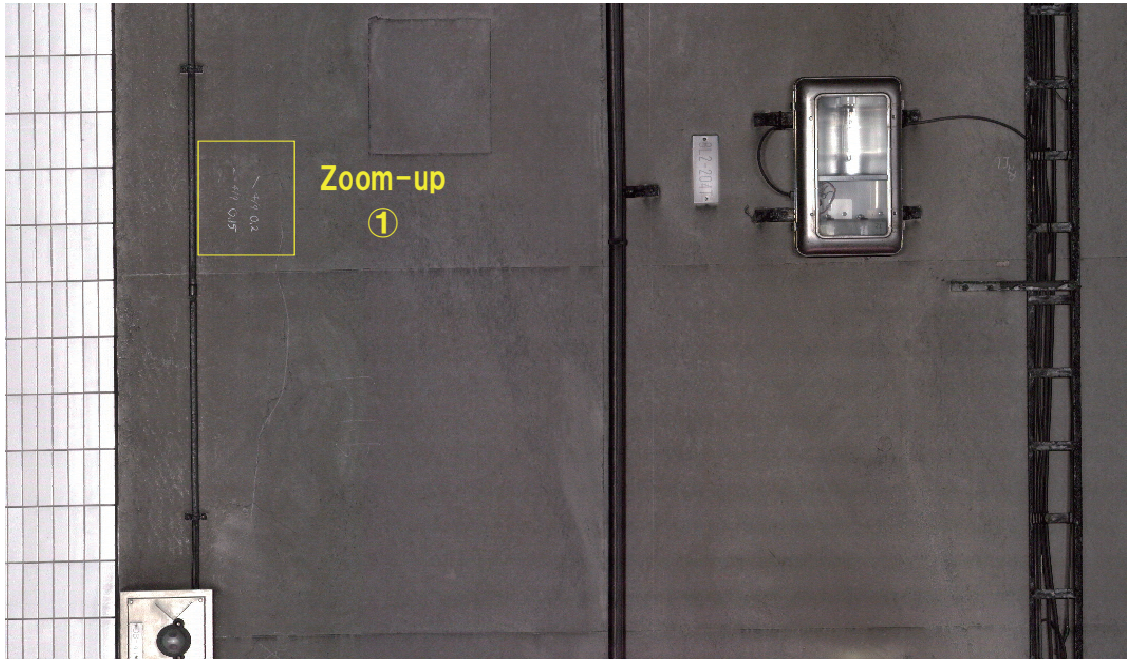
Investigation of cracking and other damages



- The width, length, and number of cracks, efflorescence, and water leakage can be investigated with high precision.
- Color images allow the inspection of corrosion and damage to the accessories attached to the tunnel lining.
- High-precision photography/analysis enables a comparison between the previous investigation and the current damage progress.

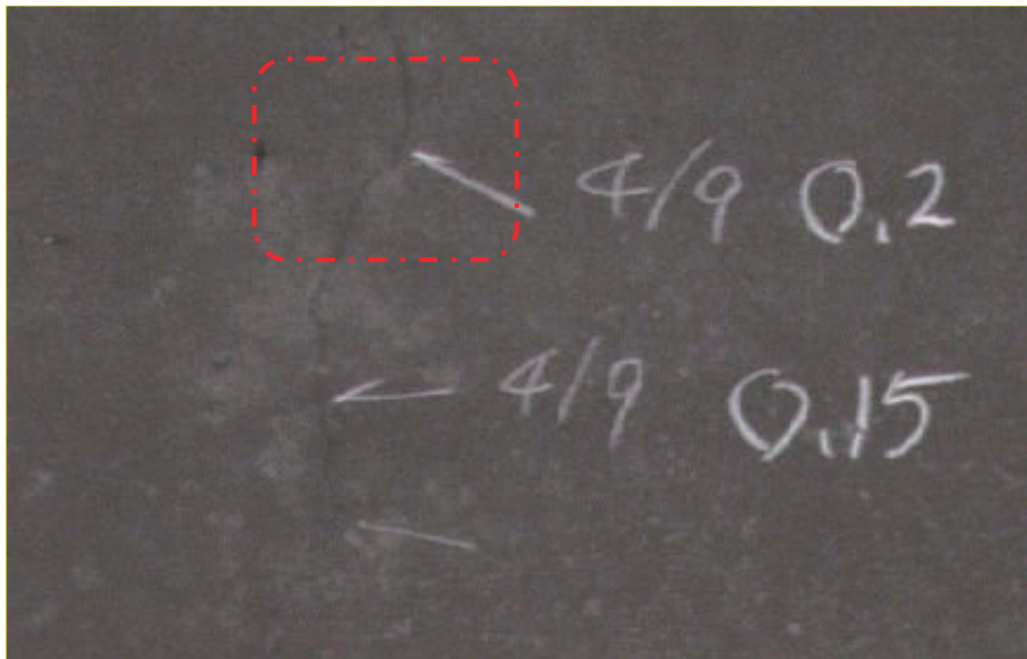
31

Visual image (tunnel)



32

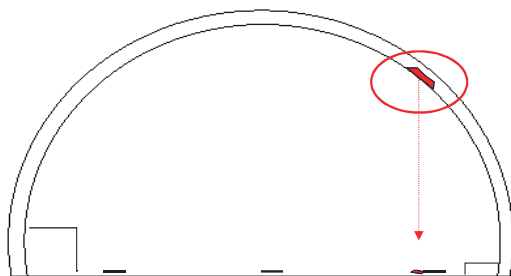
Zoom-up visual image (Cracks)



33

Further improvement

Tunnel lining concrete which is plain concrete causes concrete flaking accidents.

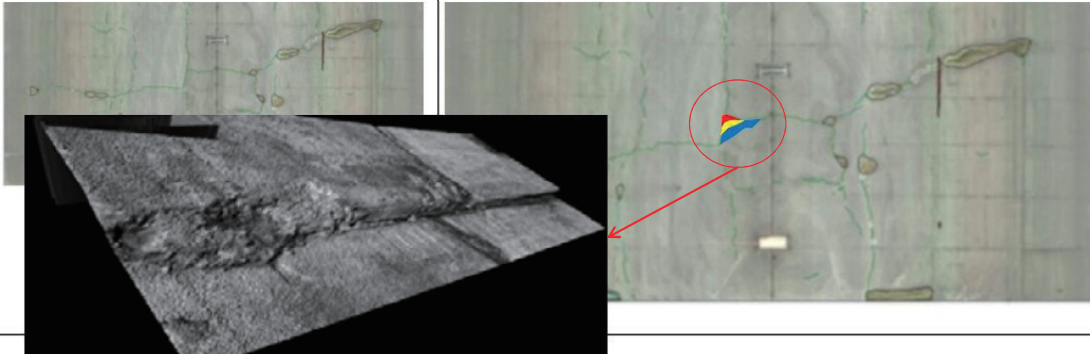


Surface status (visual image)
 & surface profiling (height data)
 ⇒ Need method for predicting flaking
 (Theory from deterioration to flaking)

34

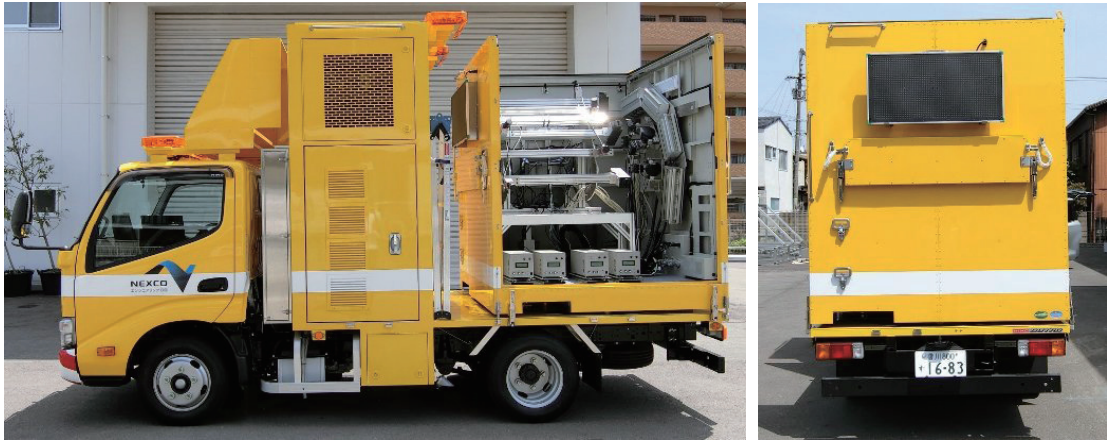
Approach for identifying hazardous areas

Infrared can not be used (TN) → We need a new approach !

Current problems	New technique
<p>No judging by the front of image whether the crack may be falling or not</p> 	<p>Detecting flaking point by obtaining height data of tunnel lining surface.</p>

35

Smart EAGLE type-T(Tunnel) Completion



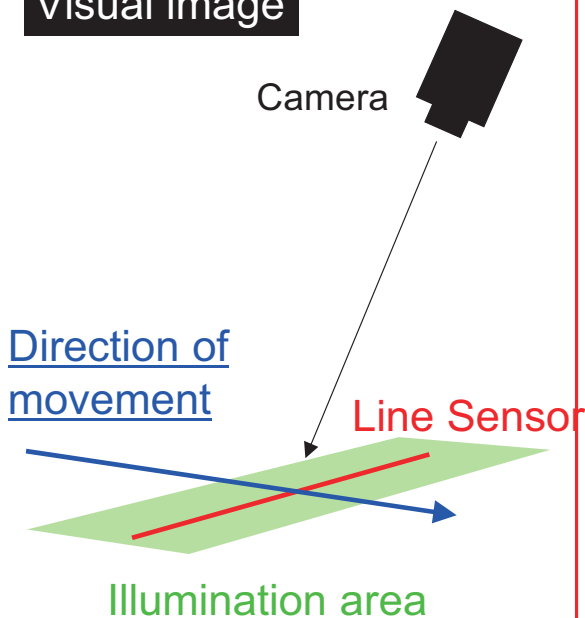
vehicle speed of 65km/h (H29)

Now, Trying at 80 to 100 km / h

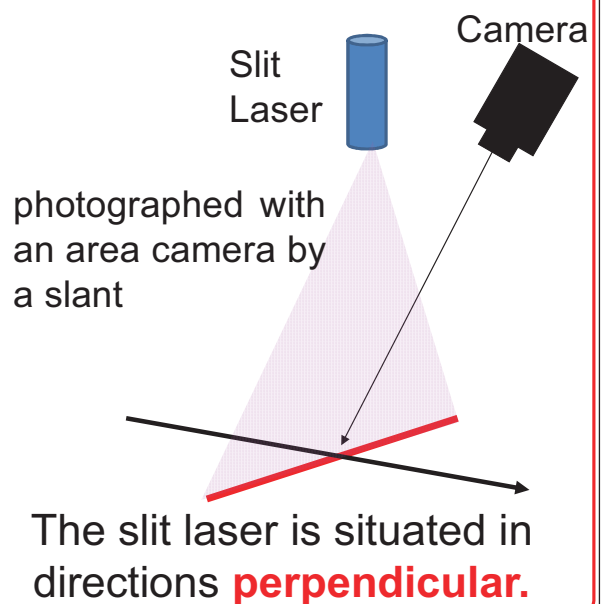
36

L&L System

Visual image



Height image Width profile



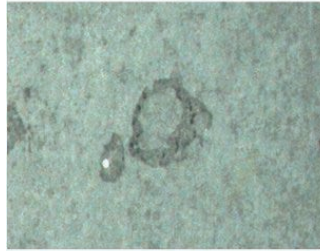
37

Measurement of tunnel conditions by height data

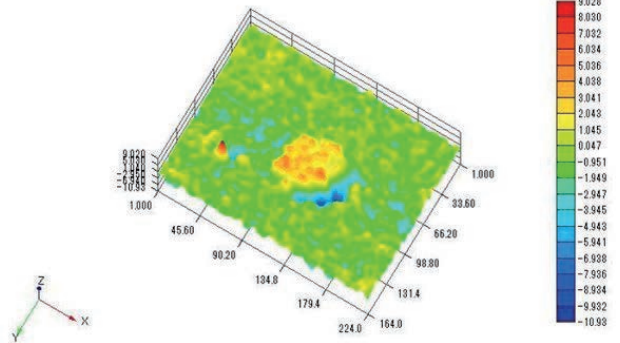
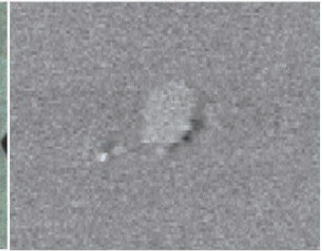


Damage of inside tunnel for verification (photo-shooting by digital camera)

Visual Image

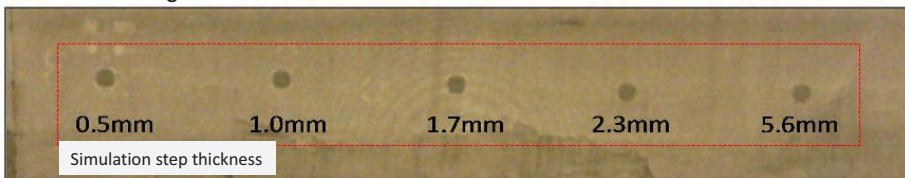


Height Image



Overview of proposed measuring technology ②

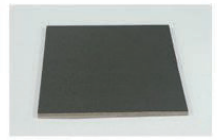
① Visual image



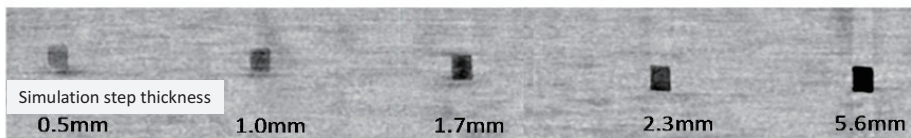
Simulate gap

□100 × 100mm

Thickness 0.5~5.6mm



② Height image

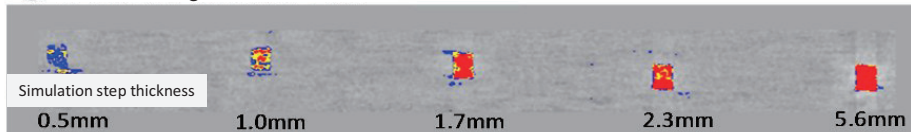


凡例



Black = Large gap

③ Process image

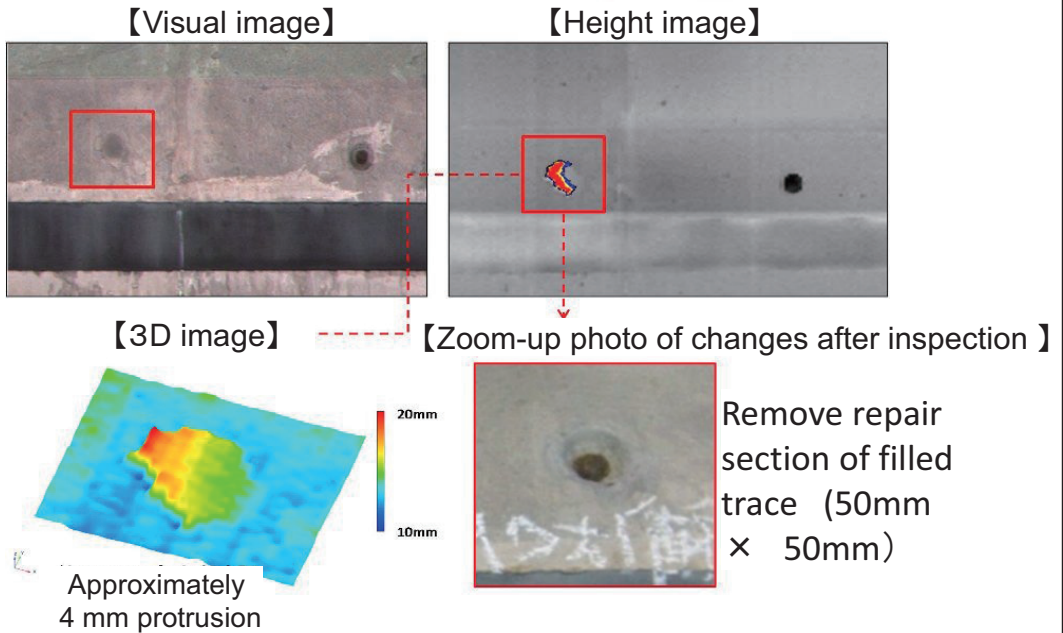


observation

caution

critical

Height measurement result of actual tunnel

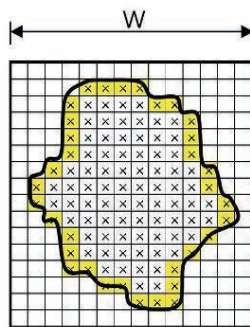
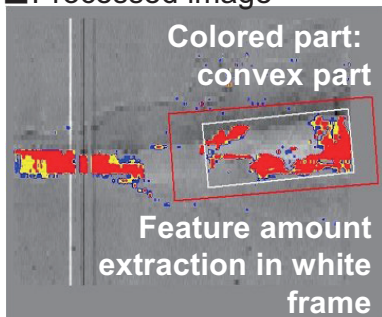


40

Extraction of damaged points (Calculation of shape feature amount)

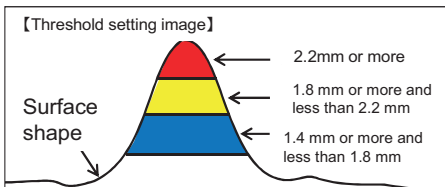
- "Shape feature amount" is calculated for each area of red, yellow, and blue which is determined by setting a threshold value as emphasis index

■ Processed image



- ① Boundary length(L)
- ② Area(S)
- ③ Occupancy (O)
- ④ Complexity (C)
- ⑤ Degree of Circularity (CC)

(S) = number of "X"
 (O) = $S / (H * W)$
 (C) = L / S
 (CC) = $4\pi S / L^2$



※ shape feature amount
 ⇒ Numerical representation of items ①~⑤ of unique shape change areas

41

Extraction of damaged points

(Prediction method of damage type)

Feature amount to use for variables of formula

【 Independent variable 】

◎ Feature amount

- Length
- Area
- Occupancy
- Complexity
- Circularity

◎ Feature amount by texture analysis (14types)

- Dispersion
- Total
- Distributed total
- Contrast
-

Construction of prediction model

【 Multivariate analysis 】

↓ Various models

- ◎ Neural network analysis
- Logistic regression analysis
- Discrimination analysis
- Decision tree analysis
-

Analysis is performed with multiple multivariate analysis models and select model with high correlation.

Adopt analysis result by neural network

Answer to the formula (Result of hammering)

【 Dependent variable 】

Result of hammering N=149

Damage Float
Separation
Sheet peeling
Rock pocket

Sound protrusion
Sound
Step
Repair mark
Free lime
Contamination

42

Extraction of damaged points

(Prediction method of damage type)

Analysis result

Area of hammering : 5,900m²

149points where unique shapes were detected

		Analysis (estimation) result										total	
		Damage				Inspection	Sound						
		Float	Separation	Sheet peeling	Rock pocket		Protrusion	Sound	Step	Repair mark	Free lime		Contamination
tapping result	Damage	Float	36	1		1							38
		Separation		4									4
		Sheet peeling			8								8
		Rock pocket				1							1
	Sound	Protrusion					30						30
		Sound	1				2	41			1		45
		Step							17				17
		Repair mark								1			1
		Free lime									3		3
		Contamination										2	2
	total	37	5	8	1	33	41	17	1	4	2	149	

Oversight is 0 (84 points of hammering inspection)

43

Prospect of tunnel inspection

Height measurement is effective as screening technology of hammering !



- 1) Current tunnel lining image shooting ⇒
tunnel lining shooting + Height measurement
- 2) Detailed inspection · all hammering ⇒
Hammering at only the screening points

⇒ It is also possible to increase the frequency of detailed inspection with only hammering at screening points.

44



Pavement Inspection

45

Inspection Methods

Daily Inspection (Behind the wheel)



Detailed Inspection pavement investigation

《Our product》



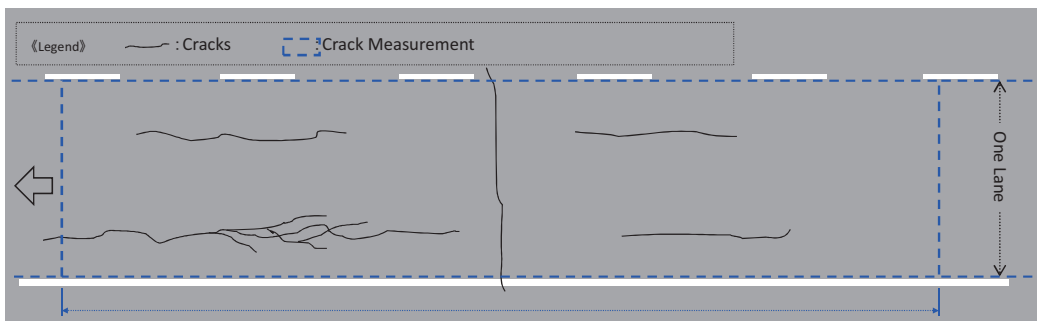
46

Control Item

■ Maintenance Target Values of Pavement

Rutting (mm)	Difference in Level (mm)		Coefficient of Sliding Friction (μ V)	Flatness IRI (mm/m)	Cracking Ratio (%)
	Bridge Mounting	Crossing Structure Mounting			
25	20	30	0.25	3.5	20

■ Cracks Evaluation (Conceptual Diagram)



Evaluation Unit: 100m

47

Data Acquisition by Periodic Inspection

Road Surface Measurement (3 Elements)

Company-owned vehicle



Cracks

Ruts

Flatness



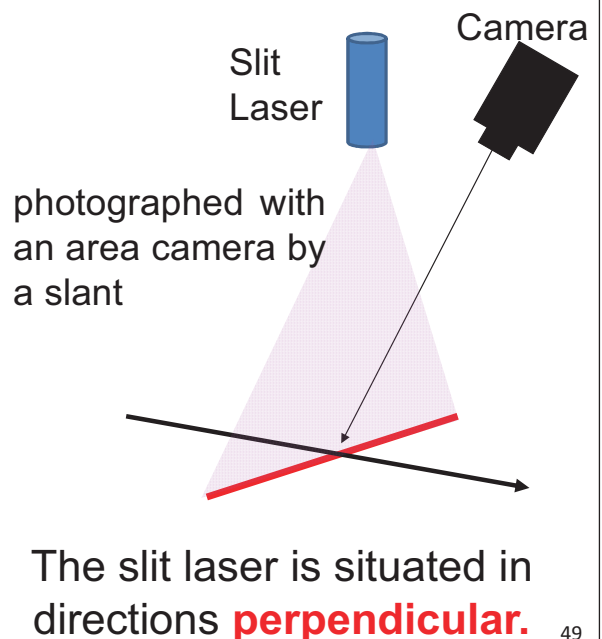
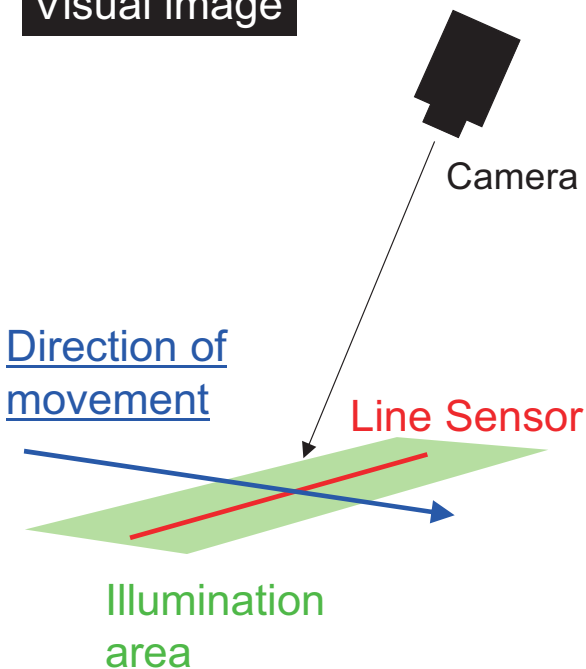
48

L&L System

Visual image

Height image

Width profile



49

Certified in the performance confirmation test in FY2018

- Examination date
May 22, 23, 24, 2018
- Testing place
The testing track of the National Institute for Land and Infrastructure Management, and others
- Performance confirmation result (**Pass**)
“Performance Confirmation Certificate No.3027”

Test items	Assessment scope	Time	Result
Accuracy of distance measurement	The vehicle obtains accuracy within +/- 5% accuracy for of the value measured by an optical measuring device.	Night	Pass
Accuracy of cracking measurement	The vehicle obtains accuracy capable of identifying cracking with width of 1mm or greater.	Night	Pass
Accuracy of rutting measurement	The vehicle obtains accuracy within +/- 3 mm of the rut depth measured by a cross-section profile meter.	Night	Pass
Accuracy of flatness measurement	The vehicle obtains accuracy within +/- 30% of the standard deviation value measured by a longitudinal profile meter.	Night	Pass



50

Visual image (pavement)



Accuracy at a speed of 100km/h
 ~ Detecting cracks ~
 Shooting width=4.5m(Color image)
 Resolution 0.8mm x 0.8mm/pixel

51

Calculation of cracking ratio

Aerial view taken by the Line Scanning Camera

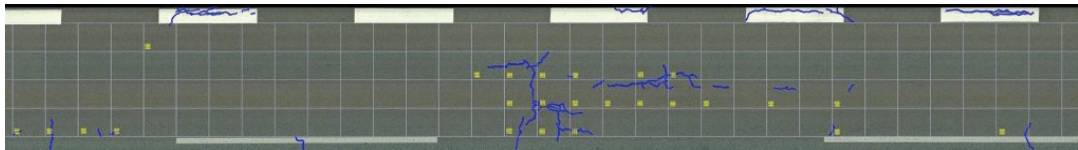


Semi-automatic identification of cracking damage

develop



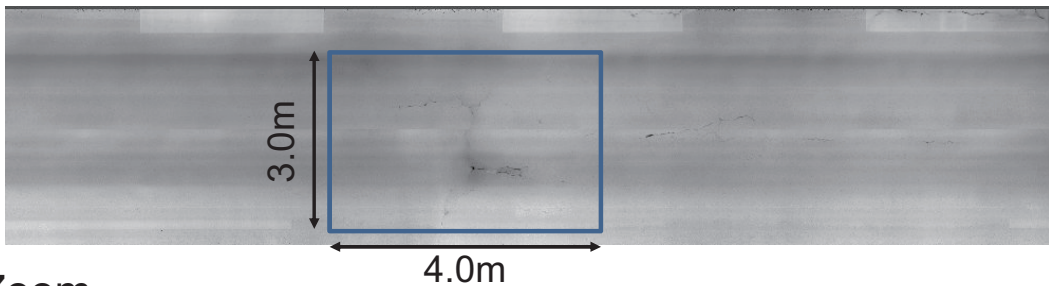
Fully-automatic line/surface Analysis (Accuracy rate is 99%)



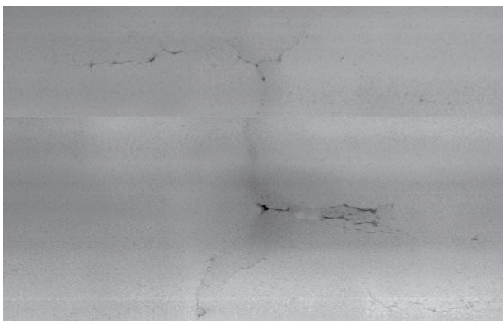
52

Height image

Surface height image



Zoom



Accuracy at a speed of 100km/h

~Rutting Measurement~

Shooting width=4.4m

Dimension of rutting:1mm or less

Resolution 1.27mm(Transversal)

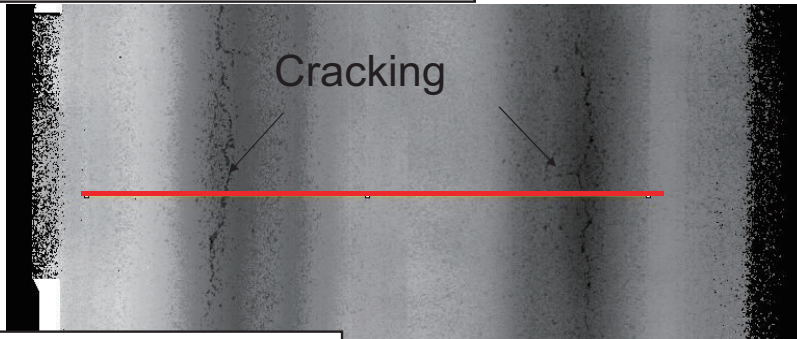
2.70mm (Longitudinal)

0.50mm (Depth)

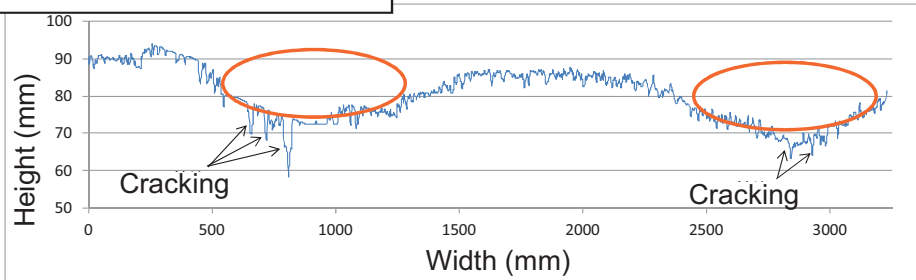
53

Ruts

Height image (Black part is low.)



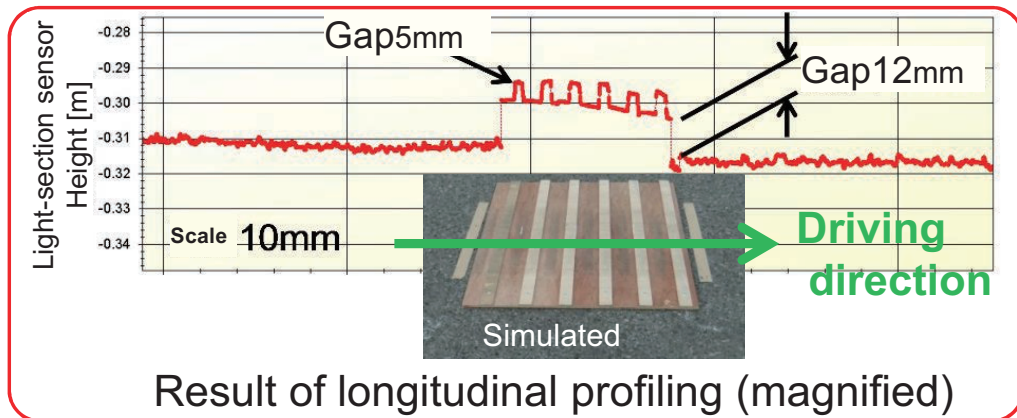
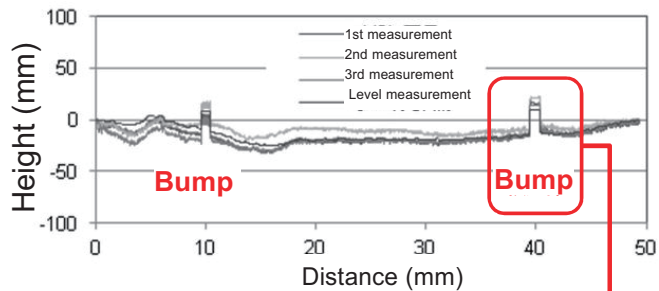
Ruts on the red line above



54

Flatness (Longitudinal profiling)

High-resolution allows us to accurately profile the longitudinal shape of a microscopic bump.



Result of longitudinal profiling (magnified)

55

Analyzing highly accurate longitudinal profile



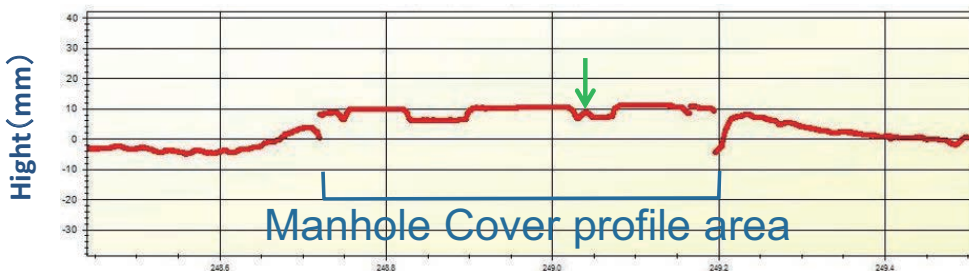
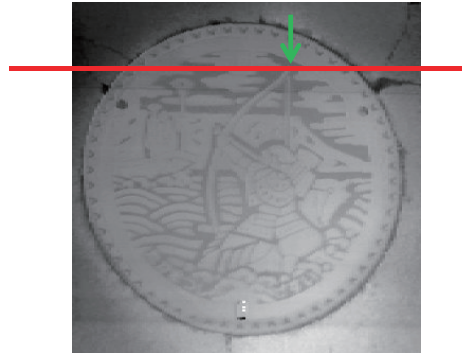
56

Analyzing highly accurate longitudinal profile

Visual image



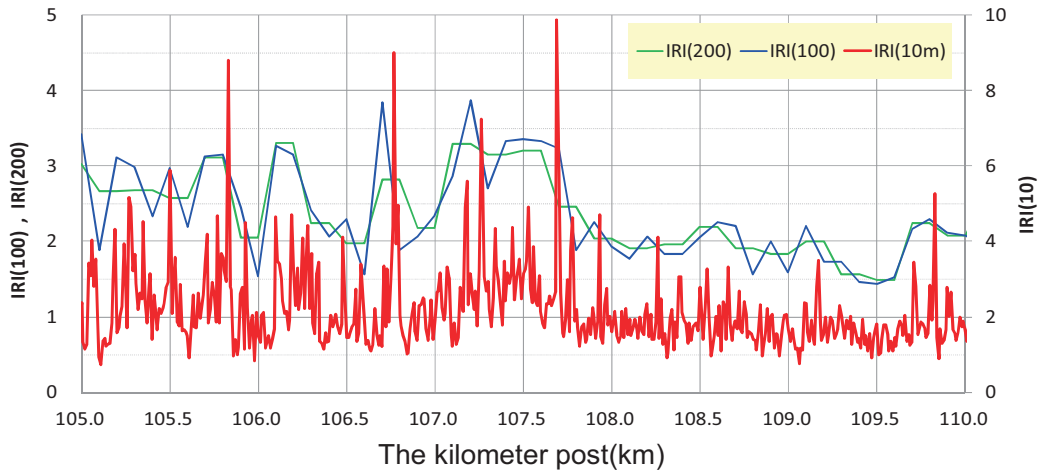
Surface height image



57

Analyzing highly accurate longitudinal profile

Future: IRI can be measured thanks to no speed dependanc



58

Developmental event of pothole on Porous asphalt pavement

Done to review the objective of preventive maintenance

- Proposal new evaluation indicator to apply for Porous asphalt pavement
- Proposal method of predicting of occurrence of pot hole

59

Proposal of a new evaluation method (Aggregate scattering) (1)

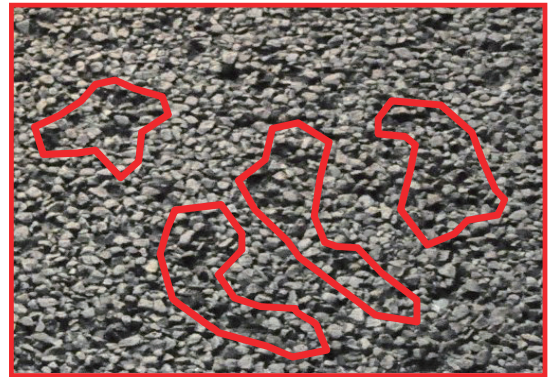
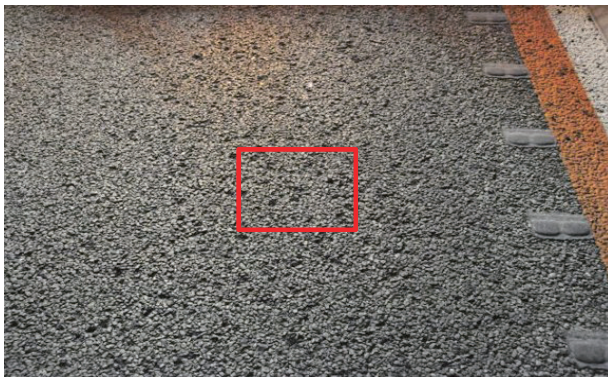
■ Current issues

Due to the spread of Porous asphalt-related road surfaces, problems caused by aggregate scattering have increased.

(1) Less noise reduction functionality

(2) Less driving safety and comfort

⇒ A quantitative evaluation method has not been established.



60

Proposal of a new evaluation method (Aggregate scattering) (2)

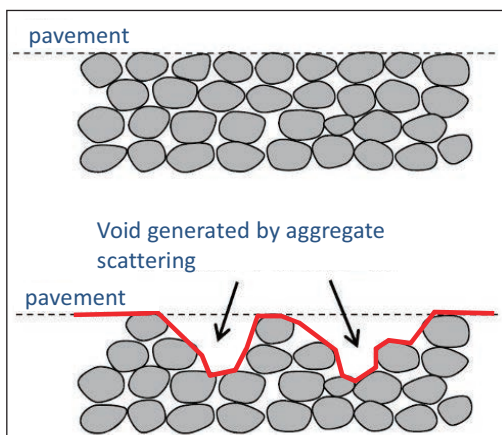
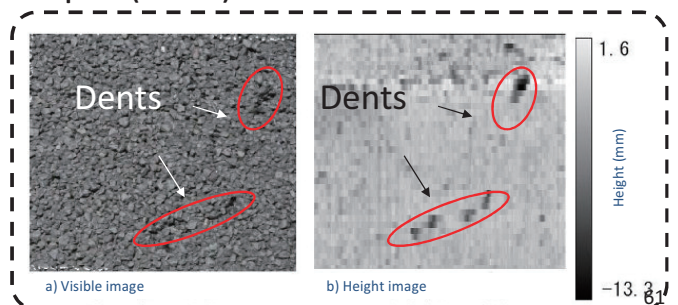


Image of aggregate scattering

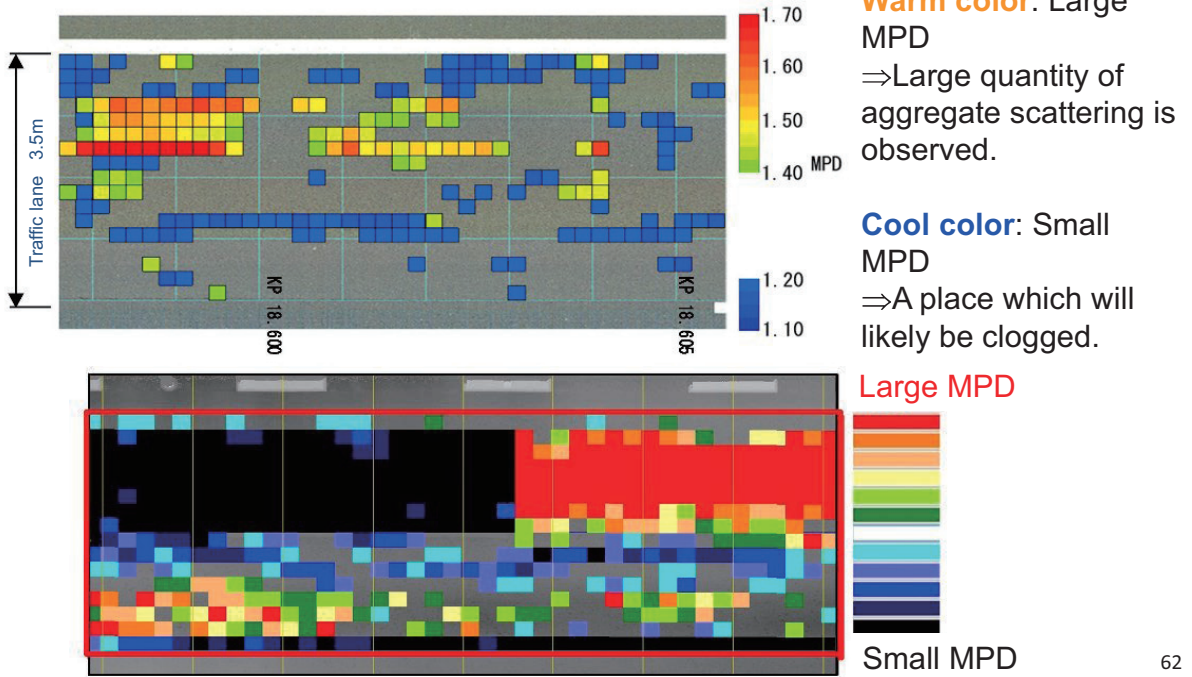
3D shape measurement by Light-Section Method allows us to measure the form of a pavement with high precision.



We focus on the relationship between aggregate scattering and mean profile depth (MPD).



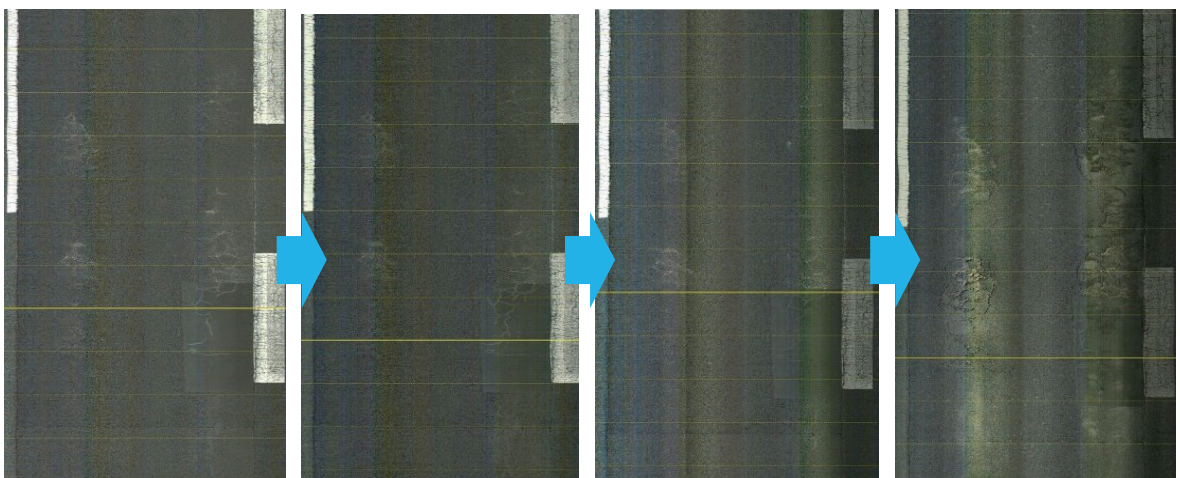
Superficial (MPD) quantitative evaluation of aggregate scattering



62

Data from periodic measurement

Visual image



Oct. 2013

Nov. 2013

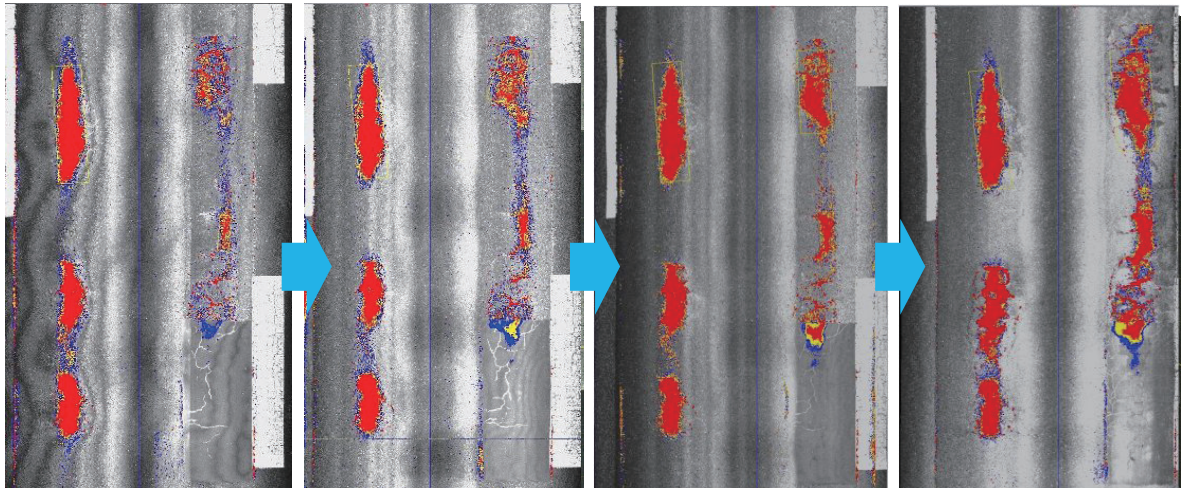
Dec. 2013

Jan. 2014

63

Data from periodic measurement

Height image



Oct. 2013

Nov. 2013

Dec. 2013

Jan. 2014

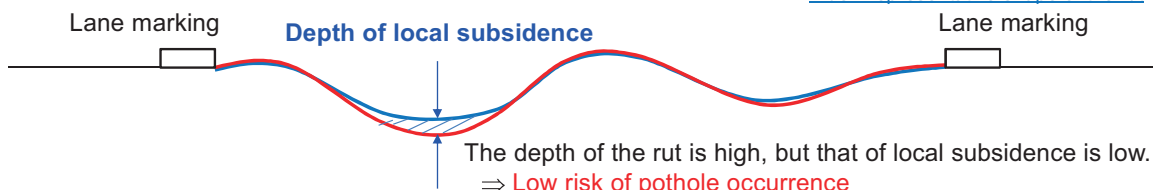
64

Proposal of a new evaluation indicator

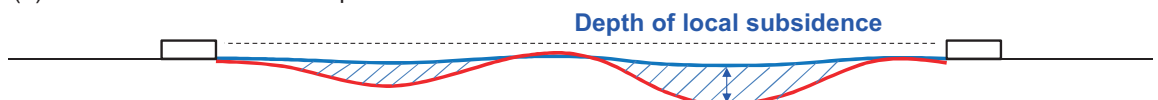
- (1) Area where the overall depth of the rut is high

Red: Shape of the rut at the objective point

Blue: Representative shape of the rut



- (2) Area where the overall depth of the rut is low



The depth of the rut is low, but that of local subsidence is high.

=> Potential risk of pothole occurrence => **Dangerous**

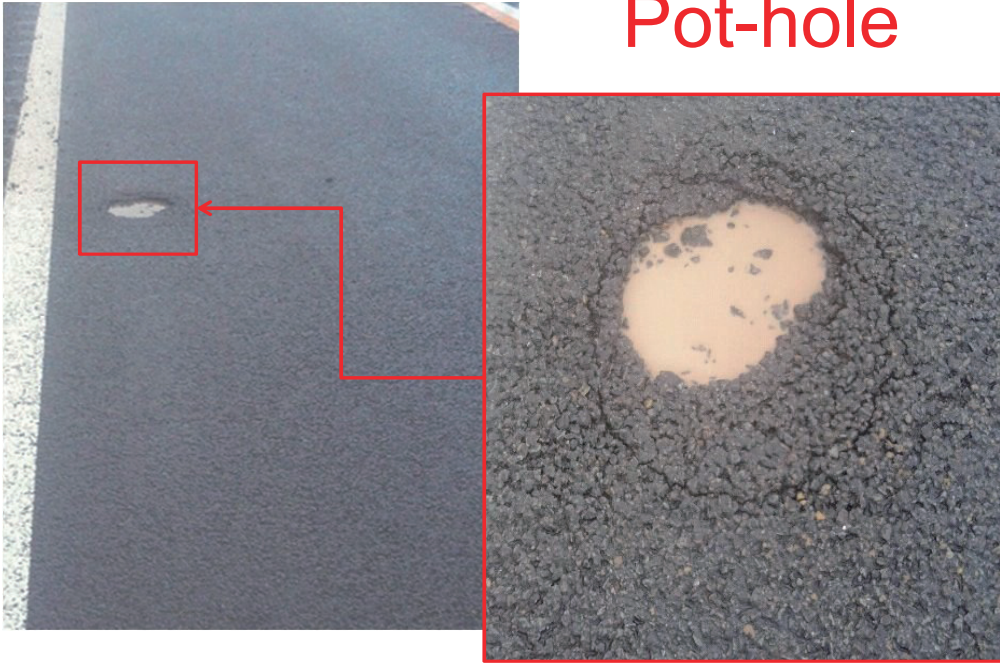
Proposal method [Evaluation based on the depth of local subsidence]

The relative depth of local subsidence is calculated as the depth of local subsidence by calculating the difference between the rut depth of the objective point and the representative rut depth which is the central value of the maximum rut depth in a vicinity of 10m.

65

High risk event

Pot-hole



66

Pot hole repair method



Cold asphalt mixture



Compacting machine

67

Current status of road surface management

① Surface inspection



Inspection frequency
Once every 3 years
(Shikoku-area)

② Daily check (On-board inspection)



Inspection frequency
5days/2weeks
(According to traffic volume)

【Current status】 Discover pothole by daily inspection
→ Emergency treatment ⇒ **Post-maintenance**

68

Smart EAGLE type-P(Pavement) Completion

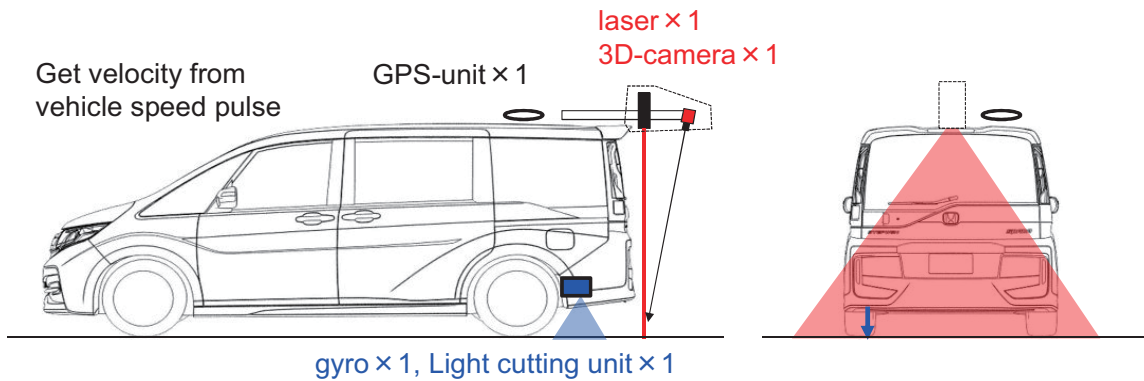


69

Proposal of Simple Road Survey Method by Smart Eagle

Characteristic

- Production cost is low
(Measuring equipment of road surface shape × 1set, IRI- equipment × 1set, GPS)
- Fully automated analysis by simplified method, so analyzing cost is low
- Grasp damaged points beforehand by increasing frequency



70

Proposal of Simple Road Inspection Method by Smart Eagle

Smart Eagle Evaluation index that automatic analysis possible

Evaluation index	Analysis value of this system
Crack ratio	Crack ratio by simplified method
Ruts amount	Test method manual・NEXCO-Test method compliance
IRI	Evaluation length can be set arbitrarily
Depth of local subsidence	Depth of local subsidence against the representative ruts
MPD	The Value calculated MPD from transverse shape data in a plane

Prediction of pothole occurrence

Evaluation index focused on this time

⇒ Depth of local subsidence & MPD

71

Regular road surface measurement by Smart Eagle

Perform periodic measurements

Measurement section : 27km

Measurement items : Depth of local subsidence
& MPD

Measurement term: 2015/06/10 ~ 2018/02/16

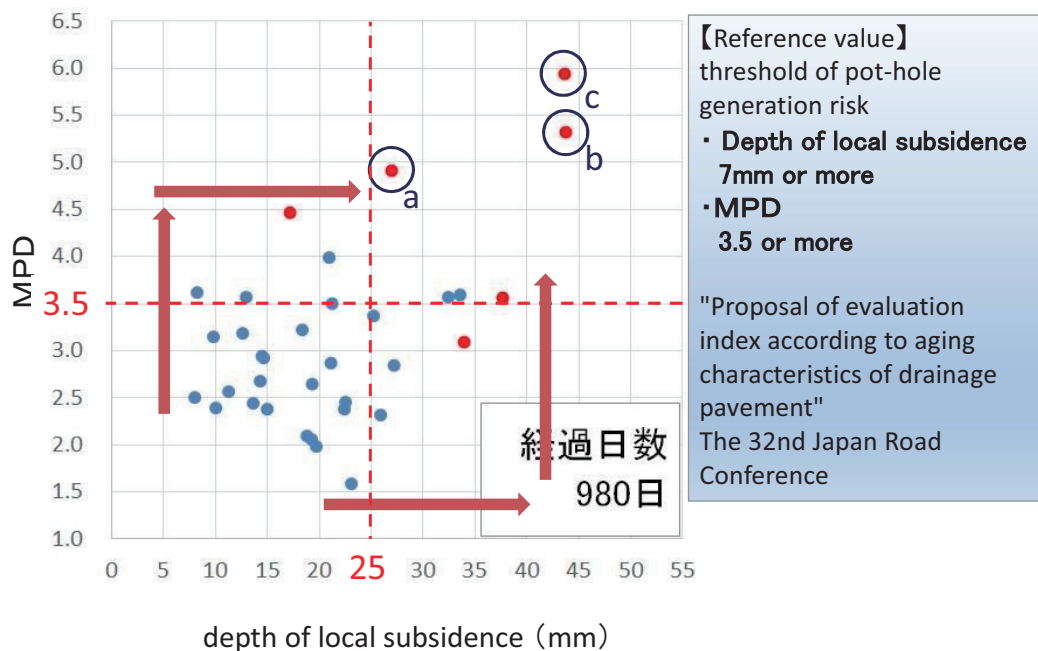
(980days)



※ Before November 2017, prepare conventional Eagle measurement data because Smart Eagle has not yet been developed

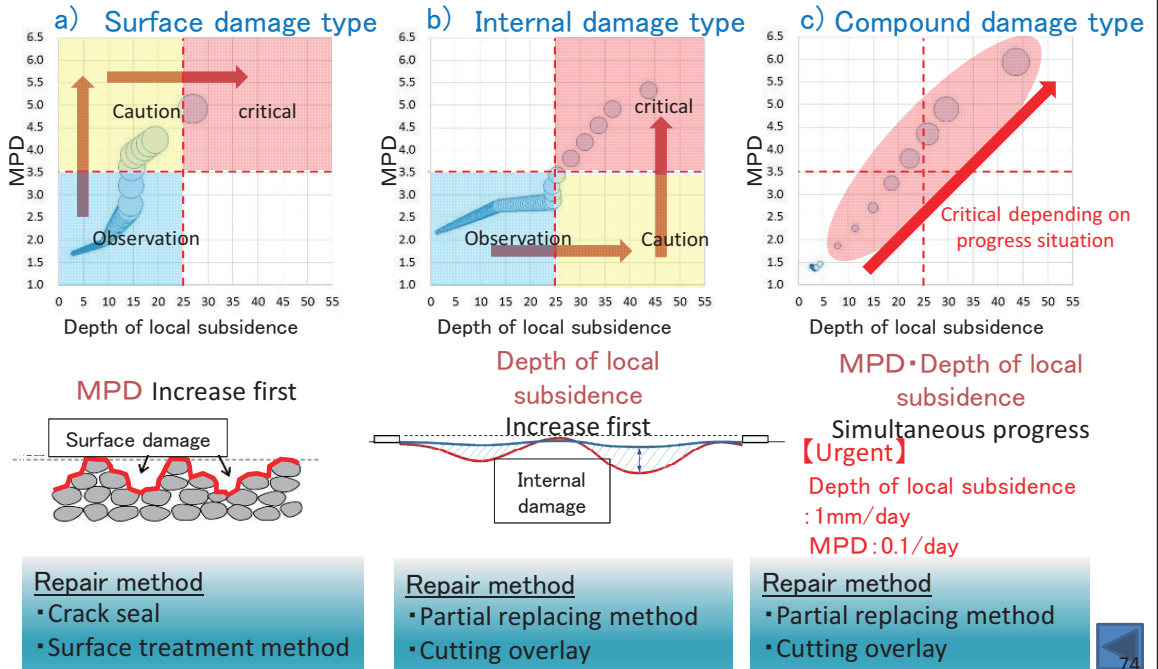
72

Result of Periodic measurement (Changes of depth of local subsidence and MPD)



73

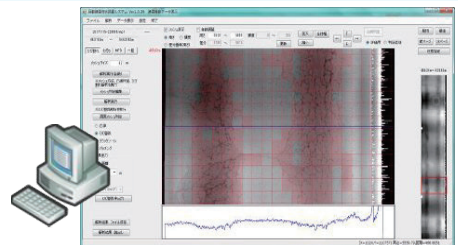
Road surface management method according to degradation type



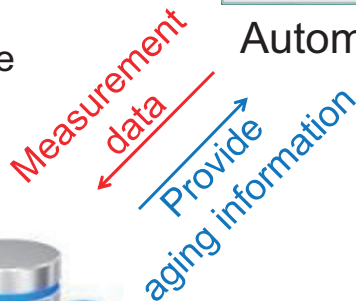
Proposal on operation method of road surface management by Smart Eagle ①



Vehicle equipped with Smart Eagle
(In the future to be installed in daily inspection vehicles)

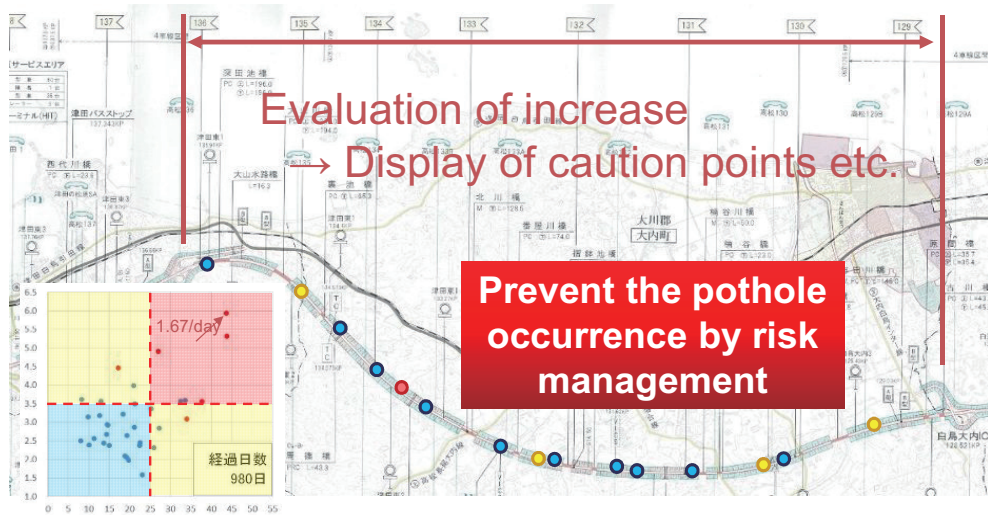


Automatic analysis



Proposal on operation method of road surface management by Smart Eagle ②

Periodic measurement (10 days pitch)



April 2019 trial introduction scheduled

Introduction and Application of CED-based Fracture Mechanics

Cheng Hua

Department of Aeronautics and Astronautics, Fudan University, Shanghai, China

Abstract: The CED (Crack Energy Density) ^[1] is introduced as the crack parameter which has the meanings of strain energy density per unit area for a completely sharp crack as the limit where the notch radius approaches zero in a notch model. The CED can be defined in an arbitrary direction at a crack tip and is a potential parameter for describing fracture behavior of a mixed-mode crack. It has also been expected as a crack parameter which controls fracture behavior in different material media. The CED in an arbitrary direction ^[2] is often evaluated by path-independent region integral or load-displacement curves. However, there is the need to compute stress and strain near crack tip even in elastic stage and this makes us uneasy to find the numerical result of the CED. On the other way, we can get relative accurate numerical result of CED through load-displacement curves, but it is not so clear about the difference between the two evaluations.

In this report, by introducing basic concepts and potential applications of CED-based fracture mechanics, it is shown that the CED in an arbitrary direction of a crack in an inhomogeneous material under monotonically increasing load can be evaluated by a new path-independent integral, including the case of the evaluation of CED by load-displacement curves. The new evaluation can also be expected to obtain practical accuracy about the CED and useful to evaluate CED in an arbitrary direction of a crack. Through the new evaluation, it also becomes to be clear about the difference between the evaluations of CED by path-independent region integral and by load-displacement curves.

Keywords: Crack Energy Density; mixed-mode crack; fracture mechanics parameter; path-independent integral

References

- [1] Watanabe K (1981), "New Proposal of Crack Energy Density Concept as a Fundamental Fracture Mechanics Parameter", *Bulletin of the JSME*, **24**(198): 2059-2066.
- [2] T. Utsunomiya and K. Watanabe (1993), "Fracture Criterion of a Mixed-mode Crack based on CED (Crack Energy Density)", *Nuclear Engineering and Design*, **142**: 101-111.

Acknowledgement

This work is partially supported by 2018 IMI Joint Use Research Program Workshop (II) "Non-destructive inspection for concrete structures and related topics", Kyushu University

This work is partially based on the discussions at 2018 IMI Joint Use Research Program Workshop (II) "Non-destructive inspection for concrete structures and related topics".

Basic Concepts and Evaluation of CED-based Fracture Mechanics

Cheng Hua

Department of Aeronautics and Astronautics, Fudan University,
Shanghai, China



Non-destructive inspection for concrete structures and related topics
Fukuoka, Japan, Oct. 23-26, 2018

The definition of CED (Crack Energy Density)

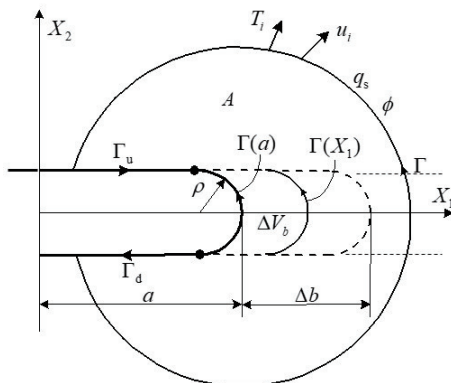
“the work, expressed per unit area in the crack plane,
done at the crack tip during deformation “

“き裂端が初期の状態から現在まで担ってきたエネルギー
をき裂を含む面内の単位面積当たりで表したもの“

Continuum Model

— 渡辺*(1981)

$$E = \lim_{\Delta b \rightarrow 0} \left(\int_{\Delta V_b} W dV \right) / \Delta b = \lim_{\Delta b \rightarrow 0} \int_a^{a+\Delta b} \left(\int_{\Gamma(X_1)} W dX_2 \right) dX_1 / \Delta b = \int_{\Gamma(a)} W dX_2$$



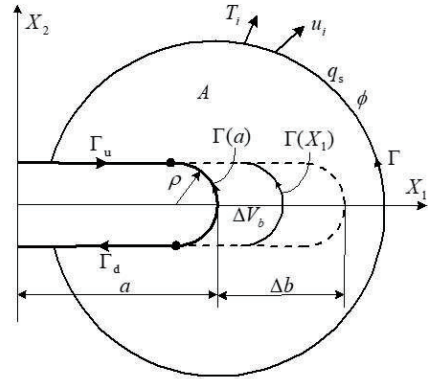
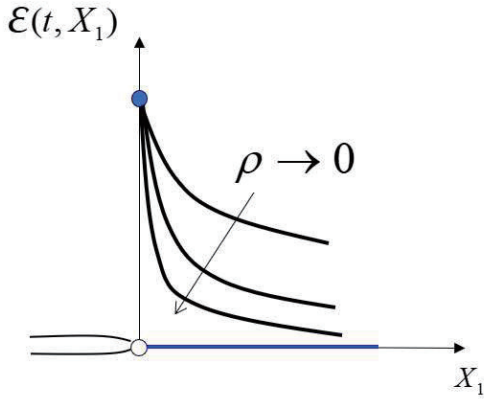
When $\mathcal{E}(t, X_1) = \int_{\Gamma(X_1)} W dX_2$,

$$\mathcal{E} = \mathcal{E}(t, a)$$

Here

$$W = \int_0^t \sigma_{ij} \dot{\epsilon}_{ij} d\tau$$

*渡辺, 機論, 47-416, A(1981), 406.



For a crack of $\rho = 0$ $\mathcal{E}^{(c)} = \lim_{\rho \rightarrow 0} \mathcal{E}(t, a) = \lim_{\rho \rightarrow 0} \int_{\Gamma(a)} W dX_2$

When $\sigma_{ij} = \frac{\partial W}{\partial \varepsilon_{ij}} = f_{ij}(\varepsilon_{11}, \varepsilon_{22}, \dots, \varepsilon_{31})$, $\int_{\Gamma(a)} W dX_2 = \int_{\Gamma} (W dX_2 - T_i u_{i,1} d\Gamma)$

Therefore, $\mathcal{E}^{(c)} = J$

When ρ is sufficiently small, $\mathcal{E}^{(c)} \cong \mathcal{E}(t, a) = \int_{\Gamma(a)} W dX_2$

Linear Elastic Body

$$\mathcal{E}^{(c)} = J = \frac{\kappa + 1}{8G} (K_I^2 + K_{II}^2) + \frac{K_{III}^2}{2G} = \mathcal{G} = \frac{1}{2} P^2 \frac{d\lambda}{Bda}$$

Nonlinear Elastic or Elastoplastic Body (deformation theory)

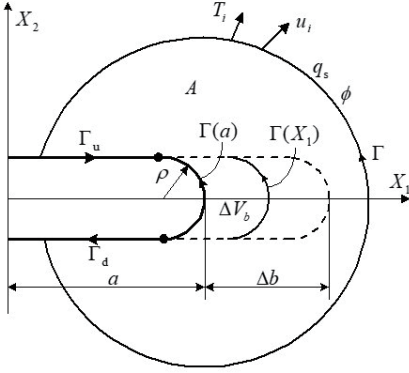
$$\mathcal{E}^{(c)} = J$$

Especially, when n power law is employed,

$$\mathcal{E}^{(c)} = J = \frac{I_n \varepsilon_0 K_\sigma^{n+1}}{\sigma_0^n} = I_n K_\sigma K_\varepsilon = \frac{I_n \sigma_0 K_\varepsilon^{(n+1)/n}}{\varepsilon_0^{1/n}}$$

Path Independent Expression of CED

$$\begin{aligned}\mathcal{E} = \mathcal{E}(t, a) &= \int_{\Gamma(a)} W dX_2 \\ &= \int_{\Gamma} (W dX_2 - T_i u_{i,1} d\Gamma) - \int_A \int_0^t (\sigma_{ij,1} \dot{\varepsilon}_{ij} - \dot{\sigma}_{ij} \varepsilon_{ij,1}) d\tau dA\end{aligned}$$



$$\text{When } \sigma_{ij} = \frac{\partial W}{\partial \varepsilon_{ij}} = f_{ij}(\varepsilon_{11}, \varepsilon_{22}, \dots, \varepsilon_{31}),$$

$$\sigma_{ij,1} \dot{\varepsilon}_{ij} - \dot{\sigma}_{ij} \varepsilon_{ij,1} = 0$$

When associated flow rule in incremental theory is employed, under monotonously increasing load

$$\sigma_{ij,1} \dot{\varepsilon}_{ij} - \dot{\sigma}_{ij} \varepsilon_{ij,1} \cong 0$$

When unloading occurs,

$$\sigma_{ij,1} \dot{\varepsilon}_{ij} - \dot{\sigma}_{ij} \varepsilon_{ij,1} \neq 0$$

Small Scale Yielding

$$\mathcal{E}^{(c)} \cong J \cong \frac{\kappa + 1}{8G} (K_{\text{I}}^2 + K_{\text{II}}^2) + \frac{K_{\text{III}}^2}{2G}$$

Large Scale Yielding

$$\mathcal{E}^{(c)} \cong J$$

Creep Crack

When stationary creep is realized,

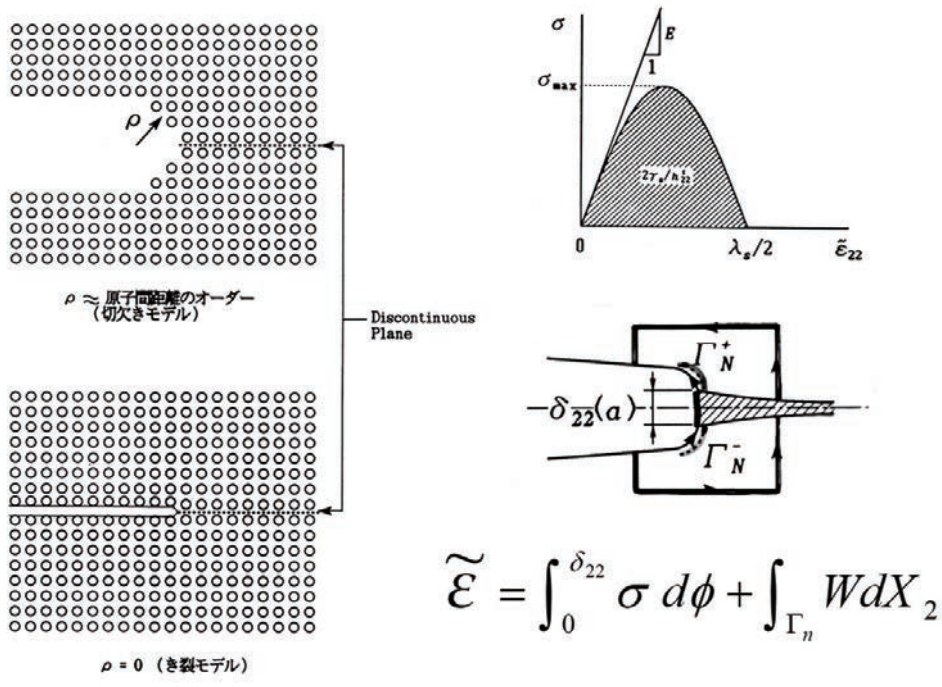
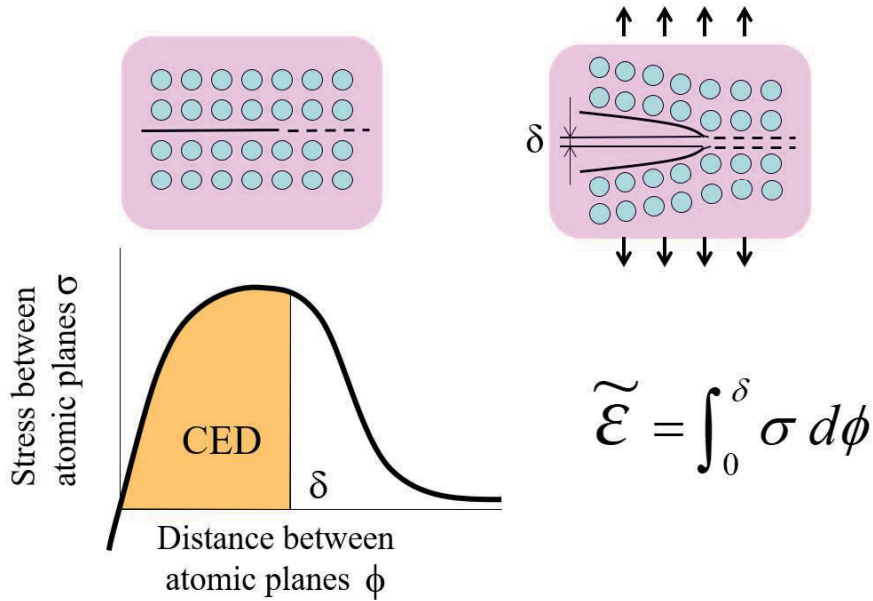
$$\dot{\mathcal{E}}^{(c)} = C C^* \quad (C : \text{const}, C^* = \int_{\Gamma} (W' dx_2 - T_i \dot{u}_{i,1} d\Gamma))$$

When Norton's rule $\dot{\varepsilon}^{cr} = A \sigma^n$ is employed,

$$C = \frac{n+1}{n}$$

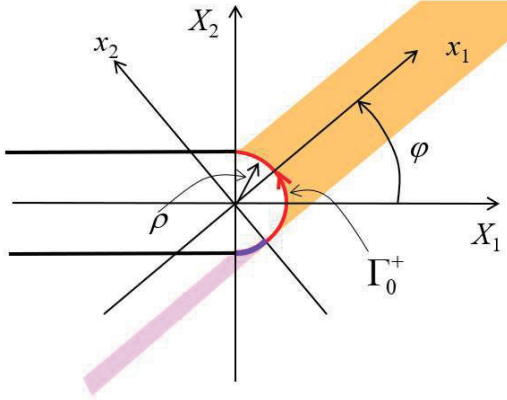
CED for Atomic Array Model

“the work, expressed per unit area in the crack plane, done at the crack tip during deformation “



Mixed Mode Crack

CED in an Arbitrary Direction



$$\mathcal{E}_\varphi = \int_{\Gamma_0^+} W dx_2$$

$$\text{Here, } W = \int_0^t \sigma_{ij} \dot{\varepsilon}_{ij} d\tau$$

For a crack of $\rho = 0$

$$\mathcal{E}_\varphi^{(c)} = \lim_{\rho \rightarrow 0} \mathcal{E}_\varphi$$

Division into mode I, mode II and mode III contributions

$$\mathcal{E}_\varphi^{(c)} = \mathcal{E}_\varphi^{\text{I}(c)} + \mathcal{E}_\varphi^{\text{II}(c)} + \mathcal{E}_\varphi^{\text{III}(c)}$$

Linear Elastic Body

$$\begin{aligned} \mathcal{E}_\varphi^{(c)} = \mathcal{E}_\varphi^{\text{I}(c)} + \mathcal{E}_\varphi^{\text{II}(c)} + \mathcal{E}_\varphi^{\text{III}(c)} &= \frac{K_I^2}{8G} \sin^2 \frac{\varphi}{2} (\kappa + \cos \varphi) + \frac{K_{II}^2}{8G} \cos^2 \frac{\varphi}{2} (\kappa - 3 \cos \varphi + 4) \\ &+ \frac{K_I K_{II}}{8G} \sin \varphi (-\kappa - 2 \cos \varphi - 1) + \frac{K_{III}^2}{2G} \cos^2 \frac{\varphi}{2} \end{aligned}$$

$$\mathcal{E}_\varphi^{\text{I}(c)} = \frac{K_I^2}{8G} \cos^4 \frac{\varphi}{2} (\kappa + \cos \varphi) + \frac{K_{II}^2}{8G} 3 \sin^2 \frac{\varphi}{2} (\kappa + 2 + 3 \cos \varphi) + \frac{K_I K_{II}}{8G} 2 \sin \frac{\varphi}{2} \cos^3 \frac{\varphi}{2} (-2\kappa - 1 - 3 \cos \varphi)$$

$$\mathcal{E}_\varphi^{\text{II}(c)} = \frac{K_I^2}{8G} \sin^2 \frac{\varphi}{2} \cos^2 \frac{\varphi}{2} (\kappa + \cos \varphi) + \frac{K_{II}^2}{8G} \sin^2 \frac{\varphi}{2} (3 \cos^2 \frac{\varphi}{2} - 2) (\kappa - 2 + 3 \cos \varphi) + \frac{K_I K_{II}}{8G} \sin \frac{\varphi}{2} (\kappa \cos \varphi + 1 - \frac{3}{2} \sin^2 \varphi)$$

$$\mathcal{E}_\varphi^{\text{III}(c)} = \frac{K_{III}^2}{2G} \cos^2 \frac{\varphi}{2}$$

When $\varphi = 0^\circ$,

$$\mathcal{E}_\varphi^{\text{I}(c)} = \frac{\kappa + 1}{8G} K_I^2$$

$$\mathcal{E}_\varphi^{\text{II}(c)} = \frac{\kappa + 1}{8G} K_{II}^2$$

$$\mathcal{E}_\varphi^{\text{III}(c)} = \frac{K_{III}^2}{2G}$$

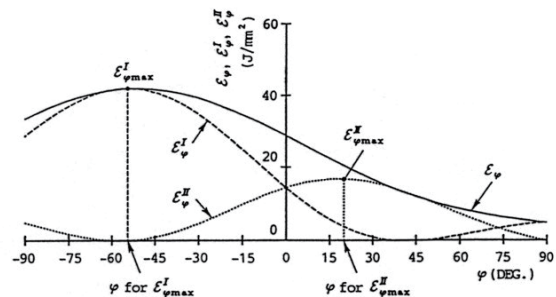


図4 $\mathcal{E}_\varphi, \mathcal{E}_\varphi^{\text{I}}, \mathcal{E}_\varphi^{\text{II}}$ と φ の関係
($K_{II}/K_I = 1.0$)

Fracture Criterion

▪ $\mathcal{E}_{\varphi \max}^I$ criterion :

When $\mathcal{E}_{\varphi \max}^I = \mathcal{E}_{IC} \cong J_{IC}$,

mode I fracture occurs in the

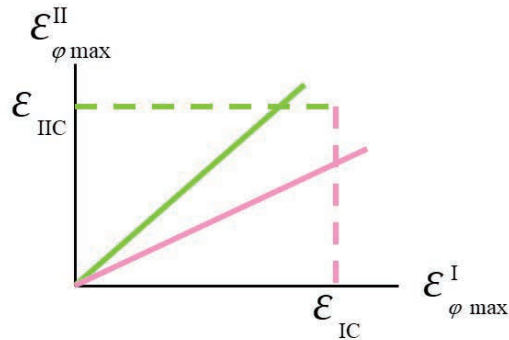
direction of $\mathcal{E}_{\varphi \max}^I$.

▪ $\mathcal{E}_{\varphi \max}^{II}$ criterion :

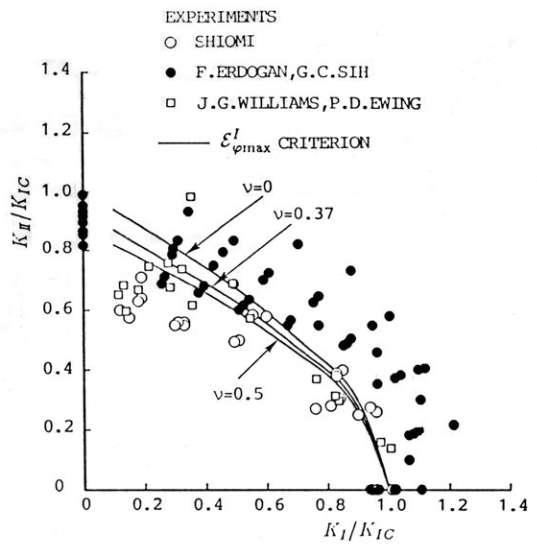
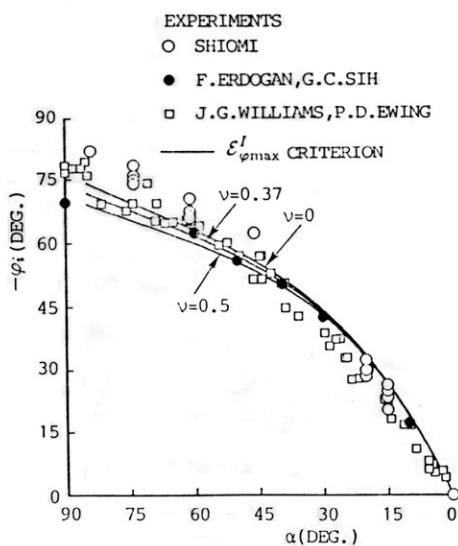
When $\mathcal{E}_{\varphi \max}^{II} = \mathcal{E}_{IIC}$,

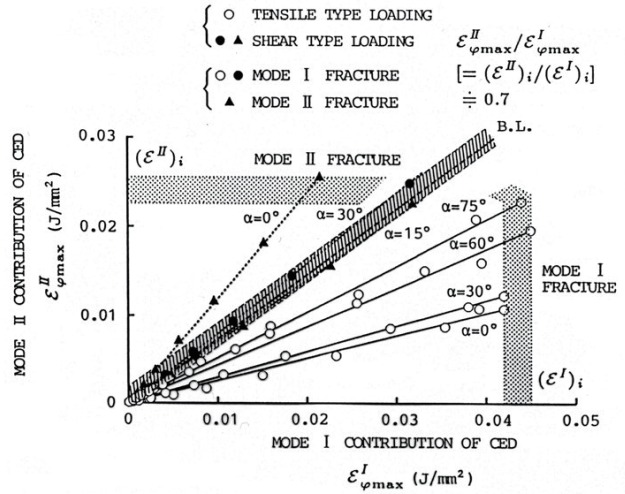
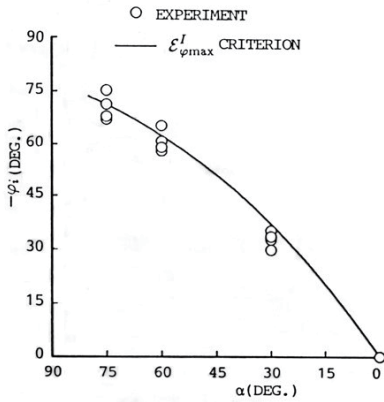
mode II fracture occurs in the

direction of $\mathcal{E}_{\varphi \max}^{II}$.



Brittle Fracture under Mixed Mode Load





Relationship between $E^I_{\phi_{max}}$ and $E^{II}_{\phi_{max}}$ before a crack growth

$(E^I)_i$: Critical value for mode I fracture
 $(E^{II})_i$: Critical value for mode II fracture
 : Boundary across which the fracture mode changes

Problems in Conventional Fracture Mechanics

1. The concept of energy release rate was considered successfully applied to inelastic fracture under small scale yielding. But, it failed to explain inelastic fracture under large scale yielding.
2. There exists no crack parameter that can be defined without depending on constitutive equation. Elastoplastic crack parameter J is defined just under deformation theory. It loses its meaning when unloading occurs and it is applicable just before the onset of crack growth. There is no way to deal with a growing inelastic crack.
3. There is no parameter for mixed mode inelastic crack.
4. Depending on phenomena, different parameters are required depending on phenomena.

Conventional Fracture Mechanics

Brittle Fracture (no plasticity)

$$K_I = K_{IC} \text{ (also for a stably growing crack)}$$

or

$$G = G_{IC} = \frac{\kappa+1}{8G} K_{IC}^2 (= 2\gamma, \text{Griffith})$$

Quasi-brittle Fracture (small scale yielding)

$$K_I = K_{IC} \text{ (also for a stably growing crack)}$$

or

$$G = G_{IC} = \frac{\kappa+1}{8G} K_{IC}^2 (= 2\gamma, \text{Griffith - Orowan})$$

(?)

Ductile Fracture (large scale yielding)

$$J = J_{IC} \text{ (? for a stably growing crack)}$$

CED-based Fracture Mechanics

Always,

$$\mathcal{E} = \mathcal{E}_{IC} \cong J_{IC}$$

Linear elastic

$$\mathcal{E}^{(e)} = \frac{\kappa+1}{8G} K_I^2 = G$$

Small Scale Yielding

$$\mathcal{E}^{(e)} \cong \frac{\kappa+1}{8G} K_I^2 \neq G$$

In these cases, the fracture condition above can be expressed also by

$$K_I = K_{IC}$$

Mixed Mode Fracture

Brittle or quasi-brittle fracture

$\sigma_{\theta \max}$ criterion

Ductile fracture

?

Fatigue Crack

$$\frac{da}{dN} = f(\Delta K)$$

Creep Crack

$$\frac{da}{dt} = f(C^*)$$

for stationary creep

Mixed Mode Fracture

$$\mathcal{E}_{\varphi \max}^I = \mathcal{E}_{IC} \cong J_{IC}$$

or

$$\mathcal{E}_{\varphi \max}^{II} = \mathcal{E}_{IIC}$$

Fatigue Crack

$$\frac{da}{dN} = f(\Delta \mathcal{E})$$

Creep Crack

$$\frac{da}{dt} = f(\dot{\mathcal{E}})$$

\mathcal{E} : Cumulative Damage

弾塑性 CED の
径路独立線積分による評価
(第 1 報, 基本関係の導出)

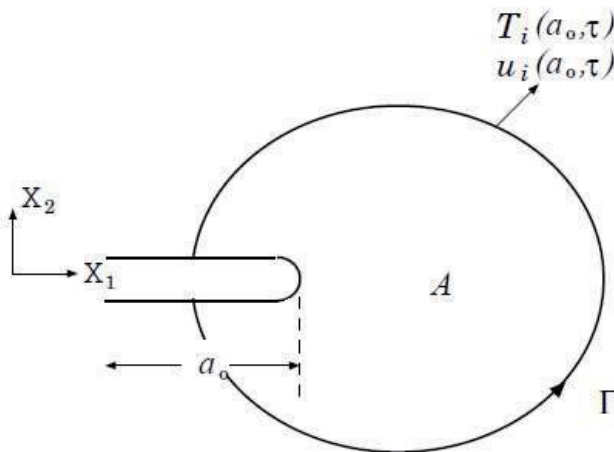
研究の背景と目的

き裂エネルギー密度 CED の評価法

- 直接評価
- 荷重－荷重点変位曲線
- 径路独立積分

従来の CED の径路独立積分 \mathcal{E}_J

$$\mathcal{E}_J(a_o, t) = \int_{\Gamma} (W dx_2 - T_i u_{i,1} d\Gamma) - \int_A \int_0^t (\sigma_{ij,1} \varepsilon_{ij,\tau} - \varepsilon_{ij,1} \sigma_{ij,\tau}) d\tau dA$$



前提条件

- 任意の構成条件に従う弾塑性体
- き裂の進展が開始するまで
- 静的な負荷が加えられ、その間除荷は起こらない
- 簡単のため厚さ方向には単位厚さを考える

初期き裂長さの異なる二つのき裂材

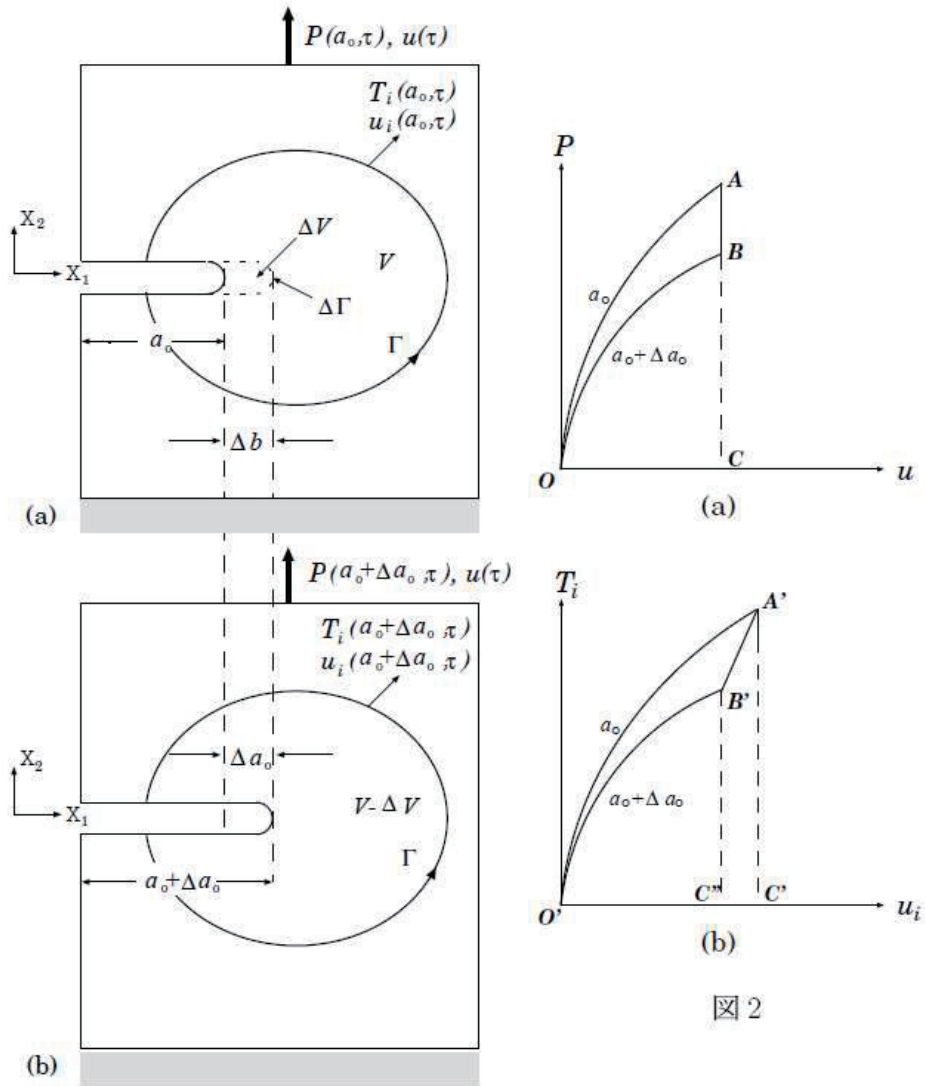
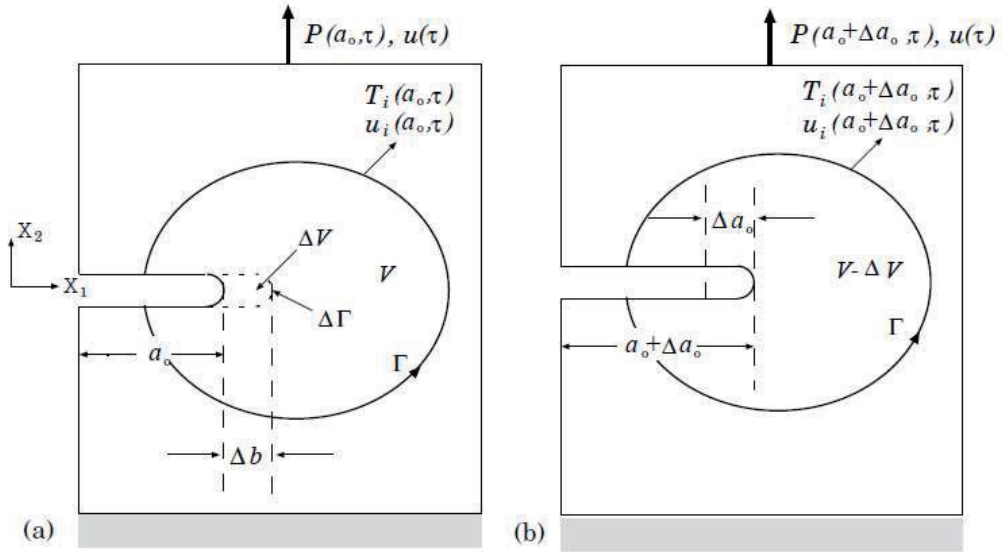


図 1

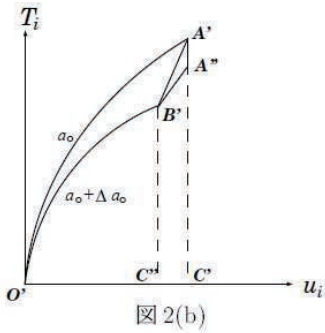
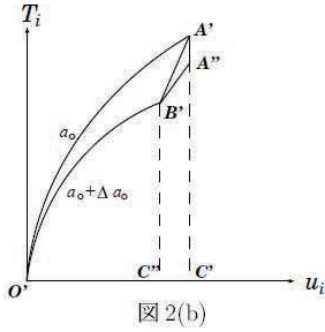
図 2



$$\begin{aligned}
 U(a_o, t) &= \int_V W(a_o, t) dV \\
 &= \int_{\Gamma} \int_0^t T_i(a_o, \tau) \dot{u}_i(a_o, \tau) d\tau d\Gamma
 \end{aligned}$$

共通である領域 $V - \Delta V$ に注目

$$\begin{aligned}
 \int_{V-\Delta V} W(a_o, t) dV &= U(a_o, t) + \int_{\Delta\Gamma} \int_0^t T_i(a_o, \tau) \dot{u}_i(a_o, \tau) d\tau d(\Delta\Gamma) \\
 &= U(a_o + \Delta a_o, t) + \int_{\Gamma} \int_{T_i(a_o + \Delta a_o, t), u_i(a_o + \Delta a_o, t)}^{T_i^*, u_i(a_o, t)} T_i' du_i' d\Gamma \\
 &\quad + \int_{\Delta\Gamma} \int_{0,0}^{T_i^{**}, u_i^{**}} T_i'' du_i'' d(\Delta\Gamma)
 \end{aligned}$$



$$\begin{aligned}
 & U(a_0, t) - U(a_0 + \Delta a_0, t) \\
 &= - \int_{\Delta\Gamma} \left\{ \int_0^t T_i(a_0, \tau) \dot{u}_i(a_0, \tau) d\tau - \int_{0,0}^{T_i^{**}, u_i^{**}} T_i'' du_i'' \right\} d(\Delta\Gamma) \\
 & \quad + \int_{\Gamma} \text{面積} A' B' C'' C' d\Gamma
 \end{aligned}$$

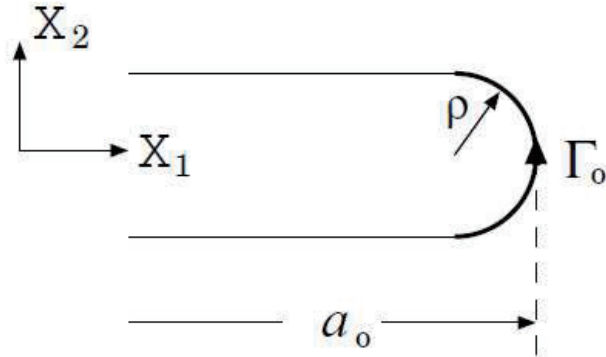
$$\begin{aligned}
 \Delta S &= \int_{\Gamma} \text{面積} O' A' B' d\Gamma \\
 &= \int_{\Gamma} \text{面積} O' A' C' d\Gamma - \int_{\Gamma} \text{面積} O' B' C'' d\Gamma - \int_{\Gamma} \text{面積} A' B' C'' C' d\Gamma \\
 &= U(a_0, t) - U(a_0 + \Delta a_0, t) - \int_{\Gamma} \text{面積} A' B' C'' C' d\Gamma \\
 &= - \int_{\Delta\Gamma} \left\{ \int_0^t T_i(a_0, \tau) \dot{u}_i(a_0, \tau) d\tau - \int_{0,0}^{T_i^{**}, u_i^{**}} T_i'' du_i'' \right\} d(\Delta\Gamma) \\
 & \quad - \int_{\Gamma} \text{面積} A' B' A'' d\Gamma
 \end{aligned}$$

$$\int_0^t T_i(a_0, \tau) \dot{u}_i(a_0, \tau) d\tau = \int_{0,0}^{T_i(a_0,t), u_i(a_0,t)} T_i(a_0, \tau) du_i$$

$\Delta a_0 (= \Delta b) \rightarrow 0$ のとき

$$T_i(a_0, t) \rightarrow 0, \quad u_i(a_0, t) \rightarrow 0, \quad T_i^{**} \rightarrow 0, \quad u_i^{**} \rightarrow 0$$

$$\begin{aligned}
\Delta \mathcal{S} &= - \int_{\Delta \Gamma} \int_0^t T_i(a_o, \tau) \dot{u}_i(a_o, \tau) d\tau d(\Delta \Gamma) \\
&= \int_{\Delta V} W(a_o, t) dV = \Delta b \int_{\Gamma_o} W(a_o, t) dX_2 \\
&= \Delta a_o \int_{\Gamma_o} W(a_o, t) dX_2
\end{aligned}$$



$$\mathcal{E}(\rho, t) = \int_{\Gamma_o} W(a_o, t) dX_2 : CED \text{ の定義}$$

$$\mathcal{E}(\rho, t) = \lim_{\Delta a_o \rightarrow 0} \frac{\Delta \mathcal{S}}{\Delta a_o}$$

徑路獨立線積分による表示

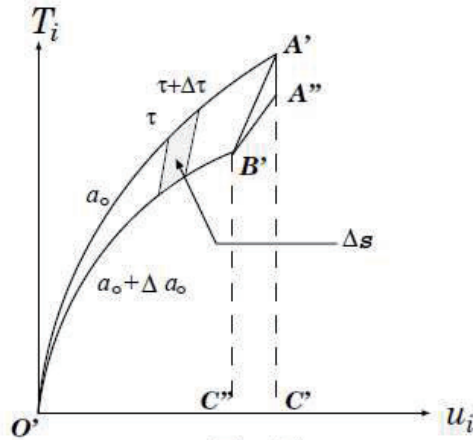


図 2(b)

$$\begin{aligned} \Delta S &= \begin{vmatrix} u_i & T_i & 1 \\ u_i + \frac{\partial u_i}{\partial a} \Delta a & T_i + \frac{\partial T_i}{\partial a} \Delta a & 1 \\ u_i + \dot{u}_i \Delta \tau & T_i + \dot{T}_i \Delta \tau & 1 \end{vmatrix} \\ &= \left(\dot{T}_i \frac{\partial u_i}{\partial a_0} - \dot{u}_i \frac{\partial T_i}{\partial a_0} \right) \Delta a_0 \Delta \tau \end{aligned}$$

$$\Delta S = \int_{\Gamma} \text{面積 } O'A'B' d\Gamma$$

$$= \Delta a_0 \int_{\Gamma} \int_0^t \left(\dot{T}_i \frac{\partial u_i}{\partial a_0} - \dot{u}_i \frac{\partial T_i}{\partial a_0} \right) d\tau d\Gamma$$

$$\mathcal{E}(\rho, t) = \lim_{\Delta a_0 \rightarrow 0} \frac{\Delta S}{\Delta a_0} = \int_{\Gamma} \int_0^t \left(\dot{T}_i \frac{\partial u_i}{\partial a_0} - \dot{u}_i \frac{\partial T_i}{\partial a_0} \right) d\tau d\Gamma$$

シャープなき裂

$$\mathcal{E}^{(c)}(t) = \lim_{\rho \rightarrow 0} \mathcal{E}(\rho, t) = \int_{\Gamma} \int_0^t \left(\dot{T}_i \frac{\partial u_i}{\partial a_o} - \dot{u}_i \frac{\partial T_i}{\partial a_o} \right)_{\rho=0} d\tau d\Gamma$$

Γ として最外縁の径路をとるとき

$$\mathcal{E}(\rho, t) = - \int_0^t \frac{\partial P}{\partial a_o} \dot{u} d\tau$$

弾性の場合：CED = エネルギー解放率

$$\mathcal{E}(\rho, t) = \int_{\Gamma} \int_0^t \left(\dot{T}_i \frac{\partial u_i}{\partial a} - \dot{u}_i \frac{\partial T_i}{\partial a} \right) d\tau d\Gamma : E積分$$

弾塑性CEDの

径路独立線積分による評価

(第2報, 基本関係の各種問題への拡張)

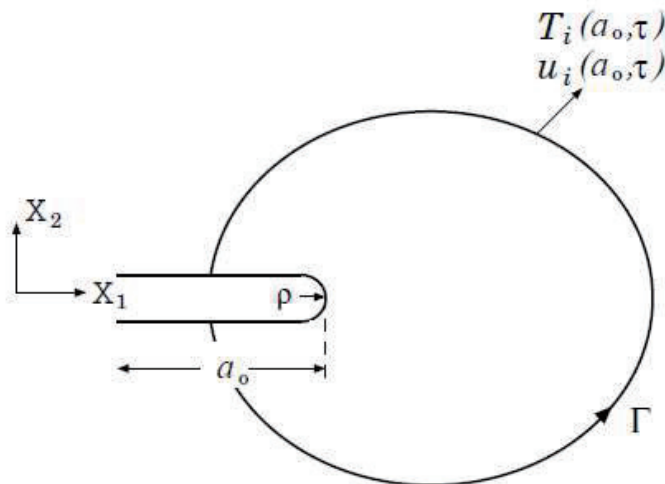
本報告の背景

き裂エネルギー密度 CED の評価法

- 直接評価
- 荷重－荷重点変位曲線
- 径路独立積分 (\mathcal{E}_J)

直進方向の CED の径路独立線積分の表示

$$\mathcal{E}(\rho, t) = \int_{\Gamma} \int_0^t \left(\dot{T}_i \frac{\partial u_i}{\partial a_o} - \dot{u}_i \frac{\partial T_i}{\partial a_o} \right) d\tau d\Gamma$$



本報告の目的

非均質な弾塑性体中の任意方向
CED に対しても, 同様な径路独立
線積分が存在することを示すこと

前提条件

- 構成条件が場所の連続関数として与えられる任意の弾塑性体

$$\sigma_{ij} = f_{ij}(\varepsilon_{11}, \varepsilon_{22}, \dots, x_1, x_2, x_3, H)$$

- き裂の進展が開始するまで
- 単調に増加する静的な負荷
- 厚さ方向には単位厚さを考える

屈折分だけ異なる二つのき裂材

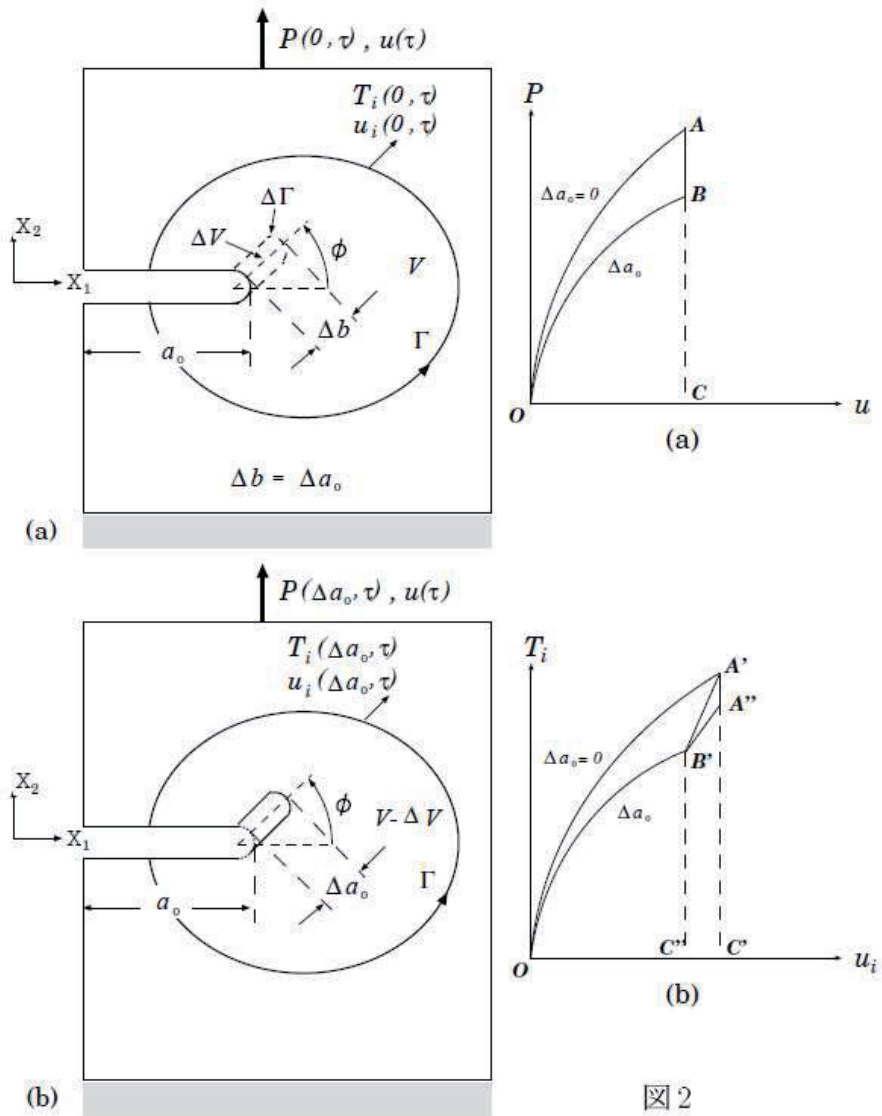
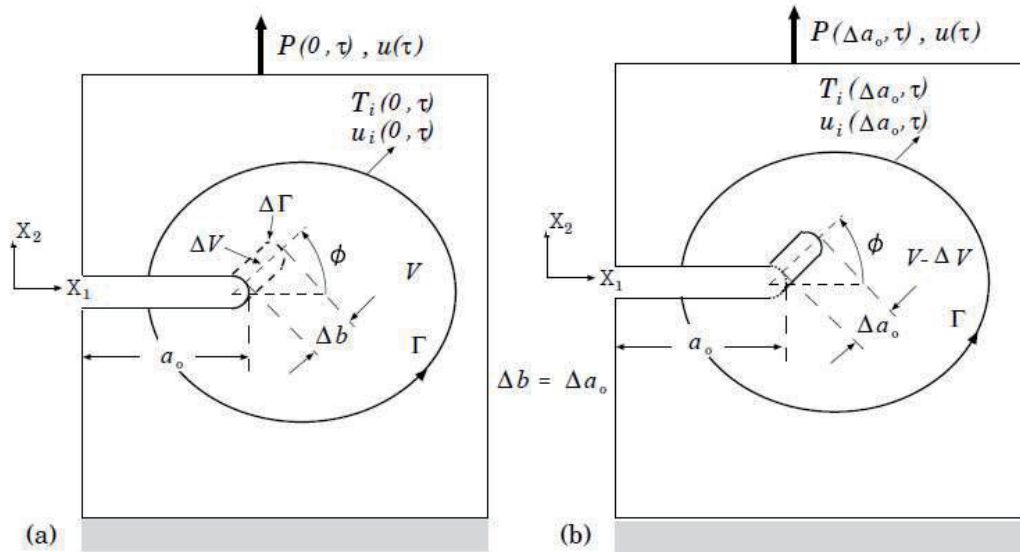


図1

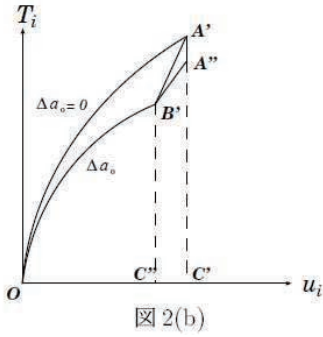
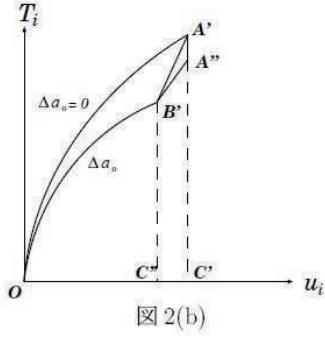
図2



$$\begin{aligned}
 U(\Delta a_0, t) &= \int_V W(\Delta a_0, t) dV \\
 &= \int_{\Gamma} \int_0^t T_i(\Delta a_0, \tau) \dot{u}_i(\Delta a_0, \tau) d\tau d\Gamma
 \end{aligned}$$

共通である領域 $V - \Delta V$ に注目

$$\begin{aligned}
 \int_{V-\Delta V} W(0, t) dV &= U(0, t) + \int_{\Delta\Gamma} \int_0^t T_i(0, \tau) \dot{u}_i(0, \tau) d\tau d(\Delta\Gamma) \\
 &= U(\Delta a_0, t) + \int_{\Gamma} \int_{T_i(\Delta a_0, t), u_i(\Delta a_0, t)}^{T_i^*, u_i(0, t)} T_i' du_i' d\Gamma \\
 &\quad + \int_{\Delta\Gamma} \int_{0,0}^{T_i^{**}, u_i^{**}} T_i'' du_i'' d(\Delta\Gamma)
 \end{aligned}$$



$$\begin{aligned}
 & U(0, t) - U(\Delta a_o, t) \\
 &= - \int_{\Delta\Gamma} \left\{ \int_0^t T_i(0, \tau) \dot{u}_i(0, \tau) d\tau - \int_{0,0}^{T_i^{**}, u_i^{**}} T_i'' du_i'' \right\} d(\Delta\Gamma) \\
 & \quad + \int_{\Gamma} \text{面積} A'' B' C'' C' d\Gamma
 \end{aligned}$$

$$\Delta S = \int_{\Gamma} \text{面積} O' A' B' d\Gamma$$

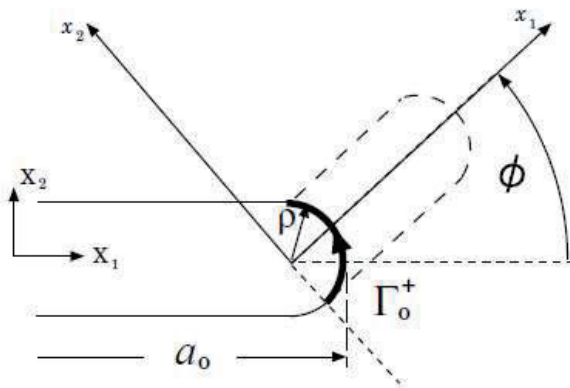
$$\begin{aligned}
 &= \int_{\Gamma} \text{面積} O' A' C' d\Gamma - \int_{\Gamma} \text{面積} O' B' C'' d\Gamma - \int_{\Gamma} \text{面積} A' B' C'' C' d\Gamma \\
 &= U(0, t) - U(\Delta a_o, t) - \int_{\Gamma} \text{面積} A' B' C'' C' d\Gamma \\
 &= - \int_{\Delta\Gamma} \left\{ \int_0^t T_i(0, \tau) \dot{u}_i(0, \tau) d\tau - \int_{0,0}^{T_i^{**}, u_i^{**}} T_i'' du_i'' \right\} d(\Delta\Gamma) \\
 & \quad - \int_{\Gamma} \text{面積} A' B' A'' d\Gamma
 \end{aligned}$$

$$\int_0^t T_i(0, \tau) \dot{u}_i(0, \tau) d\tau = \int_{0,0}^{T_i(0,t), u_i(0,t)} T_i(0, \tau) du_i$$

$\Delta a_o (= \Delta b) \rightarrow 0$ のとき

$$T_i(0, t) \rightarrow 0, \quad u_i(0, t) \rightarrow 0, \quad T_i^{**} \rightarrow 0, \quad u_i^{**} \rightarrow 0$$

$$\begin{aligned}
\Delta \mathcal{S} &= - \int_{\Delta \Gamma} \int_0^t T_i(0, \tau) \dot{u}_i(0, \tau) d\tau d(\Delta \Gamma) \\
&= \int_{\Delta V} W(0, t) dV = \Delta b \int_{\Gamma_o^+} W(0, t) dx_2 \\
&= \Delta a_o \int_{\Gamma_o^+} W(0, t) dx_2
\end{aligned}$$



$\mathcal{E}_\varphi(\rho, t) = \int_{\Gamma_o^+} W(0, t) dx_2$: 任意方向CEDの定義

$$\mathcal{E}_\varphi(\rho, t) = \lim_{\Delta a_o \rightarrow 0} \frac{\Delta \mathcal{S}}{\Delta a_o}$$

徑路獨立線積分による表示

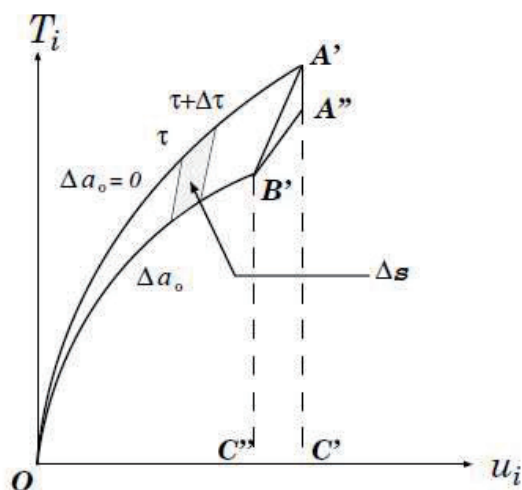


図 2(b)

$$\begin{aligned} \Delta S &= \begin{vmatrix} u_i & T_i & 1 \\ u_i + \frac{\partial u_i}{\partial a} \Delta a & T_i + \frac{\partial T_i}{\partial a} \Delta a & 1 \\ u_i + \dot{u}_i \Delta \tau & T_i + \dot{T}_i \Delta \tau & 1 \end{vmatrix} \\ &= \left(\dot{T}_i \frac{\partial u_i}{\partial a_o} - \dot{u}_i \frac{\partial T_i}{\partial a_o} \right) \Delta a_o \Delta \tau \end{aligned}$$

$$\Delta S = \int_{\Gamma} \text{面積 } O'A'B' d\Gamma$$

$$= \Delta a_o \int_{\Gamma} \int_0^t \left(\dot{T}_i \frac{\partial u_i}{\partial a_o} - \dot{u}_i \frac{\partial T_i}{\partial a_o} \right) d\tau d\Gamma$$

$$\mathcal{E}_{\varphi}(\rho, t) = \lim_{\Delta a_o \rightarrow 0} \frac{\Delta S}{\Delta a_o} = \int_{\Gamma} \int_0^t \left(\dot{T}_i \frac{\partial u_i}{\partial a_o} - \dot{u}_i \frac{\partial T_i}{\partial a_o} \right) d\tau d\Gamma$$

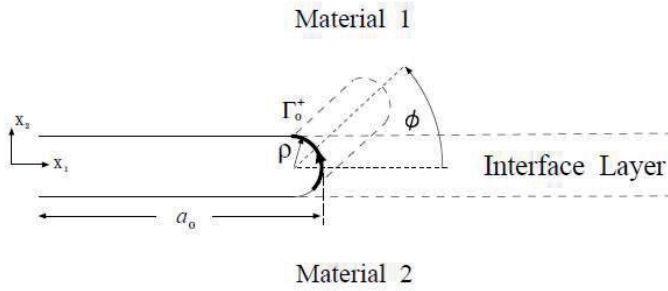
シャープなき裂

$$\mathcal{E}_\varphi^{(c)}(t) = \lim_{\rho \rightarrow 0} \mathcal{E}_\varphi(\rho, t) = \int_\Gamma \int_0^t \left(\dot{T}_i \frac{\partial u_i}{\partial a_o} - u_i \frac{\partial T_i}{\partial a_o} \right)_{\rho=0} d\tau d\Gamma$$

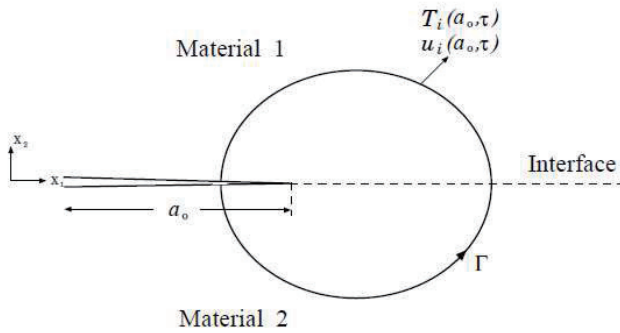
Γ として最外縁の径路をとるとき

$$\mathcal{E}_\varphi(\rho, t) = - \int_0^t \frac{\partial P}{\partial a_o} \dot{u} d\tau$$

界面き裂の場合



$$\mathcal{E}_\varphi(\rho, t) = \int_\Gamma \int_0^t \left(\dot{T}_i \frac{\partial u_i}{\partial a_0} - \dot{u}_i \frac{\partial T_i}{\partial a_0} \right) d\tau d\Gamma$$



$$\mathcal{E}_\varphi^{(c)}(t) = \int_\Gamma \int_0^t \left(\dot{T}_i \frac{\partial u_i}{\partial a_0} - \dot{u}_i \frac{\partial T_i}{\partial a_0} \right)_{\rho=0} d\tau d\Gamma$$

弾塑性 CED の

径路独立線積分による評価

(第3報, 有限要素解析に基づく検討)

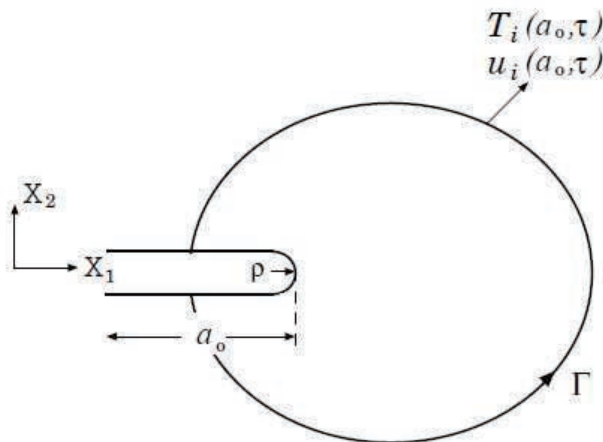
本報告の背景と目的

き裂エネルギー密度 CED の評価法

- 直接評価
- 荷重－荷重点変位曲線
- 径路独立積分 (\mathcal{E}_J)

新たな CED の評価法－径路独立線積分 (\mathcal{E}^L)

$$\mathcal{E}^L(\rho, t) = \int_{\Gamma} \int_0^t \left(\dot{T}_i \frac{\partial u_i}{\partial a_o} - \dot{u}_i \frac{\partial T_i}{\partial a_o} \right) d\tau d\Gamma$$



解析モデル

ヤング率 E	ポアソン比 ν	降伏応力 σ_Y	硬化率 H'
$2.06 \times 10^2 GPa$	0.3	$2.0 \times 10^2 MPa$	$2.06 \times 10^3 MPa$

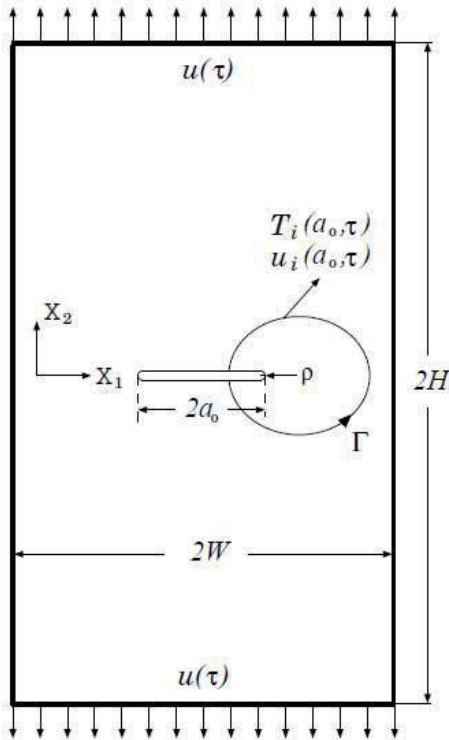


Fig.1 Center-cracked specimen

W	H	a_o	ρ/W
25mm	50mm	8.5mm	0.004

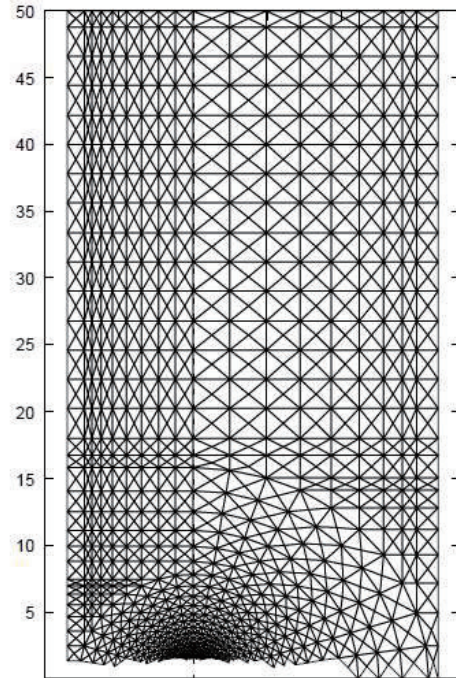


Fig.2 Mesh for FEM Analysis

要素数	節点数
4806	2487

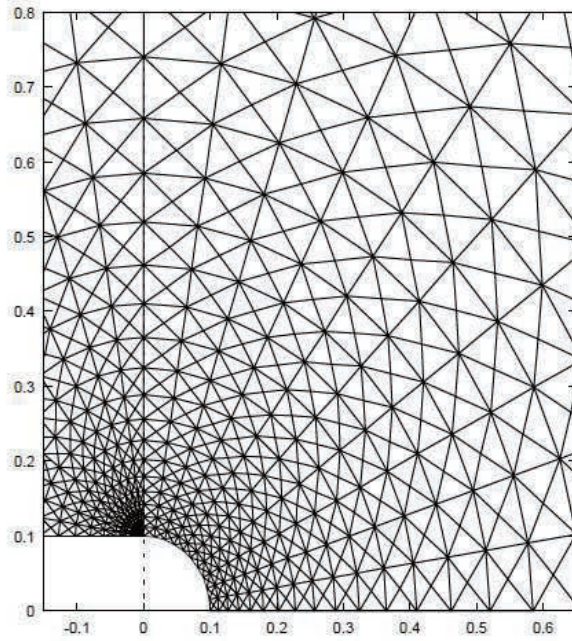


Fig.3(a) 初期き裂長さ = a_0

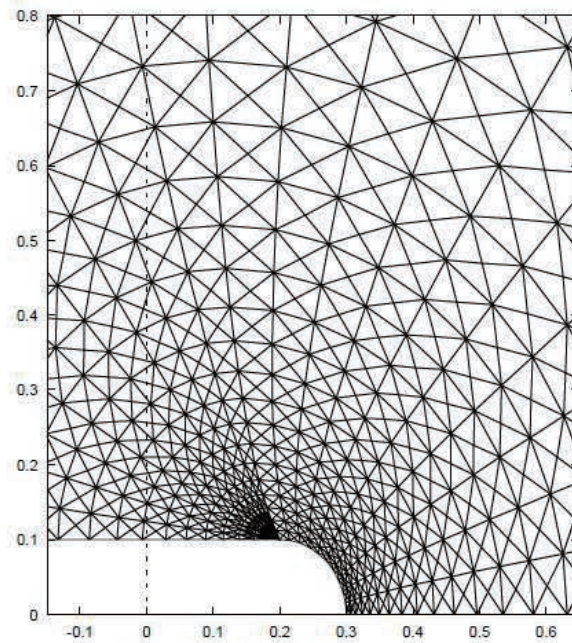


Fig.3(b) 初期き裂長さ = $a_0 + \Delta a_0$

$\Delta a_0(mm)$	0.003125	0.00625	0.0125	0.025	0.05	0.1
$\Delta a_0/a_0$	3.68×10^{-4}	7.35×10^{-4}	0.00147	0.00294	0.00588	0.01176

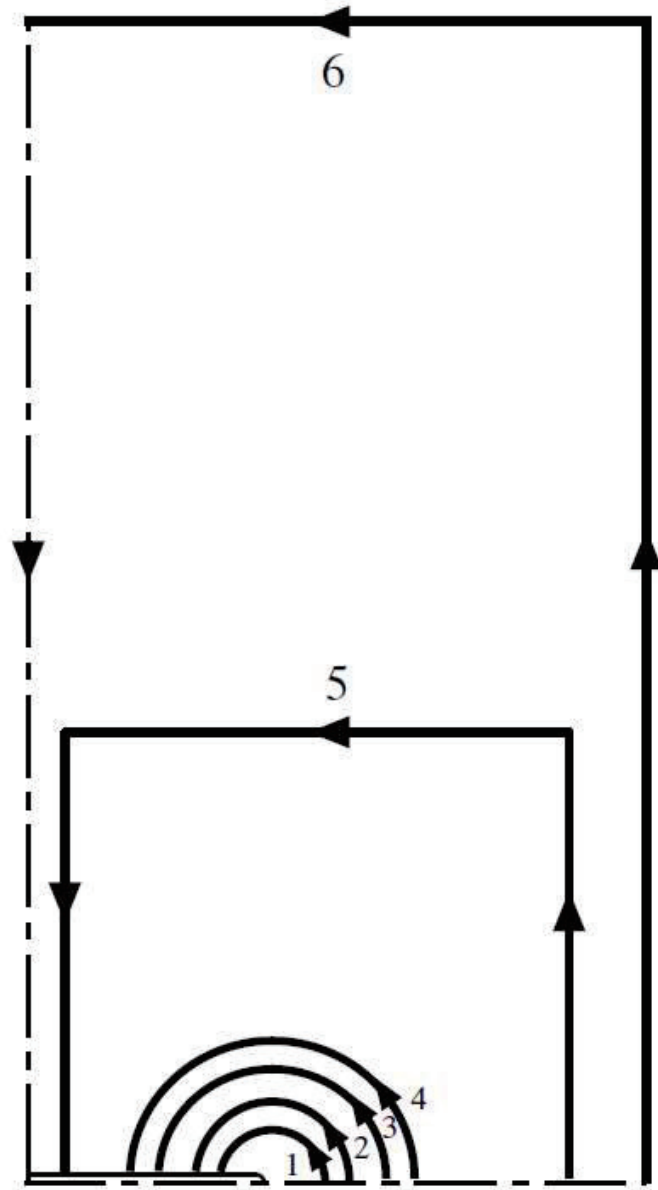
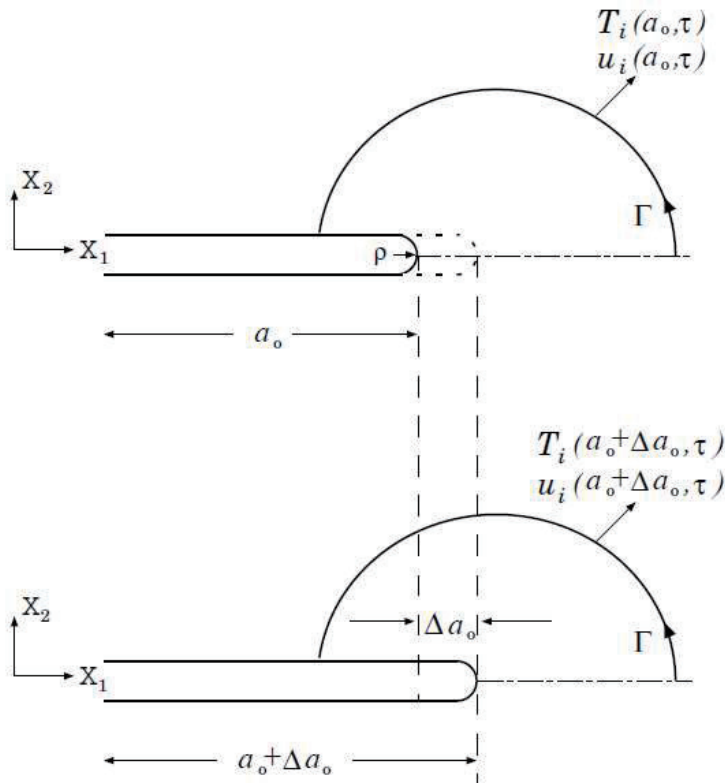


Fig.4 Integration path surrounding a notch tip

径路独立線積分 \mathcal{E}^L の数値評価式

$$\begin{aligned} \mathcal{E}^L(\rho, t) &= 2 \int_{\Gamma} \int_0^t \left(\dot{T}_i \frac{\partial u_i}{\partial a_o} - \dot{u}_i \frac{\partial T_i}{\partial a_o} \right) d\tau d\Gamma \approx \\ &2 \int_{\Gamma} \int_0^t \left(\frac{T_i(a_o, \tau + \Delta\tau) - T_i(a_o, \tau)}{\Delta\tau} \frac{u_i(a_o + \Delta a_o, \tau) - u_i(a_o, \tau)}{\Delta a_o} \right. \\ &\quad \left. - \frac{u_i(a_o, \tau + \Delta\tau) - u_i(a_o, \tau)}{\Delta\tau} \frac{T_i(a_o + \Delta a_o, \tau) - T_i(a_o, \tau)}{\Delta a_o} \right) d\tau d\Gamma \end{aligned}$$



ほかの評価法

\mathcal{E}_J 積分

$$\begin{aligned}\mathcal{E}_J(\rho, t) &= \int_{\Gamma} (W n_1 - T_i u_{i,1}) d\Gamma \\ &\quad - \int_A \int_0^t (\sigma_{ij,1} \varepsilon_{ij,\tau} - \varepsilon_{ij,1} \sigma_{ij,\tau}) d\tau dA \quad (\text{表示1}) \\ &= \int_{\Gamma} (W n_1 - \int_0^t T_i u_{i,1\tau} d\tau) d\Gamma \\ &\quad - \int_A \int_0^t \sigma_{ij,1} \varepsilon_{ij,\tau} d\tau dA \quad (\text{表示2})\end{aligned}$$

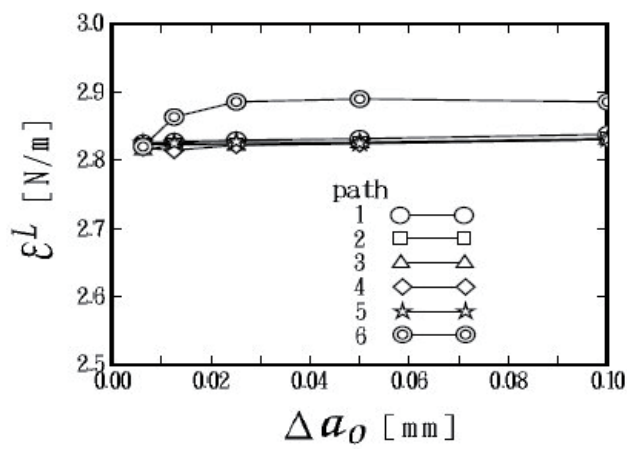
J 積分

$$J = \int_{\Gamma} (W n_1 - T_i u_{i,1}) d\Gamma$$

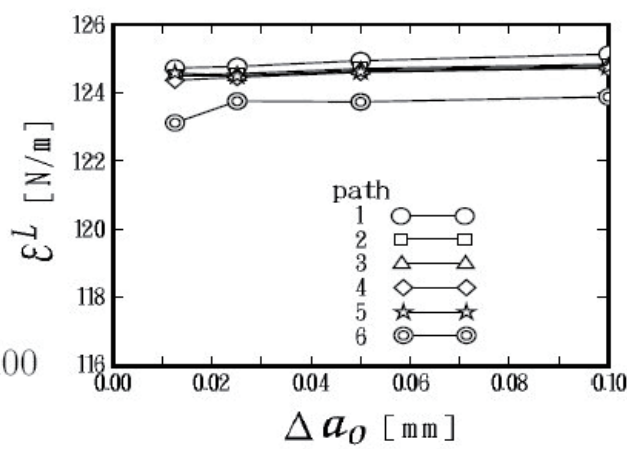
\mathcal{E}^K の値

$$\mathcal{E}^K = \frac{1 - \nu^2}{E} K^2$$

(a) $r_P/a_0 = 0$
 弾性状態



(b) $r_P/a_0 \approx 1/100$
 小規模降伏状態



(c) $r_P/a_0 \approx 1$
 大規模降伏状態

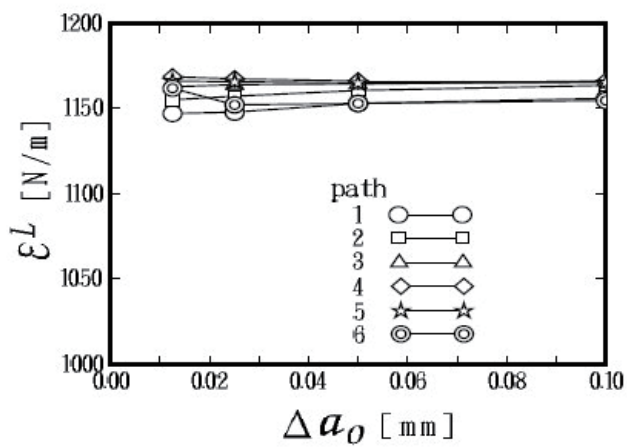
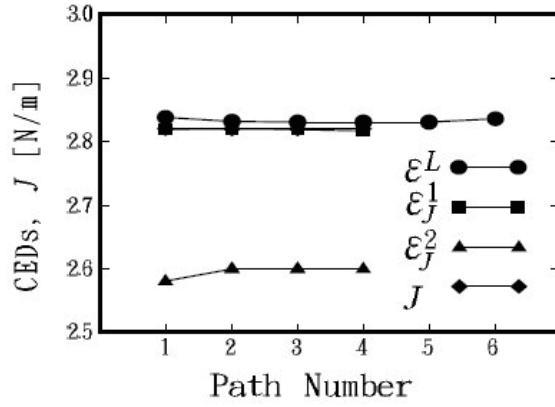
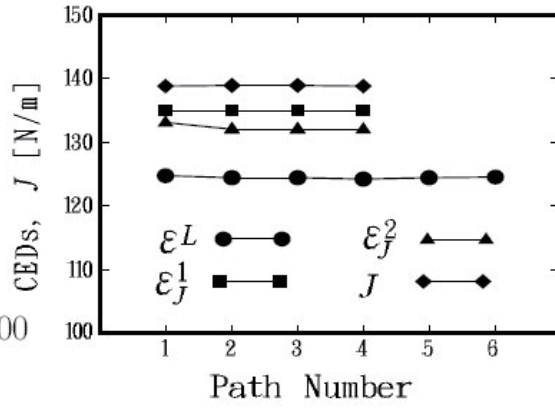


Fig.5 Dependency of CED on Δa_0

(a) $r_P/a_0 = 0$
 弾性状態



(b) $r_P/a_0 \approx 1/100$
 小規模降伏状態



(c) $r_P/a_0 \approx 1$
 大規模降伏状態

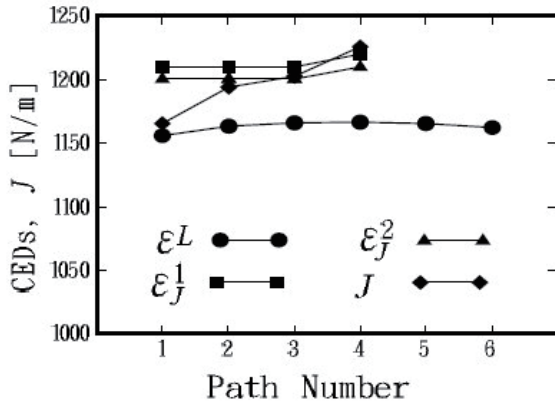


Fig.6 Dependency of CED on integration path

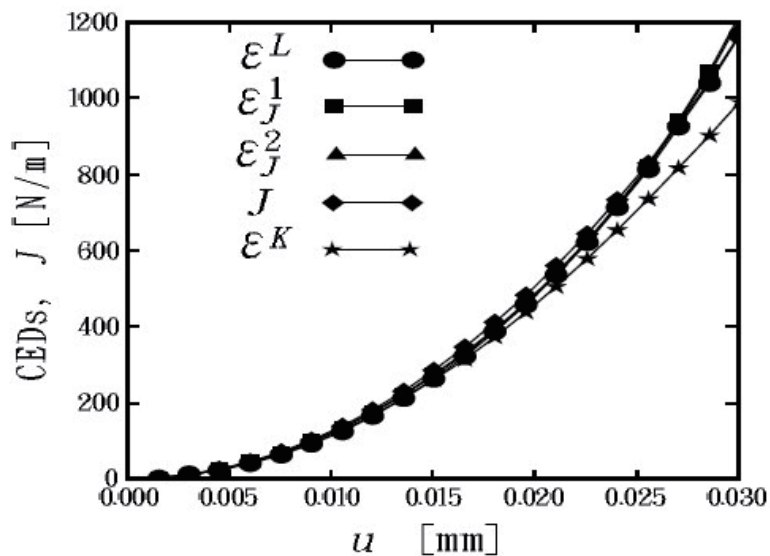


Fig.6(a) CEDs and J with load

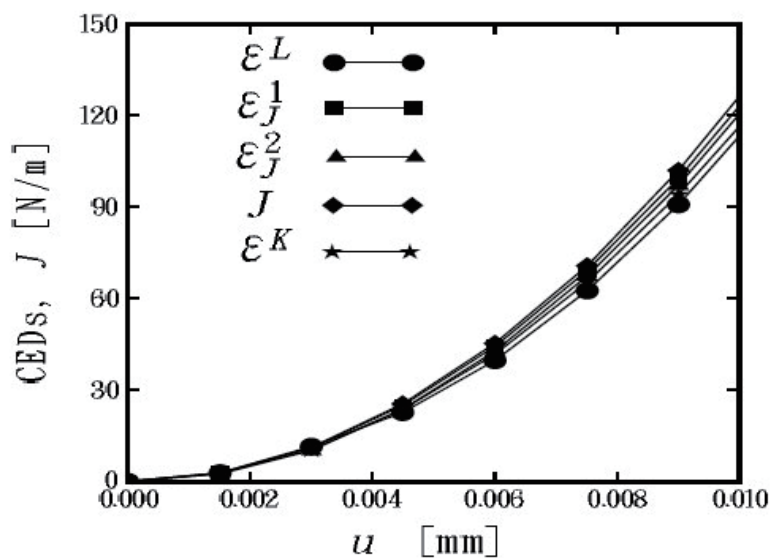


Fig.6(b) CEDs and J with load (in early stage)

弾塑性 CED の

径路独立線積分による評価

(第4報, 異種材料界面が存在する場合)

本報告の背景と目的

新たな CED の評価法 - 径路独立線積分 (\mathcal{E}^L)

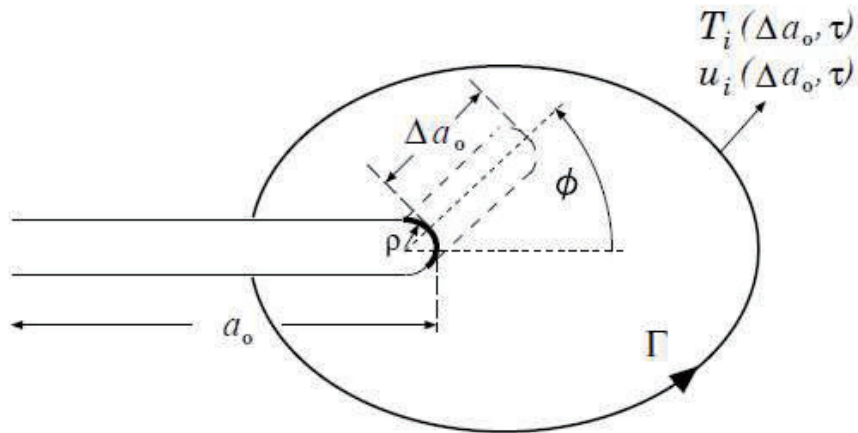


Fig.1 Notch Model

$$\mathcal{E}_\varphi^L(\rho, t) = \int_\Gamma \int_0^t \left(\dot{T}_i \frac{\partial u_i}{\partial(\Delta a_0)} - \dot{u}_i \frac{\partial T_i}{\partial(\Delta a_0)} \right) d\tau d\Gamma$$

シャープなき裂

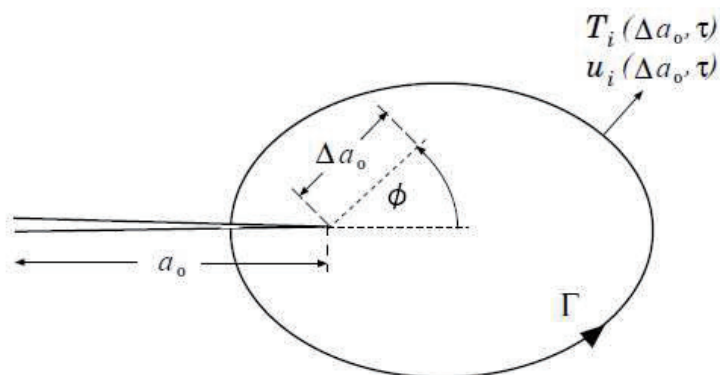


Fig.2 Crack Model

$$\mathcal{E}_\varphi^L(t) = \int_\Gamma \int_0^t \left(\dot{T}_i \frac{\partial u_i}{\partial(\Delta a_0)} - u_i \frac{\partial T_i}{\partial(\Delta a_0)} \right)_{\rho=0} d\tau d\Gamma$$

本報告の目的

異種材料界面が存在する場合の直進方向CEDの評価を試み、理論結果を数値的に確認すること

解析モデル

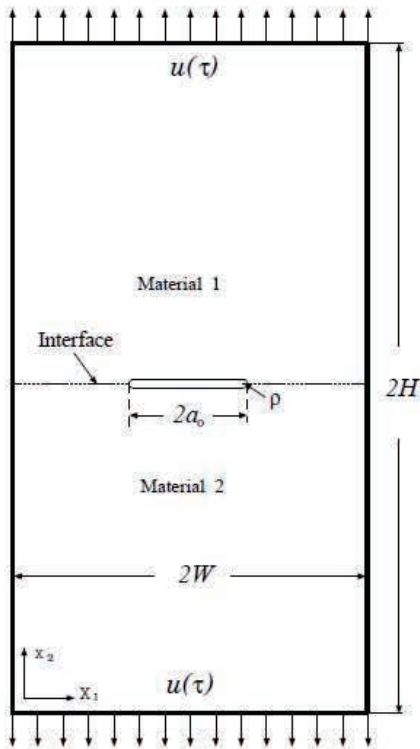


Fig.3 Interface crack

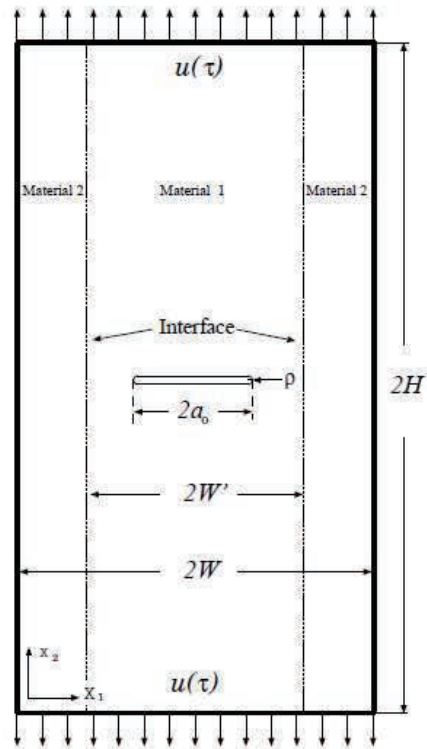


Fig.4 Crack perpendicular to interface

Table 1 Model Dimensions

W	W'	H	a_0	ρ/W
25mm	17mm	50mm	8.5mm	0.0

Table 2 Material Constants

	ヤング率 E	ポアソン比 ν	降伏応力 σ_Y	硬化率 H'
Material 1	200.0 GPa	0.3	450.0 MPa	2.0 GPa
Material 2	304.0 GPa	0.27	—	—

Table 3 Differences in initial crack lengths

Δa_0 (mm)	0.01	0.017	0.024	0.032	0.041
$\Delta a_0/a_0$	0.00125	0.00199	0.00283	0.00377	0.00483

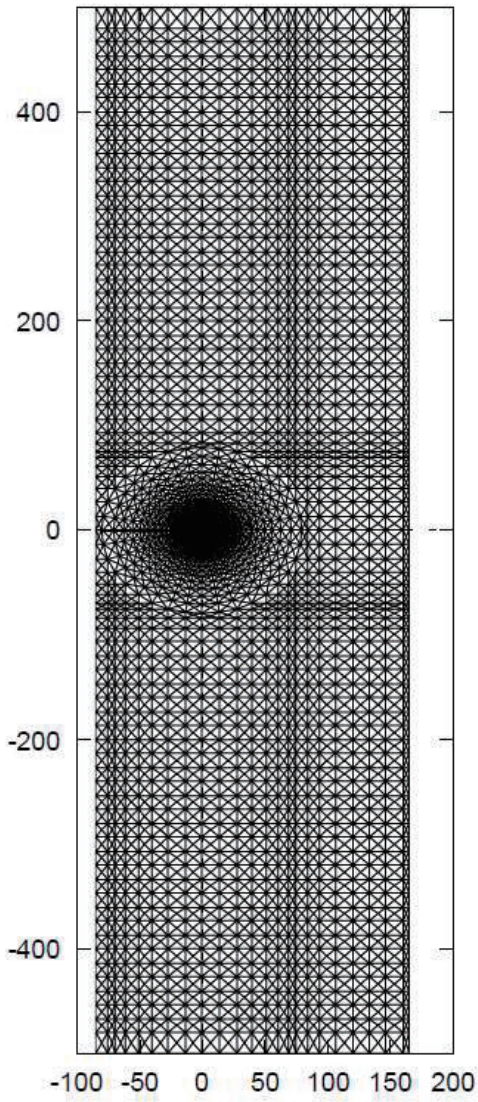


Fig.5 Mesh for FEM Analysis

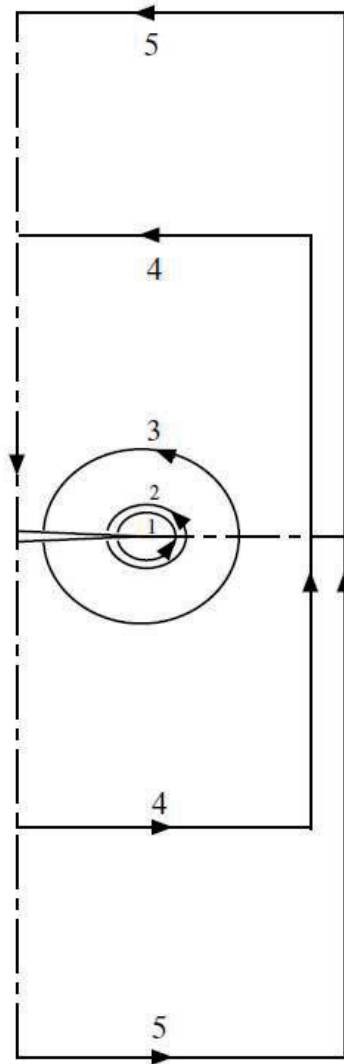


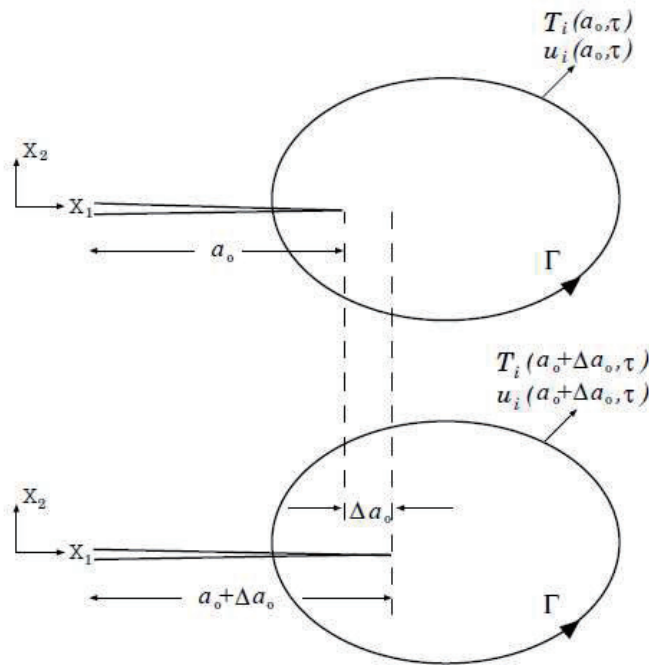
Fig.6 Integration paths surrounding a crack tip

径路独立線積分 \mathcal{E}^L の数値評価式

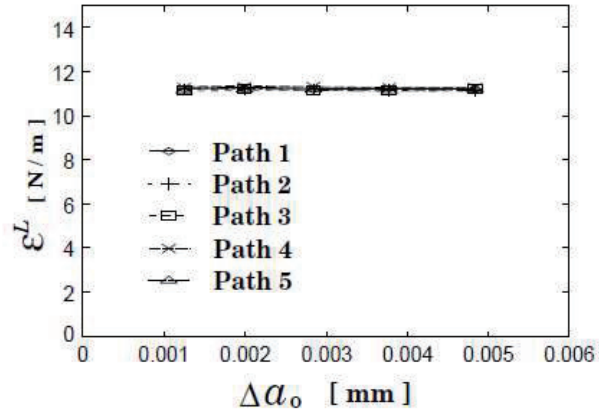
$$\mathcal{E}^L(t) = \int_{\Gamma} \int_0^t \left(\dot{T}_i \frac{\partial u_i}{\partial a_o} - \dot{u}_i \frac{\partial T_i}{\partial a_o} \right) d\tau d\Gamma \approx$$

$$\int_{\Gamma} \int_0^t \left(\frac{T_i(a_o, \tau + \Delta\tau) - T_i(a_o, \tau)}{\Delta\tau} \frac{u_i(a_o + \Delta a_o, \tau) - u_i(a_o, \tau)}{\Delta a_o} \right.$$

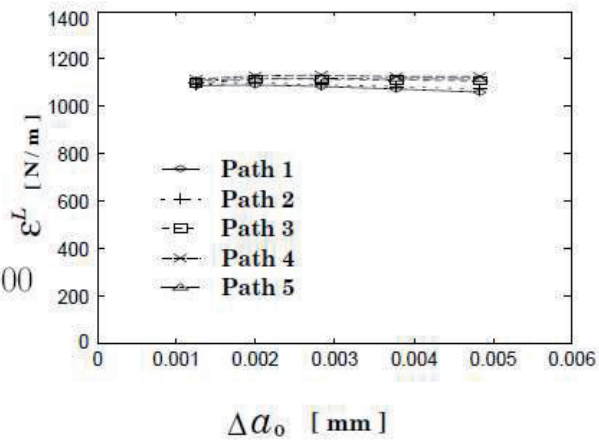
$$\left. - \frac{u_i(a_o, \tau + \Delta\tau) - u_i(a_o, \tau)}{\Delta\tau} \frac{T_i(a_o + \Delta a_o, \tau) - T_i(a_o, \tau)}{\Delta a_o} \right) d\tau d\Gamma$$



(a) $r_P/a_0 = 0$
 弾性状態



(b) $r_P/a_0 \approx 1/100$
 小規模降伏状態



(c) $r_P/a_0 \approx 1/10$
 大規模降伏状態

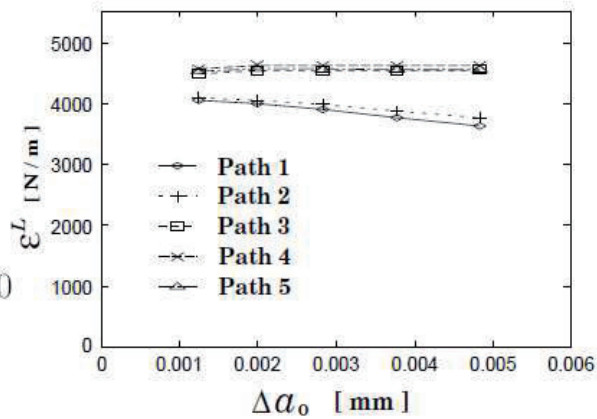


Fig.7 Dependency of CED on Δa_0

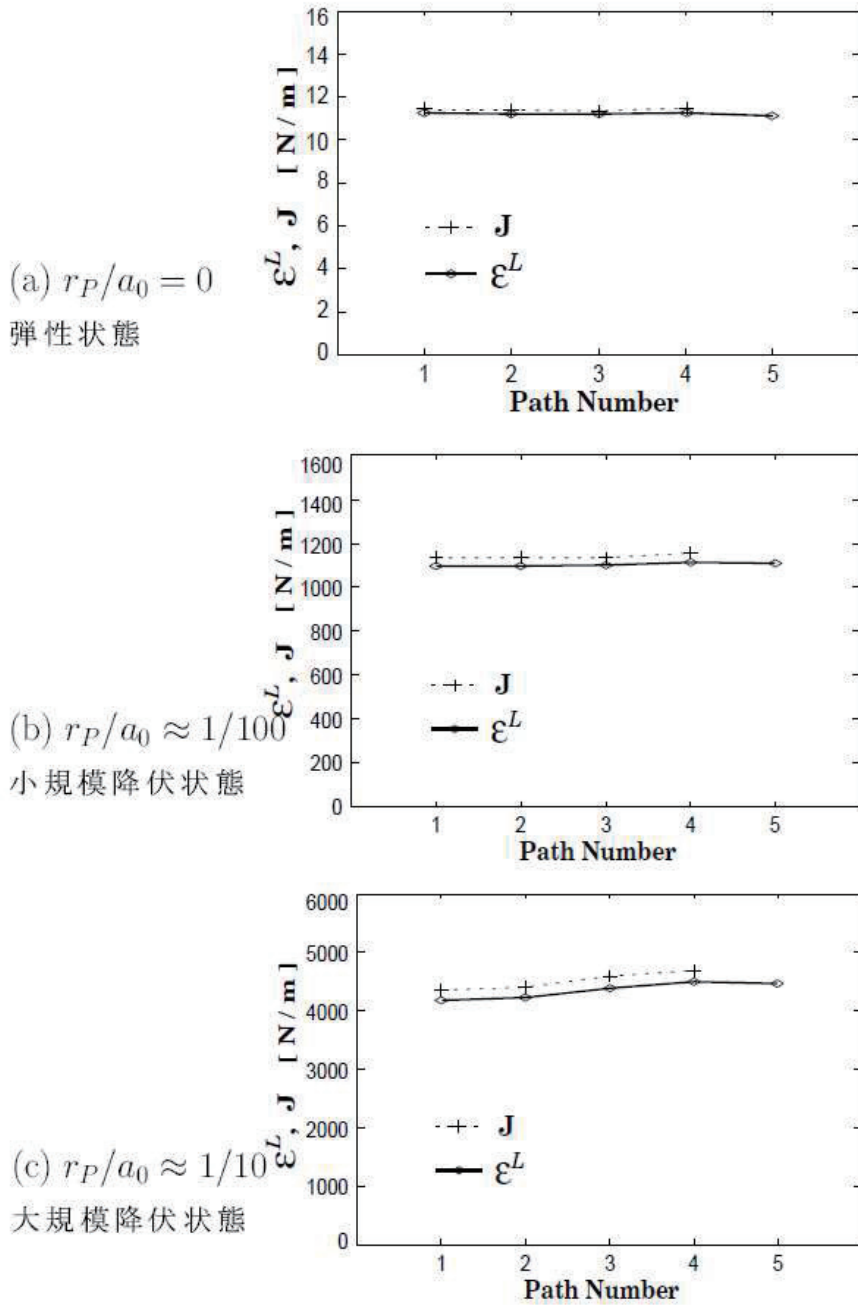


Fig.8 Dependency of CED on integration path (Model of Fig.3)

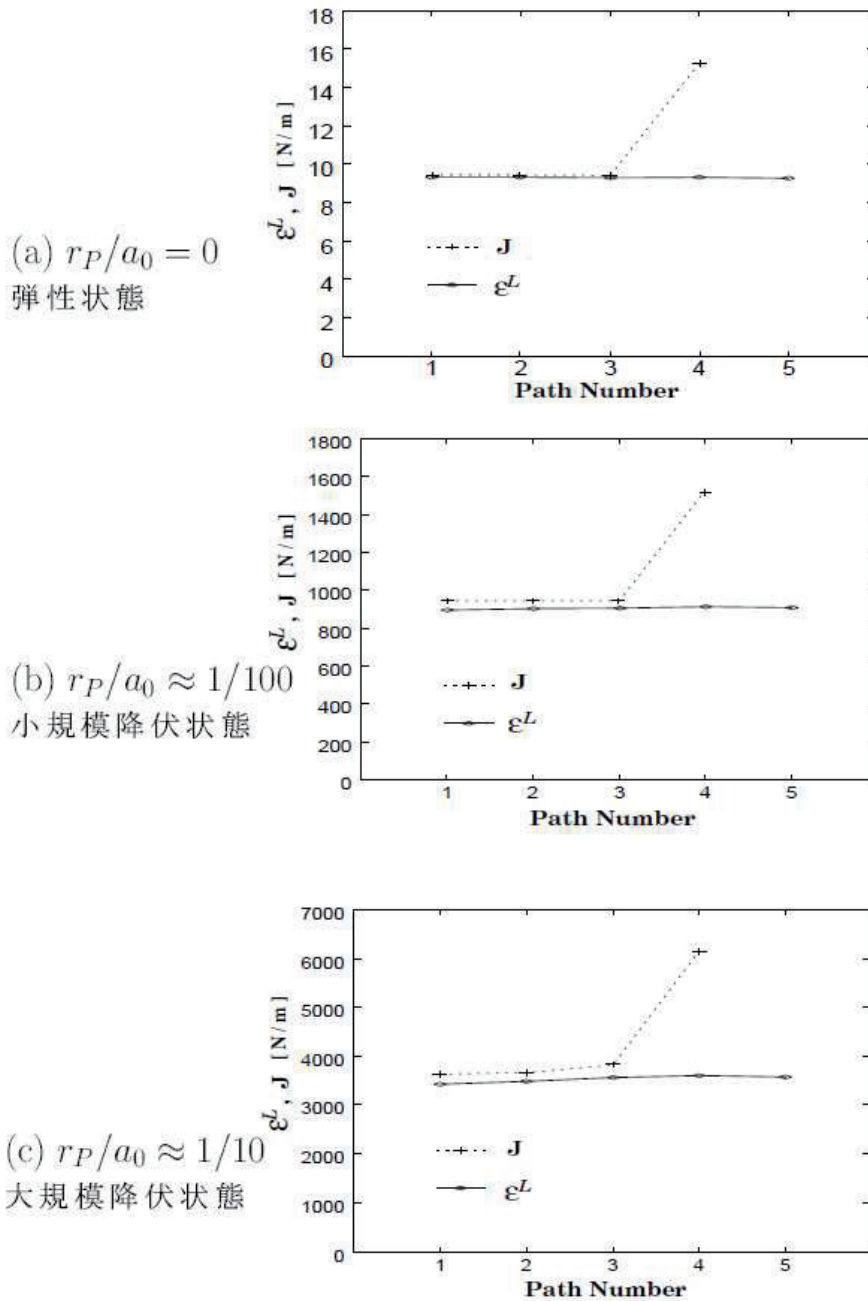


Fig.9 Dependency of CED on integration path (Model of Fig.4)

弾塑性 CED の 径路独立線積分による評価 (第 5 報, 混合モードき裂の場合)

本報告の背景と目的

任意方向のき裂エネルギー密度 CED の定義

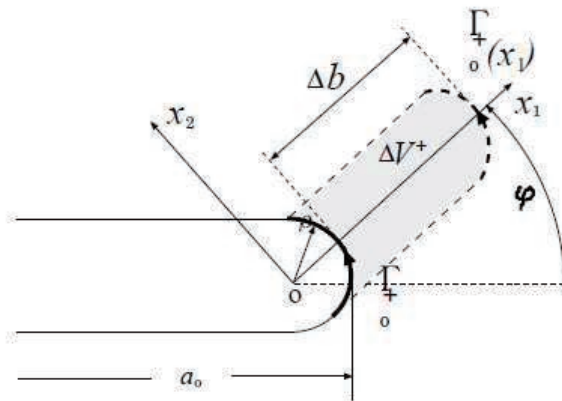


Fig. 1 The definition of CED in an arbitrary direction

切欠き状き裂モデル

$$\begin{aligned}
 \mathcal{E}_\varphi(\rho, t) &= \lim_{\Delta b \rightarrow 0} \frac{1}{\Delta b} \int_{\Delta V^+} W dV \\
 &= \lim_{\Delta b \rightarrow 0} \frac{1}{\Delta b} \int_0^{\Delta b} \left(\int_{\Gamma_0^+(x_1)} W dx_2 \right) dx_1 \\
 &= \int_{\Gamma_0^+} W dx_2
 \end{aligned}$$

シャープなき裂の場合

$$\mathcal{E}_\varphi^{(c)}(t) = \lim_{\rho \rightarrow 0} \mathcal{E}_\varphi(\rho, t)$$

任意方向 CED と応力拡大係数との基本関係

$$\begin{aligned}\mathcal{E}_{\varphi}^{(e)} &= \frac{K_I^2}{8G} \cos^2 \frac{\varphi}{2} (\kappa + \cos \varphi) \\ &\quad + \frac{K_{II}^2}{8G} \cos^2 \frac{\varphi}{2} (\kappa - 3 \cos \varphi + 4) \\ &\quad + \frac{K_I K_{II}}{8G} \sin \varphi (-\kappa - 2 \cos \varphi - 1)\end{aligned}$$

K_I, K_{II} : モード I, モード II 応力拡大係数

G : せん断弾性係数

$$\kappa = \begin{cases} (3 - \nu)/(1 + \nu) & (\text{平面応力の場合}) \\ (4 - 3\nu) & (\text{平面ひずみの場合}) \end{cases}$$

$\varphi = 0^\circ$ なら,

$$\mathcal{E}_{\varphi=0^\circ}^{(e)} = \frac{\kappa + 1}{8G} (K_I^2 + K_{II}^2)$$

任意方向 CED の径路独立線積分 \mathcal{E}_φ^L 評価法

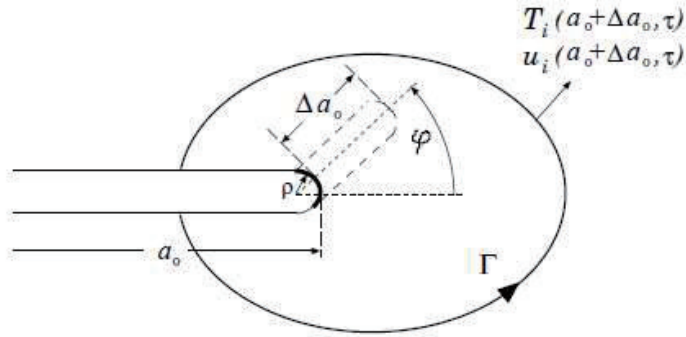


Fig. 2 Notch model

$$\mathcal{E}_\varphi^L(\rho, t) = \int_\Gamma \int_0^t \left(\dot{T}_i \frac{\partial u_i}{\partial a_0} - \dot{u}_i \frac{\partial T_i}{\partial a_0} \right) d\tau d\Gamma$$

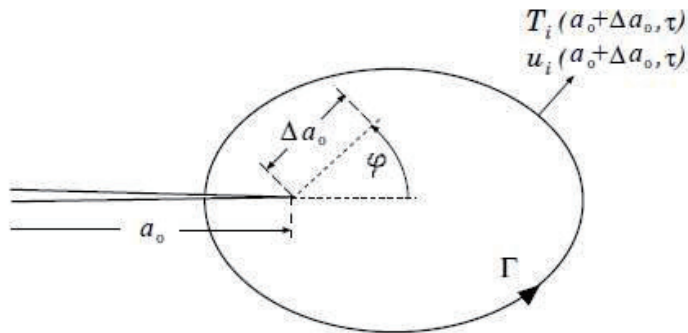


Fig. 3 Crack model

$$\mathcal{E}_\varphi^L(t) = \int_\Gamma \int_0^t \left(\dot{T}_i \frac{\partial u_i}{\partial a_0} - \dot{u}_i \frac{\partial T_i}{\partial a_0} \right)_{\rho=0} d\tau d\Gamma$$

解析モデル

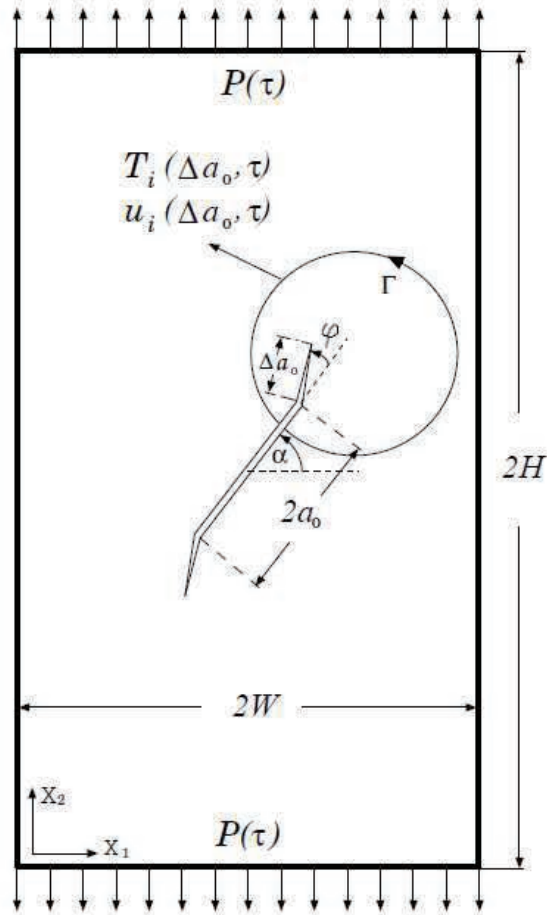


Fig. 4 inclined center-cracked specimens

Table 1 Model Dimensions

W	H	a_0
25mm	50mm	7.5mm

Table 2 Material Constants

ヤング率 E	ポアソン比 ν	降伏応力 σ_Y	硬化率 H'
200.0 GPa	0.3	450.0 MPa	2.0 GPa

Table 3 Lengths of kinked part

Δa_0 (mm)	0.1	0.2125	0.339	0.4814	0.6416	0.8218
$\Delta a_0/a_0$	0.01333	0.02833	0.04521	0.06419	0.08555	0.10958

傾斜角 $\alpha = 30^\circ, 60^\circ$ の場合の要素分割

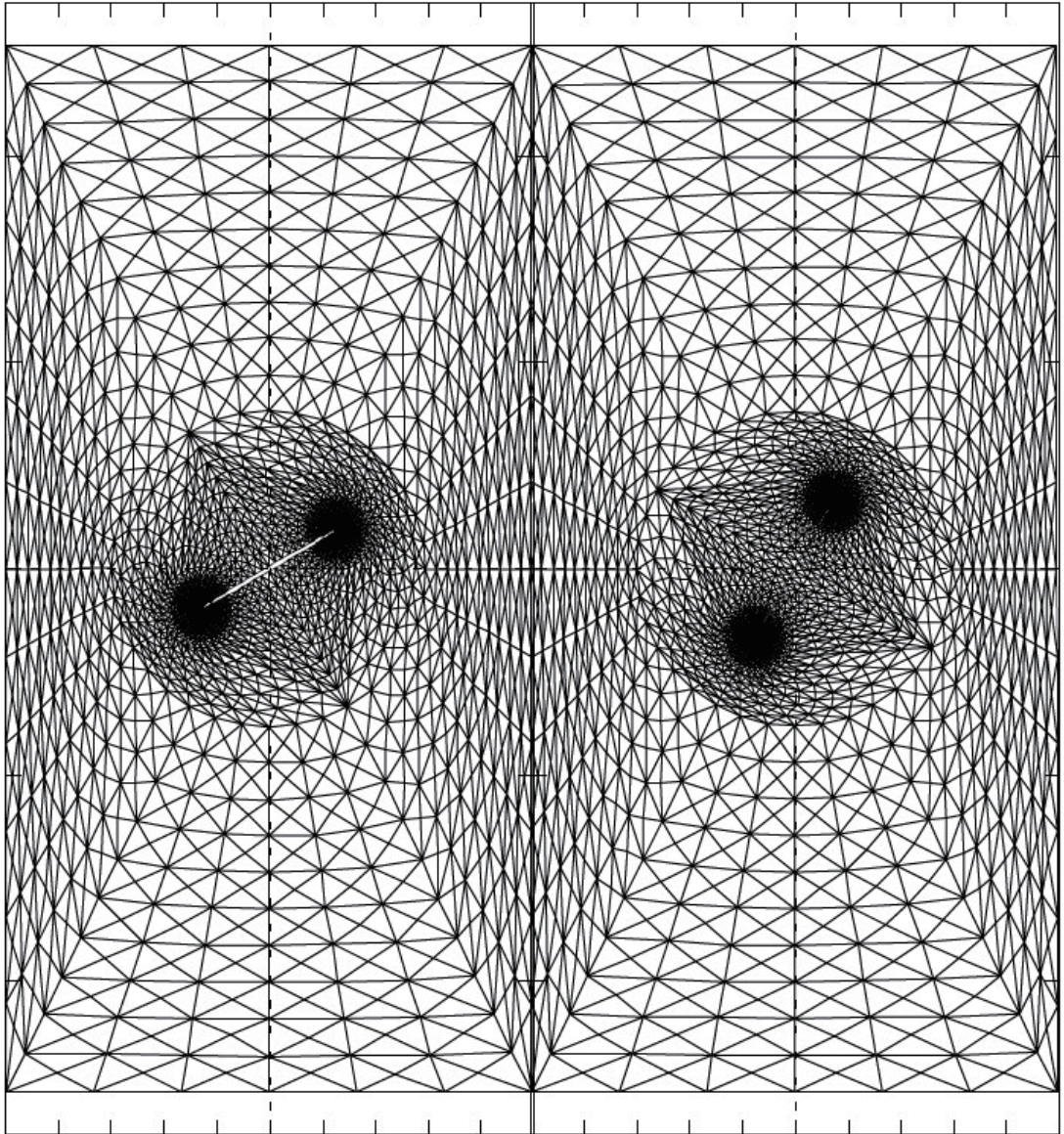


Fig.5 Mesh for $\alpha = 30^\circ$

Fig.6 Mesh for $\alpha = 60^\circ$

き裂先端近傍の要素分割の様子

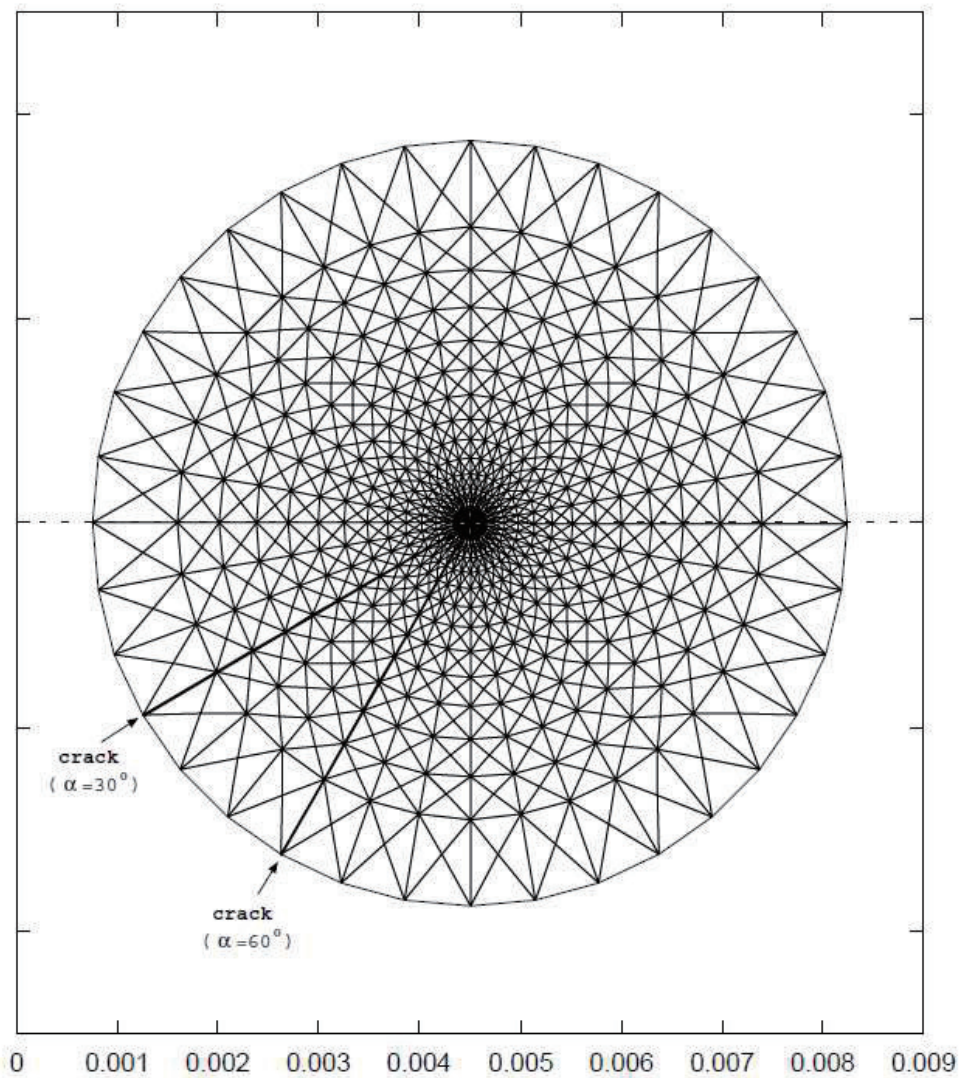


Fig. 7 Mesh near the crack tip

ε_{ϕ}^L の積分経路

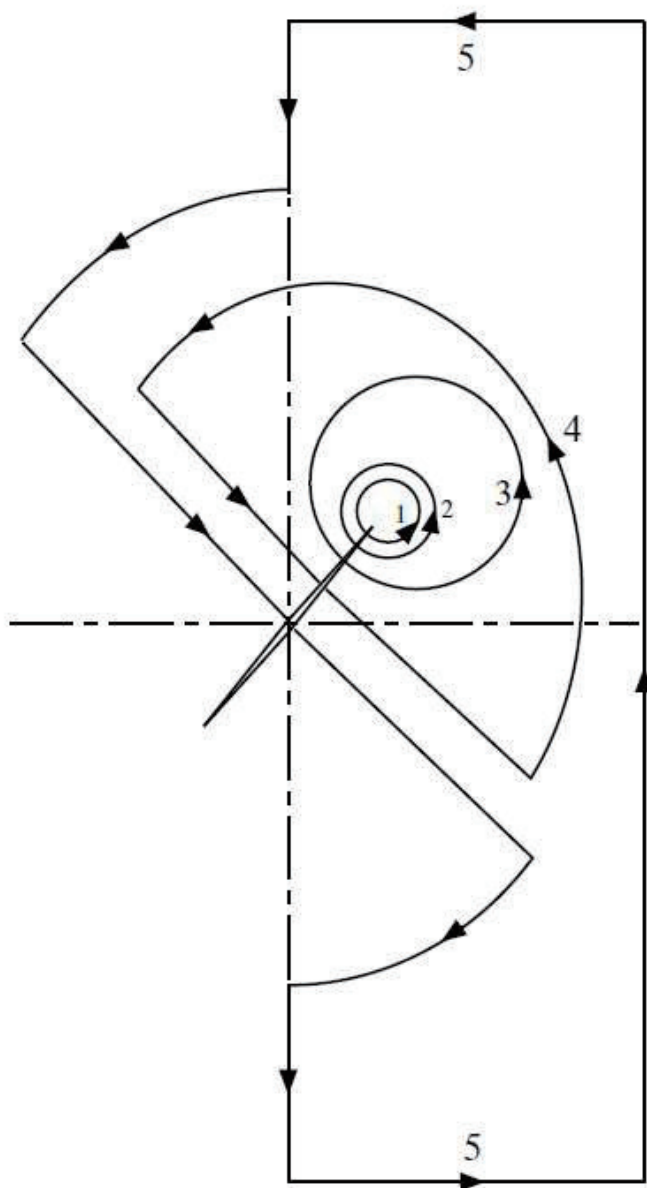
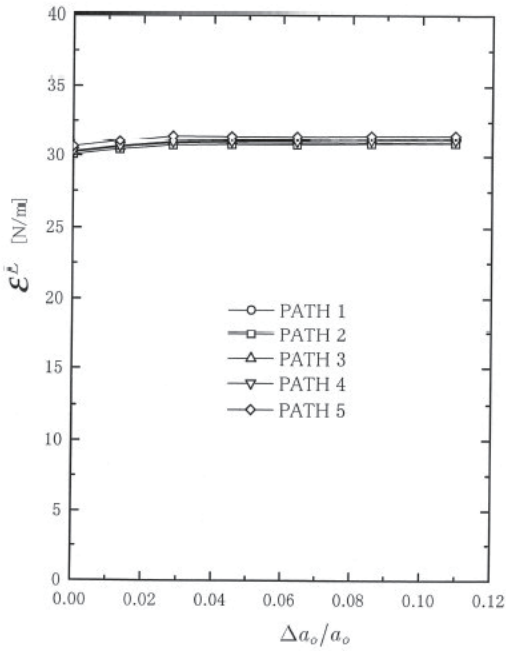


Fig. 8 Integration paths surrounding the crack

評価結果と考察

屈折部の長さおよび径路独立性の検討 (弾性状態の場合)



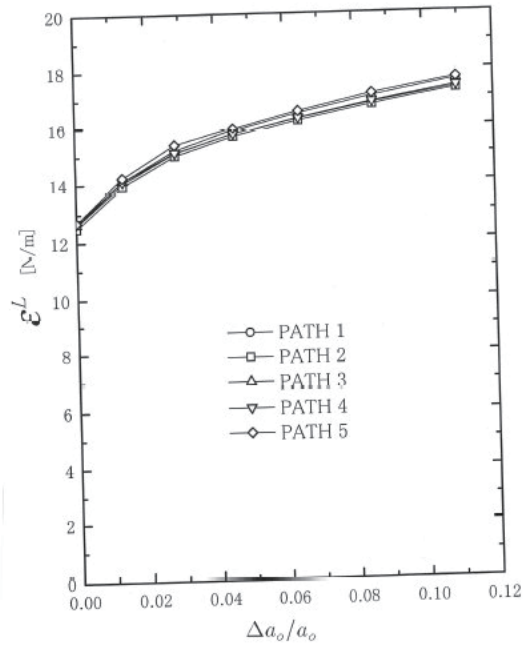
Stage 1, Elastic state

Fig.9(a) Dependency of $\mathcal{E}_{\varphi=-40^\circ}^L$ on Δa_o

($\alpha = 30^\circ$)

$$K_I/K_{II} = 1.8168$$

$$k_o/k_t = 0.55$$



Stage 1, Elastic state

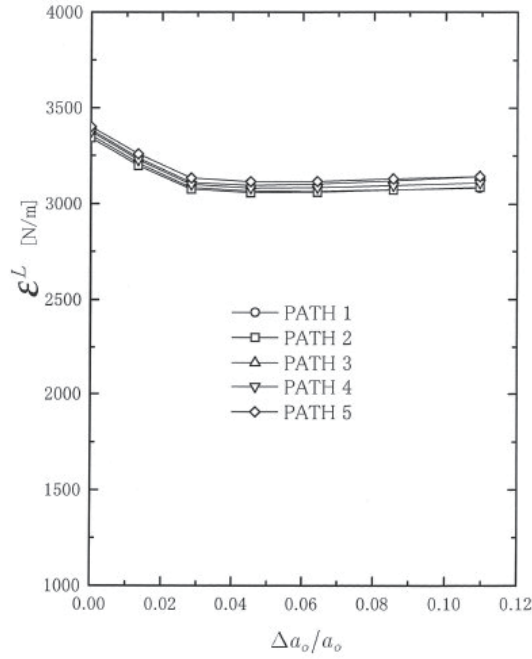
Fig.10(a) Dependency of $\mathcal{E}_{\varphi=-60^\circ}^L$ on Δa_o

($\alpha = 60^\circ$)

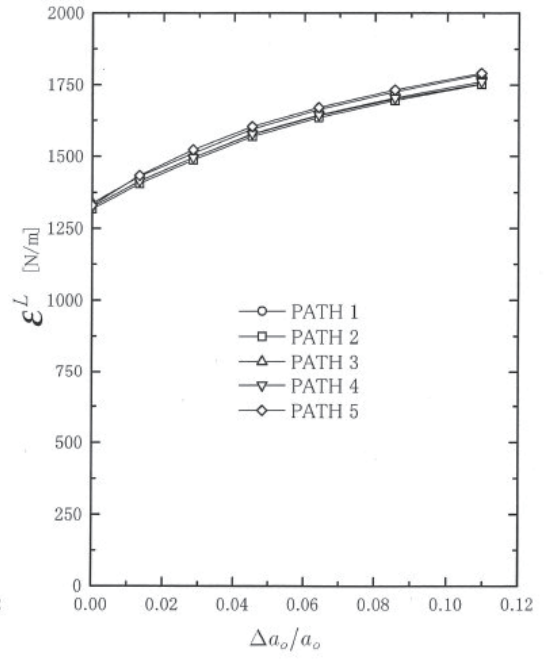
$$K_I/K_{II} = 0.6038$$

$$k_o/k_t = 1.656$$

屈折部の長さおよび径路独立性の検討
 (比較的降伏域が小さい状態の場合)

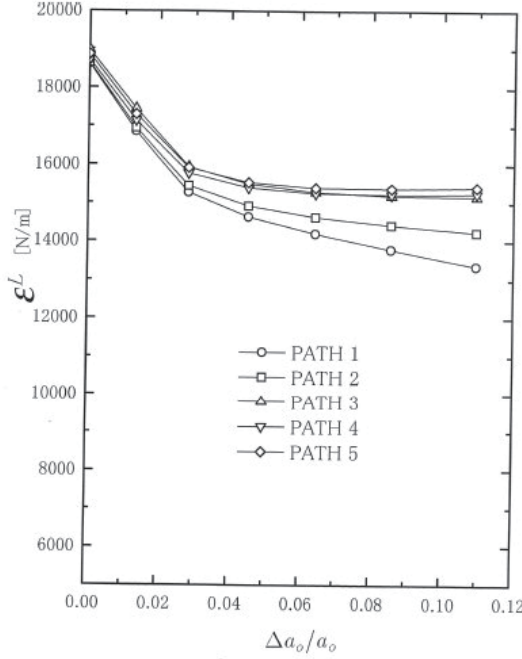


Stage 10, Small scale yielding
 Fig.9(b) Dependency of $\varepsilon_{\varphi=-40^\circ}^L$ on Δa_o
 ($\alpha = 30^\circ$)
 $r_P/a_o \approx 0.035$



Stage 10, Small scale yielding
 Fig.10(b) Dependency of $\varepsilon_{\varphi=-60^\circ}^L$ on Δa_o
 ($\alpha = 60^\circ$)
 $r_P/a_o \approx 0.02$

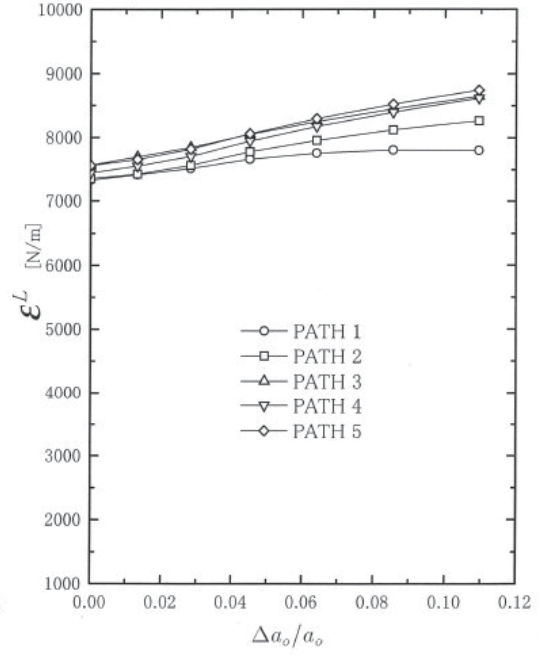
屈折部の長さおよび径路独立性の検討
(大規模降伏状態の場合)



Stage 20, Large scale yielding
Fig.9(c) Dependency of $\varepsilon_{\varphi=-40^\circ}^L$ on Δa_o

$$(\alpha = 30^\circ)$$

$$r_P/a_o \approx 1$$



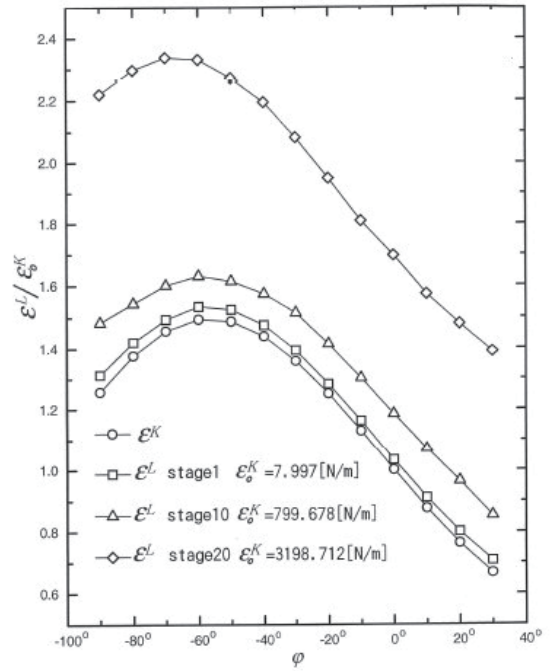
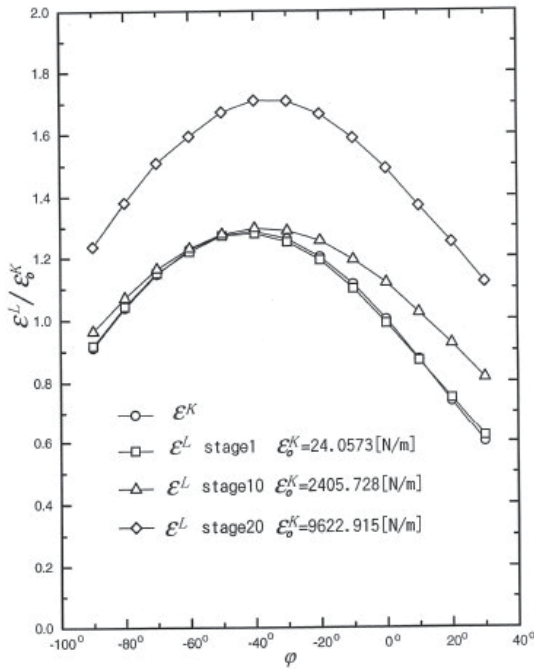
Stage 20, Large scale yielding
Fig.10(c) Dependency of $\varepsilon_{\varphi=-60^\circ}^L$ on Δa_o

$$(\alpha = 60^\circ)$$

$$r_P/a_o \approx 0.65$$

$$\varepsilon^L = \int_{\Gamma} \int_0^t \left(\dot{T}_i \frac{\partial u_i}{\partial a_o} - \dot{u}_i \frac{\partial T_i}{\partial a_o} \right) d\tau d\Gamma$$

傾斜き裂に対する任意方向 CED



$$\varepsilon_o^k = \varepsilon_{\varphi=0^\circ}^{(c)} = \frac{\kappa + 1}{8G} (K_I^2 + K_{II}^2)$$

結論

有限板中の混合モードとなるシャープな傾斜き裂に対し、有限要素解析により任意方向CEDの新たな評価法 \mathcal{E}_φ^L 積分による評価を試み、以下の事項について示した。

- \mathcal{E}_φ^L 積分の補助モデルの屈折部の長さの影響を調べた。弾性状態のとき、傾斜き裂の傾斜角 α が小さい場合($\alpha = 30^\circ$)には補助モデルの屈折分長さによる影響が比較的小さく、 α が大きくなると($\alpha = 60^\circ$)、それが大きくなる傾向があった。塑性変形が始まると、両方の場合ともに屈折分長さによる影響がある。 $\Delta a_0 = 0$ に向けて二次曲線による外挿を行うことが必要であると考えられる。
- \mathcal{E}_φ^L 積分による任意方向CEDの評価値を用いて、線形弾性における任意方向CEDの応力拡大係数との関係を数値的に確認した。本研究の \mathcal{E}_φ^L 評価法は、従来シャープなき裂に直接適用が困難であった任意方向CEDの径路積分に基づく評価方法を一步進め、シャープなき裂に対してき裂先端部の応力-ひずみ場を用いずに評価できる方法が可能となることを示すものである。

Thank You Very Much!

DEPARTMENT OF AERONAUTICS AND ASTRONAUTICS
FUDAN UNIVERSITY



Structure of the least square solutions and its application to non-destructive inspections

Takashi TAKIGUCHI*

Abstract

In this article, we study the structure of the least square solutions to over determined systems, by which we establish how to approximately solve overdetermined systems established by practical requirement. We also mention that our main theorem, the structure of the least square solutions, plays an important role for non-destructive inspection for reinforced concrete structures.

Keywords: least square solution, non-destructive inspection, inverse problems

2010 Mathematics Subject Classification ; Primary 65F20, Secondary 35R30

*Department of Mathematics, National Defense Academy of Japan, 1-10-20, Hashirimizu, Yokosuka, Kanagawa, 239-8686, JAPAN. email: takashi@nda.ac.jp

1 Introduction

In this article, we study the structure of the least square solutions to the following overdetermined system

$$\begin{cases} F_1(x_1, x_2, \dots, x_n) = 0 \\ \dots \\ F_m(x_1, x_2, \dots, x_n) = 0 \end{cases} \quad (1)$$

where F_j 's are general functions and $m \gg n$.

We apply its structure and study how to solve the following overdetermined system

$$\begin{cases} (x - x_1)^2 + (y - y_1)^2 + (z - z_1)^2 = r_1^2 \\ \dots \\ (x - x_n)^2 + (y - y_n)^2 + (z - z_n)^2 = r_n^2 \end{cases} \quad (2)$$

for $n \gg 3$, which plays an important role for a non-destructive inspection to probe the precise position of the rebar in the reinforced concrete structures.

We also mention other applications of the structure of the least square solutions to the system (1), to some non-destructive inspections.

This article consists of the following sections.

- §1. Introduction
- §2. Main theorem
- §3. Applications
- §4. Conclusion

In this section, as the introduction of this article, we introduce the outline of our article as well as the main problem in this article, how to give the least square solutions to the overdetermined system (1).

In the next section, we study the main problem and give the main theorem in this article. Roughly summing up, our theorem reads that if we can derive an overdetermined system of linear equations from the system (1) by equivalent deformations. then we can easily obtain the least square solution to the original system (1). We also mention the merits of our main theorem from both viewpoints of theory and practice.

In the third section, we study application of our main theorem in practice. We study how to detect the endpoints of the rebar in reinforced concrete ('RC' for short) structures. For the time being, there being no non-destructive inspection technique to exactly probe the rebar for reinforcement, the results in this section are very important for the maintenance of RC structures. Detection of the exact position of the rebar is closed related to the development of ultrasonic tomography for RC structures, as a part of which, we shall also introduce how to inspect the cover concrete for reinforcement by application of the principle of ultrasonic tomography. The author claims that the results in this section are also very important for the maintenance of RC structures.

In the final section, we shall summarize our conclusions in this article.

2 Main theorem

In this section, we study the structure of the least square solutions to the system (1), which is formulated as;

Problem 2.1. *Give the least square solutions to the system (1).*

For the system (1) the following proposition clearly holds.

Proposition 2.1. *If $\mathbf{x} \in \mathbb{R}^n$ is a solution to (1) then it is also a solution to a system derived from the system (1) by equivalent deformations.*

Conversely, by Proposition , we obtain the following proposition.

Proposition 2.2. *If the solution to a system derived from the system (1) by equivalent deformations is unique then it must be the unique solution to (1). In this case, it is also proved that the system (1) has the unique solution.*

It is not unusual in practice that the system (1) itself is an overdetermined system of linear equations. or an overdetermined system of linear equations is derived from the system (1) by equivalent deformations. An example of the former one is G. N. Hounsfields overdetermined system of linear equations, for which confer [4]. As an example of the latter, we take (2), where if we subtract j-th equation from i-th equation then we obtain an overdetermined system of $\frac{m(m-1)}{2}$ linear equations. In this article, we focus on the case where the system (1) itself is an overdetermined system of linear equations. or an overdetermined system of linear equations is derived from the system (1) by equivalent deformations.

Assume that a system of $k \geq m$ linear equations

$$\begin{cases} a_{11}x_1 + a_{12}x_2 + \cdots + a_{1n}x_n = s_1, \\ a_{21}x_1 + a_{22}x_2 + \cdots + a_{2n}x_n = s_2, \\ \dots\dots\dots \\ a_{k1}x_1 + a_{k2}x_2 + \cdots + a_{kn}x_n = s_k \end{cases} \quad (3)$$

or equivalently

$$A\mathbf{x} = \mathbf{s} \quad (4)$$

is obtained derived from the system (1) by equivalent deformations.

In practice, the system (1), itself, would not be obtained. By errors and noises, what we can obtain is the system (1) with a small error in each equation, consequently, we obtain a following overdetermined system (5) of linear equations;

$$\begin{cases} a_{11}x_1 + a_{12}x_2 + \cdots + a_{1n}x_n = \tilde{s}_1, \\ a_{21}x_1 + a_{22}x_2 + \cdots + a_{2n}x_n = \tilde{s}_2, \\ \dots\dots\dots \\ a_{k1}x_1 + a_{k2}x_2 + \cdots + a_{kn}x_n = \tilde{s}_k \end{cases} \quad (5)$$

or equivalently

$$A\mathbf{x} = \tilde{\mathbf{s}}, \quad (6)$$

where $\tilde{s}_i = s_i + \varepsilon_i$ with small ε_i for $1 \leq i \leq k$.

It is often the case that the derived overdetermined system (3) must theoretically have the unique solution if no errors and noises are included, henceforth so must the original system (1) by Proposition 2, but because of the errors and noises the system (1) with errors and noises becomes to allow no solution, consequently, neither does the derived linear system (5).

In this article, we assume the following;

Assumption 2.1. In the system (1), we assume the following; it is possible derive an overdetermined linear system (3) which allows the unique solution.

By Assumption 2.1 we have

Proposition 2.3.

$$\text{rank}A = n, \tag{7}$$

where the matrix A is defined in (4) and (6).

and

Proposition 2.4. *The solution to the overdetermined system (1) is unique.*

In order to construct an approximate solution, we study the overdetermined system (5).

If the system (3) allows a solution \mathbf{x} if and only if

$$A\mathbf{x} - \mathbf{s} = \mathbf{0}. \tag{8}$$

In view of (8), we define

Definition 2.1. A vector $\mathbf{x} \in \mathbb{R}^n$ is called as a least square solution to (3) (or (4)) if and only if it minimizes the norm

$$\|A\mathbf{x} - \mathbf{s}\| \tag{9}$$

Let us review the basic theory for the least square solutions to a system of linear equations. Let us study the following system of linear equations.

Problem 2.2. *Solve the following system of linear equations in y_1, y_2, \dots, y_n .*

$$\begin{cases} b_{11}y_1 + b_{12}y_2 + \dots + b_{1n}y_n & = s_1, \\ b_{21}y_1 + b_{22}y_2 + \dots + b_{2n}y_n & = s_2, \\ \dots\dots\dots & \\ b_{m1}y_1 + b_{m2}y_2 + \dots + b_{mn}y_n & = s_m, \end{cases} \tag{10}$$

or equivalently

$$B\mathbf{y} = \mathbf{s}, \tag{11}$$

where B is the matrix in (10), $\mathbf{y} = {}^t(y_1, y_2, \dots, y_n)$ and $\mathbf{s} = {}^t(s_1, s_2, \dots, s_m)$.

For the least square solutions to the system (10), the following propositions are known to hold.

Proposition 2.5. *Let $M_{mn}(\mathbb{R})$ be the set of $m \times n$ matrices whose components are real numbers. For $B \in M_{mn}(\mathbb{R})$, the following conditions are equivalent.*

(i) $\mathbf{y} \in \mathbb{R}^n$ is a least square solution to (10).

(ii) For any $\mathbf{z} \in \mathbb{R}^n$, there holds

$$\langle B\mathbf{z}, B\mathbf{y} - \mathbf{s} \rangle_{\mathbb{R}^m} = 0 \quad (12)$$

where $\langle \cdot, \cdot \rangle_{\mathbb{R}^m}$ represents the inner product in \mathbb{R}^m .

(iii) There holds the following equation.

$${}^tBB\mathbf{y} - {}^tB\mathbf{s} = \mathbf{0}. \quad (13)$$

Confer [2], for the proof of this proposition. The following proposition is clear from the condition (iii) in Proposition 2.5.

Proposition 2.6. *If $\text{rank}(B) = n$, for $B \in M_{mn}(\mathbb{R})$, then the least square solution to the system (3) is uniquely given by the unique solution to the following system;*

$${}^tBB\mathbf{y} = {}^tB\mathbf{s}. \quad (14)$$

In fact, we can prove that $\text{rank}(B) = \text{rank}({}^tBB)$, though we omit its proof. The condition $\text{rank}(B) = n$ is equivalent to the one that matrix tBB is regular, in other words, tBB has its inverse.

The least square solutions to the system (10) has strong relation with the practicalization of CT, for which, confer [4].

Let us go back to study the system (5). By Assumption 2.1 and Proposition 2.6, we have

Theorem 2.1. *The least square solution to (10) is unique.*

By Assumption 2.1 and Proposition 2.2, the systems (1) and (5) has the same unique solution, and the least square solution to (10) is an approximate solution to the original system (1). Therefore, we have proved that

Theorem 2.2. *In order to construct an approximate solution to an overdetermined system (1) with errors and noises, if Assumption 2.1 is satisfied, then the least square solution to the system (10) gives what is required.*

Remark 2.1. Assume that the unique solution to the system (1) is \mathbf{x} and there exists $\mathbf{x}' \neq \mathbf{x}$ satisfying $F(\mathbf{x}') \approx 0$ for all $j = 1, 2, \dots, m$. In this case, if we directly give a least square solution to the original system (1) with errors and noises, it may approximate \mathbf{x}' , not \mathbf{x} which is required. In the case where Assumption 2.1 is satisfied, it is much better to give the least square solution to the system (10) than to give a least square solution to the original system (1). In the treatment of the system (10) of linear equations, such kind of confusion would never happen.

3 Applications

In this section, we first discuss how to detect the exact position of the rebar in RC structures. We note that there many researches to detect the rebar in RC structures, for example, [1, 5], there exists no non-destructive technique to exactly probe the rebar.

Assume that a cuboid RC structure contains, in its interior, a rebar which locates parallelly or perpendicularly to each edge surface. Confer Figure 1 for its image.

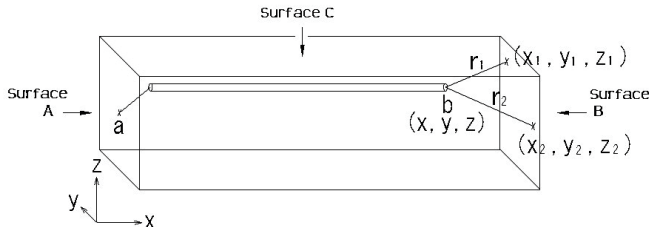


Figure 1: A cuboid test piece

In Figure 1, we set the axes as shown. We first reconstruct the endpoints of the rebar. For the reconstruction of the endpoint b in Figure 1, we take many observation points on the edge surface B and its around and measure the thickness of concrete cover, equivalently the distance between the observation and the endpoints. We let the endpoint $b = (x, y, z)$ and take n observation points $(x_1, y_1, z_1), \dots, (x_n, y_n, z_n)$, whose distances from the endpoint b are measured as r_1, \dots, r_n , respectively. We shall explain how to take the observation points in the real structure in the next section.

By measurement, we obtain an overdetermined system (2) of quadratic equations, however, it is well known that it is impossible to measure the thickness of concrete cover by the existing devices. Henceforth all measurements necessarily contain errors and noises. Therefore, we have make an approximate solution of the system (2) with errors and noises, where we can apply our main theorem, Theorem 2.2 since by subtracting i -th equation in system (2) by the j -th one and dividing the both hand sides of the difference by 2, we obtain the overdetermined system of $\frac{n(n-1)}{2}$ linear equations;

$$(x_i - x_j)x + (y_i - y_j)y + (z_i - z_j)z = \frac{1}{2}(x_i^2 + y_i^2 + z_i^2 - x_j^2 - y_j^2 - z_j^2 + r_j^2 - r_i^2). \quad (15)$$

For more detail of this analysis, as well as its practical background, confer the papers by Prof. Ochi and Mr. Takabatake in these proceedings.

Let us turn to how to inspect concrete cover for reinforcement by ultrasound measurement. By the detection of the endpoints of the rebar and scanning on the surface of the structure by the device to measure the thickness of concrete cover by electromagnetic induction, yields the exact position of the rebar, in other words, by application of our main theorem we can correct the exactness of the measurement. If the exact position of the rebar in the interior of an RC structure is given, then non-destructive inspection of the concrete cover by application of an ultrasonic tomography is possible, for which confer [3].

4 Conclusion

As the closing of this article, we summarize the conclusion.

Conclusion 4.1 (Conclusion).

- (i) *We have studied the structure of the least square solution to overdetermined systems (Theorem 2.2).*
- (ii) *We have developed a non-destructive inspection technique to exactly probe the rebar by application of an apparatus to measure thickness of concrete cover for reinforcing steel by electromagnetic induction method, application of which makes it possible to non-destructively inspect the concrete cover for reinforcement by application of an ultrasonic tomography (Section 3).*

References

- [1] He, X. Q., Shu, Z. Q., Lid, Q. Y. and ALU, G. Y. : *Review of CPR Rebar Detection*, PIERS Proceedings, Beijing, China, March 23-27, 2009 (2009) BP. 804-813.
- [2] Nakamura, I. : *Linear Algebra*, Sugaku Shobou, Tokyo, 2007 (in Japanese).
- [3] Mita, N. and Takiguchi, T. : *Principle of ultrasonic tomography for concrete structures and non-destructive inspection of concrete cover for reinforcement*, Pacific Journal of Mathematics for Industry (2018) 10:6.
- [4] Takiguchi, T. : *How the computerized tomography was practicalized*, Bulletin of JS-SAC, **21** (2015) pp. 50–57.
- [5] Tanaka, S. and Wakabayashi, M. : *On Measurement of the Depth and the Diameter of Steel Bars in Reinforced Concrete Using Electromagnetic Wave (Radar)*, 2006 SICE-ICASE International Joint Conference (2006) pp.2555–2559.

Takashi TAKIGUCHI
Department of Mathematics,
National Defense Academy of Japan,
1-10-20, Hashirimizu, Yokosuka,
Kanagawa, 239-8686, JAPAN
e-mail: takashi@nda.ac.jp

Structure of the least square solutions and its application to non-destructive inspections

Takashi TAKIGUCHI

National Defense Academy of Japan

Non-destructive inspection for concrete structures and related topics
Oct. 24th, 2018 at IMI, Kyushu University

- 1 Introduction
- 2 Study of Problem 1.1
- 3 Application
- 4 ND inspection of concrete cover
- 5 Conclusion

1. Introduction

Motivation of this study

$$\begin{cases} (x - x_1)^2 + (y - y_1)^2 + (z - z_1)^2 = r_1^2 \\ \dots \\ (x - x_n)^2 + (y - y_n)^2 + (z - z_n)^2 = r_n^2 \end{cases} \quad (1)$$

It being not easy to give the unique least square solution to the system (1), we gave the unique least square solution to the following equivalent system (2) of (1), which consists of $\frac{n(n-1)}{2}$ linear equations;

$$\begin{aligned} & (x_i - x_j)x + (y_i - y_j)y + (z_i - z_j)z \\ & = \frac{1}{2}(x_i^2 + y_i^2 + z_i^2 - x_j^2 - y_j^2 - z_j^2 + r_j^2 - r_i^2) \end{aligned} \quad (2)$$

Problem 1.1

- (i) Relation between the least square solutions to the systems (1) and (2).
- (ii) Can the the least square solutions to the system (2) be alternatives of that to the system (1)?

2. Study of Problem 1.1

Assume that

$$\begin{cases} F_1(x_1, x_2, \dots, x_n) = 0 \\ \dots \\ F_m(x_1, x_2, \dots, x_n) = 0 \end{cases} \quad (3)$$

has a solution, where $m \gg n$, F_j 's, $j = 1, 2, \dots, m$, are continuous.

Let us study the system of $\frac{m(m-1)}{2}$ equations;

$$C_i F_i(x_1, x_2, \dots, x_n) + C_j F_j(x_1, x_2, \dots, x_n) = 0 \quad (4)$$

Proposition 2.1

If \mathbf{x} is a solution to (3) then it is also a solution to (4).

Proposition 2.2

If the solution to (4) is unique then it must be the unique solution to (3). In this case, it is also proved that the system (3) has the unique solution.

Let us turn to LSSs to the system

$$\begin{cases} F_1(x_1, x_2, \dots, x_n) = \varepsilon_1 \\ \dots \\ F_m(x_1, x_2, \dots, x_n) = \varepsilon_m \end{cases} \quad (5)$$

It is trivial that any LSS of (5) is very close to the real solution \mathbf{x}^0 of (3).

Let us turn to the system of $\frac{m(m-1)}{2}$ equations;

$$C_i F_i(x_1, x_2, \dots, x_n) + C_j F_j(x_1, x_2, \dots, x_n) = C_i \varepsilon_i + C_j \varepsilon_j \quad (6)$$

Proposition 2.3

If \mathbf{x} is the unique LSS to (6) then it must be very close to a solution to (4).

By virtue of Propositions 2.1, 2.2 and 2.3,

Theorem 2.4

If the LSS to the system (6) is unique then it must be an approximate solution to the system (3).

Applying Theorem 2.6, we propose a procedure to construct a suitable approximate to the solution to the system (3) out of the observation with noises and errors, namely, out of the system (5).

Problem 2.5

Solve the following overdetermined system of linear equations in x_1, x_2, \dots, x_n .

$$\begin{cases} a_{11}x_1 + a_{12}x_2 + \cdots + a_{1n}x_n = s_1, \\ a_{21}x_1 + a_{22}x_2 + \cdots + a_{2n}x_n = s_2, \\ \dots\dots\dots \\ a_{m1}x_1 + a_{m2}x_2 + \cdots + a_{mn}x_n = s_m \end{cases} \quad (7)$$

$$Ax = s \quad (8)$$

where $m \gg n$.

The equation (7) allows the unique solution \mathbf{x} if and only if

$$A\mathbf{x} - \mathbf{s} = \mathbf{0}$$

Definition 2.1 (Least square solutions)

A vector $\mathbf{x} \in \mathbb{R}^n$ is called as a **least square solution** to (7) (or (8)) if and only if it minimizes the norm

$$\|A\mathbf{x} - \mathbf{s}\|$$

Theorem 2.6

For $A \in M_{mn}(\mathbb{R})$,

- (i) *there exists at least one LSS to (7) for any $\mathbf{s} \in \mathbb{R}^m$.*
- (ii) *Furthermore, if $m \geq n$ and $\text{rank}(A) = n$ then the solution to (7) is unique.*

Lemma 2.7

For $A \in M_{mn}(\mathbb{R})$, the following conditions are equivalent.

- (i) $\mathbf{x} \in \mathbb{R}^n$ is a LSS to (7).
- (ii) $(A\mathbf{z}, A\mathbf{x} - \mathbf{s}) = 0$ for any $\mathbf{z} \in \mathbb{R}^n$.
- (iii) There holds the following equation.

$${}^tAA\mathbf{x} - {}^tA\mathbf{s} = \mathbf{0}. \quad (9)$$

[Back](#)

Corollary 2.8

If tAA is regular then the LSS to (7) is unique.

Lemma 2.9

For any $A \in M_{mn}(\mathbb{R})$,

$$\mathbf{rank}({}^tAA) = \mathbf{rank}(A).$$

Corollary 2.10

Let $A \in M_{mn}$, $m \geq n$. If $\mathbf{rank}(A) = n$ then tAA is regular.

Lemma 2.11

For any $A \in M_{mn}(\mathbb{R})$ and $\mathbf{s} \in \mathbb{R}^m$, there always exists a solution to (9). Furthermore, if $m \geq n$ and $\mathbf{rank}(A) = n$ then the solution to (9) is unique.

Idea of the proof

$$U_1 := \{ {}^t A \mathbf{s} \mid \mathbf{s} \in \mathbb{R}^m \}, \quad U_2 := \{ {}^t A A \mathbf{x} \mid \mathbf{x} \in \mathbb{R}^n \} \quad (10)$$

$$U_1 \supset U_2$$

$$\text{rank}({}^t A A) = \text{rank}(A) \Rightarrow \dim U_1 = \dim U_2$$

Example

$$\left\{ \begin{array}{l} x + y = 3 \\ x + y = 1 \\ x = 2 \\ x = 0 \\ y = 2 \\ y = 0 \end{array} \right. \quad (11)$$

$${}^tAA\mathbf{x} = \begin{pmatrix} 2 & 1 \\ 1 & 2 \end{pmatrix} \begin{pmatrix} x \\ y \end{pmatrix} = \begin{pmatrix} 3 \\ 3 \end{pmatrix} = {}^tA\mathbf{s}$$

$$x = y = 1$$

Theorem 2.12

If the system (3) can be transformed into the system of linear equations (7) or (8) whose coefficient matrix A is regular by equivalent deformation, then the unique LSS to the system (7) or (8) turns out to be an approximate solution to the system (3).

3. Application of LSS

(I) Tomography

(II) Probe of the reinforcing steel in RC structures

(I) Tomography

Sir Godfrey Newbold Hounsfield

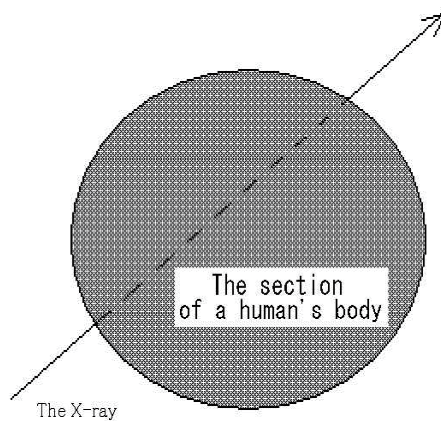
(28 August 1919 – 12 August 2004)

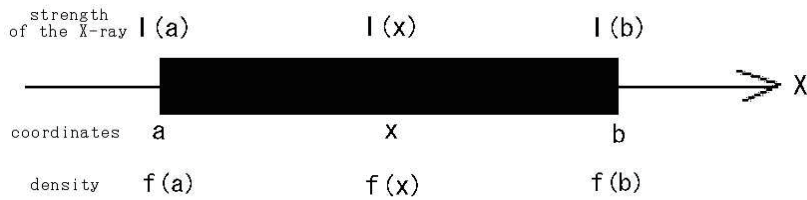
- an English electrical engineer
- developed the diagnostic technique of X-ray computerized tomography (CT)
- received the Nobel Prize in Physiology or Medicine in 1979 (with Allan McLeod Cormack)

Other awards, titles and so on

- elected to the Royal Society in 1975
- appointed Commander of the British Empire in 1976
- awarded the Howard N. Potts Medal in 1977
- knighted in 1981
- **Hounsfield scale** : a quantitative measure of radiodensity used in evaluating X-ray CT scans, whose unit is defined as Hounsfield unit (HU)

Mathematical model of CT





$$I(x + dx) - I(x) = -f(x)I(x)dx$$

$$I'(x) = -f(x)I(x)$$

$$\log I(a) - \log I(b) = \int_a^b f(x)dx$$

Mathematical problem of CT

Reconstruct the function $f(x, y)$ from the data

$$\left\{ \int_l f(x, y) dl \mid l \text{ is a line in } \mathbb{R}^2 \right\}.$$

The Radon transform

Let $\xi = \{x \in \mathbb{R}^n \mid x \cdot \theta = s\}$ be a hyperplane in \mathbb{R}^n , where $\theta \in S^{n-1}$, $s \geq 0$.

$$Rf(\xi) = Rf(\theta, s) = \int_{x \cdot \theta = s} f(x) dx.$$

An inversion formula for the Radon transform

For $f(x)$ defined on \mathbb{R}^n and $\forall \alpha < n$,

$$I^\alpha f(x) := F^{-1}(|\xi|^{-\alpha} Ff(\xi))(x),$$

$$Ff(\xi) := \int_{\mathbb{R}^n} e^{-ix \cdot \xi} f(x) dx, \quad F^{-1}\varphi(x) := \frac{1}{(2\pi)^n} \int_{\mathbb{R}^n} e^{ix \cdot \xi} \varphi(\xi) d\xi.$$

$$I^\alpha \psi(\theta, s) := F^{-1}(|\rho|^{-\alpha} \psi(\theta, \rho))(x),$$

$$F\psi(\theta, \rho) := \int_{\mathbb{R}} e^{-is\rho} \psi(\theta, s) ds, \quad F^{-1}\psi(\theta, s) := \frac{1}{2\pi} \int_{\mathbb{R}} e^{is\rho} \psi(\theta, \rho) d\rho.$$

An inversion formula for the Radon transform

$$f(x) = \frac{1}{2} (2\pi)^{1-n} I^{-\alpha} R^* I^{\alpha-n+1} R f(x), \quad (12)$$

$$R^* \psi(x) := \int_{S^{n-1}} \psi(\theta, x \cdot \theta) d\theta.$$

Johann Karl August Radon

(16 December 1887 – 25 May 1956)

- an Austrian mathematician whose doctoral dissertation was on the calculus of variations
(in 1910, at the University of Vienna)
- Über die Bestimmung von Funktionen durch ihre Integralwerte längs gewisser Mannigfaltigkeiten, Ber. Verh. Sächs. Akad. Wiss. Leipzig, Math-Nat. **69** (1917), pp. 262-277.

J. Radon's inversion formulas

For $n = 3$. Let $\alpha = 2$ in (12) then

J. Radon's inversion formula for $n = 3$

$$f(x) = -\frac{1}{8\pi^2} \Delta \int_{S^2} Rf(\theta, x \cdot \theta) d\theta \quad (13)$$

For $n = 2$. Let $\alpha = 1$ in (12) then the symmetry $Rf(-\theta, -s) = Rf(\theta, s)$ of the Radon transform yields that

J. Radon's inversion formula for $n = 2$

$$f(x) = -\frac{1}{\pi} \int_0^\infty \frac{F'_x(q)}{q} dq \quad (14)$$

$$F_x(q) := \frac{1}{2\pi} \int_{S^1} Rf(\theta, x \cdot \theta + q) d\theta$$

A present-day algorithmic idea for CT

Let $n = 2$, $\alpha = 1$ in (12)

$$f(x) = \frac{1}{4\pi} I^{-1} \left(\int_{S^1} Rf(\theta, x \cdot \theta) d\theta \right). \quad (15)$$

Hounsfield's idea

Divide the picture into n pixels.

$$f(x, y) \approx g(x, y) = \sum_{j=1}^n x_j \chi_{c_j}(x, y), \quad (16)$$

where $f(x, y)$ is the density at (x, y) .

$c_j, j = 1, 2, \dots, n$: the pixels

$I_i, i = 1, 2, \dots, m$: the projected X-rays

l_i : the line I_i passes through

$a_{ij} := |l_i \cap c_j|$: the length of $l_i \cap c_j$

I_i^0, I_i^1 : strength of the X-ray I_i before and after passing through the human body, respectively

$s_i := \log I_i^0 - \log I_i^1$

x_j : the density of the human body on the pixel c_j

Problem 3.1

Solve the following system of linear equations in x_1, x_2, \dots, x_n .

$$\begin{cases} a_{11}x_1 + a_{12}x_2 + \cdots + a_{1n}x_n = s_1, \\ a_{21}x_1 + a_{22}x_2 + \cdots + a_{2n}x_n = s_2, \\ \dots\dots\dots \\ a_{m1}x_1 + a_{m2}x_2 + \cdots + a_{mn}x_n = s_m \end{cases} \quad (17)$$

$$Ax = s \quad (18)$$

On the data of the X-rays in (17)

- In G.N. Hounsfield's CT, $m \approx \text{const} \times 10^6$, $n \approx 3 \times 10^5$
- In the present-day CT, $m \approx 5 \times 10^9$, $n \approx 3 \times 10^7$ and
- The pixel size in the present-day high precision CT is about (a few μm)².

ART

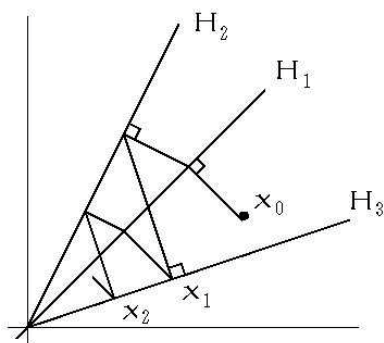


Figure 1: Image of ART

$$\mathbf{a}_i := (a_{i1}, a_{i2}, \dots, a_{in}), \quad i = 1, 2, \dots, m \quad (19)$$

$$H_i : a_{i1}x_1 + a_{i2}x_2 + \dots + a_{in}x_n = s_i \quad (20)$$

H_i : a hyperplane whose normal vector is \mathbf{a}_i
 Orthogonal projection $P_i\mathbf{x}$ of $\mathbf{x} \in \mathbb{R}^n$ to H_i is given by

$$P_i\mathbf{x} := \mathbf{x} - \frac{\mathbf{a}_i \cdot \mathbf{x} - s_i}{\|\mathbf{a}_i\|^2} \mathbf{a}_i \quad (21)$$

Take a suitable $\mathbf{x}_0 \in \mathbb{R}^n$ and define the sequence $\{\mathbf{x}_k\}$ by

$$\mathbf{x}_k := P\mathbf{x}_{k-1} \equiv P_m P_{m-1} \cdots P_1 \mathbf{x}_{k-1}, \quad k = 1, 2, \dots$$

G.N. Hounsfield's algorithm for CT

$$\mathbf{x}^H := \lim_{k \rightarrow \infty} \mathbf{x}_k \approx \mathbf{x} \quad (22)$$

Ultrasonic CT

- The first arrival wave of the ultrasonic one takes the route where the travel time is the shortest (which is called the fastest route) in the cement paste, the mortar and the concrete.
- In the concrete structures of the length less than 1200mm, there is no decay of the speed of the ultrasonic waves with respect to the length.

Outline of our experiments

- Ultrasonic waves;
 - The frequency of the ultrasonic waves is **54kHz**.
 - Velocity of the ultrasonic wave is denoted by V (m/s).
- Length of the test pieces;
We prepared test pieces of the length **100, 200, 300, 400, 800 and 1200mm** in order to check
 - the decay of the acoustic velocity
 - the propagation of the ultrasonic waves

■ Inclusions;

We prepared two types of test pieces of the size **100mm × 100mm × 400mm**.

- Normal test pieces
- Test pieces with styrofoam **100mm × 50mm × (200 or 300mm)** included in their inside (cf. Figure 5 below)

These test pieces are made use of to study the propagation of the ultrasonic waves.

■ Number of the test pieces;

We made three test pieces of each type mentioned above and have taken the average of the observed values of three test pieces in each experiment.

Mix Proportion of Cement Paste

	Water	Cement	Air	Total
Weight(kg)	553	1382	—	1935
Volume(ℓ)	553	437	10	1000

※W/C=40% , Air=1%

Mix Proportion of Cement Mortar

	Water	Cement	Sand	Air	Total
Weight(kg)	331	828	1035	—	2195
Volume(ℓ)	331	262	397	10	1000

※W/C=40% , S/C=1.25 , Air=1%

Table 1: Mix proportion of the test pieces

Length of the test pieces

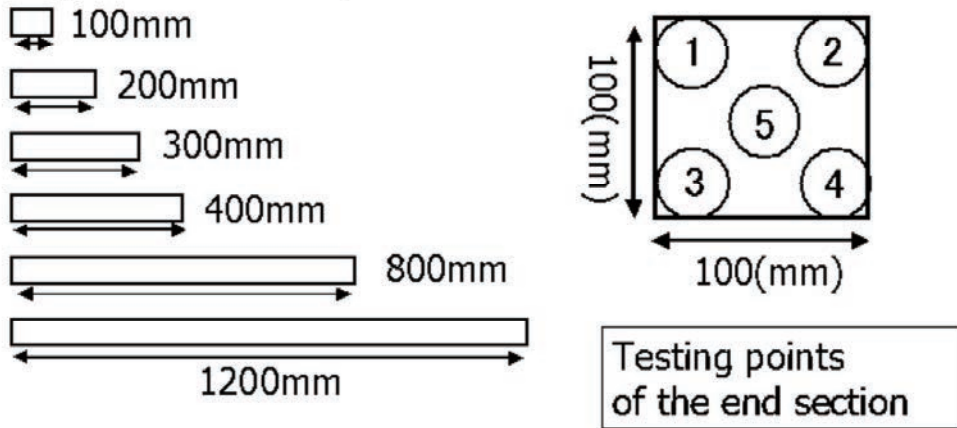
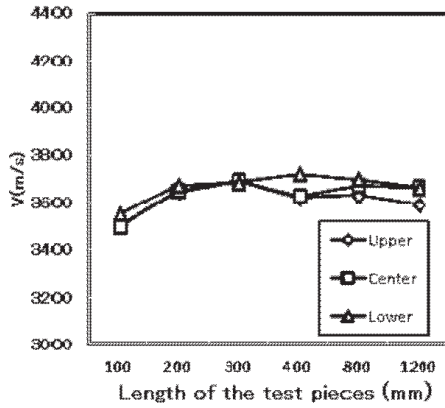


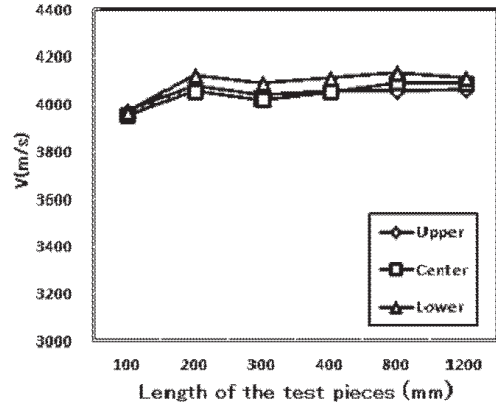
Figure 2: Length of the test pieces and inspection points

Experiment 1

- Normal test pieces of cement paste and cement mortar.
- In order to check the decay of the acoustic velocity in accordance with the length of the test pieces.

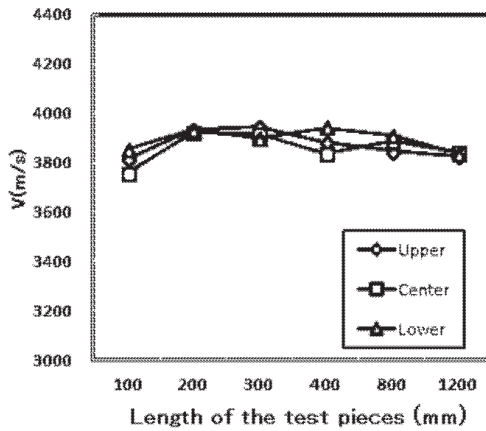


Velocity of Cement Paste

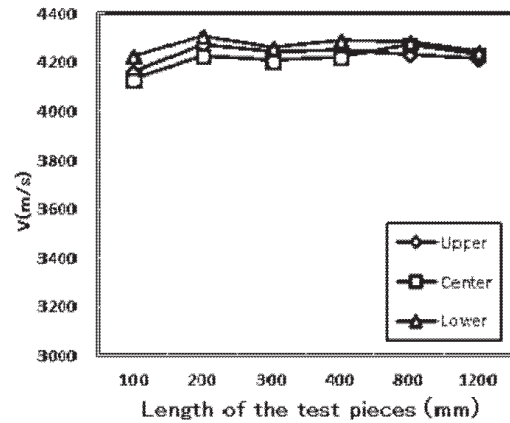


Velocity of Cement Mortar

Figure 3: Normal test pieces (age of a week)



Velocity of Cement Paste



Velocity of Cement Mortar

Figure 4: Normal test pieces (age of 4 weeks)

Property 3.2

- The more time goes by, the harder the test pieces are (the reaction of hydration).
- The gravity settling of cement and fine aggregate (sand).
- We can conclude that for the test pieces of the length less than **1200mm**, there is no decay of the acoustic velocity from the viewpoint of its first arriving time.

Experiment 2

- Test pieces of the length **400mm** (**100mm × 100mm × 400mm**) with and without the styrofoam of the length **200** and **300mm** included in their inside.
- In order to study how the ultrasonic waves propagate in the cement paste and in the cement mortar.

Test pieces with styrofoam inside : normal, styrofoam (200mm, 300mm)

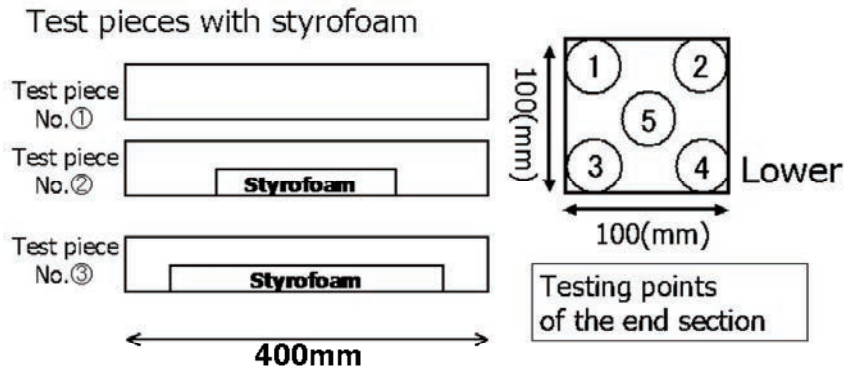


Figure 5: Test pieces with styrofoam

In Experiment 2, the (formal) velocity V calculated by

$$V = \frac{\text{length of the test piece (meters)}}{\text{arriving time (seconds)}}, \quad (23)$$

in the lower points is smaller than that of upper points (confer Table 2 below), applying which we studied the propagation of the ultrasonic waves in the test pieces.

Hypothesis 3.1

The first arrival wave of the ultrasonic one takes the fastest route in the test pieces of the cement paste and the mortar.

In view of this hypothesis, we modify the velocities between the middle and the lower points in the test pieces with stylofoam.

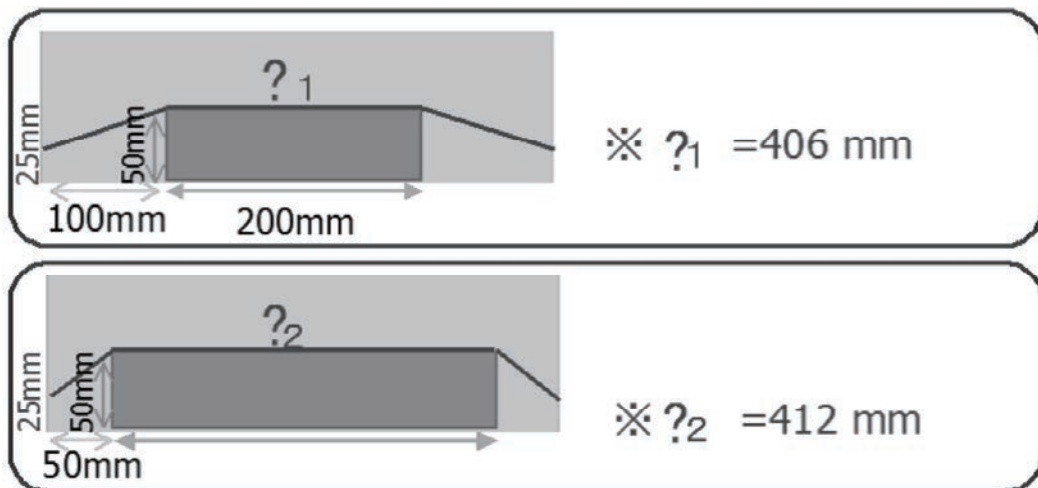


Figure 6: Propagation of the ultrasonic waves in concrete

For the lower points in the test pieces with styrofoam of the length 200mm,

$$V' = \frac{0.406 \text{ (meters)}}{\text{arriving time (seconds)}} \quad (24)$$

For the lower points in the test pieces with styrofoam of the length 300mm,

$$V' = \frac{0.412 \text{ (meters)}}{\text{arriving time (seconds)}} \quad (25)$$

Cement Paste

V	No-Styrofoam	Styrofoam 200mm	Styrofoam 300mm	V'	No-Styrofoam	Styrofoam 200mm	Styrofoam 300mm
Upper	3777	3800	3868	Upper			
Center	3788	3824	3874	Center			
Lower	3809	3700	3731	Lower		3756	3843

Cement Mortar

V	No-Styrofoam	Styrofoam 200mm	Styrofoam 300mm	V'	No-Styrofoam	Styrofoam 200mm	Styrofoam 300mm
Upper	4223	4208	4223	Upper			
Center	4204	4160	4192	Center			
Lower	4229	4080	4034	Lower		4141	4155

Table 2: Tables of modification of the velocity (age of 4 weeks)

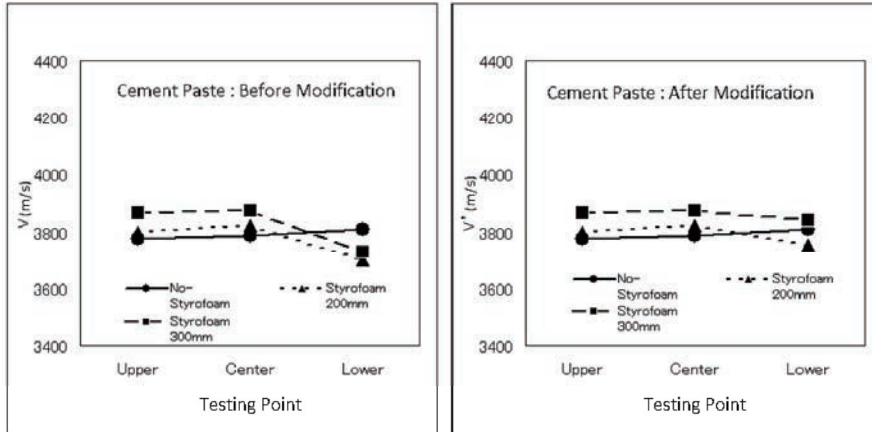


Figure 7: Cement paste with styrofoam (age of 4 weeks)

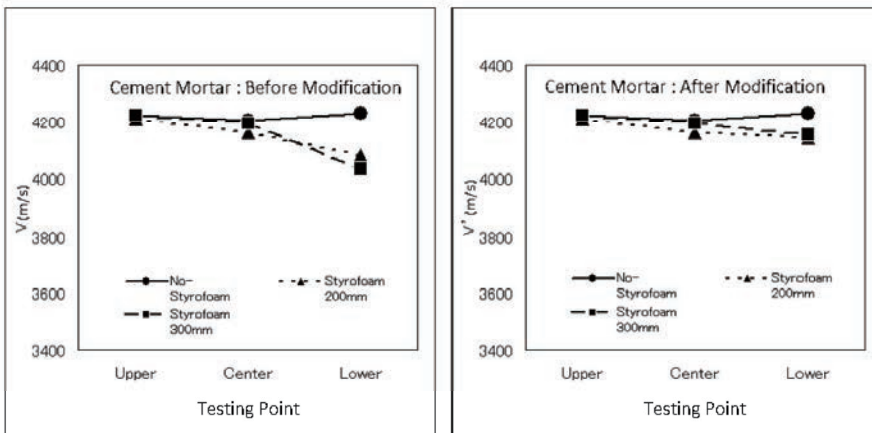


Figure 8: Mortar with styrofoam (age of 4 weeks)

Review examination of the results of Experiment 2

- The modified velocities at the lower points being not exactly the same as the test pieces without styrofoam.
 - In the test pieces with styrofoam, gravity settling of cement and fine aggregate is prevented by the styrofoam. (clearer in the test pieces of mortar)
 - We are afraid that the styrofoam may lie in the route shown in Figure 6, which makes the ultrasonic wave go a longer way around.

- The above point may result in that the velocities of the center and lower points in the test pieces with the styrofoam are a little slower than the counterparts in the test pieces without the styrofoam.
- Remark that in the center points, the ultrasonic wave propagates along the center of the test pieces, which may be prevented by the styrofoam.

Conclution 3.3 (Conclusion of Experiments 1 and 2)

- The first arrival wave of the ultrasonic one takes the fastest route in the cement paste, the mortar and the concrete.
- In the concrete structures of the length less than 1200mm, there is no decay of the speed of the ultrasonic waves with respect to the length.

Problem 3.4

Let $\Omega \subset \mathbb{R}^3$ be a domain and $f(x)$, ($x \in \Omega$) be the propagation speed of the sound. For $\alpha, \beta \in \partial\Omega$, we denote by $\gamma_{\alpha, \beta}$ a route from α to β through Ω . Reconstruct $f(x)$ ($x \in \Omega$) out of the data

$$\min_{\gamma_{\alpha, \beta}} \int_{\gamma_{\alpha, \beta}} 1/f(x) d\gamma, \quad (26)$$

for $\forall \alpha, \beta \in \partial\Omega$.

Remark 3.5 (Remarks on Problem 3.4)

- It is impossible to reconstruct the information of some points x 's where $f(x)$'s are very small (cf. Conclusion 3.3). However, it does not matter very much. For some problems, we only focus on the part where the density is relatively large, for others, the part where the density is relatively small can be determined by the phenomena that the ultrasonic wave would not go through it.
- It is an interesting problem to determine the optimal subset reconstructible by the acoustic CT established by the study of Problem 3.4.

Remark 3.6 (Importance of Problem 3.4 in mathematics)

- It is a very interesting problem to establish an reconstruction formula for Problem 3.4 in view of pure mathematics.
- In view of both applied math and integral geometry, it is another interesting problem in Problem 3.4 to determine the subset of Ω where the reconstruction is impossible because it has no intersection with any γ giving (26).
- In practice, we have to study various incomplete data problems of Problems 3.4 by the restriction arisen from various reasons in practical application, which is interesting in view of pure mathematics (integral geometry with incomplete data), applied mathematics and practice.

An algorithm for ultrasonic CT

Two iterative methods;
ART(Kaczmarz method) and iteration of its solution

(II) Probe of the reinforcing steel in RC structures

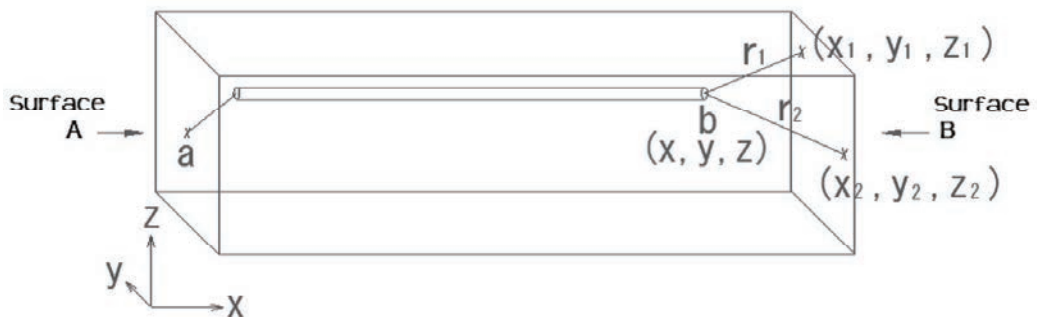


Figure 9: Test piece to probe the steel

4. Non-destructive inspection of concrete cover for reinforcing steel

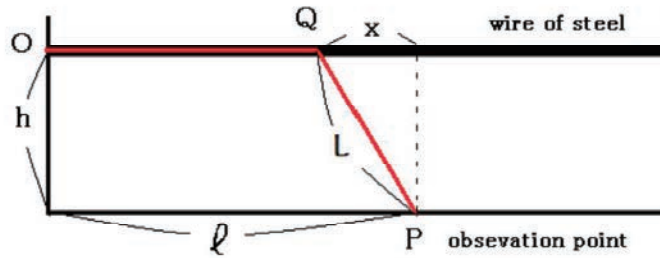


Figure 10: Propagation of ultrasonic waves in RC

V : velocity in the steel, v : the one in the concrete

$4000\text{m/s} < v < 5200\text{m/s}$, $5500\text{m/s} < V < 6500\text{m/s} \Rightarrow$ we assume $v < V$

$$x = \frac{vh}{\sqrt{V^2 - v^2}}, \quad L = \frac{Vh}{\sqrt{V^2 - v^2}}. \quad (27)$$

Determination of the acoustic velocity in the steel

$$V(t_1 - t_0) = l_1, \dots, V(t_n - t_0) = l_n \quad (28)$$

$$(V(t_1 - t_0) - l_1)^2 + \dots + (V(t_n - t_0) - l_n)^2 \quad (29)$$

$$V = \frac{l_1(t_1 - t_0) + \dots + l_n(t_n - t_0)}{(t_1 - t_0)^2 + \dots + (t_n - t_0)^2} \quad (30)$$

Determination of the average acoustic velocity in concrete

$$O_i(0, h_i), h_i < h, R_j(r_j, 0), r_j < \frac{vh}{\sqrt{v^2 - v_0^2}}$$

Observation $\{O_i, R_j\}$

$\Rightarrow L_{ij}$: the length of the segment, t_{ij} : the travel time

$$v_1 = \frac{\sum t_{ij} L_{ij}}{\sum t_{ij}^2}. \quad (31)$$

Non-destructive inspection of concrete cover (1)

If the velocity in the segment QP is much smaller than the homogenized velocity
⇒

- There is a cavity in the segment QP .
- There is a water route around the steel.
- Some part of the steel may get corroded.

Non-destructive inspection of concrete cover (2)

If the velocity in the segment QP is much larger than the homogenized velocity ⇒

We doubt the damage by salt in the segment QP .

5. Conclusion

Conclusion of this talk

- We have studied the structure of the LSS's to the system (3) (Theorem 2.12).
- By application of Theorem 2.12, the LSS to the overdetermined system (3) is obtained, which is applied for the probe of the reinforcing steel in RC structures.
- By obtaining the exact position of the reinforcing steel in RC structures, a ND inspection for concrete cover is made possible, which is essentially important for the maintenance of RC structures.

Open problems left for further development

- Relation of the LSS to (17) and solution by ART (Kaczmarz method)
- Theoretical proof of the convergence of ART to (17).

A non-destructive inspection to probe the reinforcing steel in RC structures by electromagnetic induction method.

Takayuki OCHI

Shikoku Polytechnic College, 3202, Gunge-cho, Marugame, Kagawa 763-0093, JAPAN

email: ochi@shikoku-pc.ac.jp

Abstract

In this talk, we develop a non-destructive inspection method to detect the exact position of the reinforcing steel in reinforced concrete structures. It is a very important open problem. For the development of our method to probe the reinforcing steel, we apply an apparatus to measure thickness of concrete cover for reinforcing steel by electromagnetic induction method, whose measurements are well known to be inexact because of the errors and the noises the apparatus contains. We average the effect of errors in the apparatus by application of what is called 'the least square solutions', to detect the exact position of the reinforcing steel, which turns out to work very well.

1. Introduction

Concrete and Latin *concretus*, "con" are both grown, "crescere" is growing, it means "It is sticking and solidifying things". Modern concrete is used for structures together with rebar. Accurately determining the position of the reinforcing bar in the concrete is very important in order to grasp deterioration of the internal structure of the concrete. Because reinforcing bars are responsible for the tensile force of reinforced concrete construction, rusting is fatal. Furthermore, the reinforcing bars rust, the volume expands and destroys the concrete structure. For concrete, cement, water and aggregate are basic materials, and hydrate is made by chemical reaction of cement and water, and it grows covering the aggregate. Concrete is a material to grow.

The hydrate shows alkalinity and has the effect of preventing corrosion of rebar in concrete. Furthermore, the coefficient of thermal expansion of concrete and rebar shows very close values. Because Roman Concrete is present, contemporary concrete seems like a permanent material, but that is a mistake. Concrete deteriorates. Water necessary for hydration reaction of cement is a part of water used for concrete. The remaining water is used to maintain fluidity during molding. Therefore, when the concrete is hardened, water evaporates from inside the concrete and becomes porous. Concrete gradually deteriorates from the surface because of the entry and exit of air and moisture through the hole. One example is neutralization. Carbon dioxide and calcium hydroxide react slowly to calcium carbonate. Since the alkali content in the concrete disappears, the reinforcing bars become easy to rust. It is important to accurately determine the position of the reinforcing bar in the concrete in order to grasp deterioration from the concrete surface to the reinforcing bar.

There being a number of researches for detection of the rebar, [1, 5] and so on, what we claim in this paper is that we develop a very new technique to *exactly probe the rebar*. In other words, we claim that our technique in this paper is much more accurate than the existing ones.

We develop a theory to specify the exact position of the rebar and verify it by experiments.

This paper consists of the following sections.

§1. Introduction

§2. Apparatus to measure the thickness of concrete cover

§3. Theoretical study to exactly probe the rebar

§4. Verification of the theoretical study by experiments

§5. Conclusion and open problems

In this section, as the introduction of this paper, we introduce the outline of our paper as well as our motivation for this research.

In the next section, we introduce an outline of the apparatus to measure thickness of concrete cover for the reinforcing steel, studying the properties of which motivated us to begin this study.

Section 3 is devoted to the theoretical study how to probe the rebar exactly by a non-destructive inspection by utilizing an apparatus to measure thickness of concrete cover for reinforcing steel, for which, we apply the mathematical idea of the least square solution in order to average the effects of errors in the measurements by the apparatus. Applying this result, we also introduce a method to detect the exact thickness of the concrete cover for reinforcing steel.

In the fourth section, we report the verification of our theoretical study to probe the exact position of the rebar by experiments. We took measurements of the thickness of concrete cover for reinforcing steel by the apparatus with electromagnetic induction from various surface points of the test piece, applying which we specified the endpoints of the rebar in the test piece. Utilizing the position of the endpoints, we calculated the exact thickness of the concrete cover for reinforcing steel. We have verified whether our theoretical study is right by destructing the test piece to result in that our method to probe the position of the rebar is very precise.

In the final section, we summarize the conclusion and mention open problems left to be solved for further development.

2. Apparatus to measure the thickness of concrete cover

In this section, we study properties of the apparatus to measure the thickness of concrete cover for reinforcing steel by electromagnetic induction, which is the main device to detect the exact position of the rebar in this paper.

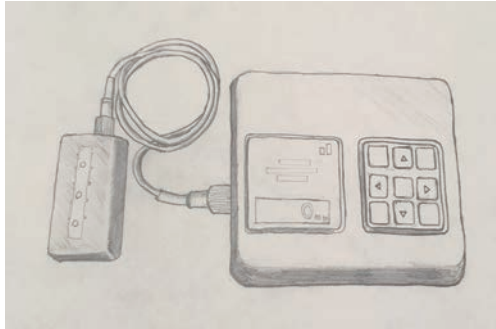


Figure 1: Apparatus to measure thickness of concrete cover by electromagnetic induction

By experience of practical use, we know the following properties of this apparatus.

Property 2.1. (Properties of the apparatus)

- (i) *The measurement is not exact.*
- (ii) *It is impossible to measure the thickness of more than 9cm.*
- (iii) *Although the measurement is not exact, it is stable.*
- (iv) *This apparatus is not suitable to detect the endpoints of the rebar by its original directions for usage.*

The property (i) is well known (cf. [2], for example). The property (ii) is natural since it can rarely be the case that the thickness of concrete cover is more than 9cm.

By the property (iii), we mean that inexactness of the measurement in this apparatus is not random. For example, let us consider a cuboid RC structure whose section is given in Figure 2. In this structure, the rebar locates parallelly to the edge surfaces. By several preliminary experiments, we have ascertained that though the measurements of thickness for concrete cover are not exact, they are all the same, that is, the measurements of thickness from points c, d, e, f, are all the same. This is what we claim the measurement is stable in the property (iii). The property (iii) motivated us to begin this research. We thought that if we found a good method to calibrate the measurement of the apparatus to measure thickness of concrete cover then we could establish a method to detect the exact thickness of concrete cover for reinforcing steel as well as the exact position of the rebar.

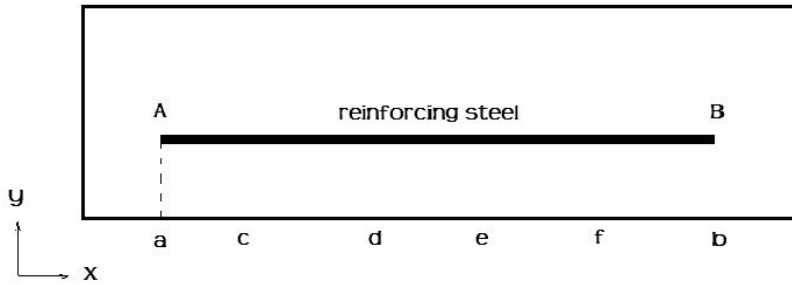


Figure 2: Detecting the endpoints of the rebar

Having known the property (iii), we recognized another big problem, which is the property (vi). In Figure 2, it is very difficult to determine the point A (equivalently, the point a) by the non-destructive inspection with application of the apparatus with electromagnetic induction to measure thickness of concrete cover. If we consider very simply, when we move the apparatus along the line going through the points f, e, d, c and a, it looks that the measured thickness is the same while the apparatus is between the points f and a and the measured thickness will increase after the apparatus goes through the point a. It does not, however. The measured thickness remains the same shortly after the apparatus goes through the point a, and the point where the measured thickness begins to increase varies in accordance with the real thickness of concrete cover.

Roughly speaking, it is our purpose to establish some good methods to compensate for the properties (i) and (vi), by virtue of the property (iii).

3. Theoretical study to exactly probe the rebar

In this section, we shall establish a theory to detect the exact position of the rebar. Assume that a cuboid RC structure contains, in its interior, a rebar which locates parallelly or perpendicularly to each edge surface. Confer Figure 3 for its image.

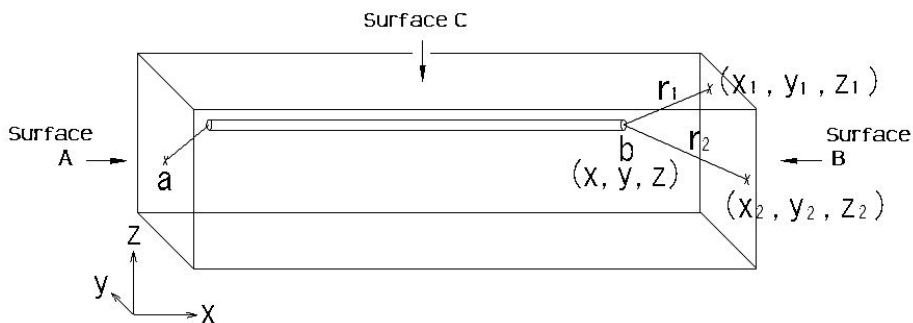


Figure 3: A cuboid test piece

In Figure 3, we set the axes as shown. We first reconstruct the endpoints of the rebar. For the reconstruction of the endpoint b in Figure 3, we take many observation points on the edge surface B and its around and measure the thickness of concrete cover,

equivalently the distance between the observation and the endpoints. We let the endpoint $b = (x, y, z)$ and take n observation points $(x_1, y_1, z_1), \dots, (x_n, y_n, z_n)$, whose distances from the endpoint b are measured as r_1, \dots, r_n , respectively. We shall explain how to take the observation points in the real structure in the next section.

By measurement, we obtain an overdetermined system of quadratic equations.

$$\begin{cases} (x - x_1)^2 + (y - y_1)^2 + (z - z_1)^2 = r_1^2 \\ \dots \\ (x - x_n)^2 + (y - y_n)^2 + (z - z_n)^2 = r_n^2 \end{cases} \quad (1)$$

In the system (1), the unknowns are x, y and z . if $n > 3$ then the system is overdetermined and it rarely admits a solution. If the measurements are exact, the system has the unique solution, however overdetermined it is. As was mentioned in Property 3.1 (i), our measurements containing errors and noises there is almost no chance that the system (1) admits the unique solution. We equalize the effect of the errors and the noises by taking what is called “the least square solution” to the system (1), which yields the exact position of the endpoint $b = (x, y, z)$.

It being not easy to give a least square solution to the system (1), we shall give the unique least square solution to the following equivalent system of (1), which consists of $\frac{n(n-1)}{2}$ linear equations;

$$(x_i - x_j)x + (y_i - y_j)y + (z_i - z_j)z = \frac{1}{2}(x_i^2 + y_i^2 + z_i^2 - x_j^2 - y_j^2 - z_j^2 + r_j^2 - r_i^2) \quad (2)$$

The system (2) is obtained by subtracting i -th equation in system (1) by the j -th one and dividing the both hand sides of the difference by 2.

Reformulation of the system (2), we have the system of $\frac{n(n-1)}{2}$ linear equations

$$a_k x + b_k y + c_k z = d_k \quad (3)$$

Where $k = 1, 2, \dots, \frac{n(n-1)}{2}$, a_k is of the form $x_i - x_j$, b_k is of the form $y_i - y_j$, c_k is of the form $z_i - z_j$ and d_k is of the form $\frac{1}{2}(x_i^2 + y_i^2 + z_i^2 - x_j^2 - y_j^2 - z_j^2 + r_j^2 - r_i^2)$.

This system has the following matrix representation

$$\begin{pmatrix} a_1 & b_1 & c_1 \\ a_2 & b_2 & c_2 \\ \vdots & \vdots & \vdots \\ a_{\frac{n(n-1)}{2}} & b_{\frac{n(n-1)}{2}} & c_{\frac{n(n-1)}{2}} \end{pmatrix} \begin{pmatrix} x \\ y \\ z \end{pmatrix} = \begin{pmatrix} d_1 \\ d_2 \\ \vdots \\ d_{\frac{n(n-1)}{2}} \end{pmatrix} \quad (5)$$

which we denote by

$$Ax = d \quad (5)$$

where A is the matrix in (4), $x = {}^t(x, y, z)$ and $d = {}^t(d_1, d_2, \dots, d_{\frac{n(n-1)}{2}})$.

where by tX , we mean the transposition of the matrix X (we take the three-dimensional vector \mathbf{x} for a 3×1 matrix).

Let us review the basic theory for the least square solutions to a system of linear equations. Let us study the following system of linear equations.

Problem 3.1. Solve the following system of linear equations in y_1, y_2, \dots, y_n .

$$\begin{cases} b_{11}y_1 + b_{12}y_2 + \dots + b_{1n}y_n = s_1 \\ b_{21}y_1 + b_{22}y_2 + \dots + b_{2n}y_n = s_2 \\ \dots \\ b_{m1}y_1 + b_{m2}y_2 + \dots + b_{mn}y_n = s_m \end{cases} \quad (6)$$

or equivalently

$$B\mathbf{y} = \mathbf{s} \quad (7)$$

where B is the matrix in (6), $\mathbf{y} = {}^t(y_1, y_2, \dots, y_n)$ and $\mathbf{s} = {}^t(s_1, s_2, \dots, s_m)$.

For the least square solutions to the system (6), the following propositions are known to hold.

Proposition 3.1. Let $M_{mn}(\mathbf{R})$ be the set of $m \times n$ matrices whose components are real numbers. For $B \in M_{mn}(\mathbf{R})$, the following conditions are equivalent.

- (i) $\mathbf{y} \in \mathbf{R}^n$ is a least square solution to (6).
- (ii) There holds the following equation.

$${}^tB B \mathbf{y} - {}^tB \mathbf{s} = \mathbf{0} \quad (8)$$

Proposition 3.2. For $A \in M_{mn}(\mathbf{R})$, the following conditions are equivalent.

- (i) There exists at least one least square solution to (6) for any $\mathbf{s} \in \mathbf{R}^m$.
- (ii) Furthermore, if $\text{rank}(B) = n$ then the solution to (6) is unique.

The least square solutions to the system (6) has strong relation with the practicalization of computerized tomography ('CT' for short), for which. confer [4].

Let us turn to our system (4) of linear equations. In practice, we can assume that $\text{rank}(A) = 3$ for $n \geq 3$, since the theoretical possibility that $\text{rank}(A) < 3$ is 0. Therefore, the least square solution to the system (4) is unique and it is given by solving the system of linear equations

$${}^tA A \mathbf{x} = {}^tA \mathbf{d} \quad (9)$$

which is obtained by multiplying the transposed matrix

$${}^tA = \begin{pmatrix} a_1 & a_2 & \cdots & a_{\frac{n(n-1)}{2}} \\ b_1 & b_2 & \cdots & b_{\frac{n(n-1)}{2}} \\ c_1 & c_2 & \cdots & c_{\frac{n(n-1)}{2}} \end{pmatrix} \quad (10)$$

to the both hand sides in (4) or (5). We note that the solution to the system is unique since $\text{rank}({}^tAA) = 3$. Therefore, we obtain the following theorem to determine the endpoints of the rebar.

Theorem 3.1. *In practice, the uniquely determined least square solution to the system (4) is given as the unique solution to the system (9).*

Remark 3.1. If the inexactness of the measurement by the apparatus is random, then the least square solution to the system (9) for large n gives satisfactorily approximate solution for the edges of the rebar. As we have mentioned in Property 2.1 (iii), however, it is unfortunate that the it is stable. In view of this argument, we remark the following two points.

- (i) The y - and z -coordinates determined by Theorem 4.1 are very close to the real values.
- (ii) The the x -coordinates determined by Theorem 4.1 are not very approximate.

For the reason of the point (i), consider the circle $x^2 + y^2 = 2$, for a very typical example. If we try to reconstruct the center as the least square solution from the four points $(\pm 1, 0), (0, \pm 1)$ with the distance

$\rho > 0$ between the origin and these four points, then, for any value $\rho > 0$, we obtain the exact center, the origin, as the least square solution. On the other hand, consider the case we try to reconstruct the point $C = (1, 0)$ in the plane from the points $D_k \left(0, \frac{k}{10}\right), k = -10, -9, \dots, 9, 10$, where the distance between C and D_k is given by $d(C, D_k) = \sqrt{100 + k^2/10}$. If we take the distance between C and D_k smaller than the real one. $d(C, D_k) = \sqrt{100 + k^2/10}$ then the least square solution gives the coordinates of the point C as $(x, 0)$, where $x < 1$. If we take the distance between C and D_k larger than the real one, $d(C, D_k) = \sqrt{100 + k^2/10}$ then the least square solution gives the coordinates of the point C as $(x, 0)$, where $x > 1$.

Therefore, we conclude that the stability in inexactness of the measurement of the apparatus, the property (iii) Property 2.1, affects the determination of the x -coordinate of the endpoint very much, while it does not matter on the determination of the y - and z -coordinates.

In view of this remark, we have to prepare another method to determine the x -coordinate of the endpoint. It may seem easy to determine the x -coordinates of the endpoints. For example, if we consider the 2-dimensional structure in Figure 2. When we scan the line through the points b and a , the x -coordinate of the point A seems to be easily determined as the point where the thickness of concrete cover begins to increase (at the point a in Figure 2). In fact, however, the thickness of concrete cover would not begin to increase at the point a . It does shortly after passing through the point a and its length

varies in accordance with the thickness of concrete cover. A solution to this problem shall be discussed in the next section in a practical way.

Applying Theorem 3.1, we can give a method to measure the exact thickness of concrete cover by an apparatus with electromagnetic induction.

Method 3.1. (A method to measure the exact thickness of concrete cover)
Consider the case where we measure the exact thickness of concrete cover from Surface C in Figure 3.

1. Scan the Surface C with the apparatus near the points where the end- point a locates.
2. Compare the minimal measured value in the above procedure and the z- coordinate of the point a, which gives the correction value of the thick- ness of concrete cover.
3. Modify the thickness of concrete cover by the above correction value.

Let us explain this method more in detail. Let the calculated coordinates of the endpoints be $a = (x_a, y_a, z_a)$, $b = (x_b, y_b, z_b)$ and the surface C be included in the plane $z = z_c$. First, scan the surface C near the point (x_a, y_a, z_c) with the apparatus with electromagnetic induction, which gives the minimal measured thickness \tilde{z}_a near the point (x_a, y_a, z_c) . Since the exact thickness at the point (x_a, y_a, z_c) is $z_c - z_a$ then we can determine the correction value on the points on the line $\frac{x-x_a}{x_b-x_a} = \frac{y-y_a}{y_b-y_a}$, $z = z_c$ near (x_a, y_a, z_c) as $\tilde{z}_a - (z_c - z_a) = \tilde{z}_a + z_a - z_c$.

In the same way, we can determine the correction value near the point (x_b, y_b, z_c) .

If $z_a = z_b$, as almost all cases are, then the correction value at any point $(x_a + t(x_b - x_a), y_a + t(y_b - y_a), z_c)$, $0 \leq t \leq 1$ is the same. In this case, scanning the line $\frac{x-x_a}{x_b-x_a} = \frac{y-y_a}{y_b-y_a}$, $z = z_c$ with the apparatus with electromagnetic induction and the modification of the thickness with the correction value $\tilde{z}_a + z_a - z_c = \tilde{z}_a + z_a - z_c$. would yield the exact thickness at the point $(x_a + t(x_b - x_a), y_a + t(y_b - y_a), z_c)$, $0 \leq t \leq 1$.

If $z_a \neq z_b$, then the correction value at the point $(x_a + t(x_b - x_a), y_a + t(y_b - y_a), z_c)$, $0 \leq t \leq 1$ is given by $\tilde{z}_a + z_a - z_c + t(\tilde{z}_b + z_b - (\tilde{z}_a + z_a))$.

4. Verification of the theoretical study by experiments

In order to verify our theoretical study in the previous section, we made a test piece of reinforced concrete and experimented on them. We constructed three cuboid RC test pieces of the size $150 \times 150 \times 530mm^3$ as shown in Figure 3. In these test pieces, the diameter of the rebar is 10mm and the coordinates of the endpoints were designed as

$$a = (95, 95, 50), b = (95, 95, 440) \quad (11)$$

on the construction. We note that the coordinates of the endpoints a, b represents the center of the section of the rebar, that is, in our test pieces, the rebar is designed to locate in the cylinder domain

$$(y - 95)^2 + (z - 95)^2 \leq 25, 50 \leq x \leq 440 \quad (12)$$

We show the materials, the mix proportion and the quality of the test pieces in Tables 1, 2 and 3.

Table 1: Materials of the concrete

Materials	Symbol	Type	Density (g/cm^3)	Coefficients of water absorption(%)	Fineness modulus(%)
Cement	C	Normal potland cement	3.16	-	-
Fine aggregate	S1	Limestone	2.69	1.02	2.79
Fine aggregate	S2	Sea sand	2.57	1.51	2.14
Fine aggregate	S	Mixed S1:S2=7:3	2.65	1.17	2.60
Coarse aggregate	G	Limestone	2.70	0.46	6.69
Water-reducing admixture	-	MasterPolyheed15H[N]	1.05	-	-
Air-entraining admixture	-	MasterAir202	1.04	-	-

In Table 3, the first three data, the slump, the air-content and the density, were obtained at the casting of the test pieces and the others were at the age of eight weeks.

We tried to detect the endpoints a, b of the test piece by application of Theorem 3.1. We took the observation points as shown in Figure 4 and measured the shortest distance between the observation points and the rebar, whose results are summed up in Table 4.

Table 2: Mix proportion of the concrete

W/C (%)	A/C	s/a (%)	Unit volume (kg/m^3)					admixture (kg/m^3)	
			C	W	S1	S2	G	Water-reduce	Air-entraining
46.2	5.64	42.0	331	153	544	233	1092	1.99	0.0132

Table 3: Quality of the concrete

At the casting			Standard curing (8 weeks)		Field curing (8 weeks)	
Slump (cm)	Air-content (%)	Density (kg/l)	Compressive strength(N/mm^2)	Density (kg/l)	Compressive strength(N/mm^2)	Density (kg/l)
11.0	5.9	2.33	52.8	2.39	35.7	2.38

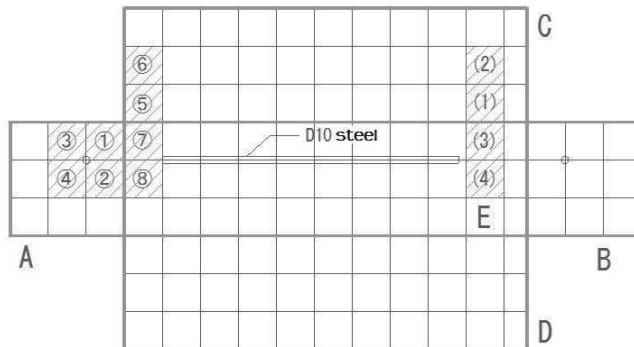


Figure 4: Observation points

Table 4: Measured distance from the rebar

Edge surface	Point	Coordinates	Distance (<i>mm</i>)
A	①	(0,125,125)	74
	②	(0,75,125)	75
	③	(0,125,75)	73
	④	(0,75,75)	75
	⑤	(25,150,125)	67
	⑥	(25,150,75)	67
	⑦	(25,125,150)	66
	⑧	(25,75,150)	67
B	(1)	(475,150,125)	68
	(2)	(475,150,75)	70
	(3)	(475,125,150)	68
	(4)	(475,75,150)	68

Application of Theorem 3.1 with the data in Table 4, yields the coordinates of the endpoints a, b as

$$a = (69, 100, 101), b = (427, 100, 100). \quad (13)$$

As we have discussed in the previous section, the y - and z -coordinates in (13) being reliable, the x -coordinates are not. In our test pieces, the average sonic velocity in the concrete part is about $5200m/s$, which is faster than usual concrete (between $3600m/s$ and $5000m/s$). In view of the above discussion, we can conclude that our concrete is denser and solider than usual one and it is expected that the measured thickness of concrete cover is longer than the real one, since, in our preliminary experiments, we ascertained that the denser and the solider the concrete part is, the thicker value for the concrete cover the apparatus with electromagnetic induction measures. Therefore, for the real position of $a = (x_a, y_a, z_a)$ and $b = (x_b, y_b, z_b)$, it is expected that

$$y_a \approx 100, z_a \approx 101, y_b \approx 100, z_b \approx 100, x_a < 69, x_b > 427. \quad (14)$$

In order to precisely determine the x -coordinates of the endpoints, we made a model in Figure 5 where the steel can be moved in the x -direction and y - and z -coordinates of the steel is fixed as 100.

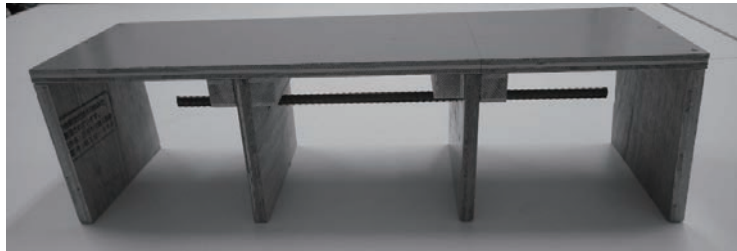


Figure 5: A model to probe the x -coordinate of the endpoint

We scanned the segment $\{(x, 100, 150); 0 \leq x \leq 530\}$ on this model by the apparatus with electromagnetic induction and checked the relation between the endpoint of the steel and the position of the sensor of the apparatus, by which we can conclude the following.

Property 4.1. *If the thickness of concrete cover is 45mm then the measured thickness of concrete cover begins to increase when the x-coordinates of top of the sensor goes farther than 35mm from x_a , confer Figure 6 for its image.*

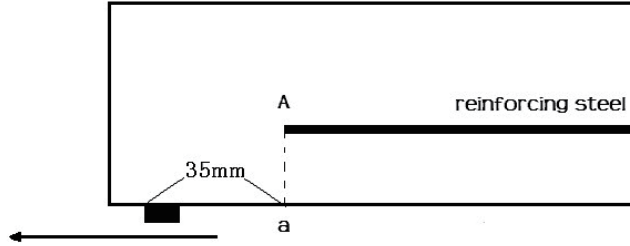


Figure 6: Image of calibration

By this calibration, we reconstructed the x -coordinates of the endpoints. We scanned the apparatus with electromagnetic induction on the segment $\{(x, 100, 100); 0 \leq x \leq 530\}$ and measured the points where the thickness of concrete cover began to increase with application of the above modification whose results are summarized in Table 5.

Table 5: Reconstruction of the x coordinates

Endpoint	y-coordinate	z-coordinate	Measurement surface	Scanning direction	Dist.	Avr. dist.
a	100	101	Surface C	Surface B \rightarrow A	51	50
				Surface A \rightarrow B	53	
			Surface E	Surface B \rightarrow A	51	
				Surface A \rightarrow B	46	
b	100	100	Surface C	Surface A \rightarrow B	87	84
				Surface B \rightarrow A	87	
			Surface E	Surface A \rightarrow B	79	
				Surface B \rightarrow A	83	

By these measurements, the x -coordinates of the endpoints are determined as $x_a = 50$ and $x_b = 446$. Therefore, the result of our non-destructive inspection for the endpoints of the rebar is the following.

$$a = (50, 100, 101), b = (446, 100, 100). \quad (15)$$

We show the result (15) by our non-destructive inspection in Figure 7.

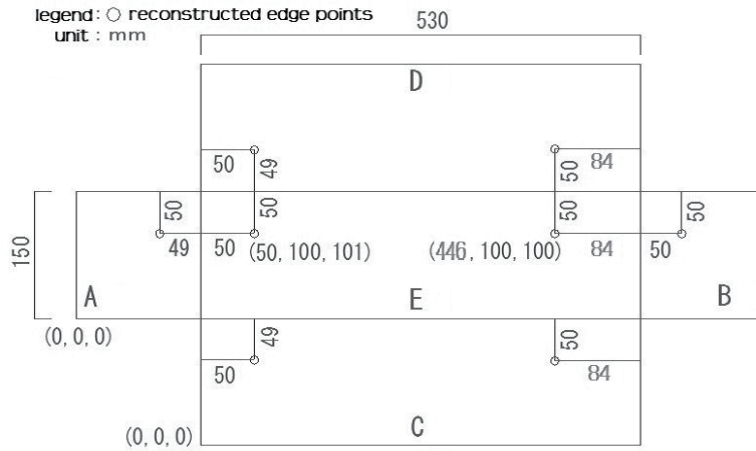


Figure 7: Reconstruction of the endpoints

After these theoretical study had finished, we cut-off the test piece in order to check whether the result (15) by our non-destructive inspection was correct. In Figure 8, we show the real photos of the section of the test piece and the expansion plan of the real endpoints is shown in Figure 9.

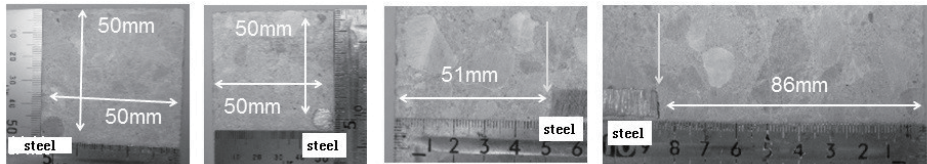


Figure 8: The sections of the test piece

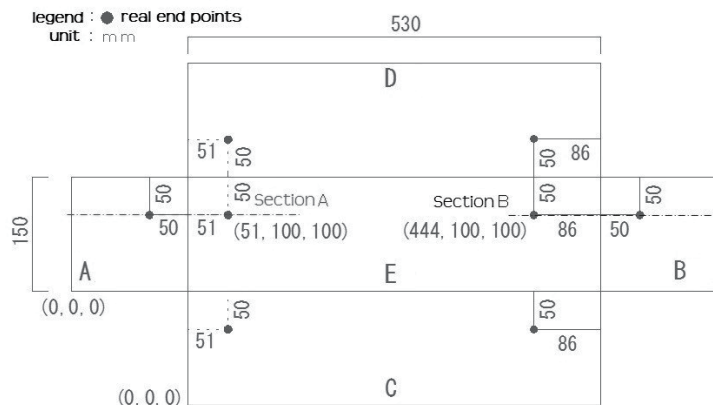


Figure 9: Expansion plan of the test piece

As shown in Figures 8 and 9, the real position of the endpoints are

$$a = (51, 100, 100), b = (444, 100, 100). \quad (16)$$

Comparing (15) and (16), we can conclude that our reconstruction of the endpoints by non-destructive inspection is very precise. Furthermore our reconstruction (15) is much closer to the real position (16) than the designed position. Let us sum up the designed value, the reconstructed one and the real one in Table 6.

Table 6: Table of the results

Endpoint	Coordinate	(i) Real value	(ii) Designed value	(iii)Reconstructed value	(i)-(ii)	(i) - (iii)
a	x	51	50	50	1	1
	y	100	95	100	5	0
	z	100	95	101	5	-1
b	x	444	440	446	4	-2
	y	100	95	100	5	0
	z	100	95	100	5	0

The absolute value of each component in the last row is equal to or smaller than its counterpart in the row before the last, which supports the claim that the reconstructed values are closer to the real ones than the designed ones.

Scanning the segment $\{(x, 100, 100); 50 \leq x \leq 446\}$ by the apparatus to measure the concrete cover for the rebar yielded that same thickness 53mm of concrete cover at any point on the segment, which yields that the correction value of the thickness of the concrete cover is uniformly -8mm for this test piece. By the above argument, it was proved that the steel paralleled the surfaces C, D and E , by non-destructive inspection. It was also shown that the steel did not curve, did not get corroded, nor was it cut off, in a non-destructive way. These proclaims were also verified to be true by cutting off the test piece (cf. Figure 8).

5. Conclusion and open problems

As the closing of this paper, we summarize the conclusion in this paper and mention open problems left to be solved for further development. We first summarize the conclusion.

Conclusion 5.1 (Conclusion of this paper).

- (i) *We have developed a non-destructive inspection technique to exactly probe the rebar by application of an apparatus to measure thickness of concrete cover for reinforcing steel by electromagnetic induction method (Theorem 3.1 and Property 4.1).*
- (ii) *In order to obtain the above conclusion (i), the idea of 'the least square solutions' played an important role.*
- (iii) *As a by-product of the above result (i), we have also developed a technique to measure the exact thickness of the concrete cover for reinforcing steel (Method 3.1).*
- (iv) *Our theoretical studies to exactly probe the rebar (conclusion (i)) and to precisely measure the thickness of concrete cover for reinforcing steel (conclusion (iii)) has been verified to be good by our experiments (Section 4).*

There are open problems left to be solved for further development, which shall be discussed at the end of this paper.

Problem 5.1 (Open problems for further development).

- (i) *The method to reconstruct the y- and z-coordinates of the endpoint of the rebar (Theorem 2.1) being good and sophisticated, the one to reconstruct the x-coordinates (Property 3.1) is very primitive and it requires to make a model in accordance with the reconstructed y- and z-coordinates of the endpoints. It is required to modify Property 3.1 in a much better way or to develop another better method to reconstruct the x-coordinates.*
- (ii) *We shall verify our techniques to exactly probe the rebar and to precisely measure the concrete cover for the reinforcing steel, in the non- destructive inspection of the real RC structures, for example, bridge piers and floorboards in expressways, which may require some modification of our theory in accordance with the structures. The authors claim that it is a very important and interesting problem.*
- (iii) *The authors conjecture that the measurement of concrete cover by the apparatus with electromagnetic inductions depends on the density and the solidity of the concrete as we have verified in our preliminary experiment.*

The Problem (i) is very important in relation with development of an ultrasonic tomography technique for RC structures (cf. [3]). As for the problem (ii), the authors are preparing to conduct experiments on expressways. In order for the solution to the problem (iii), new experiments by the authors are under investigation.

References

- [1] He, X. Q., Zhu, Z. Q., Liu, Q. Y. and Lu, G. Y. : *Review of GPR Rebar Detection*, PIERs Proceedings, Beijing, China, March 23-27, 2009 (2009) pp. 804-813.
- [2] Li, X., Kemi, T. and Fuji, K.: *Study on soundness evaluation of reinforced concrete structures – Investigation of concrete cover using the electromagnetic induction method–*, AIJ J. Technol. Des. **13** (2001) pp. 29-32 (in Japanese).
- [3] Mita, N. and Takiguchi, T. : *Principle of ultrasonic tomography for concrete structures and non-destructive inspection of concrete cover for reinforcement*, Pacific Journal of Mathematics for Industry (2018) 10:6.
- [4] Takiguchi, T. : *How the computerized tomography was practicalized*, Bulletin of JSSAC, **21** (2015) pp. 50–57.
- [5] Tanaka, S. and Wakabayashi, M. : *On Measurement of the Depth and the Diameter of Steel Bars in Reinforced Concrete Using Electromagnetic Wave (Radar)*, 2006 SICE-ICASE International Joint Conference (2006) pp.2555–2559.

A non-destructive inspection to
exactly probe the reinforcing steel by
an electromagnetic induction method

Takayuki OCHI

Shikoku Polytechnic College

Oct. 25th, 2018
IMI KYUSHU UNIVERSITY

Takayuki OCHI

A non-destructive inspection to exactly probe the reinforcing steel by an electromagnetic induction method

Shikoku Polytechnic College

1

1. Introduction
2. Properties of concrete
3. Why to probe the steel
4. Theory for exactly probe
5. Probe of the steel
6. Conclusion

Takayuki OCHI

A non-destructive inspection to exactly probe the reinforcing steel by an electromagnetic induction method

Shikoku Polytechnic College

2

Joint work with

Takashi TAKIGUCHI
National Defense Academy of Japan

Kenji HASHIZUME and Toshiaki TAKABATAKE
West Nippon Expressway Engineering Shikoku Company

3

The purpose of this talk

- We shall introduce basic properties of concrete and discuss the differences between the concrete materials and megaliths.
- The superior and the inferior points of the concrete materials to the megaliths.
- How to improve the above inferior points.
- In view of the above discussion, there arises a problem how to maintain the concrete structures, to study which is the main purpose of this talk.

4

II. Basic properties of concrete

Definition 2.1 (The concrete)

The concrete is the mixture of

- The cement (C),
- The water (W),
- The sand (fine aggregate: S) and
- The gravel (coarse aggregate: G).
- The air as the fifth element.

Remark 2.1

- (i) The mixture of the cement and the water is called the cement paste.
- (ii) The mixture of the cement, the water, and the sand (the cement paste and the sand) is called the mortar.
- (iii) The concrete can be understood as the mixture of the mortar and the gravel.
- (iv) It is very important to add the air as the fifth component, since the concrete is a porous medium.

Property 2.2 (Merits of the concrete)

- (a) Durability against the weather, the chemical materials and the mechanical force.
- (b) High fire-resistance and water-resistance.
- (c) High compressive strength.
- (d) High corrosion resistance for steel.
- (e) The coefficients of thermal expansion (CTE) of the concrete and the steel are exactly the same.
- (f) Easily made and shaped in any form. (by its fluidity)
- (g) The cost is very cheap.

7

Remark 2.3 (remarks on Property 2.2)

- The properties (a), (b) and (c) are almost the same as ones of the megaliths.
- The properties (d) and (e) are essentially important for the RC structures.
- The property (d) is by the chemical property of the cement.
- The properties (f) and (g) are much superior to the megaliths as the building material.

8

Property 2.4 (Demerits of the concrete)

- (α) Low tensile strength.
- (β) It easily gets cracks in and on itself.
- (γ) It is very heavy in the RC structures.

Remark 2.5 (Remarks on Property 2.4)

- As for (α), the tensile strength of the concrete is about **1/10** of its compressive one (very weak). Its bending strength is about a third of its compressive one.
→ the necessity to reinforce the concrete
- The demerit (β) causes problems in the load bearing ability and durability. It also causes the water leakage.
- The RC structures are generally said to be weak to the damage by the earthquake because of the demerit (γ).
- The demerits (α) and (β) are inferior to the megaliths as the building material.
- The demerit (γ) is the same one as the megaliths.

On the properties (d) and (e)

- The main component of the cement is calcium oxide (CaO).
- $CaO + H_2O \rightarrow Ca(OH)_2$
- The calcium hydroxide ($Ca(OH)_2$) shows strong alkalinity.
→ It prevents the steel from getting oxidized.
- If the CTE of the concrete and the steel are different, the RC structure easily have some cracks in their interior by the change of the temperature.

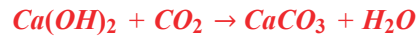
11

By virtue of the properties (d) and (e), the RC was called as
“the miracle and the permanent material”
at its initial stage of application as the building material.

It turned out, however, that it was neither miracle nor permanent.

12

- The concrete gets neutralized by the carbon dioxide (CO_2) in the air a few decades after its foundation;



- Calcium carbonate ($CaCO_3$) is chemically neutral.
- After the neutralization of the concrete, a part of the steel inside the RC structure gets corroded.
 - The corroded steel intumesces very much, which would make cracks or ruin the structure.
- The life span of the RC structure is called about a half century, these days.

Problem 2.6 (Improvement of the concrete)

- (i) Develop a method to make solid, stubborn and stable concrete without reinforcement, by which we can literally make artificial megaliths.
- (ii) Develop a method to maintain RC structures in order that their lifespan can be much longer.

In view of Problem 2.6 (ii), we pose the following problem.

Problem 2.7

Establish an acoustic CT method for concrete structures.

III. Why we have to exactly probe the reinforcing steel?

Important problem in the maintenance of RC structures

In the maintenance of RC structures, one of the most important problem is to prevent the steel from getting corroded.

Why to exactly probe the reinforcing steel

- In order to check whether the structure has been constructed as it was designed.
- To determine the chipping (or break up) in the destructive inspection or on the repair of the structure.
- It helps us to check whether the steel for reinforcement is fine
- For the development of ultrasonic CT.

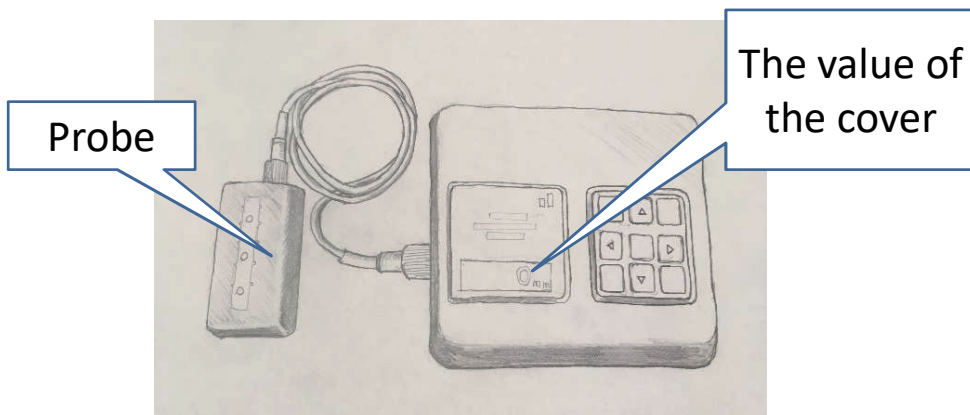
Takayuki OCHI

Shikoku Polytechnic College

A non-destructive inspection to exactly probe the reinforcing steel by an electromagnetic induction method

17

Apparatus to measure the thickness of concrete cover



Apparatus to measure thickness of concrete cover by electromagnetic induction

Takayuki OCHI

Shikoku Polytechnic College

A non-destructive inspection to exactly probe the reinforcing steel by an electromagnetic induction method

18

Properties of the apparatus

Property 3.1. (Properties of the apparatus)

- (i) The measurement is not exact.
- (ii) It is impossible to measure the thickness of more than 9cm.
- (iii) Although the measurement is not exact, it is stable.
- (iv) This apparatus is not suitable to detect the endpoints of the reinforcing steel by its original directions for usage.

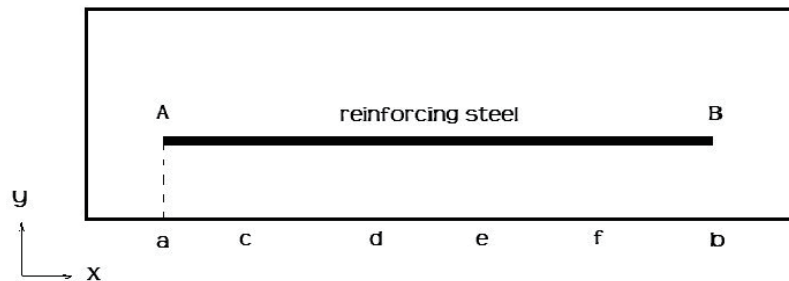


Figure 3.2 Detecting the endpoints of the reinforcing steel

it is our purpose to establish some good methods to compensate for the properties (i) and (vi), by virtue of the property (iii).

IV. Theory to exactly probe the reinforcing steel

We shall establish a theory to detect the exact position of the reinforcing steel.

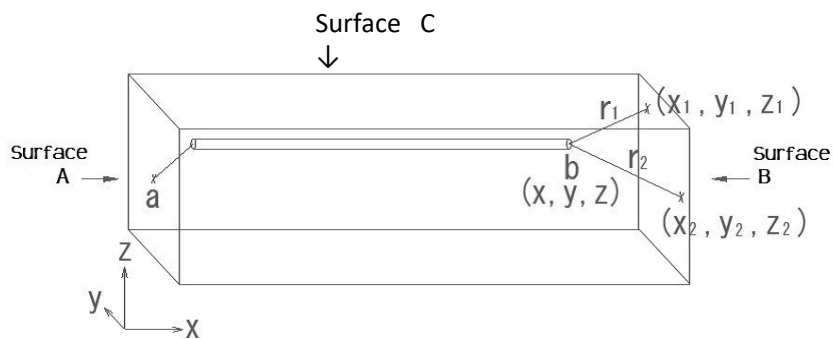
Takayuki OCHI

Shikoku Polytechnic College

A non-destructive inspection to exactly probe the reinforcing steel by an electromagnetic induction method

21

Test piece



A cuboid test piece

Takayuki OCHI

Shikoku Polytechnic College

A non-destructive inspection to exactly probe the reinforcing steel by an electromagnetic induction method

22

The least square solution to

In the system (1), the unknowns are x , y and z .

$$\begin{cases} (x - x_1)^2 + (y - y_1)^2 + (z - z_1)^2 = r_1^2 \\ (x - x_k)^2 + (y - y_k)^2 + (z - z_k)^2 = r_k^2 \end{cases} \quad (1)$$

We remove the effect of the errors and the noises by taking what is called “the least square solution” to the system (1)

The system (2) is obtained by subtracting i -th equation in system (1) by the j -th one and dividing the both hand sides of the difference by 2.

$$(x_i - x_j)x + (y_i - y_j)y + (z_i - z_j)z = \frac{1}{2}(x_i^2 + y_i^2 + z_i^2 - x_j^2 - y_j^2 - z_j^2 + r_i^2 - r_j^2) \quad (2)$$

we have the system of $\frac{n(n-1)}{2}$ linear equations

where $a_k = (x_i - x_j)^{k=1,2,\dots, \frac{n(n-1)}{2}}$

$$b_k = (y_i - y_j)$$

$$c_k = (z_i - z_j)$$

$$d_k = \frac{1}{2}(x_i^2 + y_i^2 + z_i^2 - x_j^2 - y_j^2 - z_j^2 + r_i^2 - r_j^2)$$

$$a_k x + b_k y + c_k z = d_k \quad (3)$$

Replacing each formula with another symbol.
It can be expressed as Equation 3

$$\begin{pmatrix} a_1 & b_1 & c_1 \\ a_2 & b_2 & c_2 \\ \dots & \vdots & \vdots \\ a_{\frac{n(n-1)}{2}} & b_{\frac{n(n-1)}{2}} & c_{\frac{n(n-1)}{2}} \end{pmatrix} \begin{pmatrix} x \\ y \\ z \end{pmatrix} = \begin{pmatrix} d_1 \\ d_2 \\ \vdots \\ d_{\frac{n(n-1)}{2}} \end{pmatrix} \quad (4)$$

$$k=1,2,\dots, \frac{n(n-1)}{2}$$

Replacing equation (3) with a determinant yields
equation (4)

$$Ax = d \quad (5)$$

$$A = \begin{pmatrix} a_1 & b_1 & c_1 \\ a_2 & b_2 & c_2 \\ \vdots & \vdots & \vdots \\ a_{\frac{n(n-1)}{2}} & b_{\frac{n(n-1)}{2}} & c_{\frac{n(n-1)}{2}} \end{pmatrix} \quad x = \begin{pmatrix} x \\ y \\ z \end{pmatrix} \quad d = \begin{pmatrix} d_1 \\ d_2 \\ \vdots \\ d_{\frac{n(n-1)}{2}} \end{pmatrix}$$

Let us study the following system of linear equations.

Problem 4.1.

Solve the following system of linear equations in y_1, y_2, \dots, y_n

$$\begin{cases} b_{11}y_1 + b_{12}y_2 + \dots + b_{1n}y_n = s_1 \\ b_{21}y_1 + b_{22}y_2 + \dots + b_{2n}y_n = s_2 \\ \dots\dots\dots \\ b_{m1}y_1 + b_{m2}y_2 + \dots + b_{mn}y_n = s_m \end{cases} \quad (6)$$

Or equivalently

$$By = s \quad (7)$$

$$B = \begin{pmatrix} b_{11} & \cdots & b_{1n} \\ b_{22} & \cdots & b_{2n} \\ \vdots & & \vdots \\ b_{m1} & \cdots & b_{mn} \end{pmatrix} \quad y = \begin{pmatrix} y_1 \\ \vdots \\ y_n \end{pmatrix} \quad s = \begin{pmatrix} s_1 \\ s_2 \\ \vdots \\ s_m \end{pmatrix}$$

For the least square solutions to the system (6) or (7), the following propositions are known to hold.

Proposition 4.1.

Let $M_{mn}(\mathbf{R})$ be the set of $m \times n$ matrices whose components are real numbers. For $B \in M_{mn}(\mathbf{R})$, the following conditions are equivalent.

(i) $y \in \mathbf{R}^n$ is a least square solution to (6).

(ii) There holds the following equation.

$${}^t B B y - {}^t B s = 0 \quad (8)$$

Proposition 4.2.

For $A \in M_{mn}(\mathbb{R})$, the following conditions are equivalent.

- (i) There exists at least one least square solution to (6) for any $s \in \mathbb{R}^m$.
- (ii) Furthermore, if $\text{rank}(B) = n$ then the solution to (6) is unique.

$${}^t A A x = {}^t A d \quad (9)$$

$${}^t A = \begin{pmatrix} a_1 & a_2 & \cdots & a_{\frac{n(n-1)}{2}} \\ b_1 & b_2 & \cdots & b_{\frac{n(n-1)}{2}} \\ c_1 & c_2 & \cdots & c_{\frac{n(n-1)}{2}} \end{pmatrix} \quad (10)$$

Theorem 4.1.

In practice, the uniquely determined least square solution to the system (4) is given as the unique solution to the system (9).

$$\begin{pmatrix} a_1 & b_1 & c_1 \\ a_2 & b_2 & c_2 \\ \dots & \vdots & \vdots \\ a_{\frac{n(n-1)}{2}} & b_{\frac{n(n-1)}{2}} & c_{\frac{n(n-1)}{2}} \end{pmatrix} \begin{pmatrix} x \\ y \\ z \end{pmatrix} = \begin{pmatrix} d_1 \\ d_2 \\ \vdots \\ d_{\frac{n(n-1)}{2}} \end{pmatrix} \quad (4)$$

$${}^t A A x = {}^t A d \quad (9)$$

Remark 4.1.

If the inexactness of the measurement by the apparatus is random, then the least square solution to the system (9) for large n gives satisfactorily approximate solution for the edges of the reinforcing steel bar.

As we have mentioned in Property 3.1 (iii), however, it is unfortunate that the it is stable.

In view of this argument, we remark the following two points.

- i. The y - and z -coordinates determined by Theorem 4.1 are very close to the real values.
- ii. The the x -coordinates determined by Theorem 4.1 are not very approximate.

V. Exact probe of the reinforcing steel

In this section, we shall give a procedure to detect the exact position of the reinforcing steel.

Takayuki OCHI

Shikoku Polytechnic College

A non-destructive inspection to exactly probe the reinforcing steel by an electromagnetic induction method

35

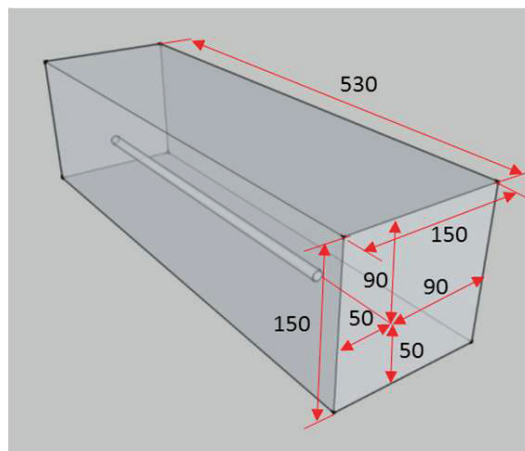


Figure5.1 : Test piece

Takayuki OCHI

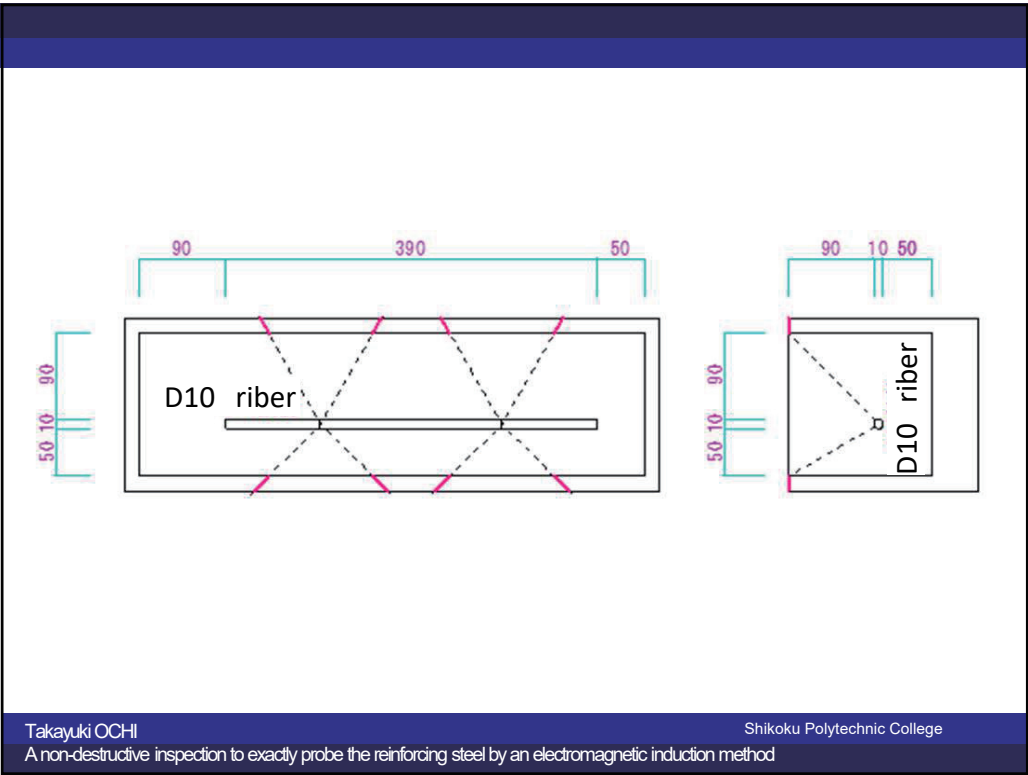
Shikoku Polytechnic College

A non-destructive inspection to exactly probe the reinforcing steel by an electromagnetic induction method

36



37



38

In these test pieces the diameter of the reinforcing steel is 10mm and the coordinates of the endpoints are designed as

$$a = (95, 95, 50), b = (95, 95, 440) \quad (11)$$

We note that the coordinates of the endpoints a, b represents the center of the section of the reinforcing steel, that is, in our test pieces, the reinforcing steel is designed to locate in the cylinder domain

$$(y - 95)^2 + (z - 95)^2 \leq 25, 50 \leq x \leq 440 \quad (12)$$

Table 5.1: Materials of the concrete

Materials	Symbol	Type	Density (g/cm ³)	Coefficients of water absorption(%)	Fineness Modulus (%)
Cement	C	Normal potland cement	3.16	-	-
Fine aggregate	S1	Limestone	2.69	1.02	2.79
Fine aggregate	S2	Sea sand	2.57	1.51	2.14
Fine aggregate	S	Mixed S1:S:2=7:3	2.65	1.17	2.60
Coarse aggregate	G	Limestone	2.70	0.46	6.69
Water-reducing admixture	-	MasterPolyheed 15H[N]	1.05	-	-
Air-entraining admixture	-	MasterAir202	1.04	-	-

Table 5.2: Mix proportion of the concrete

W/C (%)	A/C	S/A (%)	Unit volume (kg/m ³)					admixture (kg/m ³)	
			C	W	S1	S2	G	Water-reduce	Air-extrain
46.2	5.64	42.0	331	153	544	233	1092	1.99	0.0132

Table 5.3: Quality of the concrete

At the casting			Standard curing (8 weeks)		Field curing (8 weeks)	
Slump (cm)	Air-content (%)	Density (kg/l)	Compressive strength (N/mm ²)	Density (kg/l)	Compressive strength (N/mm ²)	Density (kg/l)
11.0	5.9	2.33	52.8	2.39	35.7	2.38

Observation points

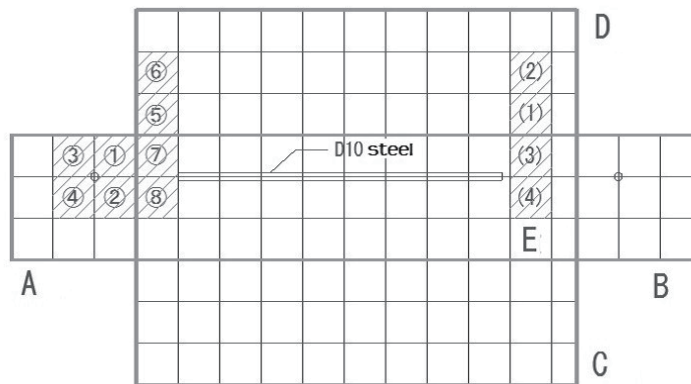


Figure 5.2: Observation points

Table 5.4: Measured distance from the reinforcing steel

Edge surface	Point	Coordinates	Distance (mm)
A	①	(0,125,125)	74
	②	(0,75,125)	75
	③	(0,125,75)	73
	④	(0,75,75)	75
	⑤	(25,150,125)	67
	⑥	(25,150,75)	67
	⑦	(25,125,150)	66
	⑧	(25,75,150)	67
B	(1)	(475,150,125)	68
	(2)	(475,150,75)	70
	(3)	(475,125,150)	68
	(4)	(475,75,150)	68

$$a = (69, 100, 101), b = (427, 100, 100). (13)$$

Reconstruction of the x -axis



Figure 5.3: A model to calibrate the device

Takayuki OCHI

Shikoku Polytechnic College

A non-destructive inspection to exactly probe the reinforcing steel by an electromagnetic induction method

45

Property 5.1.

If the thickness of concrete cover is 45mm then the measured thickness of concrete cover begins to increase when the x -coordinates of top of the sensor goes farther than 35mm from x_a , confer Figure 5.4 for its image.

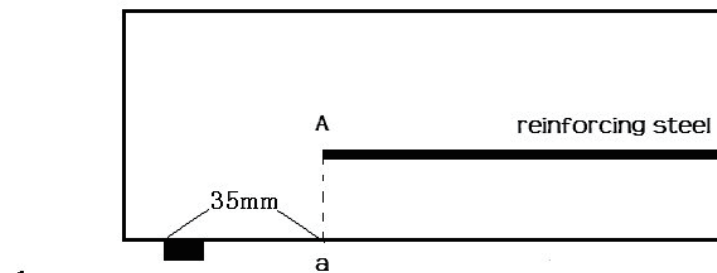


Figure 5.4: Image of calibration

Takayuki OCHI

Shikoku Polytechnic College

A non-destructive inspection to exactly probe the reinforcing steel by an electromagnetic induction method

46

Table 5.5: Reconstruction of the x-coordinates

End point	y-coordinate	z-coordinate	Measurement surface	Scanning direction	Distance	Average distance
a	100	101	Surface C	Surface B → A	51	50
				Surface A → B	53	
			Surface E	Surface B → A	51	
				Surface A → B	46	
b	100	100	Surface C	Surface A → B	87	84
				Surface B → A	87	
			Surface E	Surface A → B	79	
				Surface B → A	83	

47

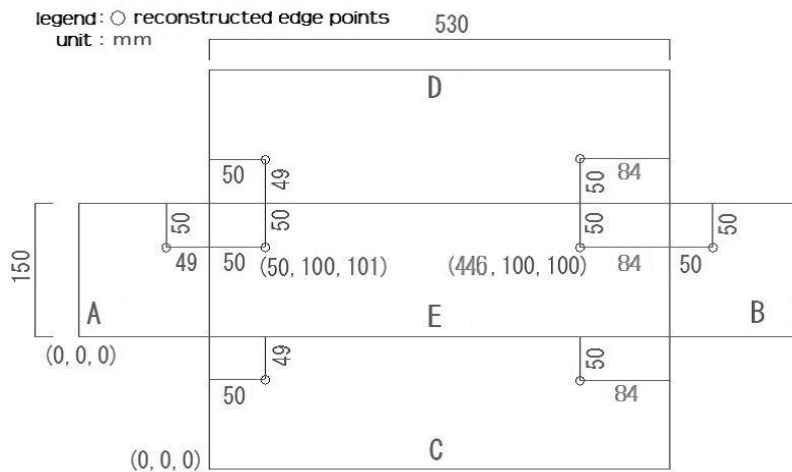


Figure 5.5: Reconstruction of the endpoints

48

The section of the test pieces

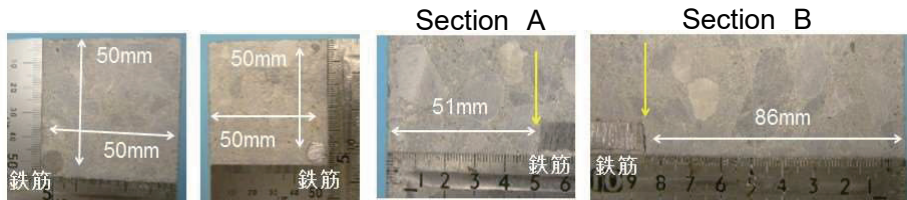


Figure 5.6: The sections of the test pieces

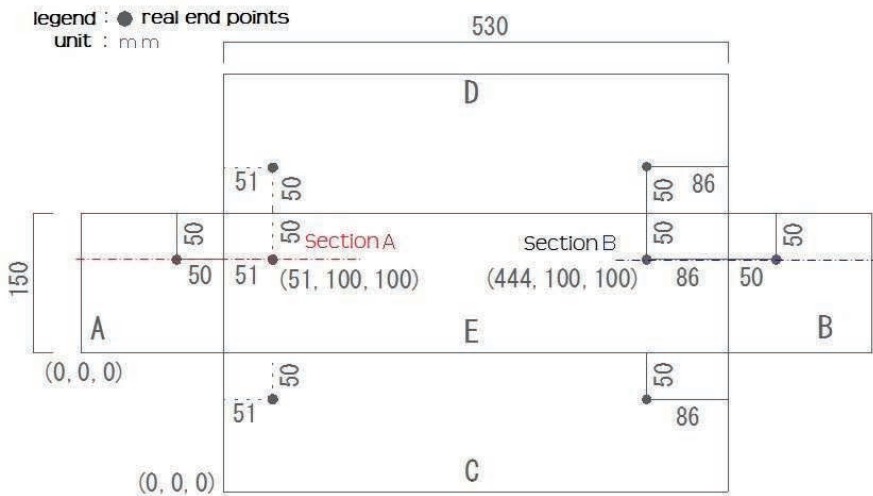


Figure 5.7: Expansion plan of the test piece

Real endpoint $a = (51, 100, 100)$, $b = (444, 100, 100)$.

Table 5.6: Table of the results

Endpoint	Coordinate	(i) Real value	(ii) Designed value	(iii)Reconstructed value	(i)-(ii)	(i) - (iii)
a	x	51	50	50	1	1
	y	100	95	100	5	0
	z	100	95	101	5	-1
b	x	444	440	446	4	-2
	y	100	95	100	5	0
	z	100	95	100	5	0

The reconstructed values are closer to the real ones than the designed ones.

VI. Conclusion and open problems

Conclusion of this talk

- i. We have developed a non-destructive inspection technique to exactly probe the reinforcing steel by application of an apparatus to measure thickness of concrete cover for reinforcing steel by electromagnetic induction method
- ii. In order to obtain the above conclusion (i), the idea of ‘the least square solutions’ played an important role.

- iii. As a by-product of the above result (i), we have also developed a technique to measure the exact thickness of the concrete cover for the reinforcing steel .
- iv. Our theoretical studies to exactly probe the reinforcing steel (conclusion (i)) and to precisely measure the thickness of concrete cover for reinforcing steel (conclusion (iii)) has been verified to be good by our experiments.

Open problems

- The method to reconstruct the x-coordinates (Property 5.1) is very primitive and it requires to make a model in accordance with the reconstructed y- and z-coordinates of the endpoints. It is required to modify Property 5.1 in a much better way or to develop another better method to reconstruct the x-coordinates.
- We shall verify our techniques to exactly probe the reinforcing steel and to precisely measure the concrete cover for the reinforcing steel, in the non-destructive inspection of the real RC structures.

NONDESTRUCTIVE INSPECTION OF BIOLOGICAL TISSUE BY OPTICAL TOMOGRAPHY

MANABU MACHIDA

ABSTRACT. Optical tomography is a medical imaging modality. It is similar to X-ray CT but uses near-infrared light instead of X-rays. Optical tomography is free from radiation exposure and can be done by rather small devices with a near-infrared laser. However, the underlying mathematics is more difficult compared with X-ray CT because near-infrared light experiences multiple scatterings in biological tissue. Optical tomography is formulated as inverse problems of determining coefficients in the radiative transport equation or the diffusion equation. Here we discuss how these inverse problems are used to obtain tomographic images.

1. INTRODUCTION

We try to look inside biological tissue with near infrared light. Infrared light of wavelength from 700 nm to 1 μ m, which is called the optical window, is used. The propagation of near-infrared light in biological tissue is characterized by scattering and absorption. Biological tissue exhibits strong scattering. The specific intensity of light is governed by the radiative transport equation, which is a linear Boltzmann equation. The radiative transport equation is a first-order differential equation but has an integral term. The equation has angular variables in addition to time and spatial variables. The radiative transport equation is often approximated by the diffusion equation. Optical tomography is formulated as inverse problems of determining coefficients of the radiative transport equation or the diffusion equation from boundary measurements.

2. STABILITY ANALYSIS

Let Ω be a bounded domain of \mathbb{R}^n , $n \geq 2$ with C^1 -boundary $\partial\Omega$. We consider

$$P_0 u(x, v, t) + \sigma_t(x, v)u - \int_V k(x, v, v')u(x, v', t)dv' = 0, \quad (2.1)$$
$$x \in \Omega, v \in V, 0 < t < T,$$

$$u(x, v, 0) = a(x, v), \quad x \in \Omega, \quad v \in V, \quad (2.2)$$

$$u(x, v, t) = g(x, v, t), \quad 0 < t < T, \quad (x, v) \in \Gamma_-, \quad (2.3)$$

where

$$P_0 u(x, v, t) := \partial_t u(x, v, t) + v \cdot \nabla u(x, v, t).$$

INSTITUTE FOR MEDICAL PHOTONICS RESEARCH, HAMAMATSU UNIVERSITY SCHOOL OF MEDICINE, HAMAMATSU 431-3192, JAPAN

Date: January 16, 2019.

Here and henceforth for $v, v' \in \mathbb{R}^n$, by $v \cdot v'$ we denote the scalar product in \mathbb{R}^n , let $\nabla = \nabla_x = \left(\frac{\partial}{\partial x_1}, \dots, \frac{\partial}{\partial x_n} \right)$, and $V \subset \mathbb{R}^n$ be a bounded sub-domain or a measurable subset of $\{v \in \mathbb{R}^n; |v| = c\}$ with constant $c > 0$. Here and henceforth \bar{V} denotes the closure of V .

Let $\nu(x)$ be the outward normal unit vector to $\partial\Omega$ at $x \in \partial\Omega$. We define Γ_+ and Γ_- by

$$\Gamma_+ = \{(x, v) \in \partial\Omega \times V; (\nu(x) \cdot v) > 0\}, \quad (2.4)$$

$$\Gamma_- = \{(x, v) \in \partial\Omega \times V; (\nu(x) \cdot v) < 0\}.$$

In (2.1), we let a real-valued function $u(x, v, t)$ denote the angular density of particles or the specific intensity of light at time $t \in (0, T)$ and position $x \in \Omega \subset \mathbb{R}^n$ with velocity $v \in V$.

Let $\sigma_t(x, v)$ denote the total attenuation and satisfy

$$\sigma_t \in L^\infty(\Omega \times V) \quad (2.5)$$

and let $k(x, v, v')$ be a scattering kernel which indicates the amount of particles scattering from a direction v' into a direction v at position x .

We assume that k is independent of t and

$$k(x, v, v') \equiv \sigma_s(x, v)p(x, v, v'), \quad (2.6)$$

$$\sigma_s \in L^\infty(\Omega \times V), \quad (2.7)$$

$$p \in L^\infty(\Omega \times V \times V), > 0 \quad \text{in } \Omega \times V \times V.$$

In this section, $p \in L^\infty(\Omega \times V \times V)$ is fixed, and σ_t or σ_s is unknown to be determined.

We assume that there exist $\gamma \in \mathbb{R}^n$, $\neq 0$ and $\theta > 0$ such that

$$\bar{V} \subset \{v; (\gamma \cdot v) \geq \theta\}. \quad (2.8)$$

This means that we should restrict the distribution of v in a sector with angle $< \pi$ with vertex 0. We can consider the following experiment of optical tomography for example. That is, in (2.1), $u(x, v, t)$ is the specific intensity of light at time t and point $x \in \Omega$ with velocity $v \in V \subset \{v \in \mathbb{R}^n; |v| = c\}$, where c is the speed of light. Let a slab-shaped box Ω be filled with a random medium such as biological tissue. An array of sources on a face of Ω illuminates the medium and the outgoing light is collected by an array of detectors on the other face. We suppose that the width of the box is thin in the sense that few scatterings take place while the light travels from one side to the other. If light is scattered in the forward direction when it collides with impurity, i.e., the direction does not change much by scattering, then light stays within V when it reaches the other side. Thus in this situation, we can assume that v is confined in V . That is, by taking γ in the direction perpendicular to the source and detector faces, we have $V = \{v \in \mathbb{R}^n; |v| = c, (\gamma \cdot v) \geq \theta\}$, where $\theta > 0$ is some constant. Thus (1.8) is satisfied.

Let us rewrite (2.1) as

$$P_0 u(x, v, t) + \sigma_t(x, v)u - \sigma_s(x, v) \int_V p(x, v, v')u(x, v', t)dv' = 0. \quad (2.9)$$

We consider inverse problems of determining total attenuation σ_t or a scattering coefficient σ_s in the radiative transport equation (2.9) by boundary data

$$u(x, v, t), \quad (x, v) \in \Gamma_+, \quad 0 < t < T,$$

after setting up the initial value (2.2) and boundary value (2.3) once. Our inverse problem is motivated for example by optical tomography, in which we recover σ_t and/or σ_s from boundary measurements. An incident laser beam $g(x, v, t)$ enters the sample through the sub-boundary $\Gamma_- \times (0, T)$, and the outgoing light $u(x, v, t)$ is measured on the sub-boundary $\Gamma_+ \times (0, T)$. The positivity for an initial value $a(x, v)$ is needed.

Let us adopt a similar formulation to [3] and we consider the inverse problems of determining σ_s or σ_t by the boundary value on $\Gamma_+ \times (0, T)$ with a suitable single input of the initial value and boundary data on $\Gamma_- \times (0, T)$. Our main results are Lipschitz stability estimates in determining σ_s or σ_t . To the best knowledge of the authors, there are no publications on the Lipschitz stability with single measurement data related to the initial/boundary value problem (2.9), (2.2), and (2.3).

Our proof is based on the methodology by Bukhgeim and Klivanov [1] which uses a Carleman estimate, which is an L^2 -weighted estimate for solutions to the differential equation under consideration. Although the principle of our method is same as [1] and [3], our key Carleman estimate is of different character and so we do not need any extensions of the solution u to $(-T, T)$. On the other hand, [3] needs the extension of the solution u to $(-T, T)$ and so further requires extra conditions for unknown coefficients σ_t and initial value a such as $(a(x, v)\sigma_t(x, v))^2 = (a(x, -v)\sigma_t(x, -v))^2$ for $x \in \Omega$ and $v \in V$ in the case of $V = \{v; |v| = 1\}$. Klivanov and Pamyatnykh [2] proved the Lipschitz stability in determining σ_t when we consider the transport equation (2.9) for $-T < t < T$ with (2.2) and (2.2) is prescribed at an intermediate time $t = 0$ and is not an initial value. In [2], the extension argument is not necessary and the application of the relevant Carleman estimate is more direct.

Our arguments in the case $V \subset \{v \in \mathbb{R}^n; |v| = c\}$ is the same as in the case of sub-domain $V \subset \mathbb{R}^n$. Therefore, henceforth we assume that V is a sun-domain in \mathbb{R}^n . Throughout this article, $H^m(\Omega)$ denotes usual Sobolev spaces. We set

$$X = H^1(0, T; L^\infty(\Omega \times V)) \cap H^2(0, T; L^2(\Omega \times V)).$$

For an arbitrarily fixed constant $M > 0$, we set

$$U = \{u \in X; \|u\|_X + \|\nabla u\|_{H^1(0, T; L^2(\Omega \times V))} \leq M\}. \quad (2.10)$$

By the geometric configuration assumption (2.8) of V , we can choose $\gamma \in \mathbb{R}^n$ such that

$$\min_{v \in \overline{V}} (\gamma \cdot v) > 0.$$

We recall that $p \in L^\infty(\Omega \times V \times (0, T))$ is given.

We can prove the following theorem [6].

Theorem 2.1 (Determination of σ_t). *Let $u^i = u(\sigma_t^i)(x, v, t)$, $i = 1, 2$ be solutions to the transport equation:*

$$\begin{aligned} & \partial_t u(x, v, t) + v \cdot \nabla u + \sigma_t^i(x, v)u \\ & - \sigma_s(x, v) \int_V p(x, v, v') u(x, v', t) dv' = 0, \quad x \in \Omega, v \in V, 0 < t < T, \\ & u(x, v, 0) = a_i(x, v), \quad x \in \Omega, v \in V, \\ & u = g \quad \text{on } \Gamma_- \times (0, T). \end{aligned}$$

Let $u^i \in \mathcal{U}$ and $\|\sigma_t^i\|_{L^\infty(\Omega \times V)}$, $\|\sigma_s\|_{L^\infty(\Omega \times V)} \leq M$. We assume that

$$T > \frac{\max_{x \in \bar{\Omega}}(\gamma \cdot x) - \min_{x \in \bar{\Omega}}(\gamma \cdot x)}{\min_{v \in \bar{V}}(\gamma \cdot v)}. \quad (2.11)$$

and there exists a constant $a_0 > 0$ such that

$$a_1(x, v) \geq a_0 \quad \text{or} \quad a_2(x, v) \geq a_0, \quad \text{almost all } (x, v) \in \Omega \times V.$$

Then there exists a constant $C = C(M, a_0) > 0$ such that

$$\left\{ \begin{array}{l} \|\sigma_t^1 - \sigma_t^2\|_{L^2(\Omega \times V)} \leq C \left(\int_0^T \int_{\Gamma_+} (\nu(x) \cdot v) |\partial_t(u^1 - u^2)(x, v, t)|^2 dS dv dt \right)^{\frac{1}{2}} \\ + C(\|a_1 - a_2\|_{L^2(\Omega \times V)} + \|\nabla a_1 - \nabla a_2\|_{L^2(\Omega \times V)}), \\ \left(\int_0^T \int_{\Gamma_+} (\nu(x) \cdot v) |\partial_t(u^1 - u^2)(x, v, t)|^2 dS dv dt \right)^{\frac{1}{2}} \\ \leq C(\|\sigma_t^1 - \sigma_t^2\|_{L^2(\Omega \times V)} + \|a_1 - a_2\|_{L^2(\Omega \times V)} + \|\nabla a_1 - \nabla a_2\|_{L^2(\Omega \times V)}). \end{array} \right.$$

Here $C(M, a_0) \rightarrow \infty$ as $M \rightarrow \infty$ or $a_0 \rightarrow 0$.

In particular, if we assume $a_1 = a_2$ in $\Omega \times V$, then we have a two-sided estimate:

$$\begin{aligned} C^{-1} \left(\int_0^T \int_{\Gamma_+} (\nu(x) \cdot v) |\partial_t(u^1 - u^2)(x, v, t)|^2 dS dv dt \right)^{\frac{1}{2}} &\leq \|\sigma_t^1 - \sigma_t^2\|_{L^2(\Omega \times V)} \\ &\leq C \left(\int_0^T \int_{\Gamma_+} (\nu(x) \cdot v) |\partial_t(u^1 - u^2)(x, v, t)|^2 dS dv dt \right)^{\frac{1}{2}}. \end{aligned}$$

This means that the choice of the norm of the boundary data on $\Gamma_+ \times (0, T)$ is the best possible for our inverse problem.

Similar stability estimates can be proved for σ_s .

3. OPTICAL TOMOGRAPHY

Let us consider the following time-independent radiative transport equation (RTE).

$$\hat{\mathbf{s}} \cdot \nabla I + (\mu_a + \mu_s)I = \mu_s \int_{\mathbb{S}^2} p(\hat{\mathbf{s}}, \hat{\mathbf{s}}') I(\mathbf{r}, \hat{\mathbf{s}}') d\hat{\mathbf{s}}'.$$

3.1. Formulation. We assume that the scattering coefficient μ_s is constant everywhere in the medium but the absorption coefficient μ_a varies with position. We thus decompose μ_a into a constant part $\bar{\mu}_a$ and a spatially varying part $\delta\mu_a$:

$$\mu_a(\mathbf{r}) = \bar{\mu}_a + \delta\mu_a(\mathbf{r}).$$

The RTE thus becomes

$$\hat{\mathbf{s}} \cdot \nabla I + \mu_t I + \delta\mu_a(\mathbf{r})I = \mu_s \int_{\mathbb{S}^2} p(\hat{\mathbf{s}}, \hat{\mathbf{s}}') I(\mathbf{r}, \hat{\mathbf{s}}') d\hat{\mathbf{s}}',$$

where $\mu_t = \bar{\mu}_a + \mu_s$. The solution is formally given by

$$I(\mathbf{r}, \hat{\mathbf{s}}) = I_0(\mathbf{r}, \hat{\mathbf{s}}) - \int_{\mathbb{S}^2} \int_{\Omega} G(\mathbf{r}, \hat{\mathbf{s}}; \mathbf{r}', \hat{\mathbf{s}}') \delta\mu_a(\mathbf{r}') I(\mathbf{r}', \hat{\mathbf{s}}') d\mathbf{r}' d\hat{\mathbf{s}}'.$$

Here I_0 is the solution in the case of $\mu_a = \bar{\mu}_a$. The Green's function G satisfies the equation

$$\hat{\mathbf{s}} \cdot \nabla_{\mathbf{r}} G(\mathbf{r}, \hat{\mathbf{s}}; \mathbf{r}', \hat{\mathbf{s}}') + \mu_t G(\mathbf{r}, \hat{\mathbf{s}}; \mathbf{r}', \hat{\mathbf{s}}') = \mu_s \int_{\mathbb{S}^2} p(\hat{\mathbf{s}}, \hat{\mathbf{s}}') G(\mathbf{r}, \hat{\mathbf{s}}; \mathbf{r}', \hat{\mathbf{s}}') d\hat{\mathbf{s}}' + \delta(\mathbf{r} - \mathbf{r}') \delta(\hat{\mathbf{s}} - \hat{\mathbf{s}}').$$

By the Born approximation, we have

$$I(\mathbf{r}, \hat{\mathbf{s}}) = I_0(\mathbf{r}, \hat{\mathbf{s}}) - \int_{\Omega} \int_{\mathbb{S}^2} G(\mathbf{r}, \hat{\mathbf{s}}; \mathbf{r}', \hat{\mathbf{s}}') \delta\mu_a(\mathbf{r}') I_0(\mathbf{r}', \hat{\mathbf{s}}') d\mathbf{r}' d\hat{\mathbf{s}}'.$$

The Rytov approximation is given by

$$-\ln \left(\frac{I(\mathbf{r}, \hat{\mathbf{s}})}{I_0(\mathbf{r}, \hat{\mathbf{s}})} \right) = \frac{1}{I_0(\mathbf{r}, \hat{\mathbf{s}})} \int_{\Omega} \int_{\mathbb{S}^2} G(\mathbf{r}, \hat{\mathbf{s}}; \mathbf{r}', \hat{\mathbf{s}}') \delta\mu_a(\mathbf{r}') I_0(\mathbf{r}', \hat{\mathbf{s}}') d\mathbf{r}' d\hat{\mathbf{s}}'.$$

It is convenient to introduce the data function ϕ , which is defined by

$$\phi = \begin{cases} I_0 - I, & \text{Born,} \\ -I_0 \ln(I/I_0), & \text{Rytov.} \end{cases}$$

In either case, ϕ obeys the integral equation

$$\phi(\boldsymbol{\rho}_s, \boldsymbol{\rho}_d) = \int_{\mathbb{S}^2} \int_{\Omega} G(\mathbf{r}, \hat{\mathbf{s}}; \mathbf{r}', \hat{\mathbf{s}}') \delta\mu_a(\mathbf{r}') I_0(\mathbf{r}', \hat{\mathbf{s}}') d\mathbf{r}' d\hat{\mathbf{s}}',$$

where $\boldsymbol{\rho}_s$ and $\boldsymbol{\rho}_d$ are the transverse coordinates of the source and detector, respectively.

We assume a three-dimensional slab-shaped medium for Ω . The incident field is taken to be generated by a point-source oriented in the inward normal direction located on the $z = 0$ plane. Thus $I_0 = G(\mathbf{r}, \hat{\mathbf{s}}; \boldsymbol{\rho}', 0, \hat{\mathbf{z}})$. Light exiting the slab in the normal direction is collected by a point-detector that is located on the plane $z = L$. Thus the integral equation becomes

$$\phi(\boldsymbol{\rho}_s, \boldsymbol{\rho}_d) = \int_{\mathbb{S}^2} \int_{\Omega} G(\boldsymbol{\rho}_d, L, \hat{\mathbf{z}}; \mathbf{r}, \hat{\mathbf{s}}) G(\mathbf{r}, \hat{\mathbf{s}}; \boldsymbol{\rho}_s, 0, \hat{\mathbf{z}}) \delta\mu_a(\mathbf{r}) d\mathbf{r} d\hat{\mathbf{s}},$$

where $\boldsymbol{\rho}_s$ and $\boldsymbol{\rho}_d$ are the transverse coordinates of the source and detector, respectively.

We make use of the method of rotated reference frames [7] to express the Green's function as an expansion in two-dimensional plane waves and spherical harmonics. We have [4]

$$G(\mathbf{r}, \hat{\mathbf{s}}; \mathbf{r}', \hat{\mathbf{s}}') = \int_{\mathbb{R}^2} \frac{1}{(2\pi)^2} e^{-i\mathbf{q} \cdot (\boldsymbol{\rho} - \boldsymbol{\rho}')} \sum_{l=0}^{\infty} \sum_{m=-l}^l Y_{lm}(\hat{\mathbf{s}}') i^m k_{lm}(\mathbf{q}, z) d\mathbf{q}.$$

Hence,

$$\phi(\boldsymbol{\rho}_s, \boldsymbol{\rho}_d) = \int_{\Omega} \int_{\mathbb{R}^2} \frac{1}{(2\pi)^2} \int \frac{1}{(2\pi)^2} e^{i(\mathbf{q}_1 - \mathbf{q}_2) \cdot \boldsymbol{\rho}} e^{-i(\mathbf{q}_1 \cdot \boldsymbol{\rho}_s - \mathbf{q}_2 \cdot \boldsymbol{\rho}_d)} \kappa(\mathbf{q}_1, \mathbf{q}_2, z) \delta\mu_a(\mathbf{r}) d\mathbf{q}_2 d\mathbf{q}_1 d\mathbf{r},$$

where

$$\kappa(\mathbf{q}_1, \mathbf{q}_2, z) = \sum_{l=0}^{\infty} \sum_{m=-l}^l (-1)^m k_{lm}(\mathbf{q}_1, z) k_{lm}^*(\mathbf{q}_2, L - z).$$

Let us consider the inverse problem of recovering the absorption $\delta\mu_a$ from measurements of the data function ϕ . To proceed, we assume that the sources and

detectors are placed on square lattices with lattice spacings h_s and h_d , respectively. The positions of the sources and detectors are given by

$$\boldsymbol{\rho}_s = h_s(n_{sx}\hat{\mathbf{x}} + n_{sy}\hat{\mathbf{y}}), \quad \boldsymbol{\rho}_d = h_d(n_{dx}\hat{\mathbf{x}} + n_{dy}\hat{\mathbf{y}}),$$

where n_{sx} , n_{sy} , n_{dx} , and n_{dy} are integers. Consider the Fourier transform of the data function:

$$\tilde{\phi}(\mathbf{q}_s, \mathbf{q}_d) = \sum_{\boldsymbol{\rho}_s, \boldsymbol{\rho}_d} e^{i(\mathbf{q}_s \cdot \boldsymbol{\rho}_s + \mathbf{q}_d \cdot \boldsymbol{\rho}_d)} \phi(\boldsymbol{\rho}_s, \boldsymbol{\rho}_d).$$

Here the vectors \mathbf{q}_s and \mathbf{q}_d lie in the first Brillouin zone (FBZ) of the source and detector lattices:

$$-\frac{\pi}{h_s} \leq q_s^{(x)}, q_s^{(y)} \leq \frac{\pi}{h_s}, \quad -\frac{\pi}{h_d} \leq q_d^{(x)}, q_d^{(y)} \leq \frac{\pi}{h_d}.$$

We obtain

$$\tilde{\phi}(\mathbf{q}_s, \mathbf{q}_d) = \frac{1}{h_s^2 h_d^2} \sum_{\boldsymbol{\nu}_s, \boldsymbol{\nu}_d} \int_0^L \kappa(\mathbf{q}_s + \boldsymbol{\nu}_s, -\mathbf{q}_d + \boldsymbol{\nu}_d, z) \widetilde{\delta\mu_a}(\mathbf{q}_s + \mathbf{q}_d + \boldsymbol{\nu}_s - \boldsymbol{\nu}_d, z) dz,$$

where

$$\widetilde{\delta\mu_a}(\mathbf{q}, z) = \int_{\mathbb{R}^2} e^{i\mathbf{q} \cdot \boldsymbol{\rho}} \delta\mu_a(\boldsymbol{\rho}, z) d\boldsymbol{\rho}.$$

Next, we perform the change of variables

$$\mathbf{q}_s = \frac{\mathbf{q}}{2} + \mathbf{p}, \quad \mathbf{q}_d = \frac{\mathbf{q}}{2} - \mathbf{p},$$

where \mathbf{q}_s and \mathbf{q}_d are two-dimensional vectors. We also assume that $\delta\mu_a$ is transversely band-limited to the FBZs of the source-detector lattices (corresponding to the band limit $\min\{2\pi/h_s, 2\pi/h_d\}$) and therefore put $\boldsymbol{\nu}_s = 0$ and $\boldsymbol{\nu}_d = 0$, which thus becomes

$$\Phi(\mathbf{q}, \mathbf{p}) = \int_0^L K(\mathbf{q}, \mathbf{p}, z) \widetilde{\delta\mu_a}(\mathbf{q}, z) dz,$$

where

$$\begin{aligned} \Phi(\mathbf{q}, \mathbf{p}) &= h_s^2 h_d^2 \tilde{\phi}\left(\frac{\mathbf{q}}{2} + \mathbf{p}, \frac{\mathbf{q}}{2} - \mathbf{p}\right), \\ K(\mathbf{q}, \mathbf{p}, z) &= \kappa\left(\mathbf{p} + \frac{\mathbf{q}}{2}, \mathbf{p} - \frac{\mathbf{q}}{2}, z\right). \end{aligned}$$

For fixed \mathbf{q} , We have a system of one-dimensional integral equations for the Fourier transform $\widetilde{\delta\mu_a}$. Following the general approach, we construct the pseudoinverse solution and perform an inverse Fourier transform to obtain the inversion formula [5]

$$\begin{aligned} \delta\mu_a(\boldsymbol{\rho}, z) &= \int_{\text{FBZ}} \frac{1}{(2\pi)^2} e^{-i\mathbf{q} \cdot \boldsymbol{\rho}} \sum_{\nu} \frac{R_{\epsilon}(\sigma_{\nu}(\mathbf{q}))}{\sigma_{\nu}^2(\mathbf{q})} \sum_{\mathbf{p}} \langle f_{\nu}(\mathbf{q}) | \mathbf{p} \rangle \Phi(\mathbf{q}, \mathbf{p}) \\ &\quad \times \sum_{\mathbf{p}'} K^*(\mathbf{q}, \mathbf{p}', z) \langle \mathbf{p}' | f_{\nu}(\mathbf{q}) \rangle d\mathbf{q}. \end{aligned}$$

Here f_{ν} and σ_{ν} are the singular functions and singular values of the matrix M :

$$\sum_{\mathbf{p}'} \langle \mathbf{p} | M(\mathbf{q}) | \mathbf{p}' \rangle \langle \mathbf{p}' | f_{\nu}(\mathbf{q}) \rangle = \sigma_{\nu}^2(\mathbf{q}) \langle \mathbf{p} | f_{\nu}(\mathbf{q}) \rangle,$$

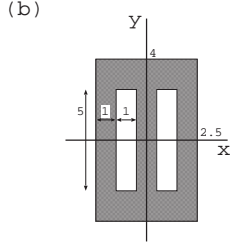


FIGURE 1. The bar target in the x - y plane. The height and width of the bar in the middle are $5\ell^*$ and ℓ^* , respectively, whereas the height and width of the whole bar target are $8\ell^*$ and $5\ell^*$, respectively.

where

$$\langle \mathbf{p} | M(\mathbf{q}) | \mathbf{p}' \rangle = \int_0^L K(\mathbf{q}, \mathbf{p}, z) K^*(\mathbf{q}, \mathbf{p}', z) dz.$$

It is important to note that regularization must be introduced to control the effect of small singular values. This we do by introducing the regularizer R_ϵ , where ϵ is a small parameter. Common choices for R_ϵ are the Tikhonov regularizer $R_\epsilon(\sigma) = \sigma^2 / (\sigma^2 + \epsilon)$ or the step function $R_\epsilon(\sigma) = \theta(\sigma - \epsilon)$. In our computations, both approaches give numerically equivalent results.

Let us consider numerical calculation and obtain reconstruction from simulated forward data. The data are stored in the data function with the Born approximation. Our target is a bar target shown in Fig. 1. Gaussian noise with zero mean and standard deviation of 1% of the average signal is added to the data function Φ for the numerical experiment. The sum over l is truncated at $l_{max} = 9$. The optical properties of the background medium are taken to be

$$\bar{\mu}_a = 0.05 \text{ cm}^{-1}, \quad \mu_s = 100 \text{ cm}^{-1}, \quad g = 0.9.$$

Note that $\ell^* = 1.00 \text{ mm}$ in this case. The above values are typical for biological tissues in the near-IR spectral range. We have $-N_s \leq n_{sx}, n_{sy} \leq N_s$ and $-N_d \leq n_{dx}, n_{dy} \leq N_d$. We also set $N_d = 120$ and $N_s = 120h_d/h_s$. The wave vectors \mathbf{q} and \mathbf{p} are discretized as

$$\begin{aligned} \mathbf{q} &= \frac{2\pi}{h_d(2N_{\text{FBZ}}+1)} (j_x \hat{\mathbf{x}} + j_y \hat{\mathbf{y}}), & -N_q \leq j_x, j_y \leq N_q, \\ \mathbf{p} &= \frac{2\pi}{h_d(2N_{\text{FBZ}}+1)} (k_x \hat{\mathbf{x}} + k_y \hat{\mathbf{y}}), & 0 \leq k_x, k_y \leq N_p - 1, \end{aligned}$$

where N_{FBZ} is the number of points in the FBZ. We take N_q and N_p to be much smaller than N_{FBZ} to control numerical stability at high frequencies. We have found that $N_{\text{FBZ}} = 120$, $N_q = 28$, and $N_p = 7$ are suitable choices. Finally, we note that numerical integration over z is carried out using Simpson's rule, with discretization $z_j = j(L - 2\ell^*)/N_z + \ell^*$ ($j = 0, 1, \dots, N_z$). We take N_z to be 160. The step function regularizer is used. The bar target shown in Fig. 1 has absorption

$$\delta\mu_a(\boldsymbol{\rho}, z) = f(x, y)\delta(z - z_0),$$

where $f(x, y) = 1$ if (x, y) lies in the shaded region and $f(x, y) = 0$ otherwise. We put $L = 6\ell^*$, $z_0 = 3\ell^*$, $h_s = 0.2\ell^*$ and $h_d = 0.1\ell^*$. The reconstructed images are

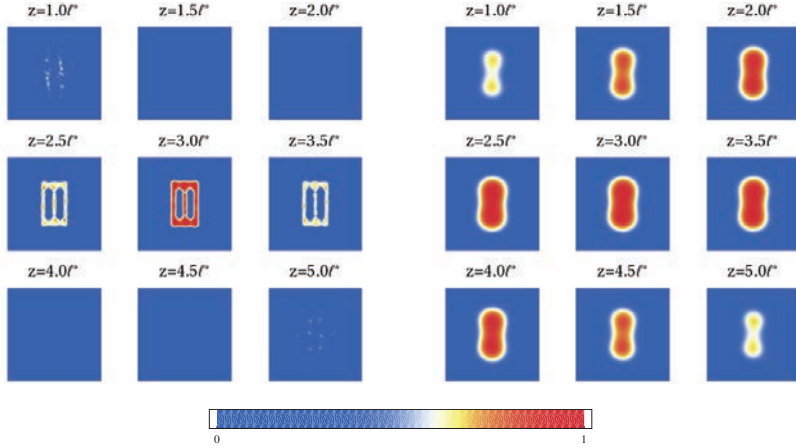


FIGURE 2. The reconstructed $\delta\mu_a/\max(\delta\mu_a)$ of the bar target are shown. The results from the RTE (left) and DE (right) are compared.

shown in Fig. 2. Reconstruction by RTE is compared with reconstruction by the diffusion equation (DE).

3.2. Experimental setup. We assume that only the absorption coefficient depends on $\mathbf{r} = (\boldsymbol{\rho}, z)$.

$$\mu_a(\mathbf{r}) = \bar{\mu}_a + \delta\mu_a(\boldsymbol{\rho}, z).$$

Two experiments are performed. In the first experiment, the (background) reference intensity $I_0(\boldsymbol{\rho}_s, \boldsymbol{\rho}_d)$ is measured. From this, $\bar{\mu}_a$, μ_s , and g are determined. In the second experiment, the target is placed in the slab and the (signal) intensity $I(\boldsymbol{\rho}_s, \boldsymbol{\rho}_d)$ is measured. From this, the data function ϕ is calculated:

$$\phi = G \ln \frac{I_0}{I},$$

where G is the Green's function corresponding to I_0 . Within the Rytov approximation, we have

$$\phi = \int G(\boldsymbol{\rho}_d, \mathbf{r}) \delta\mu_a(\mathbf{r}) G(\mathbf{r}, \boldsymbol{\rho}_s) dr.$$

The experimental setup is shown in Figs. 3 and 4.

We have $(2N_s + 1)^2$ sources and $(2N_d + 1)^2$ detectors.

$$2N_s + 1 = 29, 51, 75, \quad 2N_d + 1 = 397,$$

Before calculating the data function ϕ , we

- shift the origin of the lattice for sources and
- subtract the dark current from I and I_0 .

3.3. Optical properties of Intralipid. The box in Fig. 3 is filled with Intralipid. The table below shows optical properties for Intralipid-10% and the infrared light of $\lambda = 774$ nm.

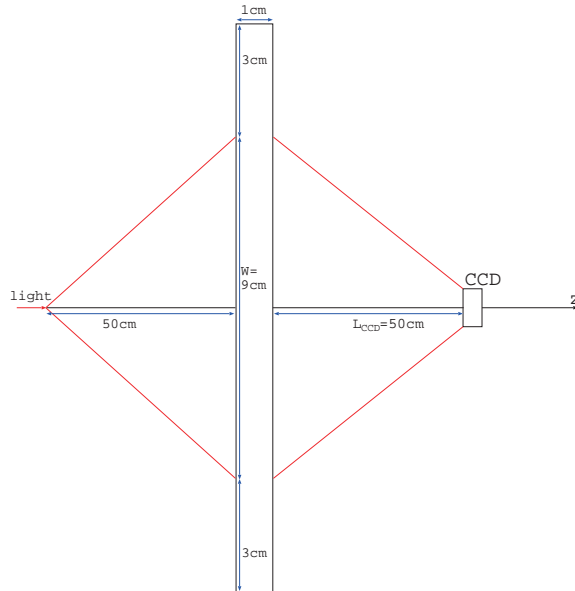


FIGURE 3. The emitted infrared light is detected by the CCD through the slab.

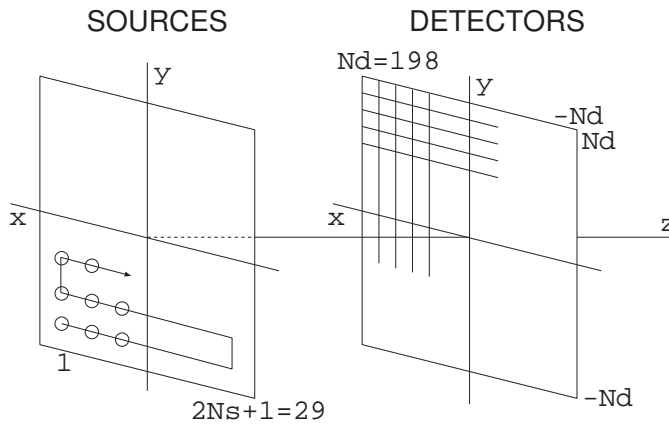


FIGURE 4. Numbering of the sources and coordinates of the detectors in experiments. $h_s = 3.21$ mm and $h_d = 0.363$ mm.

	μ_a (cm^{-1})	μ_s (cm^{-1})	g	μ'_s (cm^{-1})
van Staveren (1991)	-	300	0.65	110
Flock (1992)	-	217	0.802	43.0
Michels (2008)	0.0313	112	0.335	70.8

According to Michels et al. [Optics Express **16** (2008) 5907], g strongly depends on the concentration of Intralipid. They also showed that μ_a for Intralipid-10% is almost identical to μ_a for water in the present wavelength.

Ko et al. [Jpn. J. Appl. Phys. **45** (2006) 7158] compared Moes (1989), Flock (1992), and van Staveren (1991), and concluded that μ_a is well predicted by Flock (1992) and μ'_s is well predicted by van Staveren (1991).

McGlone et al. [Phys. Med. Biol. **52** (2007) 2367] suggested that μ'_s predicted by van Staveren (1991) is larger than the true value.

It is not easy to determine the optical properties of Intralipid. Different results for the laser wave length $\lambda = 633$ nm are compared in the table below.

	Intralipid	μ_a (cm ⁻¹)	μ_s (cm ⁻¹)	g
Flock (1988)	10%	0.11	323	0.675
Moes (1989)	10%	0.57	386	0.71
van Staveren (1991)	10%	0.159	476	0.807
Hielscher (1997)	0.8%	-	29.6	0.76
Jacques (1998)	10%	0.02	630	0.83
Chen (2006)	20%	2.4	420	0.58
Chen (2006)	10%	1.4	300	0.59

The above table is taken from C. Chen, et al., Optics Express **14** (2006) 7420. In the table, Flock is S. T. Flock, Hamilton, Ontario, Canada: McMaster University, 1988; Moes is C. J. M. Moes, et al., Appl. Opt. **28** (1989) 2292; van Staveren is H. G. van Staveren, et al., Appl. Opt. **30** (1991) 4507; Jacques is S. L. Jacques, (Oregon Medical Laser Center, 1998), <http://omlc.ogi.edu/spectra/intralipid/index.html>.

If we estimate the optical properties of Intralipid-1% as $\mu_a = 0.01$ cm⁻¹, $\mu_s = 20$ cm⁻¹, $g = 0.65$, we obtain $\mu'_s = 7$ cm⁻¹ and $\ell^* = 1.4$ mm.

REFERENCES

- [1] Bukhgeim A L and Klibanov M V 1981 Global uniqueness of a class of multidimensional inverse problems *Soviet Math. Dokl.* **24** 244–247
- [2] Klibanov M V and Pamyatnykh S E 2006 Lipschitz stability of a non-standard problem for the non-stationary transport equation via a Carleman estimate *Inverse Problems* **22** 881–90
- [3] Klibanov M V and Pamyatnykh S E 2008 Global uniqueness for a coefficient inverse problem for the non-stationary transport equation via Carleman estimate *J. Math. Anal. Appl.* **343** 352–65
- [4] Machida M, Panasyuk G Y, Schotland J C and Markel V A 2010 The Green’s function for the radiative transport equation in the slab geometry *J. Phys. A: Math. Theor.* **43** 065402
- [5] Machida M, Panasyuk G Y, Wang Z-M, Markel V A and Schotland J C 2016 Radiative transport and optical tomography with large datasets *J. Opt. Soc. Am. A* **33** 551–558
- [6] Machida M and Yamamoto M 2014 Global Lipschitz stability in determining coefficients of the radiative transport equation *Inverse Problems* **30** 035010
- [7] Markel V A 2004 Modified spherical harmonics method for solving the radiative transport equation *Waves Random Media* **14** L13–L19

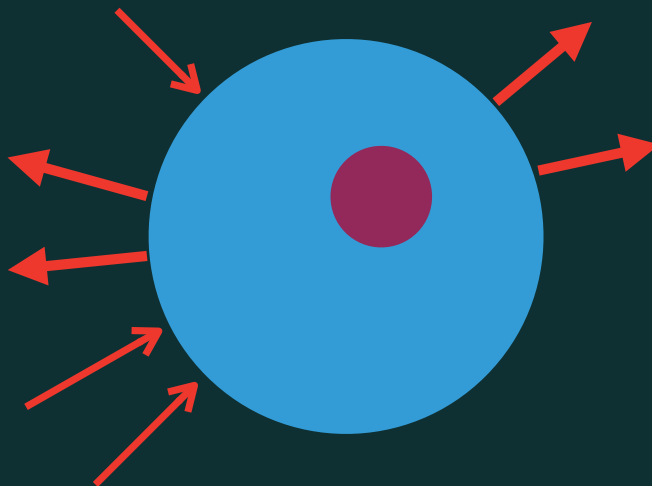
Nondestructive inspection of biological tissue by optical tomography

Manabu Machida
Institute for Medical Photonics Research,
Hamamatsu University School of Medicine, Hamamatsu

*Non-destructive inspection for concrete structures
and related topics*
IMI, Kyushu University, October 24, 2018

1

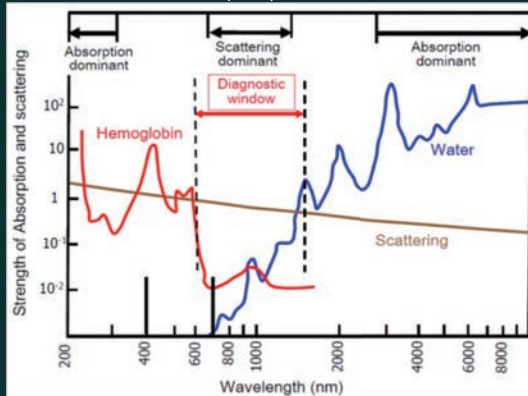
Look inside with near infrared light



2

Optical window

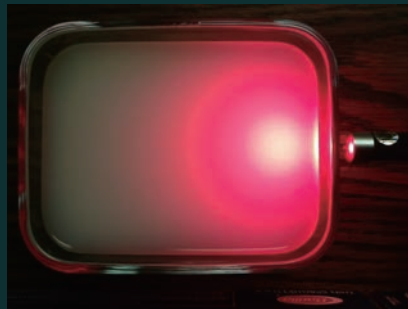
700nm - 1000nm = 1 μ m



Y.Tanikawa, PhD thesis (2014)

3

Strong scattering



Light propagation in biological tissue:
Strong scattering and weak absorption

4

Radiative transport equation (RTE)

The specific intensity $u(x, \theta, t)$, $x \in \Omega \subset \mathbb{R}^3$, $\theta \in \mathbb{S}^2$, $t > 0$.

$$\left\{ \begin{array}{l} \left(\frac{1}{c} \frac{\partial}{\partial t} + \theta \cdot \nabla + \mu_a + \mu_s \right) u - \mu_s \int_{\mathbb{S}^2} \Theta(\theta \cdot \theta') u(x, \theta', t) d\theta' = 0, \\ x \in \Omega, \quad \theta \in \mathbb{S}^2, \quad 0 < t < T, \\ u(x, \theta, t) = g(x, \theta, t), \quad (x, \theta) \in \Gamma_-, \quad 0 < t < T, \\ u(x, \theta, 0) = a(x, \theta), \quad x \in \Omega, \quad \theta \in \mathbb{S}^2. \end{array} \right.$$

$$\Gamma_{\pm} = \{ (x, \theta) \in \partial\Omega \times \mathbb{S}^2; \pm \theta \cdot \nu(x) > 0 \}$$

$\nu(x)$: outer unit normal

$$\mu_a, \mu_s \in L^\infty(\Omega)$$

$$\int_{\mathbb{S}^2} \Theta(\theta \cdot \theta') d\theta = 1$$

5

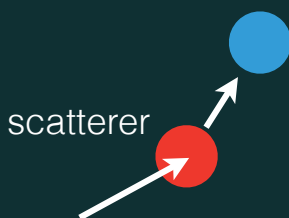
Linear Boltzmann equation

RTE = linear Boltzmann equation

$$\left(\frac{1}{c} \frac{\partial}{\partial t} + \theta \cdot \nabla + \mu_a + \mu_s \right) u - \mu_s \int_{\mathbb{S}^2} \Theta(\theta \cdot \theta') u(x, \theta', t) d\theta' = 0$$

\Leftrightarrow

$$\left(\frac{1}{c} \frac{\partial}{\partial t} + \theta \cdot \nabla + \mu_a \right) u = \mu_s \int_{\mathbb{S}^2} \Theta(\theta \cdot \theta') (u(x, \theta', t) - u(x, \theta, t)) d\theta'$$



collision integral

6

Physical meaning

$$\mu_t(x) = \mu_a(x) + \mu_s(x), \quad \mu_s(x)u(x, \theta) = \mu_s(x) \int_{\mathbb{S}^2} \Theta(\theta' \cdot \theta) u(x, \theta') d\theta'$$

total attenuation

$$\left(\frac{1}{c} \frac{\partial}{\partial t} + \theta \cdot \nabla \right) u(x, \theta) = -\mu_a(x)u(x, \theta) - \mu_s(x) \int_{\mathbb{S}^2} \Theta(\theta' \cdot \theta) u(x, \theta') d\theta' + \mu_s(x) \int_{\mathbb{S}^2} \Theta(\theta, \theta') u(x, \theta') d\theta'$$

loss by absorption

loss by scattering

change

$$-\mu_s(x) \int_{\mathbb{S}^2} \Theta(\theta' \cdot \theta) u(x, \theta') d\theta'$$

$$+\mu_s(x) \int_{\mathbb{S}^2} \Theta(\theta, \theta') u(x, \theta') d\theta'$$

energy balance

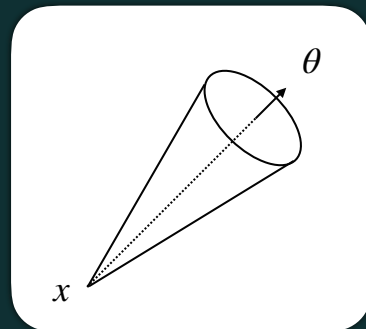
gain by scattering

7

Specific intensity

$u(x, \theta)$ is the Wigner transform of the field
 \approx energy at position x in direction θ per unit area

$$\theta = \begin{pmatrix} \sin \vartheta \cos \varphi \\ \sin \vartheta \sin \varphi \\ \cos \vartheta \end{pmatrix} \in \mathbb{S}^2$$



8

Applications

RTE: Transport phenomena characterized by scattering and absorption

- Light transport in random media such as biological tissue, clouds, fog, interstellar medium
- Light transport for CG
- Neutron transport in nuclear reactors
- Seismic wave
- etc

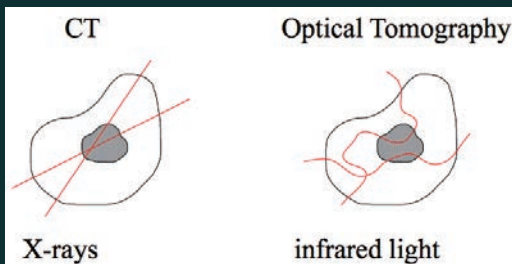


d'Eon and Irving (2011)

9

Medical imaging

CT (computed tomography)	Optical tomography
bones information: <i>anatomy</i>	tissue oxygenation (Hb/HbO ₂) information: <i>function</i>

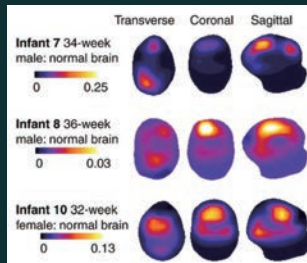


Severely ill-posed inverse problem due to scattering.

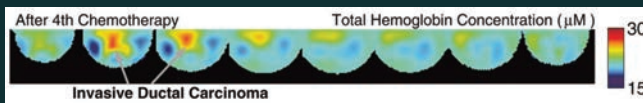
Started around 1990; an old topic, but a good example to study severely ill-posed inverse problems, and still a challenging topic.

10

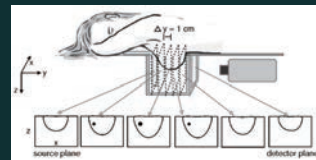
Optical tomography



Austin, et al. (2006)



Choe, et al. (2005)



11

Diffusion approximation

Assume the form $u(x, \theta, t) = u_0(x, t) + \theta \cdot J(x, t)$

or take the asymptotic limit $\epsilon x \rightarrow x, \quad \epsilon^2 \mu_a^{-1} \rightarrow \mu_a^{-1}$

$$\left(\frac{1}{c} \frac{\partial}{\partial t} + \theta \cdot \nabla + \mu_t(x) \right) u(x, \theta, t) - \mu_s(x) \int_{\mathbb{S}^2} \Theta(\theta \cdot \theta') u(x, \theta', t) d\theta' = 0$$



$$g = \int_{\mathbb{S}^2} (\theta \cdot \theta') \Theta(\theta \cdot \theta') d\theta'$$

$$\frac{1}{c} \frac{\partial}{\partial t} u_0(x, t) - \nabla \cdot \left(\frac{1}{3(1-g)\mu_s(x)} \nabla u_0(x, t) \right) + \mu_a(x) u_0(x, t) = 0$$

12

Diffuse optical tomography

The diffusion equation (DE)

$$\frac{1}{c} \frac{\partial}{\partial t} u_0 - \nabla \cdot (D \nabla u_0(x, t)) + \mu_a u_0 = 0$$

is tractable, but RTE

$$\left(\frac{1}{c} \frac{\partial}{\partial t} + \theta \cdot \nabla + \mu_t \right) u = \mu_s \int_{\mathbb{S}^2} \Theta(\theta \cdot \theta') u(x, \theta', t) d\theta'$$

is not. So, DE is used for optical tomography.

13

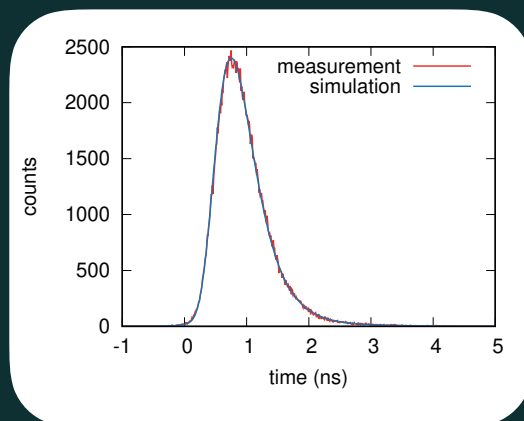
Diffusion approximation

800nm, source-detector distance = 3cm

$$\mu_a = 0.0146 \text{ mm}^{-1}, \quad \mu'_s = (1 - g)\mu_s = 1.04 \text{ mm}^{-1}, \quad n = 1.37$$



TRS80 at Hamamatsu



14

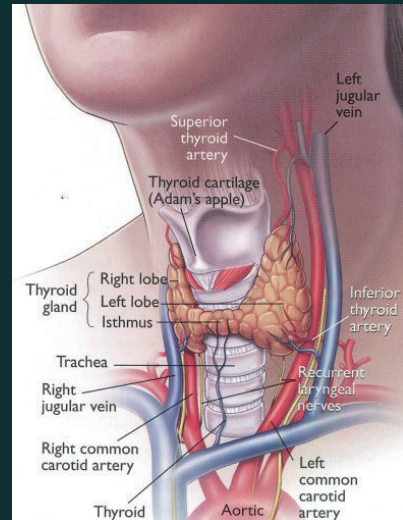
Beyond the diffusion approximation

DE  RTE

Diffusion approximation breaks near the boundary and near the source.

e.g. thyroid cancer

<https://clancy-ent.com.au/>



15

Inverse transport problems

Early stage

Bellman-Kagiyada-Kalaba-Ueno (1965),
Case (1973), McCormick-Kuscer (1974), Siewert (1978),
Kanal-Moses (1978), Larsen (1981), ...

Uniqueness

Choulli-Stefanov (1996, 1999), Stefanov (2003),
Stefanov-Tamasan (2009), ...

Stability

Romanov (1997, 1998), Wang (1999), Tamasan (2002),
Bal-Jollivet (2008), Bal (2008),
Bal-Langmore-Monard (2008), Stefanov-Uhlmann (2003),
Langmore (2008), McDowall-Stefanov-Tamasan (2010),
M.-Yamamoto (2014), ...

16

Transport-based optical tomography

Usually the **diffusion equation** is used for optical tomography except several works.

- O. Dorn (1998)
 - A. D. Klose and A. H. Hielscher (1999)
 - K. Ren, G. Bal, and A. H. Hielscher (2006)
 - S. Wright, M. Schweiger, and S. R. Arridge (2007)
 - T. Tarvainen, M. Vauhkonen, and S. R. Arridge (2008)
 - P. Gonzalez-Rodriguez and A. D. Kim (2009)
 - H. Gao and H. Zhao (2010)
 - M.M., G. Y. Panasyuk, Z.-M. Wang, V. A. Markel, and J. C. Schotland (2016)
 - ...
 - ...
 - etc.
- There are more papers but the number is limited.

17

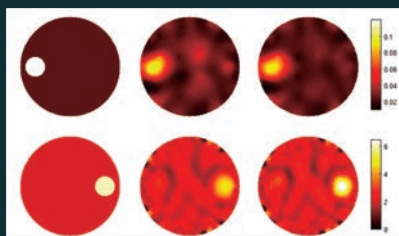
Transport-based OT (numerics)

hybrid: RTE+DE

Tarvainen, Vauhkonen, Kolehmainen, Arridge, and Kaipio,
Physics in Medicine and Biology 50 (2005) 4913-4930

damped Gauss-Newton

Tarvainen, Kolehmainen, Arridge, and Kaipio,
J. Quant. Spec. Rad. Trans. 112 (2011) 2600-2608



Absorption (top row) and scattering (bottom row) distributions within a domain with an absorbing inclusion and a scattering inclusion (case 1). Images from left to right: simulated distributions (first column), reconstructions obtained using the RTE (second column) and the coupled model (third column) as forward models.

18

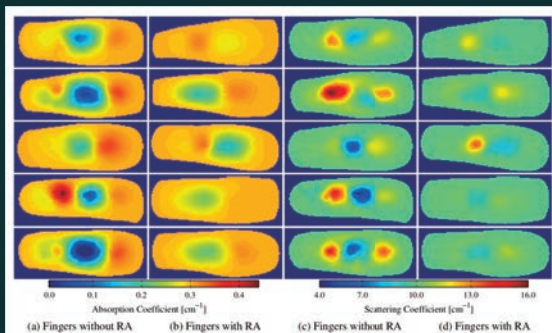
Transport-based OT (experiment)

frequency-domain RTE with SQP algorithm (reduced Hessian)

Kim and Hielscher, *Inverse Problems* 25 (2009) 015010

rheumatoid arthritis

Montejo, Jia, Kim, Netz, Blaschke, Muller, and Hielscher,
Journal of Biomedical Optics 18 (2013) 076001



(a and b) Absorption and (c and d) scattering coronal cross sections of PIP joints from subjects without (a, c) and with RA (b, d). All images are reconstructed from the data obtained with 600 MHz source modulation.

19

Examples

Example 1

M. M. and M. Yamamoto

Global Lipschitz stability in determining coefficients of the radiative transport equation

Inverse Problems **30** (2014) 035010

Example 2

M. M., G. Y. Panasyuk, Z.-M. Wang, V. A. Markel, and J. C. Schotland

Radiative transport and optical tomography with large datasets

J. Opt. Soc. Am. A **33** (2016) 551-558

20

Example 1

M. M. and M. Yamamoto

Global Lipschitz stability in determining coefficients of the radiative transport equation

Inverse Problems **30** (2014) 035010

21

Stability

Uniqueness and stability using the albedo operator:

$$\mathcal{A} : u|_{\Gamma_{-}\times(0,T)} \mapsto u|_{\Gamma_{+}\times(0,T)}$$

Hoelder-type stability is known for the albedo operator.

Our result: global Lipschitz stability from a single input

cf, Klivanov and Pamyatnykh (2008): global uniqueness

22

Carleman estimates

- Bukhgeim and Klivanov (1981): Uniqueness (pioneering work with Carleman estimate)
- Imanuvilov and Yamamoto (2001): Lipschitz stability for an inverse hyperbolic problem

See also

- Yamamoto, *Inverse Problems* (2009)
- Isakov, *Inverse Problems for PDEs* (Springer, 1998)
- Tataru, *J. Math. Pures Appl.* (1996)
-
-

23

Total attenuation term

$i = 1, 2$

$$\left\{ \begin{array}{l} (\partial_t + v \cdot \nabla + \sigma_t^i) u^i(x, v, t) - \sigma_s \int_V p(x, v, v') u^i(x, v', t) dv' \\ \quad = 0, \quad \Omega \times V \times (0, T), \\ u^i(x, v, 0) = a(x, v), \quad \Omega \times V, \\ u^i(x, v, t) = b(x, v, t), \quad \Gamma_- \times (0, T) \end{array} \right.$$

$$\Gamma_{\pm} = \{(x, v) \in \partial\Omega \times V; \pm v \cdot \nu(x) > 0\}$$

We will estimate $\sigma_t^2 - \sigma_t^1$

24

Global Lipschitz stability

Theorem

Suppose $\|u_j\|_{H^1(0,T;L^\infty(\Omega \times V)) \cap H^2(0,T;L^2(\Omega \times V))} \leq M$,

$\|\nabla u_j\|_{H^1(0,T;L^2(\Omega \times V))} \leq M$, and $\|\sigma_t^j\|_{L^\infty(\Omega \times V)} \leq M$, $\|\sigma_s\|_{L^\infty(\Omega \times V)} \leq M$.

Let $a(x, \nu) > 0$ on $\overline{\Omega \times V}$ and assume T is large.

Then there exists $C = C(M) > 0$ such that

$$C^{-1} \left(\int_{\Gamma_+} \int_0^T (\nu \cdot \nu) \left| \partial_t(u_2 - u_1) \right|^2 dS dv dt \right)^{\frac{1}{2}} \leq$$

$$\|\sigma_t^2 - \sigma_t^1\|_{L^2(\Omega \times V)} \leq C \left(\int_{\Gamma_+} \int_0^T (\nu \cdot \nu) \left| \partial_t(u_2 - u_1) \right|^2 dS dv dt \right)^{\frac{1}{2}}$$

25

Remarks

- The lower bound: forward problem <- **Energy estimate**
- The upper bound: inverse problem <- **Carleman estimate**
- The both-side estimate with the same norm:
Our result is the best possible estimate.

- $a(x, \nu) > 0$ in $\overline{\Omega \times V}$ is necessary

- $\gamma \cdot \nu$ must be positive \longrightarrow new idea??

26

Subtraction

$$y(x, v, t) = u_2 - u_1 = u[\sigma_t^2](x, v, t) - u[\sigma_t^1](x, v, t).$$

$$f(x, v) = \sigma_t^1(x, v) - \sigma_t^2(x, v), \quad R(x, v, t) = u_2(x, v, t).$$

We have

$$\begin{cases} \partial_t y + v \cdot \nabla y + \sigma_t^1 y - \sigma_s \int_V p(x, v, v') y(\cdot, v', \cdot) dv' \\ = f(x, v) R(x, v, t), & x \in \Omega, v \in V, 0 < t < T, \\ y(x, v, 0) = 0 & \text{in } \Omega \times V, \\ y = 0 & \text{on } \Gamma_- \times (0, T). \end{cases}$$

27

Inverse source problem

$$\begin{aligned} C^{-1} \left(\int_{\Gamma_+} \int_0^T (\nu \cdot \nu) |\partial_t u|^2 dS dv dt \right)^{\frac{1}{2}} &\leq \|f\|_{L^2(\Omega \times V)} \\ &\leq C \left(\int_{\Gamma_+} \int_0^T (\nu \cdot \nu) |\partial_t u|^2 dS dv dt \right)^{\frac{1}{2}} \end{aligned}$$



Let us consider the inverse problem.

$$\|f\|_{L^2(\Omega \times V)} \leq C \left(\int_{\Gamma_+} \int_0^T (\nu \cdot \nu) |\partial_t u|^2 dS dv dt \right)^{\frac{1}{2}}$$

28

Conditions

We write the transport equation as $Pw = fR$

$$Pw \equiv \partial_t w + v \cdot \nabla w + \sigma_t w - \sigma_s \int_V p(x, v, v') w(\cdot, v', \cdot) dv'$$

Note that $v \in V$ satisfies $\gamma \cdot v \geq \theta$, where

$$\gamma \in \mathbb{R}^d, \neq 0 \text{ and } \theta > 0$$

$$T > \frac{\max_{x \in \overline{\Omega}}(\gamma \cdot x) - \min_{x \in \overline{\Omega}}(\gamma \cdot x)}{\min_{v \in \overline{V}}(\gamma \cdot v)}$$

29

Carleman estimate

L^2 -weighted inequality

We set the weight function as

$$\varphi(x, t) = (\gamma \cdot x) - \beta t$$

There exists $C > 0$ such that ($Q = \Omega \times (0, T)$)

$$\begin{aligned} & s \int_{\Omega} \int_V |u(x, v, 0)|^2 e^{2s\varphi(x, 0)} dv dx + s^2 \int_Q \int_V |u(x, v, t)|^2 e^{2s\varphi(x, t)} dv dx dt \\ & \leq C \int_Q \int_V |Pu|^2 e^{2s\varphi(x, t)} dv dx dt + s \int_0^T \int_{\Gamma_+} (\nu \cdot v) |u|^2 e^{2s\varphi(x, t)} dS dv dt, \end{aligned}$$

for sufficiently large s and $u \in H^1(0, T; L^2(\Omega \times V))$,

$$\nabla u \in L^2(\Omega \times V \times (0, T)), \quad u(\cdot, \cdot, T) = 0 \text{ in } \Omega \times V$$

30

Example 2

M. M., G. Y. Panasyuk, Z.-M. Wang, V. A. Markel, and J. C. Schotland

Radiative transport and optical tomography with large datasets

J. Opt. Soc. Am. A **33** (2016) 551-558

31

Time-independent RTE

$$\begin{cases} (\theta \cdot \nabla + \mu_a + \mu_s) u = \mu_s \int_{\mathbb{S}^2} \Theta(\theta \cdot \theta') u(x, \theta') d\theta', & x \in \Omega, \theta \in \mathbb{S}^2, \\ u(x, \theta) = g(x, \theta), & (x, \theta) \in \Gamma_- . \end{cases}$$

Assume absorption inhomogeneity

$$\mu_a(x) = \bar{\mu}_a + \delta\mu_a(x), \quad \mu_s(x) = \bar{\mu}_s$$

Determine $\delta\mu_a(x)$ from boundary measurements $u|_{\Gamma_+}$

$$\begin{cases} (\theta \cdot \nabla + \bar{\mu}_a + \bar{\mu}_s) u_0 = \bar{\mu}_s \int_{\mathbb{S}^2} \Theta(\theta \cdot \theta') u_0(x, \theta') d\theta', & x \in \Omega, \theta \in \mathbb{S}^2, \\ u_0(x, \theta) = g(x, \theta), & (x, \theta) \in \Gamma_- . \end{cases}$$

32

Born series

$$\begin{aligned}
 u(x, \theta) &= u_0(x, \theta) - \int_{\mathbb{S}^2} \int_{\Omega} G(x, \theta; x', \theta') \delta\mu_a(x') u(x', \theta') dx' d\theta' \\
 &= u_0(x, \theta) - \int_{\mathbb{S}^2} \int_{\Omega} G(x, \theta; x', \theta') \delta\mu_a(x') u_0(x', \theta') dx' d\theta' + \dots
 \end{aligned}$$

where

$$\begin{cases}
 (\theta \cdot \nabla + \bar{\mu}_a + \bar{\mu}_s) G = \bar{\mu}_s \int_{\mathbb{S}^2} \Theta(\theta \cdot \theta') G(x\theta'; x_0, \theta_0) d\theta' \\
 \quad \quad \quad + \delta(x - x_0) \delta(\theta - \theta_0), \quad x \in \Omega, \theta \in \mathbb{S}^2, \\
 G(x, \theta; x_0, \theta_0) = 0, \quad (x, \theta) \in \Gamma_-.
 \end{cases}$$

33

Inverse Born series

$$\phi(x, \theta) = u_0(x, \theta) - u(x, \theta)$$

$$\phi = K_1 \delta\mu_a + K_2 \delta\mu_a \otimes \delta\mu_a + \dots \quad \longrightarrow \quad \text{Born series}$$

$$\delta\mu_a = \mathcal{K}_1 \phi + \mathcal{K}_2 \phi \otimes \phi + \dots \quad \longrightarrow \quad \text{inverse Born series}$$

$$\mathcal{K}_1 = (K_1)_{\text{reg}}^+$$

$$\mathcal{K}_2 = -\mathcal{K}_1 K_2 \mathcal{K}_1 \otimes \mathcal{K}_1,$$

$$\mathcal{K}_j = - \left(\sum_{m=1}^{j-1} \mathcal{K}_m \sum_{i_1 + \dots + i_m = j} K_{i_1} \otimes \dots \otimes K_{i_m} \right) \mathcal{K}_1 \otimes \dots \otimes \mathcal{K}_1$$

M. and Schotland, Inverse Problems **31** (2015) 095009

34

Method or rotated reference frames (1)

$$\delta\mu_a \approx \mathcal{K}_1 \phi = (K_1)_{\text{reg}}^+ \phi.$$

$$K_1 \delta\mu_a = \int_{\mathbb{S}^2} \int_{\Omega} G(x, \theta; x', \theta') \delta\mu_a(x') G(x', \theta'; x_0, \theta_0) dx' d\theta',$$

$$\text{when } g(x, \theta) = \delta(x - x_0) \delta(\theta - \theta_0).$$



idea: superposition of eigenmodes

$$G(x, \theta; x_0, \theta_0) = \sum_{\gamma} A_{\gamma}(x_0, \theta_0) \psi_{\gamma}(x, \theta).$$

$$(\theta \cdot \nabla + \bar{\mu}_a + \bar{\mu}_s) \psi_{\gamma}(x, \theta) = \bar{\mu}_s \int_{\mathbb{S}^2} \Theta(\theta \cdot \theta') \psi_{\gamma}(x, \theta') d\theta'.$$

$A_{\gamma}(x_0, \theta_0)$ are obtained from boundary conditions.

35

Method or rotated reference frames (2)

Henye-Greenstein model

$$\Theta(\theta \cdot \theta') = \frac{1 - g^2}{4\pi (1 + g^2 - 2g \cos(\theta \cdot \theta'))^{3/2}}$$

$$= \sum_{l=0}^L \sum_{m=-l}^l g^l Y_{lm}(\theta) Y_{lm}^*(\theta').$$

$$\theta = \begin{pmatrix} \sin \vartheta \cos \varphi \\ \sin \vartheta \sin \varphi \\ \cos \vartheta \end{pmatrix},$$

$$\vartheta \in [0, \pi],$$

$$\varphi \in [0, 2\pi)$$

$$g \in (-1, 1) \quad g = \int_{\mathbb{S}^2} (\theta \cdot \theta') \Theta(\theta \cdot \theta') d\theta'$$

$g \approx 0.9$ in biological tissue

Spherical harmonics:

$$Y_{lm}(\theta) = Y_{lm}(\vartheta, \varphi) = \sqrt{\frac{2l+1}{4\pi} \frac{(l-m)!}{(l+m)!}} P_l^m(\cos \vartheta) e^{im\varphi}$$

36

Method or rotated reference frames (3)

idea: Rotate the reference frame in the direction of the Fourier vector.

$$\psi_\gamma(x, \theta) = \mathcal{R}_{\hat{k}(\nu, q)} \Phi_\nu^m(\theta) e^{-\hat{k}(\nu, q) \cdot x \nu}$$

$$Y_{lm}(\theta) \rightarrow \mathcal{R}_{\hat{k}} Y_{lm}(\theta) = \sum_{m'=-l}^l D_{m'm}^l(\varphi_{\hat{k}}, \vartheta_{\hat{k}}, 0) Y_{lm'}(\theta)$$

Wigner's D-matrices

- 1964 Dede (Nukleonik)
- 1977 Kobayashi (J. Nucl. Sci. Technol.)
- 2004 Markel (Waves Random Media) -> MRRF
- 2014 M. (J. Opt. Soc. Am. A) -> analytical solution
- 2015 M. (J. Phys. A) -> 3dFN

37

Reconstruction (1)

Moore-Penrose pseudoinverse:

$$K_1^+ = K_1^\dagger (K_1 K_1^\dagger)^{-1}, \quad K_1^\dagger = \overline{K_1}^T$$

Singular value decomposition

$$K_1 = U \Sigma V^\dagger, \quad \Sigma = \text{diag}(\sigma_1, \sigma_2, \dots), \quad U = (v_1, v_2, \dots)$$

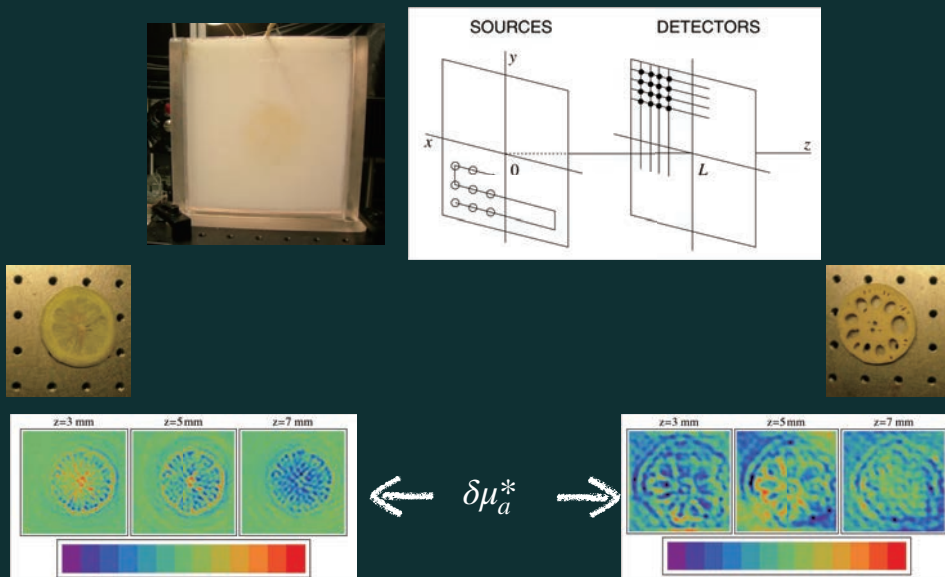
$$(K_1)_{\text{reg}}^+ = K_1^\dagger (v_1 \ v_2 \ \dots) \begin{pmatrix} (\sigma_1^2 + \alpha)^{-1} & & \\ & (\sigma_2^2 + \alpha)^{-1} & \\ & & \ddots \end{pmatrix} (v_1 \ v_2 \ \dots)^\dagger$$

α is the regularization parameter

$$\delta\mu_a^* = \mathcal{K}_1 \phi = (K_1)_{\text{reg}}^+ \phi$$

38

Reconstruction (2)



39

Summary

Optical tomography: old and new topic

Optical tomography: Inverse problems for the diffusion equation and the radiative transport equation

40

Exact probe of the reinforcing steel in RC structures by application of ultrasonic CT

Toshiaki Takabatake

West Nippon Expressway Engineering Shikoku Company Limited
3-1-1 Hanazono-cho, Takamatsu-shi, Kagawa 760-0072, Japan
Email: toshiaki.takabatake@w-e-shikoku.co.jp

We describe the development of a non-destructive inspection method for detecting the precise position of the reinforcing steel in reinforced concrete structures, which is recognized as a difficult problem for the time being. For the development of our method to probe the reinforcing steel, we apply an ultrasonic CT technique suggested by Mita-Takiguchi [1]. In our theory, the idea of “the least square solutions” plays an important role.

Key Words: non-destructive, ultrasonic, the least square solutions

1. Introduction

Highways are formed by various structures such as cuts, embankments, tunnels, bridges, etc. Regarding bridges, there are two kinds of bridges, concrete bridge and steel bridge. On the Shikoku expressway, the total length of the concrete bridge is about 118 km and that of the steel bridge is about 46 km. In general it is said that the lifetime of concrete is about 50 years, it varies greatly depending on conditions such as climate. It is very important to know how much the structure is deteriorating for maintaining highways.

There are two methods for inspecting bridges. One is a non-destructive inspection that does not damage the structure, and the other is a micro-destructive one in which samples are collected by slightly damaging the structure and tested. Although we repair parts damaged by micro-destructive inspection, it tends to be weak parts of structures, so it is desirable to be able to inspect nondestructively. In order to keep the structure healthy, we need a non-destructive inspection method to ascertain the deterioration situation inside the concrete.

2. Reinforced Concrete Bridge

2.1 Mechanism of reinforced concrete

Reinforced concrete (RC) refers to concrete with reinforcing bars inside. In RC, rebar plays a very important role. There are three main roles as follows (Figure-1).

- A) Rebar bears the tensile stress degree.
- B) Rebar bears a part of compressive stress degree.
- C) Rebar bears the shear stress.

Concrete solidifies by hydration reaction between cement and water. As a result, calcium hydroxide is produced and concrete has a high alkalinity (pH 12 to 13). Therefore, in the high alkalinity, a dense passive film is formed on the surface of the rebar and the progress of rust is prevented.

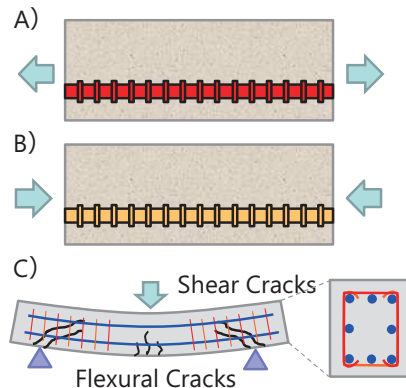


Figure-1 Role of rebar

2.2 Cause of concrete deterioration

Causes of deterioration of concrete include (1) carbonation of concrete, (2) chloride attack, (3) alkali aggregate reaction, and (4) frost damage (Figure-2).

(1) carbonation of concrete

Calcium hydroxide in concrete reacts with carbon dioxide to form calcium carbonate, which gradually loses its alkalinity. If alkalinity is lost, a passive film will not be formed and the rebar will corrode.

(2) chloride attack

When the concentration of chloride ion in concrete becomes higher than a certain level, the passive film is destroyed.

(3) alkali aggregate reaction

Chemical reaction is caused between alkali hydroxide (KOH, NaOH, etc.) and alkali reactive minerals in aggregate, and then cracks occur due to swelling accompanying water absorption of reaction products.

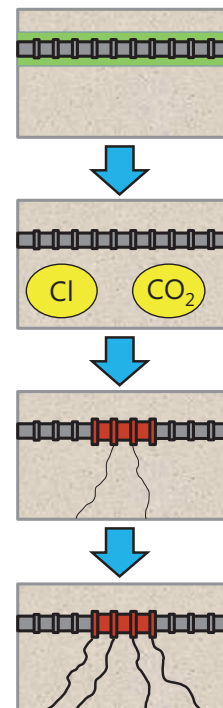


Figure-2 Progress of degradation

(4) frost damage

It is caused by freezing expansion of moisture in concrete, and concrete gradually deteriorates due to repetition of freezing and melting over many years.

In particular, there are many deterioration due to carbonation of concrete(1) and chloride attack(2). In the winter, salt is sprayed on the expressway to prevent the road surface from freezing. If the Expansion device is damaged, salt water will flow out from the end of the girder, causing salt damage on the bottom of the girder as well.

2.3 Repair of damaged part

If the damaged part remains, the damage will spread further. If it is not damaged up to the reinforcing bars, concrete structure can be kept in a healthy condition by repairing, which will extend the lifetime of the structure. The damaged part is chipped from the surface layer, and the cross section is repaired by using repair material.

In order not to damage the rebar when chipping concrete, it is important to know in advance where the reinforcing bar is and whether the cover part is healthy or not.

3. Exploration of rebar with ultrasonic waves

3.1 Propagation of ultrasonic waves

In order to grasp the position of the reinforcing bar inside the concrete nondestructively and to investigate whether the cover part is healthy or not, we consider the method of exploration inside concrete using ultrasonic waves. Ultrasonic waves have the following properties.

- Ultrasonic waves are superior in rectilinear propagation and are transmitted through gases, liquids, solids and other media, however they do not transmit in vacuum.
- The propagation speed of ultrasonic waves varies depending on the substance, and the harder the object, the faster the propagation speed.

Figure-3 schematically shows ultrasonic waves propagating in reinforced concrete. V is the velocity of ultrasonic propagation in the reinforcing bar, v is that in the concrete, Q_i is the point at which the propagation of ultrasonic waves change from reinforcing bars to concrete, and t_i is the time of ultrasonic propagation from the point O to the point P_i via the point O_i . Comparing the route from the point O to the point P_0 and the route from the point O to the point P_1 , the

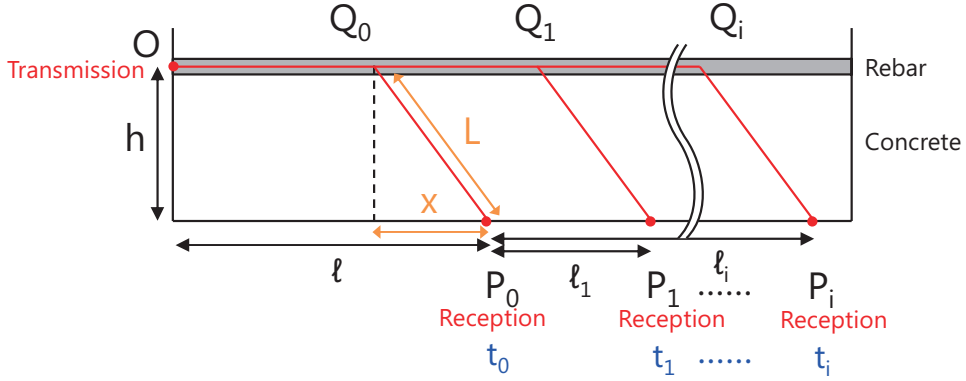


Figure-3 Propagation of ultrasonic waves

distance L propagating through the concrete is equal, so the route difference is found to be the distance l_1 . At this time, since the ultrasonic waves propagate through the reinforcing bars, V can be expressed by equation (1).

$$V = \ell_i (t_i - t_0) \quad (1)$$

If V is calculated using actually measured data, there are variations due to the measurement error, so V is determined using the least squares solution. $\Phi(V)$ is the sum of the square of the difference between the calculated path difference and the actual path difference. $\Phi(V)$ can be expressed by equation (2).

$$\Phi(V) = \sum (V(t_i - t_0) - \ell_i)^2 \quad (2)$$

When V has one solution, $\Phi'(V) = 0$, therefore we get equation (3).

$$\Phi'(V) = \sum (V(t_i - t_0)^2 - \ell_i(t_i - t_0)) = 0 \quad (3)$$

From this, V can be obtained by equation (4).

$$V = \frac{\sum \ell_i (t_i - t_0)}{\sum (t_i - t_0)^2} \quad (4)$$

Next, we consider the propagation time from point O to point P . From the propagation speed and the propagation path in the rebar and concrete, the propagation time from point O to point P can be expressed by equation (5).

$$g(x) = \frac{\ell - x}{V} + \frac{\sqrt{h^2 + x^2}}{v} \quad (5)$$

To minimize $g(x)$, we find x that $g'(x) = 0$.

$$g'(x) = -\frac{1}{V} + \frac{x^2}{v\sqrt{h^2 + x^2}} = 0 \quad (6)$$

When equation (6) is rearranged with respect to x , equation (7) is obtained, and equation (8) is obtained from the Triassic theorem.

$$x = \frac{vh}{\sqrt{V^2 - v^2}} \quad (7)$$

$$h = \frac{Vh}{\sqrt{V^2 - v^2}} \quad (8)$$

3.2 Theoretical study on accurate exploration of rebar

Next we establish a theory to detect the exact position of the rebar. As its foothold, we find the end point of the rebar. Finding the end points of reinforcing bars is very important to know the structure of reinforcing bars inside concrete. However, it is difficult to do it with existing non-destructive inspection method.

As a simple model of the structure, we consider a rectangular parallelepiped concrete block containing one reinforcing bar as shown in Figure-4. To calculate the coordinates, set the X , Y , and Z axes as shown in the figure. The ultrasonic waves traveling from the transmitting point "a" to the receiving point (X_0, Y_0, Z_0) and (X_1, Y_1, Z_1) follow the same path from the point "a" until the point "b". Therefore, the difference in propagation time from point "a" to these two points is due to the path difference from point "b" to these two points. Further, we increase the number of reception points and create simultaneous equations like (9). By

$$\begin{cases} (x - x_0)^2 + (y - y_0)^2 + (z - z_0)^2 = (r + r_0)^2 & \text{※}(r_0 = 0) \\ (x - x_1)^2 + (y - y_1)^2 + (z - z_1)^2 = (r + r_1)^2 \\ \vdots \\ (x - x_i)^2 + (y - y_i)^2 + (z - z_i)^2 = (r + r_i)^2 \\ (x - x_j)^2 + (y - y_j)^2 + (z - z_j)^2 = (r + r_j)^2 \end{cases} \quad (9)$$

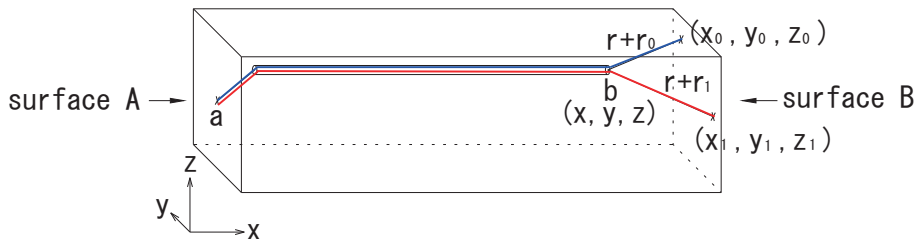


Figure-4 A cuboid test piece

solving this equation, the coordinates of point “b” can be found.

Since the unknown number to be obtained is three of x, y, z, when the number of reception points is more than three points, equation (9) is overdetermined. As measurements include errors and noise, there is rarely a single answer. There, we eliminate the influence of error and noise by using least squares solution. It is difficult to give a unique least-squares solution in equation (9), so we subtract the i-th expression from the j-th expression and obtain equation (10)~(12).

$$\begin{aligned} -2(x_j - x_i)x - 2(y_j - y_i)y - 2(z_j - z_i)z - 2(r_j - r_i)r \\ = -(x_j^2 - x_i^2) - (y_j^2 - y_i^2) - (z_j^2 - z_i^2) + (r_j^2 - r_i^2) \end{aligned} \quad (10)$$

$$\begin{cases} a_k = -2(x_j - x_i) \\ b_k = -2(y_j - y_i) \\ c_k = -2(z_j - z_i) \\ d_k = -2(r_j - r_i) \\ S_k = -(x_j^2 - x_i^2) - (y_j^2 - y_i^2) - (z_j^2 - z_i^2) + (r_j^2 - r_i^2) \end{cases} \quad (11)$$

$$a_k x + b_k y + c_k z + d_k r = S_k \quad (12)$$

At this time, there are $j \times (j-1) / 2$ number of k. When $K = 1, 2, \dots, j \times (j-1) / 2$, equation (12) can be expressed by equation (13) and equation (14).

$$\begin{pmatrix} a_1 & b_1 & c_1 & d_1 \\ a_2 & b_2 & c_2 & d_2 \\ \vdots & \vdots & \vdots & \vdots \\ a_k & b_k & c_k & d_k \end{pmatrix} \begin{pmatrix} x \\ y \\ z \\ r \end{pmatrix} = \begin{pmatrix} S_1 \\ S_2 \\ \vdots \\ S_k \end{pmatrix} \quad (13)$$

$$Ax = S \quad (14)$$

Equation (15) is obtained by multiplying both sides of equation (14) by the transposed matrix of A from the left.

$${}^t AAx = {}^t AS \quad (15)$$

By this, ${}^t AA$ is 4×4 matrix, ${}^t AS$ is 4×1 matrix, which can be easily calculated.

4. Experimental verification

4.1 Preparation of specimen

In order to verify whether the end point of the rebar can be actually obtained, we prepare a specimen and measure ultrasonic waves. As shown in Figure-5,

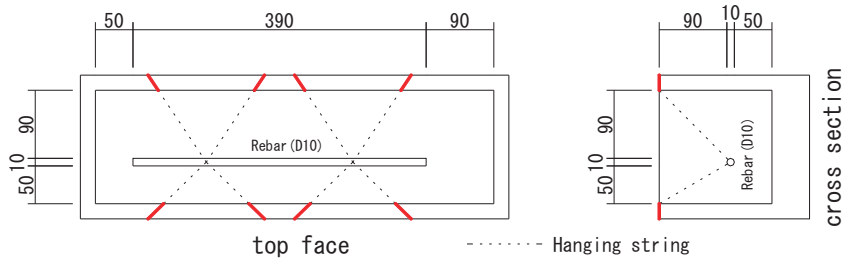


Figure-5 Formwork of test piece

we prepare a 150 x 150 x 530 mm formwork and place the reinforcing bars using threads. Then we pour liquid concrete into this formwork, and prepare test specimens.

4.2 Ultrasonic measurement

Figure-6 shows the measurement points of ultrasonic waves to be measured. The specimen is divided into 5 cm squares and its center is set as the measurement point. This measurement points are designed to develop ultrasonic CT, and this time, end points are calculated using some of these data.

Firstly, we calculate the propagation velocity (v) in concrete. From the data of the route not passing through the rebar (for instance, send from A-9 and receive on B-9 etc.), we find v by using the least squares solution. As a result of calculation using 32 pieces of data, the value of $v = 5,088.4$ [m / s] was able to

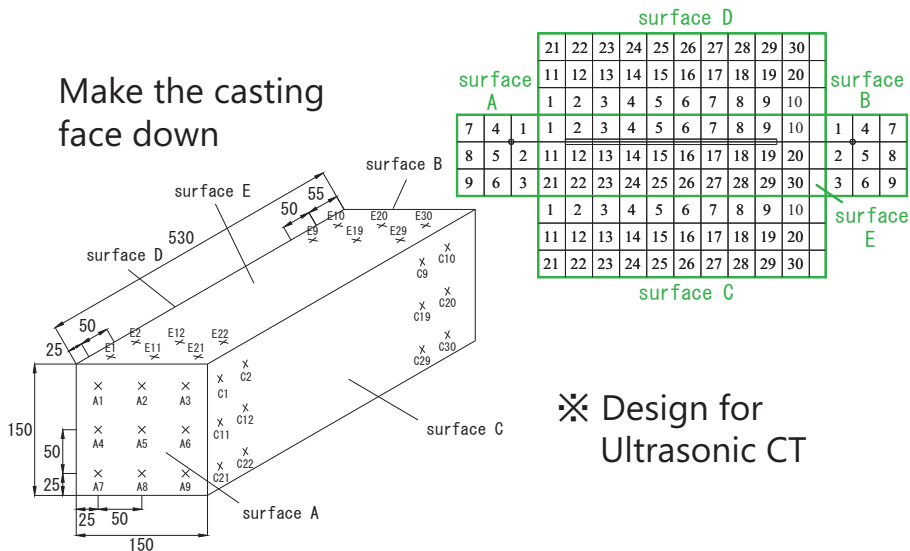


Figure-6 Ultrasonic measurement point

be obtained. This value is considerably high as the propagation speed in concrete. It seems that limestone in which ultrasonic waves propagate quickly was used as a material. Next, we find the end point of the reinforcing bar on the A side. Four points (B - 1, B - 2, B - 4, B - 5) on the B side are set as transmission points and eight points (A - 1, A - 2, A - 4, A - 5, D - 1, D - 11, E - 1, E - 11) of the A, D and E side are set as reception points. We measured a total of 32 data.

4.2 Calculation of end point coordinate

We calculate from 32 data using the calculation formula in Chapter 3 to obtain the matrix in Table-1. From this matrix and equation (15), the simultaneous equations in Table-2 are obtained. Solving this, $X = 56 \text{ mm}$, $Y = 100 \text{ mm}$, and $Z = 100 \text{ mm}$.

In addition, the specimen was cut as shown in Figure-7 and the coordinates of the actual rebar was measured. The measurement result was $X = 51 \text{ mm}$, $Y = 100 \text{ mm}$, $Z = 100 \text{ mm}$. When compared with the value obtained by calculation, a deviation of 5 mm occurred in the X coordinate, but accurate values could be

Table-1 Matrix calculation result

Matrix: tAA				Matrix: tAS
0.64	0.64	0.64	-0.7335437	0.15070235
0.64	3.84	-0.64	-0.627705	0.34523312
0.64	-0.64	3.84	-1.0722276	0.33704841
-0.7335437	-0.627705	-1.0722276	0.89263274	-0.1951307

Table-2 Simultaneous equations

①	$0.64 X +$	$0.64 Y +$	$0.64 Z +$	$-0.733543744 R =$	0.150702353
②	$0.64 X +$	$3.84 Y +$	$-0.64 Z +$	$-0.627705024 R =$	0.345233122
③	$0.64 X +$	$-0.64 Y +$	$3.84 Z +$	$-1.072227648 R =$	0.337048409
④	$-0.733543744 X +$	$-0.627705024 Y +$	$-1.072227648 Z +$	$0.892632735 R =$	-0.195130653

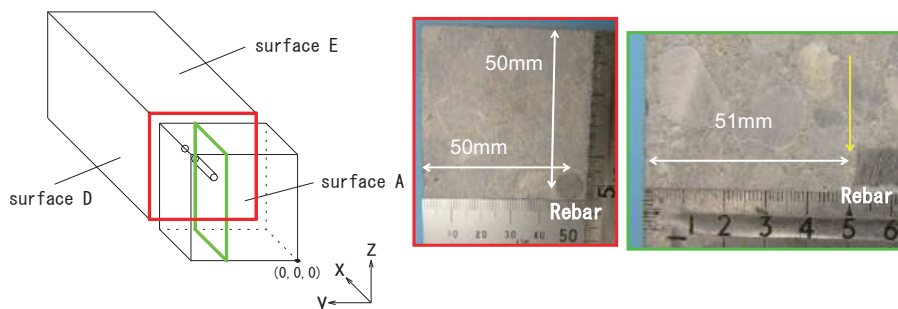


Figure-7 Cutting of test piece

obtained for the Y and Z coordinates.

5. Summary

In this study, we attempted to locate rebar with data for CT. A deviation of 5 mm occurred in the X coordinate, but accurate values could be obtained for the Y and Z coordinates. In the future, we will prepare a measurement plan of ultrasonic waves for exploring the reinforcing bars and investigate to more precisely locate the rebar positions.

The advantage of this method is that, unlike in the electromagnetic induction method, the correction is not required to find the endpoints of rebar. This method is also applicable to actual structures. If we know the position of the rebar, we can calculate the speed of the ultrasonic wave in the cover part and we can know whether there is any abnormality there. Ultimately, we are aiming to complete ultrasonic CT.

Acknowledgments

The author thanks to the discussions at 2018 IMI Joint Use Research Program Workshop (II) "Non-destructive inspection for concrete structures and related topics". This work is based on some discussion.

Reference

- [1] Mita, N. and Takiguchi, T. : Principle of ultrasonic tomography for concrete structures and non-destructive inspection of concrete cover for reinforcement, Pacific Journal of Mathematics for Industry, (2018) 10:6.

Exact probe of the reinforcing steel in RC structures by application of ultrasonic CT



West Nippon Expressway Shikoku Company Limited.

Road structure



Tunnel



Cut

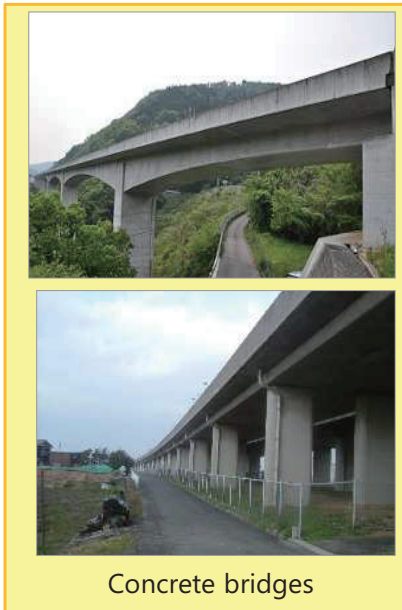


Embankment



Bridge

Highway bridge



Concrete bridges

In Shikoku

118km



Steel bridges

46km

2

Introduction

<Old aged social infrastructure>

- Understand deterioration situation
- Reliable repair

Non destructive test

- Infrared investigation
- Concrete covering depth for reinforcing steel inspection
- Strength estimation by test hammering

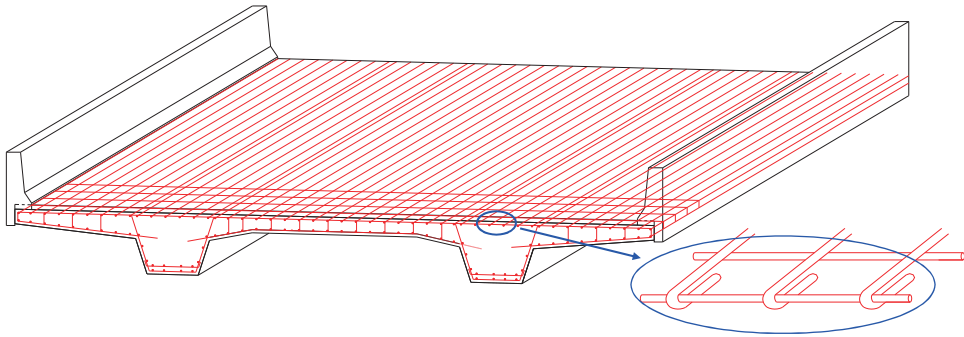
Microfracture test

- Compressive strength test
- Measurement of neutralization depth
- Determination of chloride ion content in concrete

It is necessary to have a diagnostic technique to ascertain the deterioration situation inside the concrete which causes peeling.

3

Concrete bridge and reinforcing steels



This figure shows a part of the reinforcing steels (rebars) used for concrete bridges.

Ex) Concrete bridge with a length of 35 m

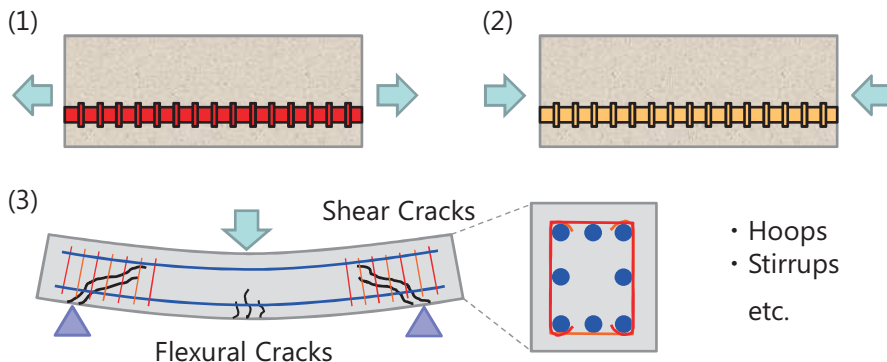
Construction type	Concrete (2.3t/m ³)	Reinforcing steels (7.87t/m ³)
Superstructure	303.9 m ³	27.56 t
Substructure	493.4 m ³	53.42 t

4

Role of rebar

The coefficients of thermal expansion of reinforcing bars and concrete are almost equal.

- (1) Rebar bears the tensile stress degree.
- (2) Rebar bears a part of compressive stress degree.
- (3) Rebar bears the shear stress.



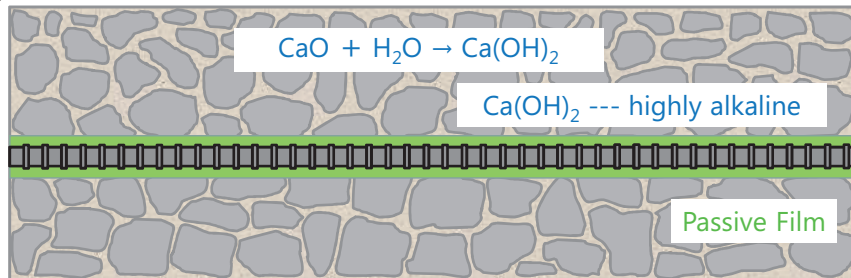
5

Internal structure of RC

<Material of RC structure>

Water, Cement, Aggregate(Gravel, Sand) , Rebar

It solidifies by hydration reaction between cement and water.
A dense passive film is formed on the surface of the rebars in high alkalinity (pH 12 to 13), and the progress of rust is prevented.

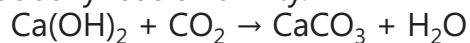


6

Cause of concrete deterioration

- Carbonation of concrete

Calcium hydroxide reacts with carbon dioxide and gradually becomes calcium carbonate, gradually lose alkalinity.



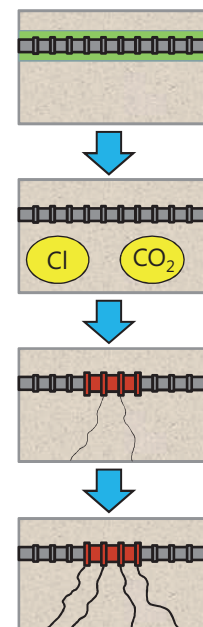
- Chloride attack

When the chloride ion concentration becomes higher than a certain level, the passive film is destroyed.

- Alkali-aggregate reaction

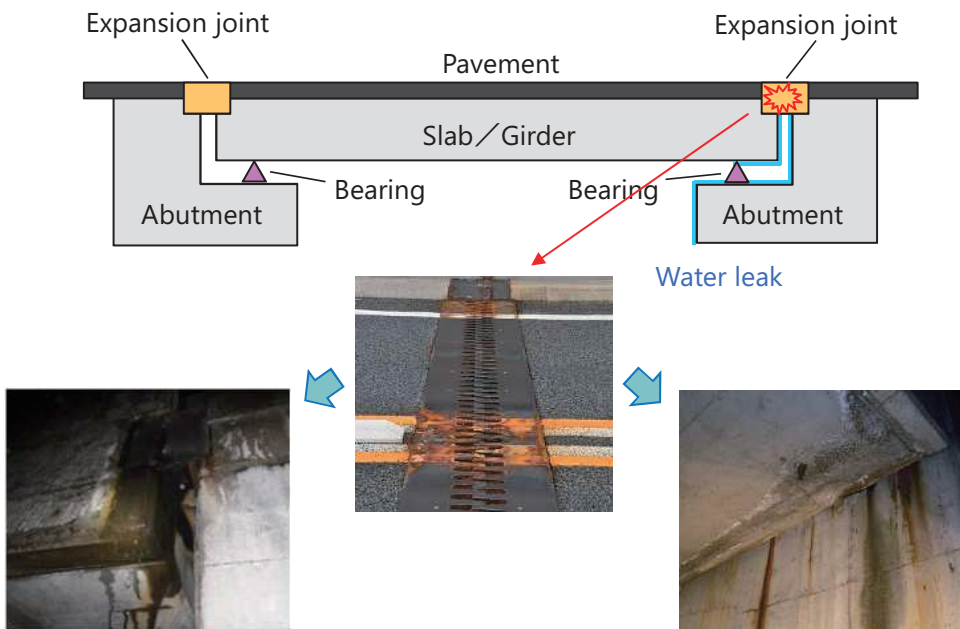
Means a chemical reaction between an alkali hydroxide (KOH, NaOH, etc.) and an alkali-reactive inorganic substance in the aggregate.

- Frost damage



7

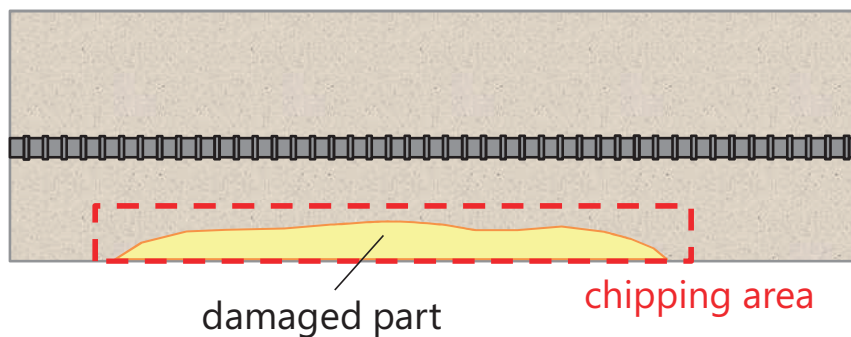
Salt damage caused by water leak



8

Repair of damaged part

- Chipping the surface layer of the concrete.
- Repair cross section with repair material such as non-shrink mortar.



9

Advantages of finding damaged parts

- If the damaged part remains, the damage will spread further.
- Maintaining the reinforcing bar in a healthy state leads to long lasting the structures.
- It is important to know where the reinforcing bar is and whether the cover part is healthy.

10

Theory for finding the end of rebar
Test method
Measurement result
Summary

Propagation of ultrasonic waves

- Ultrasonic propagation velocity in the steel $\Rightarrow V$
- Ultrasonic propagation velocity in the concrete $\Rightarrow v$
- Ultrasonic propagation time from O to $P_i \Rightarrow t_i$

$(V = 5,500 \sim 6,500 \text{ m/s}, v = 4,000 \sim 5,200 \text{ m/s})$
 $V = l_i / (t_i - t_0)$

11

Propagation of ultrasonic waves

$$V(t_1 - t_0) = \ell_1, \dots, V(t_n - t_0) = \ell_n$$

The least square solution V is the minimizer for the function

$$(V(t_1 - t_0) - \ell_1)^2 + \dots + (V(t_n - t_0) - \ell_n)^2$$

$$\Phi(V) = \sum (V(t_i - t_0) - \ell_i)^2$$

$$\Phi'(V) = 2 \sum (V(t_i - t_0) - \ell_i) \times (t_i - t_0) = 0$$

$$\sum (V(t_i - t_0)^2 - \ell_i(t_i - t_0)) = 0$$

$$V = \frac{\sum \ell_i (t_i - t_0)}{\sum (t_i - t_0)^2}$$

12

Propagation of ultrasonic waves

Propagation time from O to P

$$g(x) = \frac{\ell - x}{V} + \frac{\sqrt{h^2 + x^2}}{v} \Rightarrow \min$$

$$g'(x) = -\frac{1}{V} + \frac{1}{v} \times \frac{1}{2\sqrt{h^2 + x^2}} \times 2x = 0$$

$$\frac{x}{\sqrt{h^2 + x^2}} = \frac{v}{V} \quad \text{Squaring} \Rightarrow \frac{x^2}{h^2 + x^2} = \frac{v^2}{V^2}$$

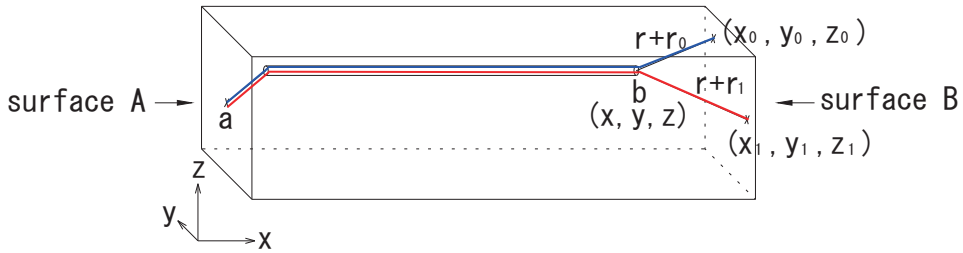
$$V^2 x^2 = v^2 (h^2 + x^2) = v^2 h^2 + v^2 x^2$$

$$(V^2 - v^2)x^2 = v^2 h^2$$

$$x = \frac{vh}{\sqrt{V^2 - v^2}}, \quad L = \frac{Vh}{\sqrt{V^2 - v^2}}$$

13

Conceptual diagram of rebar endpoint identification



$$(x-x_0)^2+(y-y_0)^2+(z-z_0)^2 = (r+r_0)^2 \dots\dots \textcircled{0} \quad (\text{※ } r_0 = 0)$$

$$(x-x_1)^2+(y-y_1)^2+(z-z_1)^2 = (r+r_1)^2 \dots\dots \textcircled{1}$$

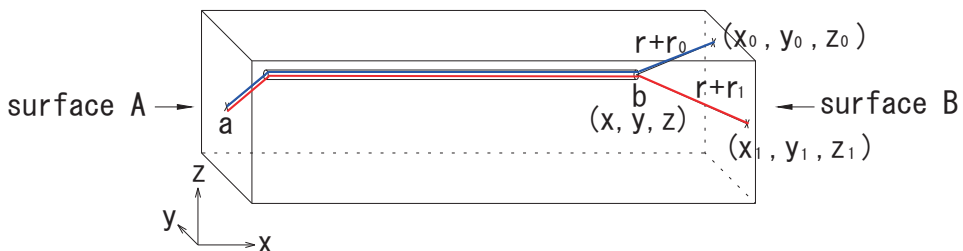
$$\vdots$$

$$(x-x_i)^2+(y-y_i)^2+(z-z_i)^2 = (r+r_i)^2 \dots\dots \textcircled{i}$$

$$(x-x_j)^2+(y-y_j)^2+(z-z_j)^2 = (r+r_j)^2 \dots\dots \textcircled{j}$$

14

Calculation of rebar end point



$$\textcircled{1} - \textcircled{0} \quad \begin{array}{l} (x-x_1)^2+(y-y_1)^2+(z-z_1)^2 = (r+r_1)^2 \\ -) (x-x_0)^2+(y-y_0)^2+(z-z_0)^2 = (r+r_0)^2 \\ \hline \end{array}$$

$$\begin{aligned} -2x(x_1-x_0)+(x_1^2-x_0^2)-2y(y_1-y_0)+(y_1^2-y_0^2)-2z(z_1-z_0)+(z_1^2-z_0^2) = \\ 2r(r_1+r_0)+(r_1^2-r_0^2) \end{aligned}$$

$$\begin{aligned} -2(x_1-x_0)x-2(y_1-y_0)y-2(z_1-z_0)z-2(r_1-r_0)r = \\ -(x_1^2-x_0^2)-(y_1^2-y_0^2)-(z_1^2-z_0^2)+(r_1^2-r_0^2) \end{aligned}$$

15

Calculation of rebar end point

$$\textcircled{1} - \textcircled{0} = 1, \textcircled{2} - \textcircled{0} = 2, \dots, \textcircled{j} - \textcircled{i} = k$$

$$\textcircled{j} - \textcircled{i} \quad \frac{-2(x_j - x_i)x - 2(y_j - y_i)y - 2(z_j - z_i)z - 2(r_j - r_i)r}{a_k \quad b_k \quad c_k \quad d_k} = \frac{-(x_j^2 - x_i^2) - (y_j^2 - y_i^2) - (z_j^2 - z_i^2) + (r_j^2 - r_i^2)}{S_k}$$

$$\begin{pmatrix} a_1 & b_1 & c_1 & d_1 \\ a_2 & b_2 & c_2 & d_2 \\ & & \vdots & \\ a_k & b_k & c_k & d_k \end{pmatrix} \begin{pmatrix} x \\ y \\ z \\ r \end{pmatrix} = \begin{pmatrix} S_1 \\ S_2 \\ \vdots \\ S_k \end{pmatrix}$$

16

Calculation of rebar end point

$$\begin{pmatrix} a_1 & a_2 & & a_k \\ b_1 & b_2 & & b_k \\ c_1 & c_2 & \dots & c_k \\ d_1 & d_2 & & d_k \end{pmatrix} \begin{pmatrix} a_1 & b_1 & c_1 & d_1 \\ a_2 & b_2 & c_2 & d_2 \\ & & \vdots & \\ a_k & b_k & c_k & d_k \end{pmatrix} \begin{pmatrix} x \\ y \\ z \\ r \end{pmatrix} = \begin{pmatrix} a_1 & a_2 & & a_k \\ b_1 & b_2 & & b_k \\ c_1 & c_2 & \dots & c_k \\ d_1 & d_2 & & d_k \end{pmatrix} \begin{pmatrix} S_1 \\ S_2 \\ \vdots \\ S_k \end{pmatrix}$$

$$\begin{matrix} {}^tA & A & {}^tA & S \\ 4 \times k & k \times 4 & 4 \times k & k \times 1 \end{matrix}$$

$${}^tAA = 4 \text{ rows} \times 4 \text{ columns}$$

$${}^tAS = 4 \text{ rows} \times 1 \text{ columns}$$

tA : transposed matrix

17

Calculation of rebar end point

$$\begin{pmatrix} x \\ y \\ z \\ r \end{pmatrix} = \mathbf{x} \begin{pmatrix} S_1 \\ S_2 \\ S_3 \\ S_4 \end{pmatrix} = \mathbf{S}$$

$$\begin{matrix} & & k \times 1 \\ 4 \times k & & \\ & & \\ & & k \times 1 \end{matrix} \mathbf{Ax} = \mathbf{S}$$

$${}^t\mathbf{AAx} = {}^t\mathbf{AS}$$

If ${}^t\mathbf{AA}$ is regular, $\mathbf{x} = ({}^t\mathbf{AA})^{-1} {}^t\mathbf{AS}$

In this case, we can easily solve by the sweep out method.

18

Formulation of specimen

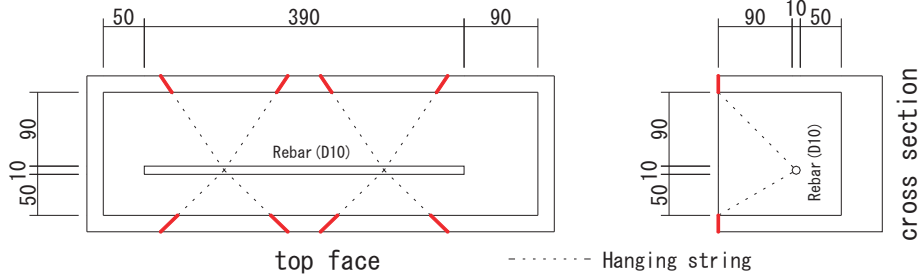
W/C (%)	Unit volumetric mass (kg/m ³)						Water reducing agent	AE agent
	W	C	S1	S2	G			
46.2	153	331	544	233	1092		1.99	0.0132

Unit volume (L)						
W	C	S1	S2	G	Air	合計
153	105	202	91	404	45	1000

Three kinds of formulations are used to prepare specimens.

19

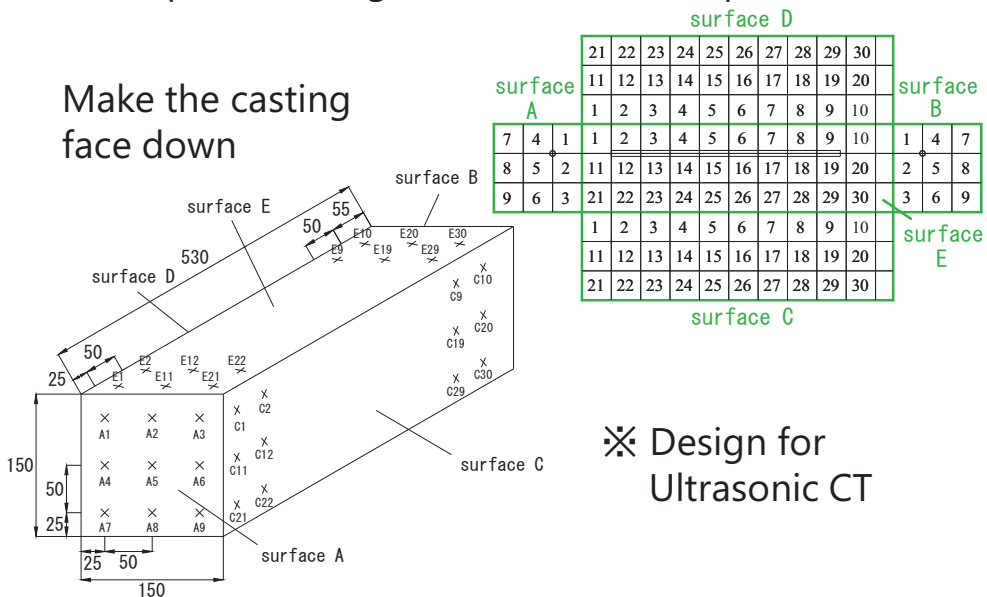
Preparation of specimen



Concrete temperature (°C)	Slump (cm)	Air quantity (%)
13.9	11.0	5.9

Station position diagram of ultrasonic exploration

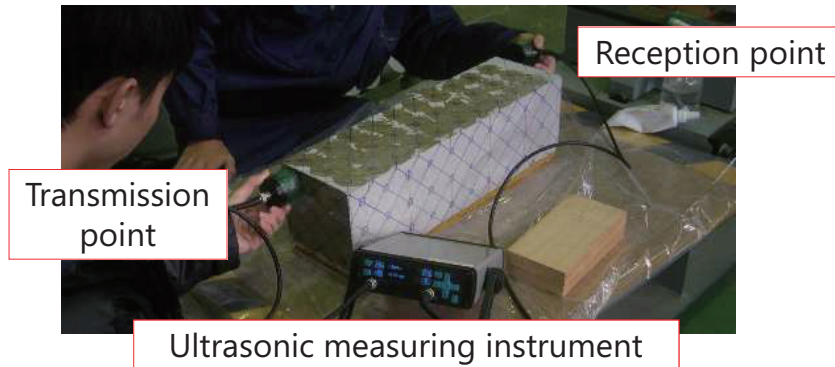
Make the casting face down



✳ Design for Ultrasonic CT

Measurement situation

Apply a contact medium to the surface, apply a terminal to measure.



22

Measurement result of ultrasonic waves

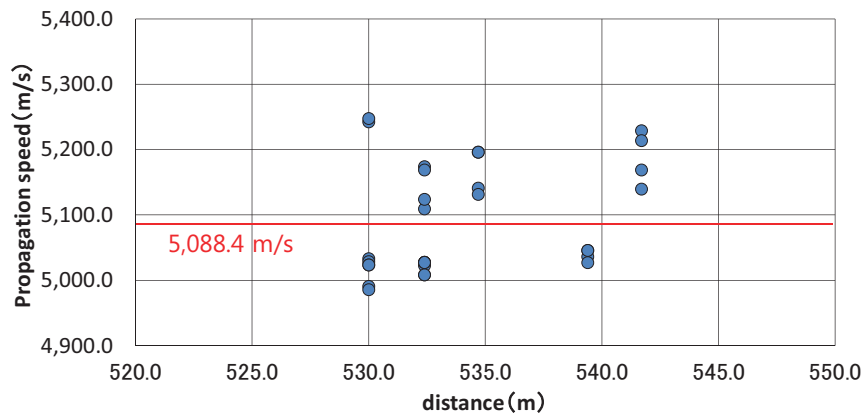
No	Moisture content(%)	Surface temperature(°C)	Room temperature(°C)	Humidity(%)	Transmission point	Reception point	Distance between station and station(mm)	Propagation time(μs)
1	4.6	10.4	11.5	33	A-6	B-6	530	101.1
2	4.6	10.4	11.5	33	A-6	B-7	542	105.4
3	4.6	10.4	11.5	33	A-6	B-8	535	104.0
4	4.6	10.4	11.5	33	A-6	B-9	532	104.2
5	4.6	10.4	11.5	33	A-7	B-6	542	103.6
6	4.6	10.4	11.5	33	A-7	B-7	530	105.3
7	4.6	10.4	11.5	33	A-7	B-8	532	105.9
8	4.6	10.4	11.5	33	A-7	B-9	539	106.9
9	4.6	10.4	11.5	33	A-8	B-6	535	102.9
10	4.6	10.4	11.5	33	A-8	B-7	532	105.9
11	4.6	10.4	11.5	33	A-8	B-8	530	105.4
12	4.6	10.4	11.5	33	A-8	B-9	532	105.9
13	4.6	10.4	11.5	33	A-9	B-6	532	102.9
14	4.6	10.4	11.5	33	A-9	B-7	539	107.1
15	4.6	10.4	11.5	33	A-9	B-8	532	106.3
16	4.6	10.4	11.5	33	A-9	B-9	530	106.2
17	4.6	10.4	11.5	33	B-6	A-6	530	101.0

⋮

We summarize the conditions for the measured propagation speed and summarized it in the table above. (N = 32)

23

Ultrasonic propagation velocity in the concrete



The ultrasonic waves propagation velocity in the concrete was calculated using the least squares method.

24

Measurement results used for calculation on the surface A

Transmission point	Reception point	T [s]	i, j	R _j (R _i) [m]	X _j (X _i) [m]	Y _j (Y _i) [m]	Z _j (Z _i) [m]
B-1	A-1	0.0000985	1	0.000	0	0.125	0.125
B-1	A-2	0.0000985	2	0.000	0	0.075	0.125
B-1	A-4	0.0000992	3	0.004	0	0.125	0.075
B-1	A-5	0.0000996	4	0.006	0	0.075	0.075
B-1	D-1	0.0000927	5	-0.030	0.025	0.15	0.125
B-1	D-11	0.0000943	6	-0.021	0.025	0.15	0.075
B-1	E-1	0.0000923	7	-0.032	0.025	0.125	0.15
B-1	E-11	0.0000931	8	-0.027	0.025	0.075	0.15
B-2	A-1	0.0000990	9	0.000	0	0.125	0.125

N=4 N=8 ⇒ 32data

⋮

25

Matrix creation

Matrix: A 496×4

	a	b	c	d
1	0	0.1	0	0
2	0	0	0.1	-0.00712
3	0	0.1	0.1	-0.01119
4	-0.05	-0.05	0	0.059025
5	-0.05	-0.05	0.1	0.042743
6	-0.05	0	-0.05	0.063096
7	-0.05	0.1	-0.05	0.054955

⋮

Matrix: S 496×1

	S
1	0.01
2	0.010013
3	0.020031
4	-0.00663
5	0.002957
6	-0.0065
7	0.003255

⋮

$$j=32, i=31$$

$$\frac{32 \times 31}{2} = 496$$

Matrix: tA 4×496

	1	2	3	4	5	6	7	
a	0	0	0	-0.05	-0.05	-0.05	-0.05	
b	0.1	0	0.1	-0.05	-0.05	0	0.1	...
c	0	0.1	0.1	0	0.1	-0.05	-0.05	
d	0	-0.0071238	-0.0111945	0.05902544	0.04274256	0.06309616	0.05495472	

26

Matrix calculation

Matrix: tAA 4×4

0.64	0.64	0.64	-0.7335437
0.64	3.84	-0.64	-0.627705
0.64	-0.64	3.84	-1.0722276
-0.7335437	-0.627705	-1.0722276	0.89263274

=

Matrix: tAS 4×1

0.15070235
0.34523312
0.33704841
-0.1951307

$${}^tAAx = {}^tAS$$

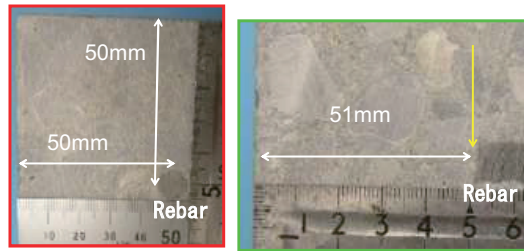
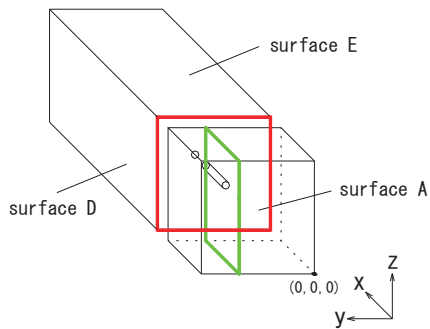
Simultaneous equations

①	0.64 X +	0.64 Y +	0.64 Z +	-0.733543744 R =	0.150702353
②	0.64 X +	3.84 Y +	-0.64 Z +	-0.627705024 R =	0.345233122
③	0.64 X +	-0.64 Y +	3.84 Z +	-1.072227648 R =	0.337048409
④	-0.733543744 X +	-0.627705024 Y +	-1.072227648 Z +	0.892632735 R =	-0.195130653

$$X = 0.056\text{m}, Y = 0.100\text{m}, Z = 0.100\text{m}, R = 0.018\text{m}$$

27

Confirm result



Cutting of test piece

$$X = 0.051\text{m}$$

$$Y = 0.150 - 0.050 = 0.100\text{m}$$

$$Z = 0.150 - 0.050 = 0.100\text{m}$$

28

Comparison with calculation result by electromagnetic
induction

Axis	Electromagnetic induction		Ultrasonic wave	
	Coordinate	Error	Coordinate	Error
X	50	-1	56	+5
Y	100	0	100	0
Z	101	+1	100	0

29

Summary (1)

In this study, we attempted to locate rebar with data for CT.

A deviation of 5 mm occurred in the X coordinate, but accurate values could be obtained for the Y and Z coordinates.

In the future, we will prepare a measurement plan of ultrasonic waves for exploring the reinforcing bars and investigate to more precisely locate the rebar positions.

30

Summary (2)

The advantage of this method is that, unlike in the electromagnetic induction method, the correction is not required to find the endpoints of rebar.

This method is also applicable to actual structures.

If we know the position of the rebar, we can calculate the speed of the ultrasonic wave in the cover part and we can know whether there is any abnormality there.

Ultimately, we are aiming to complete ultrasonic CT.

31

Thank you for your attention.

「マス・フォア・インダストリ研究」シリーズ刊行にあたり

本シリーズは、平成 23 年 4 月に設立された九州大学マス・フォア・インダストリ研究所 (IMI) が、平成 25 年 4 月に共同利用・共同研究拠点「産業数学の先進的・基礎的共同研究拠点」として、文部科学大臣より認定を受けたことにともない刊行するものである。本シリーズでは、主として、マス・フォア・インダストリに関する研究集会の会議録、共同研究の成果報告等を出版する。各巻はマス・フォア・インダストリの最新の研究成果に加え、その新たな視点からのサーベイ及びレビューなども収録し、マス・フォア・インダストリの展開に資するものとする。

平成 30 年 10 月
マス・フォア・インダストリ研究所
所長 佐伯 修

Non-destructive inspection for concrete structures and related topics

マス・フォア・インダストリ研究 No.12, IMI, 九州大学

ISSN 2188-286X

発行日 2019 年 2 月 日

編集 滝口 孝志

発行 九州大学マス・フォア・インダストリ研究所

〒819-0395 福岡市西区元岡 744

九州大学数理・IMI 事務室

TEL 092-802-4402 FAX 092-802-4405

URL <http://www.imi.kyushu-u.ac.jp/>

印刷 社会福祉法人 福岡コロニー

〒811-0119 福岡県糟屋郡新宮町緑ヶ浜 1 丁目 11 番 1 号

TEL 092-962-0764 FAX 092-962-0768

シリーズ既刊

Issue	Author / Editor	Title	Published
マス・フォア・インダストリ 研究 No.1	穴田 啓晃 安田 貴徳 Xavier Dahan 櫻井 幸一	Functional Encryption as a Social Infrastructure and Its Realization by Elliptic Curves and Lattices	26 February 2015
マス・フォア・インダストリ 研究 No.2	滝口 孝志 藤原 宏志	Collaboration Between Theory and Practice in Inverse Problems	12 March 2015
マス・フォア・インダストリ 研究 No.3	笈 三郎	非線形数理モデルの諸相：連続，離散，超離散， その先 (Various aspects of nonlinear mathematical models) (: continuous, discrete, ultra-discrete, and beyond)	24 March 2015
マス・フォア・インダストリ 研究 No.4	穴田 啓晃 安田 貴徳 櫻井 幸一 寺西 勇	Next-generation Cryptography for Privacy Protection and Decentralized Control and Mathematical Structures to Support Techniques	29 January 2016
マス・フォア・インダストリ 研究 No.5	藤原 宏志 滝口 孝志	Mathematical Backgrounds and Future Progress of Practical Inverse Problems	1 March 2016
マス・フォア・インダストリ 研究 No.6	松谷 茂樹 佐伯 修 中川 淳一 上坂 正晃 濱田 裕康	結晶のらせん転位の数理	10 January 2017
マス・フォア・インダストリ 研究 No.7	滝口 孝志 藤原 宏志	Collaboration among mathematics, engineering and industry on various problems in infrastructure and environment	1 March 2017
マス・フォア・インダストリ 研究 No.8	藤原 宏志 滝口 孝志	Practical inverse problems based on interdisciplinary and industry-academia collaboration	20 February 2018
マス・フォア・インダストリ 研究 No.9	阿部 拓郎 高島 克幸 縫田 光司 安田 雅哉	代数的手法による数理暗号解析 Workshop on analysis of mathematical cryptography via algebraic methods	1 March 2018
マス・フォア・インダストリ 研究 No.10	阿部 拓郎 落合 啓之 高島 克幸 縫田 光司 安田 雅哉	量子情報社会に向けた数理的アプローチ Mathematical approach for quantum information society	26 December 2018

Issue	Author / Editor	Title	Published
マス・フォア・インダストリ 研究 No.11	松谷 茂樹 佐伯 修 中川 淳一 濱田 裕康 上坂 正晃	結晶転位の先進数理解析 Advanced Mathematical Investigation for Dislocations	7 January 2019



Institute of Mathematics for Industry
Kyushu University

九州大学マス・フォア・インダストリ研究所

〒819-0395 福岡市西区元岡744
URL <http://www.imi.kyushu-u.ac.jp/>